MULTI-SCALE STRUCTURAL DESIGN OF TITANIUM IMPLANTS FOR IMPROVED OSSEOINTEGRATION

A Dissertation
Presented to
The Academic Faculty

by

Alice Cheng

In Partial Fulfillment
of the Requirements for the Degree of
Doctor of Philosophy in the
School of Biomedical Engineering

Georgia Institute of Technology
Emory University
Peking University
December 2016

MULTI-SCALE STRUCTURAL DESIGN OF TITANIUM IMPLANTS FOR IMPROVED OSSEOINTEGRATION

Approved by:

Dr. Barbara Boyan, Advisor
School of Biomedical Engineering
Georgia Institute of Technology

Dr. Cheng Zhu
School of Biomedical Engineering
Georgia Institute of Technology

Dr. Zvi Schwartz
School of Biomedical Engineering
Virginia Commonwealth University

Dr. Krishnendu Roy
School of Biomedical Engineering
Georgia Institute of Technology

Dr. Kenneth Sandhage
School of Biomedical Engineering
Georgia Institute of Technology

Dr. Haifeng Chen
School of Biomedical Engineering
Peking University

Date Approved: September 12, 2016

Bag lady

You gon' hurt your back

Dragging all them bags like that

I guess nobody ever told you

All you must hold on to

Is you

Erykah Badu

ACKNOWLEDGEMENTS

The first time I met Dr. Boyan, her car had just died. The next day, she drove to work in a brand new, gleaming white Mustang. I took away two things that day: 1) Dr. Boyan doesn't mess around; and 2) Dr. Boyan has great taste. Those two things still hold true today. When Dr. Boyan moved from Georgia Tech to Virginia Commonwealth University to build the School of Engineering, the lab dutifully followed. Her vision was much bigger than we could even imagine, and it is clear now after three years that she really means what she says. I continue to be amazed by how much she has done for the University, while still finding the time to write grants, publish and maintain an open office policy for students. All of these tasks require very specific skill sets, yet she seems to juggle all her responsibilities effortlessly, with poise and confidence.

Then I met Dr. Schwartz. Some people still do not believe he exists, but those of us who have worked personally with him know that his influence serves as an invisible hand that guides our daily research lives. Dr. Schwartz truly loves science, and it is evident in the many hours he puts into his students and the laboratory. When I think of someone who made a hobby into a career, I think of Dr. Schwartz. At the same time, Dr. Schwartz serves as simultaneously the most critical and supportive mentor, someone who will make you stay up all night to finish a manuscript and then buy you breakfast in the morning. I have been lucky to have not only one, but two incredible mentors. It has been a blessing to spend the last five years under their tutelage. Thank you.

I would also like to thank my committee members, Dr. Chen, Dr. Roy, Dr. Sandhage and Dr. Zhu. Dr. Chen not only provided scientific guidance, but also unique

philosophical perspectives as my primary mentor for five months in Beijing. Dr. Sandhage contributed invaluable materials science expertise, along with much wordsmithing, with each new draft of our manuscripts. Dr. Zhu has served as an advocate throughout the process, helping me navigate the process of moving to a different school and even a different country. I am honored to have worked with a committee of such established scientists and engineering, who are equally wonderful people.

There are many other people that have directly and indirectly supported work in this thesis. Being able to conduct experiments in a safe, well-stocked and beautiful laboratory environment is possible only because of Sharon Hyzy. All animal work was facilitated by Dr. Josh Cohen, whose patience and leadership have become indispensable in our laboratory. Dr. Carlos Castano and especially Dr. Dmitry Pestov from the VCU Nanocharacterization Core facility essentially served as secondary mentors and taught me so much about materials theory and characterization, and also helped me troubleshoot what seemed like impossible equipment problems. Dr. Kelly Dryden from University of Virginia and Dr. Rong Wang from Tsinghua University were instrumental in developing the electron microscopy portion of the correlative microscopy project. Aiza Humayun, my undergraduate "star," grew into a curious scientist and soon will also be a respected dentist. Illya Kajan and Louis Hopkins helped immensely with cell culture. Justin Osborne still answers my emails regarding computer problems, even if it is just reminding me to restart the computer. Even after moving 500 miles away, Shannon Sullivan was only an email away and provided technical and emotional support that allowed me to navigate and complete the PhD program. Jialei Luo from Peking University, Brentis Henderson from

Georgia Tech and now Jenilee Shanks and Kimberly Whitfield from VCU all provided administrative support.

A work hard, play hard attitude is an important part of our laboratory culture, and has led to great professional and personal relationships. I would like to thank all the past and present members of Boyan / Schwartz lab from Georgia Tech and now VCU, as well as the lab members in the Chen lab during my time in China, especially: Dr. Khairat El Baradie, Dr. David Deutsch, Dr. Christopher Lee, Dr. Jung Hwa Park, Dr. Xiaokun Wang and soon to be Drs. Mu Yang Sun and Kayla Scott. Dr. Rolando Gittens, who was in my shoes just five years ago, first initiated the surface modification studies and continues to be an integral part of this work. Dr. Zhao Lin and Dr. Junjun Zhao provided a refreshing clinical perspective and continue to serve as professional mentors. Dr. Reyhaan Chaudhri, Dr. Jiaxuan Chen and (soon to be Dr.) James Wade were always there for me as informal mentors, and are the equivalent of family. Dr. Billy Wang and (also soon to be Dr.) Tom Bongiorno, though in a neighboring lab, were just as supportive. I am so blessed to claim such talented, overall wonderful people as my friends. No amount of gratitude is sufficient for all that they have done for me.

I would never have even considered graduate school if it wasn't for my undergraduate research advisor, Dr. Erwin Vogler. He was a brilliant scientist, inspiring mentor and talented sitar player, and somehow had the clairvoyance to set a naïve undergraduate student loose in the laboratory. I still remember the pivotal conversation we had that led me to pursue a PhD; six months later, I had received a NSF fellowship and was accepted into my top choice program at Georgia Tech. I would also like to thank Dr.

Richard Ordway, who welcomed me as just a freshman and gave me my first laboratory research experience.

There are also many other educators that have contributed to building me as a scholar and professional. Khanjan Mehta was also an incredible mentor in the humanitarian engineering space, teaching me the importance of sustainable design and guiding my first two papers on social impact. Dr. George Engelmayr sparked my interest in tissue engineering and was always supportive of all my seemingly outrageous scientific and professional ideas; we never run out of content for great conversations. Dr. Gad-el-Hak served as a listening ear and unbiased mentor that was always available. Jeff Gallagher at the Virginia Biotechnology Association was the first person to professionally welcome me to Richmond. My colleagues at the Rare Genomics Institute, especially Dr. Jimmy Lin and Nolin Huddleston, taught me so much about respect, patience and leadership. James Raines, Marty Jacobson, Mark McJunkin, Dr. Alan Benesi, Robert Beaury, Dr. Bill Lewis, John Girvin, Chris Rachor, Kelly Schumaker, Joel McKee, Piroska Balogh, Stacy Vanderpool, Carol Gibson and Josh and Paige Britton were instrumental at different points of my education and transformed the learning process into something fun and enjoyable.

Graduate school is not for the faint of heart! Even with the best professional resources, there is nothing that can replace the comfort of a hug or the joy of laughter from a true friend. Sharmila Giri and Fatema Habib have been a source of sanity and lightheartedness; our email exchanges make many of life's challenges more bearable. Dr. Angela Hwang and I started our undergraduate summer research careers together as roommates, and I have adopted her as my awesome older sister. Dr. Anisha Patel and (soon to be Dr.) Shawn Hakim have become close to family in Richmond. Virgil R. was always

up for a spontaneous adventure. Trang Nguyen, Robert Revnic and Victor Badmaev were incredibly generous with their time and provided a social escape from writing. Frank and Diana Nadu always had a selection of tea for catching up at home, and homemade cookies for the trip back to school. There are many others who have touched my life and I cannot properly acknowledge them all; please know that you are appreciated.

"For I know the plans I have for you," declares the Lord, "plans to prosper you and not to harm you, plans to give you hope and a future" (Jeremiah 29:11). I am extremely grateful for God's mercy, love and guidance throughout my life. He is my source of support, hope and wisdom. I have also been blessed to have been part of many congregations as part of my spiritual journey: St. Paul's Church in Quarryville, Portland Chinese Alliance Church, Chinese Bible Church of Lancaster, Lutheran Church of the Redeemer in Atlanta, Beijing International Christian Fellowship, Eternity Church at VCU and First English Lutheran Church in Richmond. Pastor Bruce Hankee and Janet Hankee had a profound impact on my childhood, raising me in faith and guiding me in prayer and praise.

Finally, I would like to thank my family. My grandmother, Cheng Zhi Li, taught me the value of lifelong learning. My mother, Rong Rong Xu, taught me the importance of leaving a legacy. My father, Wing Cheng, taught me that success is achieved through hard work, resilience and patience. My partner, Jonathan Nadu, taught me to fight, and to be vulnerable. I am eternally grateful for all they have done and all they continue to do for me.

TABLE OF CONTENTS

LIST OF TABLES

LIST OF FIGURES

LIST OF ABBREVIATIONS

µg	microgram
µm	micrometer
2D	two dimensional
3D	three dimensional
AFM	atomic force microscope
ALP	alkaline phosphatase specific activity
AM	additive manufacturing
ANOVA	analysis of variance
ASTM	American Society for Testing and Materials
BIC	bone-to-implant contact
BMP2	bone morphogenetic protein 2
BMP4	bone morphogenetic protein 4
CNC	computer numerical control
COL1	collagen type I
cpTi	commercially pure Titanium
DMEM	Dulbecco's modified essential medium
DNA	deoxyribonucleic acid
DMLS	direct metal laser sintering
ECM	extracellular matrix
EDX	energy dispersive x-ray
ELISA	enzyme linked immunosorbent assay
FBS	fetal bovine serum
FDA	US Food and Drug Administration

FIB	focused ion beam
hOB	human osteoblast
HT	hydrothermal
LCM	laser confocal microscope
LST	laser sintering technology
MG63	human osteosarcoma derived, osteoblast-like cell line
microCT	micro-computed tomography
mL	milliliter
mm	millimeter
mRNA	messenger ribonucleic acid
MSC	mesenchymal stem cell
MWHT	microwave hydrothermal
NHOst	normal human osteoblast
ng	nanogram
nm	nanometer
OCN	osteocalcin
OPG	osteoprotegerin
PBS	phosphate buffered saline
PCR	polymerase chain reaction
PT	pretreated, smooth titanium
RUNX2	runt related transcription factor 2
Sa	average surface roughness
Sz	peak to valley surface roughness
SD	standard deviation
SEM	scanning electron microscope / standard error of the mean

SLA	sand blasted with large grit and acid etched, smooth titanium
TEM	transmission electron microscope
TGF-β	transforming growth factor β
Ti	titanium
TiO_2	titanium dioxide
Ti-6AL-4V	titanium alloyed with 6% aluminum, 4% vanadium
UV	ultraviolet
VEGF	vascular endothelial growth factor
XPS	x-ray photoelectron spectroscopy
XRD	x-ray powder diffraction

SUMMARY

Tissue engineering of bone and cartilage has progressed from simple to sophisticated materials with defined porosity, surface features and the ability to deliver biological factors. Changes in dental implant materials, structural design, and surface properties can all affect biological response. While bulk properties are important for mechanical stability of the implant, surface design ultimately contributes to osseointegration. To avoid illiciting a foreign body response, advancements in functional scaffold design harness the endogenous ability of the body to regenerate. Novel surface modifications inducing combined micro- and nano-roughness on titanium and Ti-6Al-4V substrates contribute to increased wettability and can be tailored to affect cell response. Additive manufacturing by laser sintering can produce three dimensional constructs with custom porosity.

Surface roughness has been largely studied at the micro-scale, but recent studies have highlighted the importance of hierarchical micron/submicron/nano-surface roughness, as well as surface roughness in combination with surface wettability. These multi-dimensional physical properties of scaffolds allow for tissue regeneration at different spatial and temporal scales. Osseointegration of bone-interfacing implants is reduced for many compromised patients, necessitating improved implant design. Though material and mechanical properties of titanium make it attractive for load-bearing dental and orthopaedic implants, limited advancements have been made to increase success and survival after placement in the body. An understanding of both the materials science and biology is crucial for developing novel dental implant materials and surface modifications for improved osseointegration.

Micro-to-nanoscale surface topographies of orthopaedic and dental implants can affect fluid wetting, biological response, and osseointegration. Nanoscale surface modification methods are often not readily scalable to three-dimensional implants and/or can degrade other implant properties. A novel low-temperature microwave hydrothermal (MWHT) oxidation process was examined for nanoscale roughening of titanium surfaces. Nanoscale protuberances (with average diameters of 23-105 nm) were generated on micro-rough (SLA) titanium surfaces via 200°C MWHT treatment in H2O or aqueous H2O2 or NH4OH solutions for 1-40 h. The hydrophilicity of SLA surfaces was dramatically enhanced by such MWHT treatments (contact angles decreased from 103 to < 10 degrees) and such enhanced hydrophilicity was retained after 119 days in saline. Cell lysate analyses of MG63 osteoblasts cultured on MWHT-treated (1M NH4OH, 1 h) SLA surfaces yielded similar values of DNA content, alkaline phosphatase specific activity (ALP), osteocalcin, osteoprotegerin, and vascular endothelial growth factor (VEGF) as for cells cultured on SLA control surfaces. Analyses of normal human osteoblast (NHOst) cells cultured on MWHT-treated (2.5M NH4OH, 1 h) SLA surfaces yielded higher DNA content, similar ALP, similar osteoprotegerin values, and similar VEGF values, although lower osteocalcin values, than for SLA controls. MWHT processing provides a scalable, low-temperature route for tailoring nanoscale topographies on orthopaedic and dental titanium implants for enhanced wetting without dramatically altering osteoblast cell behavior.

The correct surface properties of a material can be further improved by a better understanding of the biology-material interface. Correlative light and electron microscopy provides a way to characterize the cell-material interaction across multiple spatial scales. However, current techniques that are able to track the same cell across multiple imaging

modalities are limited to optically transparent or pre-processed materials. We present a novel correlative method that tracks the same cell on titanium substrates across confocal laser (CLM), scanning electron (SEM) and transmission electron microscopy (TEM). CLM correlates surface micro-roughness with cell morphology and cytoskeleton. SEM adds resolution at the nano-scale for additional observation of surface nano-roughness, and also provides chemical mapping through electron dispersive x-ray spectroscopy. Focused ion beam (FIB) can image cells at a >50° tilt and provide depth resolution of cross sections after milling. FIB can also prepare thin sections of the cell-material interface for high resolution imaging of regions of interest in TEM or three-dimensional reconstructions in electron tomography. This work describes single cell correlative light electron microscopy for the first time on clinically relevant, rough titanium substrates. This platform method allows for enhanced understanding of the cell-material interface for designing better biomaterials.

We then wanted to compare the in osseointegration of hierarchical surface roughness on laser sintered titanium–aluminum–vanadium (Ti–6Al–4V) implants to those of conventionally machined implants on osteoblast response in vitro and osseointegration. Laser sintered disks were fabricated to have micro-/nano-roughness and wettability. Control disks were computer numerical control (CNC) milled and then polished to be smooth (CNC-M). Laser sintered disks were polished smooth (LST-M), grit blasted (LST-B), or blasted and acid etched (LST-BE). LST-BE implants or implants manufactured by CNC milling and grit blasted (CNC-B) were implanted in the femurs of male New Zealand white rabbits. Most osteoblast differentiation markers and local factors were enhanced on rough LST-B and LST-BE surfaces in comparison to smooth CNC-M or LST-M surfaces

for MG63 and normal human osteoblast cells. To determine if LST-BE implants were osteogenic in vivo, we compared them to implant surfaces used clinically. LST-BE implants had a unique surface with combined micro-/nano-roughness and higher wettability than conventional CNC-B implants. Histomorphometric analysis demonstrated a significant improvement in cortical bone-implant contact of LST-BE implants compared to CNC-B implants after 3 and 6 weeks. However, mechanical testing revealed no differences between implant pullout forces at those time points. LST surfaces enhanced osteoblast differentiation and production of local factors in vitro and improved the osseointegration process in vivo.

Surface roughness studies have traditionally been evaluated on a two dimensional or solid surface, while implant geometry plays an often overlooked role clinically. The addition of porosity to traditionally solid titanium metal implants has been suggested to more closely mimic the natural mechanical properties of bone and increase osseointegration in dental and orthopaedic implants. In this study, we used a human trabecular bone template to design and manufacture Ti-6Al-4V constructs with varying porosity via laser sintering. Characterization of constructs revealed interconnected porosities ranging from 15-70% with compressive moduli of 2063-2954 MPa. These constructs with macro porosity were further surface-treated to create a desirable multi-scale micro-/nano-roughness, which has been shown to enhance the osseointegration process. MG63 cells exhibited high viability when grown on the constructs. DNA content and ALP, an early differentiation marker, decreased as porosity increased, while OCN, a late differentiation marker, as well as OPG, VEGF and BMPs 2 and 4 increased with increasing porosity. 3D constructs with the highest porosity and surface modification supported the

greatest osteoblast differentiation and local factor production. These results indicate that additively manufactured 3D porous constructs mimicking human trabecular bone and produced with additional surface treatment can be customized for increased osteoblast response. Increased factors for osteoblast maturation and differentiation on high porosity constructs suggest the enhanced performance of these surfaces for increasing osseointegration in vivo.

We next evaluated cellular response to three-dimensional (3D) porous Ti-6Al-4V constructs fabricated by additive manufacturing using laser sintering to have low (LP), medium (MP) and high porosity (HP) with low (LR) and high resolution (HR) based on a CT scan of human trabecular bone. After surface processing, construct porosity ranged from 41.0% to 76.1% but all possessed micro-/nano- surface roughness and similar surface chemistry containing mostly Ti, O and C. MG63 osteoblast-like cells and normal human osteoblasts favored 3D compared to 2D solid constructs. First, MG63 cells were used to assess differences in cell response to 2D compared to 3D constructs with LR or HR. MG63 cells were sensitive to porosity resolution and exhibited increased OCN, VEGF, OPG and BMP2 on HR 3D constructs compared to 2D and LR 3D constructs. MG63 cells also exhibited porosity-dependent responses on HR constructs, with up to a 6.9-fold increase in factor production on LP-HR and MP-HR constructs compared to HP-HR constructs. NHOsts were then used to validate biological response on HR constructs. NHOsts exhibited decreased DNA content and ALP activity and up to a 2.9-fold increase in OCN, OPG, VEGF, BMP2 and BMP4 on 3D HR constructs compared to 2D controls. These results indicate that osteoblasts prefer a 3D architecture compared to a 2D surface, and are

sensitive to the resolution of trabecular detail and porosity parameters of laser sintered, 3D Ti-6Al-4V constructs.

Implants in bone are colonized by mesenchymal stem cells (MSCs), which can differentiate into osteoblasts and contribute to osseointegration. We examined osteoblast differentiation and matrix mineralization of human MSCs cultured on laser sintered Ti-6Al-4V constructs with varying porosity and at different time scales. 2D solid disks and low, medium and high porosity (LP, MP, and HP) 3D constructs based on a human trabecular bone template were laser sintered from Ti-6Al-4V powder and further processed to have micro and nanoscale roughness. hMSCs exhibited greater osteoblastic differentiation and local factor production on all 3D porous constructs compared to 2D surfaces, which was sustained for 9 days without use of exogenous factors. hMSCs cultured for 8 weeks on MP constructs in osteogenic medium (OM), OM supplemented with BMP2 or collagen-coated MP constructs in OM exhibited bone-like extracellular matrix mineralization. Use of bio-inspired porosity for the 3D architecture of additively manufactured Ti-6Al-4V enhanced osteogenic differentiation of hMSCs beyond surface roughness alone. These results indicate that a 3D over a 2D environment is able to promote osteoblastic differentiation of MSCs over time, and present a novel way of evaluating MSC mineral production on 3D porous constructs.

To translate our in vitro results to osseointegration in vivo, we examined the ability of additively manufactured Ti-6Al-4V constructs with bone trabeculae-inspired porosity and micro-/nano-textured surface roughness to enhance vertical bone ingrowth in a rat calvarial onlay model. Male and female osteoblasts were seeded on constructs to analyze in vitro cell morphology and response. In vivo, implants were placed on rat calvaria for 10

weeks to assess vertical bone ingrowth, mechanical stability and osseointegration. Both male and female primary human osteoblasts showed higher levels of osteocalcin, OPG, VEGF and BMP2 on porous constructs compared to solid laser sintered controls with the same surface roughness. Porous implants placed in vivo resulted in an average of 3.1±0.60 mm3 vertical bone growth within implant pores, resulting in osseointegration of the constructs. The amount of new bone was similar with or without the use of demineralized bone matrix putty (DBX). In addition, porous implants had significantly higher pull-out strength values than solid implants, and no differences in pull-out strength were observed between porous implants with or without DBX. Scanning electron images revealed that bone failure occurred within the bone near the base of implants, indicating that newly formed bone osseointegrated well along the surface of porous implants. Histological results corroborated vertical bone growth and indicated a higher level of bone formation within the center of porous implants.

Finally, we compared the osseointegration of laser sintered solid and porous implants with a human trabeculae-inspired porosity with the same surface modification in a rabbit femoral model. After characterization, implants were inserted transaxially into rabbit femora and pull-out testing, microCT and histology were conducted after 10 weeks. Mechanical testing and histology showed no differences in pull-out strength and bone to implant contact, respectively. However, both microCT and histology showed significantly higher new bone volume for porous compared to solid implants. Bone growth was observed into porous implant pores, especially near the apical portions of the implant interfacing with the cortical bone. These results show that laser sintered Ti-6Al-4V implants with

trabecular porosity promote bone growth and may be used as a superior alternative to solid implants for bone-interfacing implants.

This work indicates that structural micro- and nano-modification at the surface, combined with macro-scale porosity, can enhance osteoblastic differentiation and maturation in vitro, and osseointegration in vivo.

CHAPTER 1

SPECIFIC AIMS

Over 880,000 total joint replacement surgeries are performed and two million dental implants are placed in the US annually [1, 2]. Titanium is a preferred material for dental and orthopaedic implants due to its high strength-to-weight ratio, low corrosion, and ability to osseointegrate with bone. However, smoking, diabetes, age and periodontal disease are all factors that impede full osseointegration of the implant with bone [3-5]. Implant surface roughness has been implicated in direct and indirect biological responses at the bone-implant interface, including regulation of osteoblastic differentiation [6, 7]. Studies have shown that combined micro- and nano-scale features on titanium implant surfaces increase MSC differentiation into osteoblasts, leading to a more differentiated phenotype in vitro [8, 9] and better osseointegration in vivo [10]. Surface modification methods such as high temperature oxidation [9], anodization [8, 11] and deposition [12] have been introduced to produce nano-features on solid titanium implant surfaces, but these methods subject the surface to high temperature or harsh solvents, which can also change the bulk mechanical and material properties of the device. In addition to the implant surface, macro-structural features of the implant such as porosity also contribute to enhanced bone growth, with mechanical properties more closely mimicking that of bone [13].

The objective of this thesis is to characterize material properties of and biological response to titanium implant modifications at the macro-, micro- and nano-scales, with the broader goal of improving osseointegration in clinical applications. **The overall**

hypothesis of this thesis is that multi-scale structural features of titanium implants can be optimized to obtain enhanced osteoblast response and osseointegration.

1.1 Specific Aim 1

Characterize effects of micro- and nano-roughness on osteoblastic response on and osseointegration of clinically relevant titanium substrates.

Hierarchical micro- / nano- roughness on titanium substrates has been shown to enhance osteoblast response. However, most methods used to produce nano-scale roughness use pre-defined templates that are not scalable, or require high temperatures that can alter the bulk mechanical properties of titanium. In addition, characterization of cell response on novel surfaces is compared in aggregate to control surfaces, which makes it challenging to elucidate which specific morphological and cytoskeletal cellular components contribute to enhanced response to surfaces. The *objective* of this aim was to develop and characterize biological response to low temperature nano-modification techniques for clinically relevant titanium substrates. The *hypothesis* was that combined micro- / nano- roughness of titanium substrates can create desirable surface properties to enhance osteoblast response and osseointegration.

1.2 Specific Aim 2

Optimize macro-scale trabecular porosity with surface micro- and nano-roughness of Ti-6Al-4V implants for enhanced cell response and osseointegration.

Implant porosity leads to a decreased elastic modulus to better mimic the natural mechanical properties of the body, and allows for bone infiltration to enhance osseointegration. Until recently, manufacturing of porous titanium constructs was limited

to porous coatings or geometric templates, and difficult to scale. Advancements in image processing and additive manufacturing allow for design versatility and high precision, scalable manufacturing. Not only can implant size and shape be tailored to the patient, but implant porosity can also be designed to mimic trabecular geometry. The *objective* of this aim was to optimize bone trabeculae-inspired porosity on laser sintered Ti-6Al-4V constructs and evaluate cell response to and osseointegration of these implants. The *hypothesis* was that a 3D trabecular environment with micro- / nano- surface roughness can enhance osteoblast differentiation and maturation, and osseointegration *in vivo*, over a comparable solid surface.

The outcome of this work will provide an innovative, scalable and clinically translatable solution for increasing osseointegration rates in compromised patients with bone-interfacing implants. This is significant due to the increasing number of dental and orthopaedic implant placements, as well as the increasing lifespan of patients receiving implants. Enhancing osseointegration can increase patient satisfaction and decrease hospital burden. In addition, novel characterization techniques can provide better insight into the material-biology interface to inform future design of biomaterials. This work is expected to provide a sufficient comprehensive material characterization and biological evaluation of a new generation of bone-interfacing implants for clinical use.

CHAPTER 2

BACKGROUND: IMPLANT SURFACE DESIGN REGULATES MESENCHYMAL STEM CELL DIFFERENTIATION AND MATURATION

In [Boyan BD, Cheng A, Olivares-Navarrete R and Schwartz Z. Implant surface design results mesenchymal stem cell differentiation and maturation. Advances in Dental Research. 2016. 28(1):10-17]

2.1. Introduction

Bone is a dynamic tissue that experiences constant remodeling. When a dental implant is placed, it causes injury to the bone and requires a cascade of events to complete regeneration. Studies on early phase healing show that implant surface design can contribute to successful osseointegration – or failure – of dental implants [14]. During early healing, proteins, blood, immune cells, and osteoprogenitor cells interact with the biomaterial (Figure 2.1). These interactions ultimately affect implant osseointegration [15].

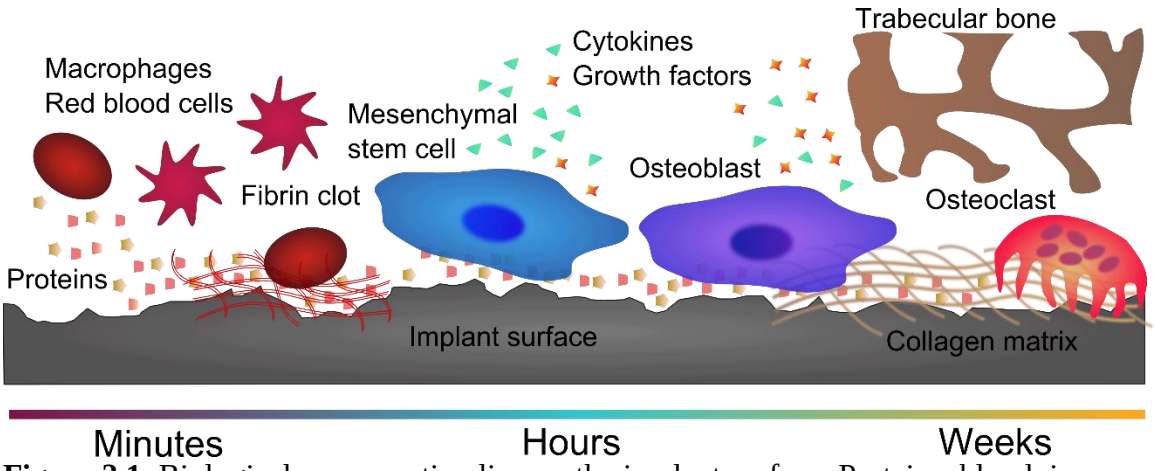

Figure 2.1. Biological response timeline on the implant surface. Proteins, blood, immune cells, and osteoprogenitor cells interact with the biomaterial during the early stages of healing. These interactions are surface dependent and can affect osteoblastic differentiation, maturation and local factor production, and finally matrix formation and implant osseointegration.

Although many studies have attempted to standardize and characterize mesenchymal stem cells (MSCs), the scientific community is still far from a complete understanding of how these cells contribute to the osseointegration process [16]. In this review, we summarize the influence of physical surface parameters on MSC response to dental implant materials. It is our hope that these insights on osteoblastic signaling pathways in response to surface roughness, cell cytoskeletal arrangement, clinical variables contributing to implant osseointegration, and differential biological responses to roughness at different scales can be used for further understanding the cell-material interface in implant dentistry, inspiring the design of a new generation of implants.

2.2 Surface Roughness

Surface roughness at the micro-scale has now become an important parameter in clinical implant design for osseointegration [17]. Surface roughness not only increases surface area, but also affects cell morphology and increases osteoblastic differentiation, bone formation and bone remodeling [18, 19]. Recent studies show that microtextured titanium surfaces, without additional osteogenic factors, are able to promote osteoblastic differentiation and maturation [7] and implant osseointegration [20].

Although various materials have been studied for use in dental implants, titanium and its alloys are still most commonly used. Our laboratory model is based on two titanium surfaces, one smooth and one rough. Pretreated surfaces (PT) are grade 2 titanium that have undergone a degreasing and acid pre-treatment procedure. These surfaces, which are smooth at the microscale, are further processed by sandblasting with large grit and acid etched to produce SLA surfaces possessing approximately a five-fold increase in surface

roughness. The PT and SLA surfaces have allowed us to explore in depth the effect of clinically relevant physical surface properties on cell response and implant osseointegration. We have shown that MSCs and immature osteoblasts consistently exhibit higher osteocalcin, a later marker of osteoblast differentiation, on SLA surfaces compared to on PT surfaces [21, 22], suggesting enhanced differentiation and maturation of osteoblast lineage cells on rough surfaces compared to smooth surfaces. *In vivo*, smooth implants result in fibrous capsule formation over time, or osseointegration with low bone-to-implant contact, whereas implants with micro-roughness are able to achieve osseointegration and higher levels of bone to implant contact [23].

Nano-structures and resulting nano-roughness on surfaces are defined by the ASTM International as having structures that are 1 to 100nm in at least one dimension [24]. Although it has been shown by our lab and others that micron scale and submicron scale roughness are important for osteoblast differentiation and maturation *in vitro* and osseointegration *in vivo*, only recently has nano-roughness been recognized as a possible contributing factor to these phenomena [25, 26]. From a biological perspective, surface nanostructures are intriguing because they have the potential to affect protein adsorption and the resulting integrin attachment, focal adhesion formation and cellular response to a biomaterial [25].

In addition to smooth PT and rough SLA surfaces, our lab has also used a hydrophilic SLA surface, which has a comparable micro-structure as SLA, to assess the effects of wettability on cell response. The modified SLA (modSLA) surface is processed in a nitrogen atmosphere and stored in isotonic sodium chloride to prevent exposure to atmospheric hydrocarbons. Hydrophilic modSLA surfaces have spontaneously formed

nanostructures in addition to their already existing micro-roughness, which were formed during aging of the surfaces in saline [27]. Prior to this finding, "nano" was considered, but not as a convoluting factor, in surface analysis. Most research had focused on nano-roughness or surface energy separately, without considering the possibility of a synergistic effect. These discoveries lead us to further attempt to delineate effects of surface nano-topography and wettability [28-30].

Multi-scale Surface Roughness

Recent studies have highlighted the need for hierarchical surface roughness, occurring at both the micron- and submicron scale, to be present in order for osteoblasts to respond synergistically to surface energy and topography [31, 32]. To understand the effects of nanostructures and hierarchical surface roughness, we developed a novel method of generating nanostructures on clinically relevant micro-rough surfaces using a thermal oxidation method [9]. Smooth PT surfaces were thermally oxidized at 740^{o}C for 45, 90, or 180 minutes. Nanostructures were homogeneously distributed on the surface, ranging from 60nm to 360nm in diameter depending on oxidation time. SLA surfaces showed a similar distribution of submicron and nanostructures across the surface. Osteocalcin, osteoprotegerin and vascular endothelial growth factor (VEGF) protein levels were all upregulated in osteoblast cultures on combined micro-/nano-rough surfaces compared to smooth, nano-rough only and micro-rough only surfaces. The ability to mimic bone, which also has hierarchical roughness, is thought to contribute to the positive biological response to these surfaces with multi-scale roughness [25].

Determining the specific role of nanoscale roughness on cell response is confounded by the complexity of the system. Responses of cells in the osteoblast lineage to surface topography vary among cell lines and osteoblast maturation state [22, 33, 34]. MG63 osteoblast-like cells are commonly used for *in vitro* studies [9, 35, 36]. MG63 cells, which were initially isolated from a human osteosarcoma, exhibited increased maturation and local factor production on combined nano-/micro-rough titanium surfaces, but human MSCs exhibited a less robust response [22]. Because all surfaces were relatively hydrophobic in this study, the impact of surface energy in comparison to that of nanotopography is unknown. These studies not only highlight the importance of experimental design when understanding biological response to materials, but also show the need to assess multiple variables to fully understand this complex system.

Surface topography is also important for three-dimensional (3D) constructs. Studies using electrospun titanium 3D scaffolds showed that cell proliferation is dependent upon surface microroughness, while osteoblastic differentiation and local factor production depends upon both surface microroughness and electrospun nanofiber diameter [33]. As is the case on 2D substrates, integrin α2β1 signaling mediates the cellular response to roughness of the 3D surfaces [37]. These 3D materials served as early prototypes for production of trabecular porosity-inspired Ti-6Al-4V constructs produced by additive manufacturing. Osteoblasts showed porosity-dependent responses in proliferation, differentiation and local factor production when grown on constructs with interconnected porosity ranging from 15-70% [38]. These studies suggest 3D porous implants as a possible option for increasing implant osseointegration in compromised patients.

The combination of nano-roughness and wettability of surfaces plays a pivotal role in the early stages of implant healing. Distinct nanostructures on a hydrophobic surface can trap air bubbles, thus influencing the adsorption profile of proteins onto the surface and the resulting cellular adhesion and healing cascade [39]. To investigate the early mechanisms of wound healing on biomaterial surfaces, researchers recently compared protein adsorption and blood coagulation on hydrophobic and hydrophilic micro-rough commercially pure Ti (cpTi), hydrophobic and hydrophilic micro-/nano-rough cpTi, hydrophobic micro-rough titanium zirconium (TiZr) alloy and hydrophilic micro-/nano-rough TiZr alloy surfaces [40]. Fibrinogen and fibronectin adsorption increased on hydrophilic micro-/nano-rough surfaces compared to any of the other surfaces, regardless of the material. The presence of micro-/nano-roughness alone was able to increase protein adsorption compared to hydrophilic surfaces without nanostructures, but not as much as the combination of hydrophilicity and nanostructures. In contrast, hydrophilicity alone was the main contributing factor to blood coagulation, and the combination of hydrophilicity and micro-/nano-roughness increased coagulation the most. These results point toward the dynamic interplay between nano-roughness and hydrophilicity on the early implant response, corroborating the importance of implant surface design on biological response.

2.3. Signaling Pathways

Several biological pathways have emerged as critical for MSC and osteoblast cell response to surface roughness (Figure 2.2). Osteoinductive factors were first reported by Marshall Urist in 1965 [41], leading to the cloning of the gene for BMP2 [42]. BMP2 is now used clinically for bone regeneration in a variety of applications, including sinus lifts

[43]. We have shown that osteoblasts produce BMP2 when cultured on microtextured Ti and Ti-6Al-4V surfaces, suggesting that they can influence osteoblast differentiation in other cells not on the surface via paracrine regulation [34, 44]. MSCs treated with conditioned medium from osteoblasts cultured on microrough surfaces were driven toward an osteogenic lineage, supporting this hypothesis [7]. Subsequent studies showed that signaling via α2β1 integrins also induced secretion of Dkk2, which had a paracrine effect on MSCs [21, 45].

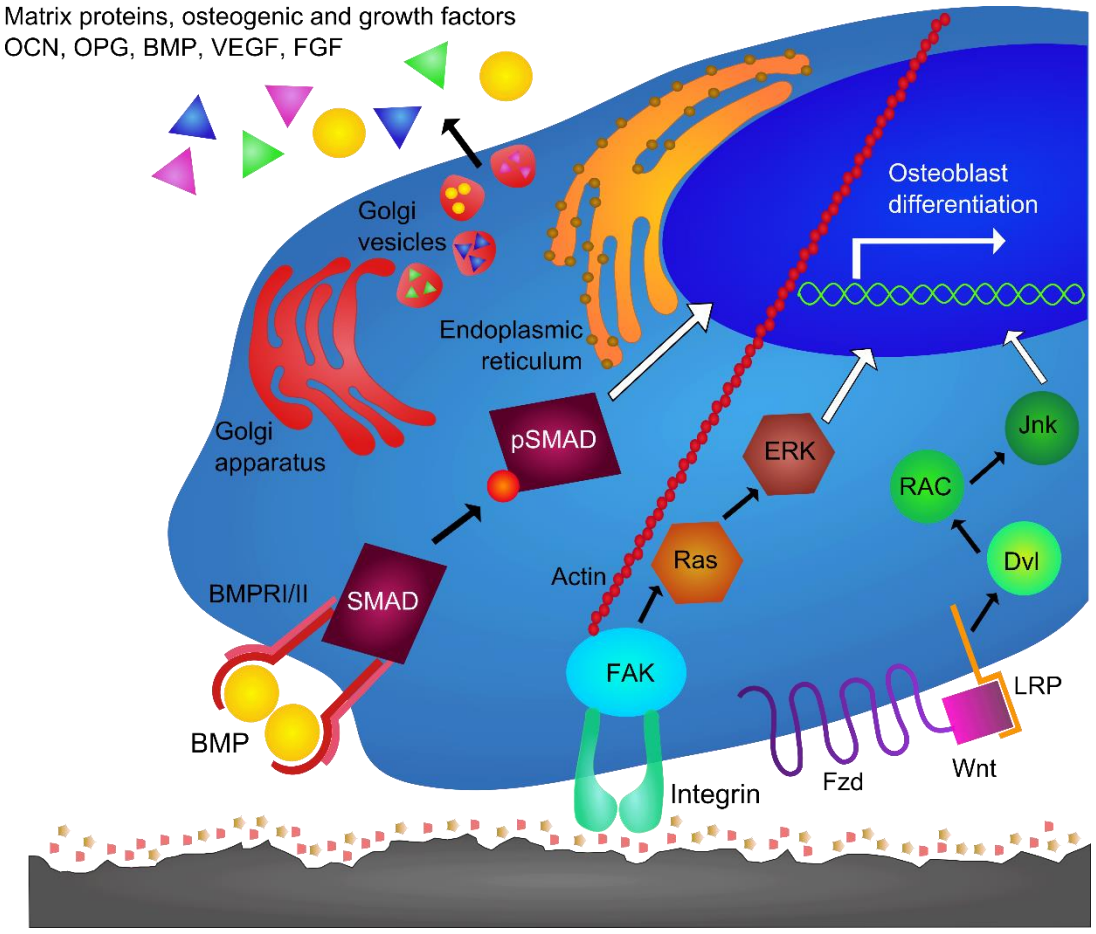

Figure 2.2. Signaling pathways involved in cellular response to implant materials. Integrins are transmembrane receptors that aid in attachment and contribute to differentiation of MSCs on implant surfaces. BMPs and Wnts are important proteins involved in the osteoblastic differentiation pathway. As cells differentiate and mature and bone is formed, local factors such as OCN, OPG, BMPs, VEGF and FGF2 are secreted.

Mechanisms regulating MSC differentiation and maturation down an osteoblastic pathway on micro-rough and hydrophilic surfaces involve a variety of signaling pathways. The Wnt signaling pathway is important in embryonic development and for cell proliferation and differentiation. Although the canonical Wnt pathway signals through Wnt3a and β-catenin, our lab has found it is the non-canonical pathway, which signals through Wnt5a and calcium, that results in the response of MSCs to surface roughness [21]. While treatment with Wnt3a maintained the mesenchymal phenotype, treatment with Wnt5a upregulated integrin subunits α2 and β1, BMP2, BMP4, and osteoblast differentiation markers on rough titanium surfaces compared to control rough surfaces. Silencing Wnt5a upregulated Wnt3a expression in MSCs. This and other studies suggest that the non-canonical Wnt5a can inhibit the Wnt3a pathway on rough implant surfaces [44, 46]. Dkk2, an inhibitor of the Wnt canonical pathway, is secreted by osteoblasts grown on microrough titanium surfaces, and secretion of this protein is thought to exert its paracrine effects on MSC differentiation distal to the implant site [7]. MG63 osteoblasts grown on microrough SLA surfaces also had increased expression of canonical Wnt inhibitor AXIN2 and BMPs 2 and 4 compared to tissue culture polystyrene (TCPS) and smooth PT surfaces [44]. Further work suggests that while canonical Wnt signaling is involved in early osteoblast differentiation, Ca^{2+} dependent Wnt5a signaling as well as Dkk2, BMPs and integrins regulates osteoblast differentiation on hydrophilic surfaces with hierarchical roughness [21, 44, 45].

These studies demonstrate that surface properties are able to regulate MSC fate through a positive-feedback loop between the calcium-dependent Wnt5a pathway, integrin α2β1 and BMPs. Recent work suggests that 1a,25-dihydroxyvitamin D3 [$1\alpha,25(OH)_2D_3$],

which also synergistically affects osteoblast response in combination with surface roughness, may compete with Wnt5a to regulate proliferation and differentiation in osteoblasts. This may have implications in patients receiving Vitamin D treatment [47, 48].

It is clear that soluble factors produced by cells in response to surface topographic cues can influence differentiation of cells not on the surface. When grown in co-culture with osteoblasts plated on titanium surfaces, human MSCs were differentiated toward osteoblastic phenotype and showed higher levels of osteocalcin, VEGF, and TGF-β1. These effects were higher when the osteoblasts were cultured on modSLA surfaces than on SLA surfaces [7]. These results point toward the indirect effects of titanium surface micro-/nano-roughness and hydrophilicity on cells distal from the implant site. MG63 cells show higher alkaline phosphatase specific activity and osteocalcin production, as well as higher BMP2 and noggin levels when grown on modSLA surfaces, which are both hydrophilic and have nano-roughness, than on micro-rough only SLA surfaces. Addition of exogenous BMP2 or knockdown of noggin in cultures enhanced osteoblast maturation, suggesting paracrine regulation of osteoblast maturation [49]. Angiogenic factors VEGF-A and FGF-2 are both increased significantly on modSLA surfaces in comparison to smooth or micro-rough only surfaces, and conditioned media from cultures grown on modSLA stimulate tube formation in cultures of human umbilical vein endothelial cells (HUVEC) to a greater extent than media from SLA cultures, suggesting the combination of roughness and hydrophilicity can enhance blood vessel formation [6].

The influence of surface roughness extends indirectly beyond the cellular level to the microenvironment by regulating inflammation and bone remodeling. Rough SLA and modSLA titanium surfaces decreased production of pro-inflammatory interleukins IL6,

IL8, and IL17 and increased anti-inflammatory IL10 by MG63 cells [50]. MSCs also produce reduced levels of pro-inflammatory cytokines and increased levels of anti-inflammatory cytokines when grown on microtextured surfaces than on smooth surfaces [51]. Factors produced by these cells also regulate osteoblast recruitment and activity, thereby delaying bone resorption during the early phase of bone formation. Osteoprotegerin, a decoy receptor for the osteoclast activating RANKL, is elevated on microrough surfaces [52]. In addition, TGF-β1 is increased, which stimulates bone matrix synthesis and inhibits osteoclasts [53, 54].

Production of these factors is mediated by signaling through α2β1 integrins. Single knockdown of α2 and double knockdown of α2β1 integrin subunits results in decreased osteoprotegerin, TGF-β1 and PKC levels on rough surfaces. Silencing integrin α2 increases VEGF-A levels and alkaline phosphatase specific activity on rough surfaces when compared to the response of wild type cells.

2.4. Cell Morphology and Integrin Signaling

Along with biological signals, surface roughness may trigger changes in the cytoskeleton and resulting morphology, causing a change in planar cell polarity and downstream activation of gene transcription and osteoblast differentiation and maturation. Morphological analysis revealed that osteoblasts grown on rough SLA surfaces exhibited lower cell length, width, area and circularity, but higher aspect ratios than cells grown on smooth PT surfaces [55]. These changes in cell morphology on rough surfaces correlated with increased osteoblast differentiation marker osteocalcin, as well as α2 and β1 integrin subunits. When α2-silenced cells were cultured on these surfaces the change in morphology

was lost, indicating the importance of signaling by α2β1 in mediating cell shape and ultimately, cell phenotype.

To more clearly determine the specific contributions of topography and chemistry, we compared responses of human MSCs and MG63 cells to smooth and microtextured Ti and to the same surfaces coated with a nanofilm of graphitic carbon [28]. Osteogenic differentiation and maturation were enhanced on rougher surfaces, regardless of the chemistry. Gene expression of integrin α1, α2, and β1 subunits were upregulated on rough SLA surfaces, and α1 and α2 were further upregulated on the hydrophilic rough modSLA surface compared to smooth PT. Silencing of the α2 integrin subunit in osteoblasts abolished surface roughness-dependent expression of mRNAs for integrin β1 and osteocalcin regardless of surface chemistry. Production of prostaglandin E2 (PGE2), osteoprotegerin, and TGF- β1, as well as the response to $1\alpha,25(OH)_2D_3$ was also decreased for integrin-α2-silenced cells. In contrast, silencing integrin α1 in osteoblasts lead to a surface chemistry dependent response, where the response to roughness was significantly lower in comparison to wild type cells on titanium but not on graphitic carbon coated surfaces. Our study suggests that the β1 subunit is involved in roughness recognition, whereas the alpha subunits are responsible for surface chemistry recognition on micro-rough surfaces [28, 56].

Our studies also suggest that different mechanisms may be involved when osteoblasts are grown on microtextured Ti with homogenous nanofeatures imposed on the microtopography. Human osteoblasts had higher expression of mRNAs for osteocalcin, bone sialoprotein, BMPs 2 and 4, noggin and gremlin 1 on micro-rough and combined nano-/micro-rough surfaces in comparison to smooth or nano-rough only titanium alloy

surfaces [57]. However, integrins α1 and α2, traditionally associated with osteoblast response to surface roughness on titanium, were downregulated on combined nano-/micro-rough surfaces, while αV and β3 expression was increased.

Whereas α2 binds mostly to collagen and laminin, αv interacts more with vitronectin, osteopontin and bone sialoprotein [58]. These studies point toward a surface-topography-specific integrin response that is critical for activating downstream signaling for osteoblast development. Potential pathways and temporal regulation have yet to be investigated for MSCs on surfaces with hierarchical roughness.

2.5. Clinical Variables

MSCs are a heterogeneous population isolated from a variety of tissues, most commonly from bone marrow, and are defined by the presence of a set of cell surface markers and by demonstration of their ability to differentiate along a number of mesenchymal cell lineages depending on the culture medium that is used [59]. They are frequently used for biological testing of implant materials, but donor variability and culture conditions can contribute to differences in apparent osteogenic potential [60]. Most studies on implant surfaces have not differentiated between male and female cells *in vitro,* and commonly use only male animals *in vivo.* However, in clinical situations, gender is an important factor that affects musculoskeletal health [61]. We have shown that female osteoblasts are sensitive to surface micro-roughness, and 17β-estradiol (E_2) plays a role in modulating their response [62]. Although both male and female cells both show increasing production of osteocalcin, TGF-β1, osteoprotegerin and PGE_2 on rough SLA compared to smooth TCPS and PT surfaces, only female osteoblasts show a roughness-dependent

increase in differentiation and local factor production in response to treatment with E_2 and E_2 that is conjugated to bovine serum albumin (E_2-BSA) [63]. In contrast, the effect of $1\alpha,25(OH)_2D_3$ on increasing osteoblast differentiation and local factor production was more evident in male cells [63, 64]. These studies highlight the importance of gender specific hormones in regulating response to implant surfaces.

In addition, age can affect healing and implant osseointegration. *In vitro* observations showing age-dependent differences in cell response to surface-roughness support *in vivo* observations. Titanium implants placed in the femoral intramedullary canal resulted in less bone to implant contact and vascularization in 9 month old mice in comparison to 2 month old mice [65]. These results suggest that MSCs may also be less active in contributing toward bone healing in aged mice. Therefore, implant surface parameters that may increase osseointegration for one population may not achieve the same clinical effects in a different population. Patient factors can play an important role in implant healing and osseointegration, and elucidating the differences between patient populations can help design more effective, personalized treatment plans.

Challenges in Standards for Characterization of Implant Surfaces

It is still unclear how nanotopography contributes to the biological response to surface energy. The lack of standard terminology and characterization of nanostructures may contribute to the conflicting reports on the beneficial effects of nanotopography. Many studies that have shown an effect of specific nanostructures on osteoblast differentiation have used models in which these structures are formed either by employing lithographic methods to define patterns on plastic substrates or by anodizing Ti to create regular shaped

features [66, 67]. In contrast, etching and saline storage of Ti and Ti-6Al-4V generates random surface nano features [27, 38]. When these are super-imposed on microtextured surfaces, a complex topography results. Common roughness algorithms (Ra) cannot take all these factors into consideration (Table 1.1). Thus, surfaces with different nanostructure geometries can still have the same Ra value. A recent study conducted by our lab showed that skewness (symmetry as evaluated by elevations or depressions on a surface) and kurtosis (sharpness of peaks) values of micro-rough titanium surfaces are also factors that may predict osteoblast lineage cell response to varying surfaces [34]. Well-defined standards for characterization of nanostructures are important and necessary for comparing surfaces and eliciting biological response to physical parameters.

A challenge in nanostructure characterization is the limited number of high-resolution techniques available for quantitative nanostructure characterization. Contact profilometry analysis can only provide information in a 2D line scan, but not for a 3D area. Although atomic force microscopy is able to capture the nano-roughness of an otherwise smooth area, it does not have the ability to provide information for clinically relevant surfaces with preexisting micro-roughness. Though qualitative, scanning electron microscopy is still the gold standard in capturing and assessing nanotopography. Most nanofeatures are analyzed manually via ImageJ or another image processing software, although development is underway for automated image analysis [9, 33, 68]. Development of these techniques can allow for better comparisons between studies with varying nanostructure shape and dimension.

Table 2.1. Commonly used terms and definitions for surface roughness.

Term	Definition
Px	Primary values (no filter)

Wx	Waviness (low pass filter)
Rx	2D Roughness (high pass filter, line)
Sx	3D Roughness (high pass filter, area)
RSa	Average roughness, an arithmetic average value
RSc	Mean z height
RSsk	Skewness, a measure of asymmetry. Skewness of zero indicates a symmetrical distribution of peaks, whereas nonzero values indicate a weighted distribution toward the right (positive values) or left (negative values)
RSku	Kurtosis, a measure of sharpness. Values above 3 indicate sharp peaks, whereas values below 3 indicate rounded peaks.
RSq	Root-mean-squared roughness
RSt	Total roughness, absolute peak-valley
RSz	Maximum peak-valley
RSp	Maximum peak height
RSv	Maximum valley depth

On surfaces with roughness at any scale, quantitative evaluation of surface energy can also present a challenge. Typical sessile drop contact angle measurements evaluate surface energy assuming a smooth surface [69]. However, the scale of roughness can contribute to droplet enveloping features or spreading, and therefore result in inaccurate contact angle measurements. Smaller droplets that may sit on a "smooth" portion of the rough surface can be affected by line tension and evaporation, while large droplets that compensate for the larger waviness of a surface can be affected by gravity-induced deformations. More sophisticated techniques like the Wilhelmy balance method, which immerses the sample into a wetting liquid and takes into consideration the sample weight and buoyancy to calculate the surface tension, may be a more suitable method for assessing wettability of complex surfaces. An alternative method for hydrophobic materials, the

captive bubble technique submerges the surface in a liquid and evaluates the interaction of an air bubble on the surface. It is important to note the nuances and shortcomings associated with each surface technique, especially when comparing across studies.

2.6. Conclusion

The field of implant dentistry has progressed tremendously since the discovery of osseointegration. However, for compromised patients such as smokers or those with a history of chronic periodontitis, implant success is significantly reduced in comparison to success in healthy patients [70]. As new characterization and manufacturing techniques are developed, we will be able to understand cellular response to implant surfaces with better clarity and produce a generation of implants that address patient needs.

While various factors can affect biological response to titanium implant surfaces, roughness at the micro-, submicro- and nano-scales and hydrophilicity seem to contribute the most to favorable osteoblast response and resulting implant osseointegration. As we begin to understand contributions of each property to protein, cellular, immune, and overall host response, we can begin to design early loading, longer lasting dental implants for a wide demographic of patients.

CHAPTER 3

SURFACE MODIFICATION OF BULK TITANIUM SUBSTRATES FOR BIOMEDICAL APPLICATIONS VIA LOW-TEMPERATURE MICROWAVE HYDROTHERMAL OXIDATION

In [Cheng A, Goodwin WB, deGlee BM, Gittens RA, Vernon JP, Hyzy SL, Schwartz Z, Sandhage KH and Boyan BD. Nanoscale surface modification of bulk titanium substrates enhances wetting behavior for biomedical applications via low-temperature microwave hydrothermal oxidation. Journal of Biomedical Materials Research Part A. 2016. Under Review]

3.1. Introduction

Commercially pure titanium (Ti) is commonly used for biomedical purposes, particularly for dental and orthopaedic implants [71]. To enhance osseointegration, a variety of approaches have been developed to introduce microscale roughness to Ti implant surfaces [17]. Microscale roughness generated by sand blasting with large grit followed by acid etching has been shown to increase osteoblast differentiation *in vitro* and osseointegration *in vivo,* when compared to smooth Ti surfaces [72, 73].

We previously demonstrated that combined microscale and nanoscale surface roughness enhanced *in vitro* osteoblast differentiation compared to microscale roughness alone [9]. Others have shown that nanoscale features present on micro-rough Ti surfaces where hydrophilicity was retained by storage in aqueous solution also stimulate osteoblast differentiation [74]. The presence of nanoscale roughness on micro-roughness has been suggested to translate into enhanced osseointegration *in vivo* [25]. However, the results of a number of studies on the influences of nanoscale roughness have been confounded by

additional differences in surface chemistry and wettability, with variable responses seen across studies [26, 75].

Methods for introducing nanoscale structures on titanium surfaces have involved the use of chemical, thermal, and/or electrical treatments, with varied nanoscale morphologies and surface properties reported for each technique [26, 76]. Thermochemical treatments are often conducted at sufficiently high temperatures as to alter the mechanical behavior of Ti and Ti alloys (e.g., so as to cause the modified surfaces to become more prone to fracture under repetitive loading) [77, 78]. Anodization-based processes can yield nanoscale tubular (hollow pore channel) structures that may increase bacterial infiltration [79, 80]. In addition, prior surface modification studies have tended to be performed on polished/smooth planar Ti surfaces, which are not used clinically for bone-facing implants. Thus, low-temperature nanoscale surface modification methods that can be applied to clinically relevant, three-dimensional Ti substrates with micro-rough surfaces need to be explored.

Microwave and microwave hydrothermal (MWHT) processes were introduced several decades ago as a means of enhancing reaction rates at relatively modest temperatures for organic and inorganic syntheses [81, 82]. Thermal and non-thermal microwave effects have since been discovered with such syntheses, and microwave processing techniques are now used for the preparation of a variety of polymers and ceramics [82-84]. The purpose of the present paper is to demonstrate that low-temperature (200°C) scalable, non-line-of-sight MWHT oxidation treatments [85] can be used to introduce nanoscale surface protuberances on bulk Ti substrates that initially possess a microrough surface or a smooth surface. The influences of MWHT conditions (i.e., the use of distilled water or aqueous solutions of

H_2O_2 or NH_4OH of varying concentrations and the hydrothermal treatment time) on the resulting surface nanostructures, hydrophilicity, and biological responses of MG63 osteoblasts and normal human osteoblasts (NHOsts) cultured on such surfaces, have been examined.

3.2. Materials and Methods

Microwave hydrothermal (MWHT) surface modification

Commercial-purity grade 2 titanium disks, with dimensions of 15 mm diameter and 1 mm height, were received from Institut Straumann AG (Basel, Switzerland) with smooth (pretreated; PT) surfaces or with microrough (sand-blasted, large grit, acid-etched; SLA) surfaces [9]. One disk was placed into a given Teflon vessel along with 20 mL of fluid. Three types of fluids were examined for the MWHT treatment: distilled water, aqueous H_2O_2 solutions, and aqueous NH_4OH solutions. The concentrations of H_2O_2 or NH_4OH selected for the latter two solutions were 1 M, 1.5 M, 2 M, or 2.5 M. Up to 6 single-specimen-bearing Teflon vessels were placed in a microwave system (MARS 230/60, 2.45 GHz, CEM Corporation, Matthews, NC, USA) for a given MWHT treatment. Each MWHT treatment was conducted for 1 hour at 200°C (operating power of 1600 Watts), with ramp up and ramp down times of 30 minutes, unless otherwise stated in the results. The typical peak pressure during MWHT treatments ranged from 220-240 psi. After MWHT treatment, the samples were ultrasonically cleaned (Symphony 97043-940, VWR, Radnor, PA, USA) twice for 15 minutes in 2% Microsoap (Micro-90, International Products Corporation, Burlington, NJ, USA) and three times for 10 minutes in ultrapure distilled water (18.2 MΩ·cm, <5 ppb total organic carbon, EMD Millipore, Billerica, MA, USA). Samples were

patted dry and covered with a lint-free wipe to dry in ambient air overnight. Cleaned samples were then stored in a covered saline solution (an aqueous solution of 0.9 wt% NaCl) or stored under a cover in the as-dried state under ambient conditions in a dark box in a temperature-controlled class 1000 cleanroom. Prior to experiments with cell cultures, samples were sent to a gamma radiation facility (AB Dental, Ashdod, Israel) for sterilization at 2.5 Mrad, or were sterilized with UV-C light (257.3 nm) for 20 minutes on each disk side in a biosafety cabinet (Thermo Scientific Model 1300 Series A2, Waltham, MA, USA, with preinstalled Atlantic Ultraviolet 05-0660 bulb, Hauppauge, NY, USA). The gamma-irradiated samples were received approximately two weeks after completion of the MWHT treatment and cleaning.

To assess the effects of different MWHT treatments on MG63 cell response, treatments were conducted at 200°C for a fixed time of 1 hour. To evaluate the influence of the MWHT treatment time on nanoscale surface topography and on the resulting NHOst response, the 200°C MWHT treatment was applied to SLA surfaces for 1, 5, 10, 15, 20, and 40 hours in distilled H_2O and in aqueous solutions of 2.5 M H_2O_2 or 2.5 M NH_4OH.

Surface characterization

Surface chemistry

The chemical composition of the surface was evaluated using X-ray photoelectron spectroscopy (XPS; Thermo K-Alpha, Thermo Fisher Scientific, Inc., Waltham, MA, USA). A given XPS analysis was conducted over an area of 400 square microns (μm^2), with 3 such XPS analyses conducted per sample and with 3 samples evaluated per group (for a total of 9 analyses, n = 9) over a combined area of 3600 μm^2. An XR5 gun was used at 15kV. Survey spectra were averaged over 3 scans using a pass energy of 150 eV, a 1 eV

energy step size, and a 20 ms dwell time. High resolution spectra of titanium (Ti2p), oxygen (O1s), and carbon (C1s), the most dominant elements on the surface, were obtained by averaging over 15 scans at 20 eV, with a 0.1 eV energy step size and a 50 ms dwell time. Analyses were conducted using Thermo Avantage software (Thermo Fisher Scientific, Inc.). Reference peaks were obtained from the LaSurface online database and the XPS Handbook of the Elements and Native Oxides (XPS International, Inc., Mountain View, CA, USA).

Contact angle

The wetting of the specimen surfaces by distilled water was evaluated with a standard sessile drop contact angle goniometer (Model 250, Ramé-Hart, Succasunna, NJ, USA) using a recording video camera and image analysis software (DROPimage, Ramé-Hart). A 4 µL drop volume was placed on the sample surface, and the average value of the contact angle was obtained every 5 seconds over a total period of 20 seconds per drop. Five such drop analyses were conducted at different locations per sample, with 3 samples evaluated per group (n = 15).

Surface topography

Scanning electron microscopy (LEO 1530 Gemini, Zeiss, Oberkochen, Germany) was used to evaluate the sizes and morphologies of surface features. In Lens setting was used with an accelerating voltage of 5 kV, and images were taken with a working distance of 4 mm. Images were obtained at magnifications of 1000 X (1kX), 10 kX, 50 kX, 100 kX, and 200 kX at five locations per sample, with 3 samples evaluated per group (n = 15). Three locations were chosen near the center of the substrate, and two locations along the edges. Morphometric analyses of nanoscale structures were conducted by overlaying a 5 x 5 grid

on each secondary electron image. The average effective diameter of the nanoscale structure closest to the center of each of the 25 intersection points of each grid was evaluated from a top-down view. For protuberances that did not possess a round footprint when viewed topdown, the longest perceived diagonal distance across the protuberance footprint was used as the effective protuberance diameter. For cases where a protuberance was not observed within a distance of half of the grid width near a particular intersection point, a value of zero was assigned as the protuberance diameter for this intersection point.

Microscale surface roughness

Laser confocal microscopy (LCM; LEXT OLS4000, Olympus Corporation, Tokyo, Japan) was used to evaluate the microscale roughness of surfaces. LCM analyses were obtained at 6 locations per sample, with each analysis conducted over a $4.1x10^5$ μm^2 (644 μm by 644 μm) region, and with 2 samples analyzed per group (n = 12). The brightness value was set between 40-50% for determining the laser scan depth. Images were flattened to remove tilt from three planes, and a 100 μm cutoff wavelength was used for average surface roughness analyses.

Nanoscale surface roughness

Atomic force microscopy (AFM, Veeco Dimension 3000, Bruker Corporation, Billerica, MA, USA) was used to evaluate the nanoscale roughness of surfaces. AFM analyses were obtained at 6 locations per sample, with each analysis conducted over a 0.25 μm^2 (0.5 μm x 0.5 μm) region, and with two samples per group (n = 12). Tapping mode analyses were conducted using a 7 nm tip radius (Point Probe Plus Non-Contact / Tapping Mode – Long Cantilever – Reflex Coating, NANOSENSORS, Neuchatel, Switzerland) with a scan rate of 0.200 Hz and a tip velocity of 2.00 μm/s. After flattening acquired

images to eliminate first degree tilt, each scan was analyzed to obtain the average surface roughness using Nanoscope v6 software (Bruker Corporation). Because the z-limit of the AFM was exceeded by the microscale roughness of SLA surfaces, AFM analyses were only conducted on PT samples.

Crystalline phase content

The crystalline phase content of MWHT-treated PT samples was examined by X-ray diffraction (XRD) analysis (X'Pert PRO Alpha-1 diffractometer, PANalytical, Almelo, The Netherlands) using 1.8 kW Cu Kα radiation, a 1° parallel plate collimator, a ¼ divergence slit, and a 0.04 rad soller slit. A θ–2θ parafocusing setup was used for grazing-angle (*i.e.,* with a 2° take-off angle) analyses. All samples were analyzed at room temperature in the ambient atmosphere.

Cell culture

Cell culture and harvest

MG63 cells (American Type Culture Collection CRL-1427, Manassas, Virginia, USA) were used for the first set of experiments. All culture disks (including controls) were stored in saline for 56 days after nanoscale surface modification and sterilized via gamma irradiation prior to cell culturing. Normal human osteoblasts (NHOsts, Lonza CC-2538, Basel, Switzerland) were used for the second set of experiments. Surfaces were stored for 56 days under ambient conditions and were then sterilized via ultraviolet (UV) radiation for 20 minutes on each side prior to cell culturing. MG63 or NHOst cells were cultured in T75 flasks until 70% confluence, and then placed on tissue culture polystyrene (TCPS) or Ti surfaces in a 24-well plate at a density of 10,000 cells/cm^2 (20,000 cells/well). Cells were fed with full medium (DMEM supplemented with 10% fetal bovine serum and 1%

penicillin-streptomycin) 24 hours after plating, and then again after every 48 hours until confluence. At confluence on TCPS, cells on all surfaces were fed with fresh medium. After 24 hours from confluence, aliquots of the culture medium were obtained for protein analyses. The cell layer was rinsed twice with 1xPBS, then lysed with 0.05% Triton-X 100 and stored at -20°C prior to further analyses.

Cell lysate and medium analyses

After sonication of the whole cell lysate for 10 seconds, the alkaline phosphatase (ALP) specific activity, total protein content, and DNA content were evaluated. ALP activity was assessed as the production of *p*-nitrophenol from *p*-nitrophenyl phosphate at pH 10.2 and was then normalized over total protein content determined via a BCA protein assay (ThermoFisher). The DNA content was determined using the Quant-iT PicoGreen assay (ThermoFisher). Osteocalcin (Alfa Aesar, Haverhill, Massachusetts, USA), osteoprotegerin and vascular endothelial growth factor (VEGF) (R&D Systems) analyses were conducted via enzyme-linked immunosorbent assays and were then normalized relative to the DNA content. Cell experiments were performed at least twice to ensure reproducibility.

Statistical analyses

All materials characterization data are presented as the average ± standard deviation (SD). All cell data are presented as the average ± standard error of the mean for 6 independent cultures per variable, and are from a single representative experiment. For comparisons between two groups, a Student's t-test was used. For comparisons between more than two groups, one way analysis of variance was used with a Bonferroni post-correction test. For all comparisons, statistical signification was indicated by $p<0.05$.

3.3. Results

Influences of MWHT treatments on the nanoscale topographies of PT and SLA titanium surfaces

Secondary electron (SE) images of the surfaces of the smooth PT control, the micro-rough SLA control, and MWHT-treated PT and SLA specimens in Figure 1 revealed that the MWHT treatments resulted in a noticeable increase in the density of nanoscale protuberances on the PT and SLA titanium surfaces. The average values of effective nanoprotuberance diameter for a given treatment are shown in Figures 3.1(a) and 3.1(b), whereas relative variations in nanoprotuberance size for a given treatment are shown in the histograms of Figures 3.1(c) to 3.1(h). Morphometric analyses of PT and SLA surfaces exposed to the MWHT treatment in distilled H_2O indicated that the effective diameters of most of the protuberances fell in the range of 10-40 nm, with average diameter values of 22 nm and 23 nm for the MWHT/H_2O-treated PT and SLA surfaces, respectively (Figures 3.2(a) to (d)). SE images (Figures 1(b) and 1(e)) and morphometric analyses (Figures 3.2(a)-(d), (e), (g)) of the PT and SLA surfaces after MWHT treatment with relatively concentrated aqueous H_2O_2 solutions (i.e., 1.5 M - 2.5 M H_2O_2 solutions for PT surfaces; 2 M - 2.5 M H_2O_2 solutions for SLA surfaces) revealed nanoscale protuberances of distinctly larger average effective diameter (in the range of 32-51 nm), and with a wider distribution of sizes, than for MWHT treatments of these surfaces in distilled H_2O or in aqueous 1M H_2O_2 solutions (in the range of 22-28 nm). SE images (Figures 3.1(c) and 3.1(f)) and morphometric analyses (Figures 3.2(a)-(d), (f), (h)) of the PT and SLA surfaces after MWHT treatment with relatively concentrated aqueous NH_4OH solutions (2 M - 2.5 M NH_4OH solutions for PT surfaces; 1.5 M - 2.5 M NH_4OH solutions for SLA surfaces)

revealed nanoscale protuberances of distinctly larger average effective diameter (in the range of 28-60 nm), and with a wider distribution of sizes, than for MWHT treatments of these surfaces in distilled water or in aqueous 1M NH_4OH solutions (22-34 nm). No appreciable spatial variations across the surface of a given specimen were observed in nanoprotuberance coverage with MWHT treatment (Figure 3.3).

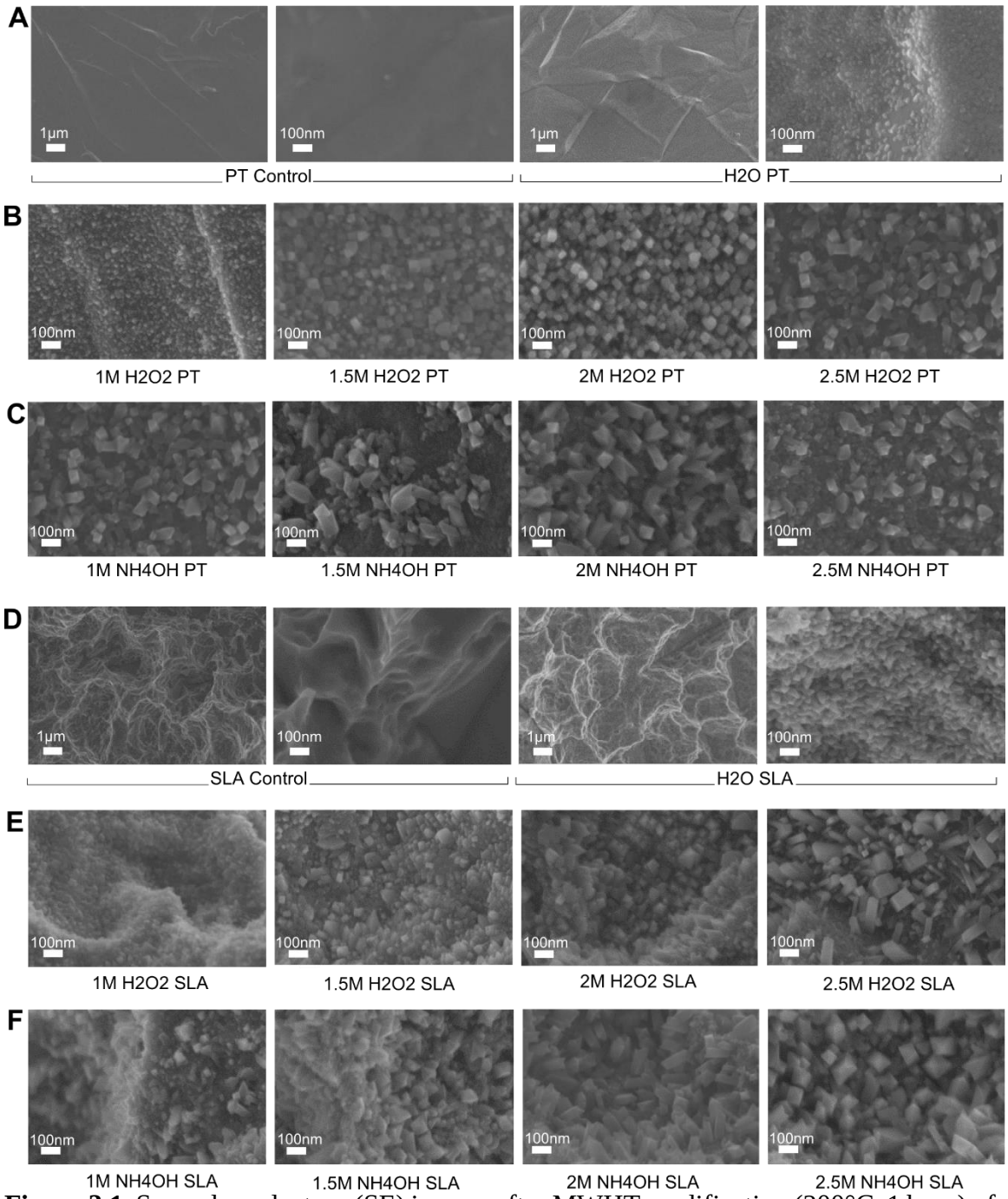

Figure 3.1. Secondary electron (SE) images after MWHT modification (200°C, 1 hour) of: (a-c) PT surfaces and (d-f) SLA Ti surfaces. From left to right: (a) PT control surfaces and MWHT/H2O-treated PT surfaces at low and high magnifications; (b) PT surfaces after MWHT treatment in aqueous 1 M, 1.5 M, 2 M, and 2.5 M H2O2 solutions; (c) PT surfaces after MWHT treatment in aqueous in 1 M, 1.5 M, 2 M, and 2.5M NH4OH solutions; (d) SLA control surfaces and MWHT/H2O-treated SLA surfaces at low and high magnifications; (e) SLA surfaces after MWHT treatment in aqueous 1 M, 1.5 M, 2 M, and 2.5 M H2O2 solutions and (f) SLA surfaces after MWHT treatment in aqueous 1 M, 1.5 M, 2 M, and 2.5 M NH4OH solutions.

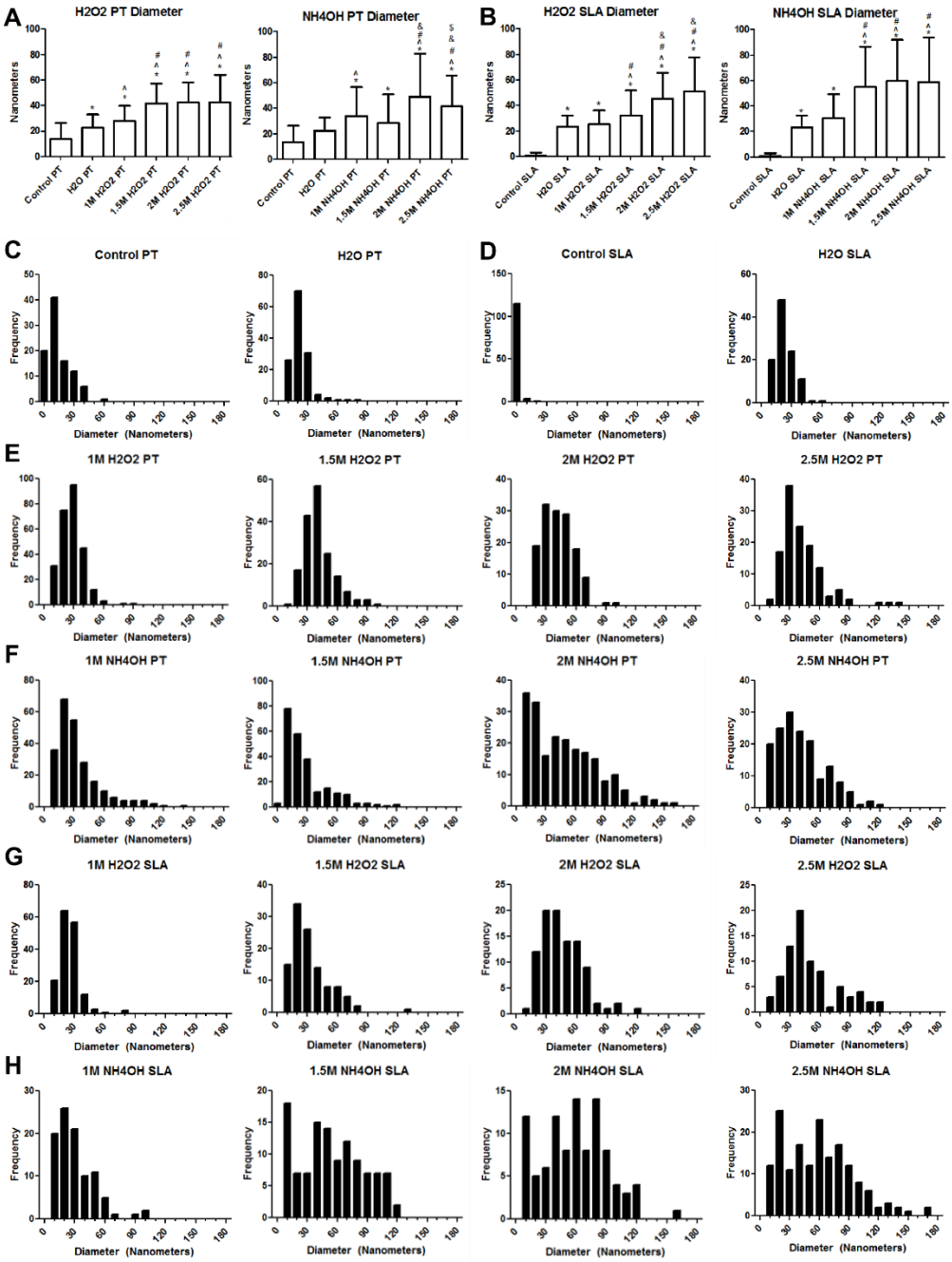

Figure 3.2. Morphometric analyses (obtained from SE images) of the nanoscale surface protuberances formed upon MWHT modification (200°C, 1 hour). The average effective diameters of the nanoscale protuberances (with +1 SD error bars) are shown for: (a) MWHT-modified PT surfaces and (b) MWHT-modified SLA surfaces. The symbols *, ^, #, &, and $ refer to p values <0.05 upon comparison to data for control surfaces, MWHT/H2O-treated surfaces, MWHT-treated aqueous solutions with 1 M H2O2 or 1 M NH4OH, MWHT-treated aqueous solutions with 1.5 M H2O2 or 1.5 M NH4OH, and MWHT-treated aqueous solutions with 2 M H2O2 or 2 M NH4OH, respectively. Histograms of the effective diameters of the nanoscale protuberances are shown for: (c,e,f) MWHT-modified PT surfaces and (d,g,h) MWHT-modified SLA surfaces.

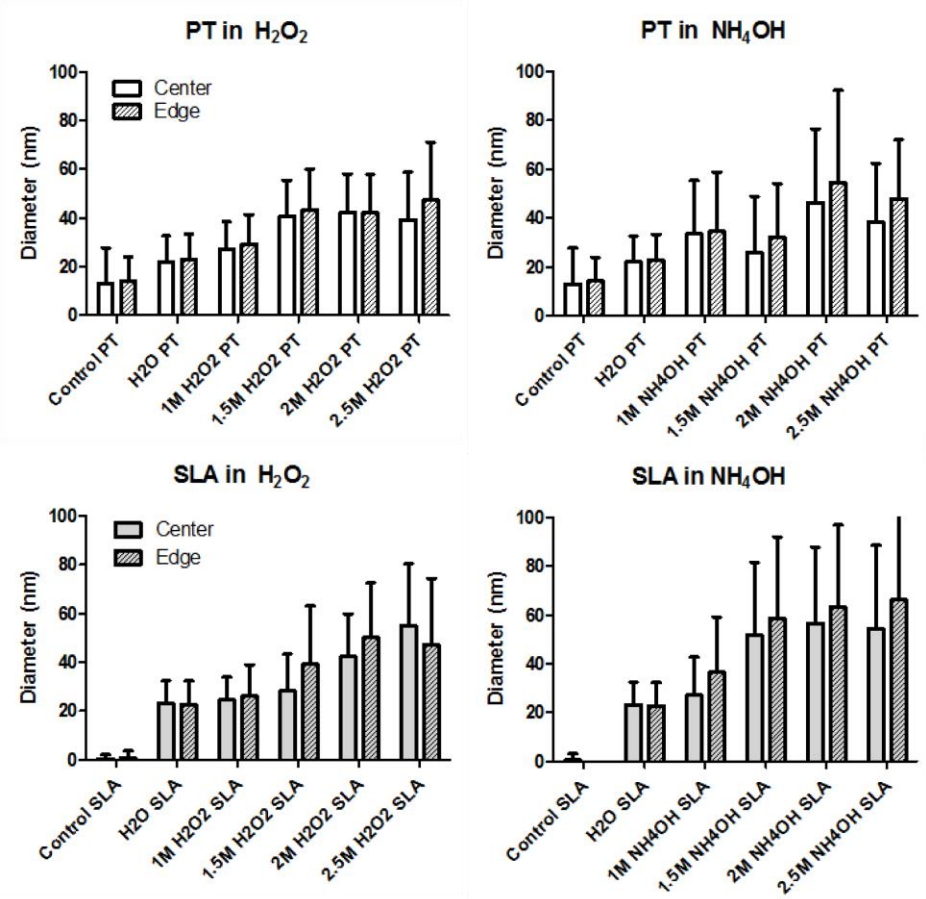

Figure 3.3. Nanostructure diameters near the center (solid) and edge (striped) of substrates. No appreciable spatial variations were observed.

Laser confocal microscopy (LCM, Table 1) revealed no appreciable differences in the microscale surface roughness values for all MWHT-modified PT or SLA surfaces compared to control PT or SLA surfaces, respectively. The average microscale roughness (Ra) values were in the range of 0.6 μm to 0.7 μm for all MWHT-modified or unmodified PT surfaces and in the range of 2.5 μm to 2.8 μm for all MWHT-modified or unmodified SLA surfaces; that is, the MWHT treatments did not significantly alter (enhance or degrade) the microscale roughness of the PT or SLA surfaces. AFM analyses (which could only be conducted on the PT surfaces) of MWHT-treated samples using distilled H_2O, and of MWHT-treated samples using 1M and 2.5 M H_2O_2 solutions, yielded average nano-scale roughness values below 7 nm (i.e., below the AFM tip radius), so that statistical

comparisons between these samples were not conducted. However, AFM analyses indicated larger average measured nanoscale roughness values of 8.1±2.5 nm and 11.3±5.1 nm on MWHT-modified PT surfaces using aqueous 1 M NH_4OH and 2.5 M NH_4OH solutions, respectively; that is, the average nanoscale roughness for these specimens was greater than for the PT control samples.

Table 3.1. Surface roughness analysis by laser confocal microscopy

	Average Roughness Ra Value (Average ± Standard Deviation)
PT Control	0.56 ± 0.03
PT H2O	0.63 ± 0.04
PT 1M H2O2	0.65 ± 0.04
PT 1M NH4OH	0.61 ± 0.03
PT 2.5M H2O2	0.66 ± 0.06
PT 2.5M NH4OH	0.65 ± 0.04
SLA Control	2.54 ± 0.07
SLA H2O	2.76 ± 0.19
SLA 1M H2O2	2.66 ± 0.12
SLA 1M NH4OH	2.63 ± 0.14
SLA 2.5M H2O2	2.51 ± 0.11
SLA 2.5M NH4OH	2.45 ± 0.10

The effects of MWHT on nanoscale topography were dependent on treatment time. Morphometric analyses indicated that the specimens exposed to the MWHT treatment for $\geq$10 hours with distilled H_2O, and for $\geq$20 hours with aqueous solutions of 2.5 M H_2O_2 or 2.5 M NH_4OH, possessed nanoprotuberances with distinctly larger average effective diameters than the specimens exposed to the MWHT treatments in these fluids for 1 hour (Figure 3.4). The average nanoprotuberance diameters after the 20 hour MWHT treatments using distilled H_2O, an aqueous 2.5 M H_2O_2 solution, and an aqueous 2.5 M NH_4OH

solution were 34 nm, 59 nm, and 93 nm, respectively. The significant increase in nanoprotuberance diameter with the MWHT fluids in the order H_2O < 2.5 M H_2O_2 < 2.5 M NH_4OH for the 20 hour treatment was also quite apparent in the secondary electron images shown in Figure 3.4.

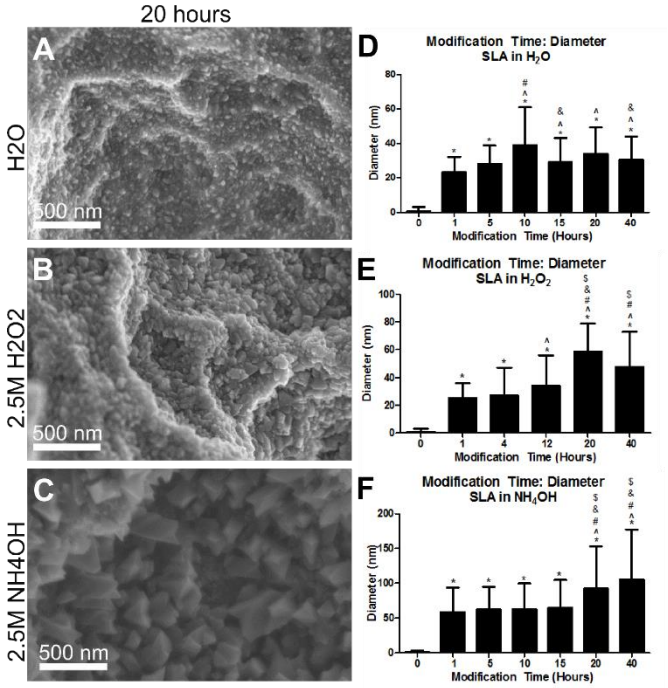

Figure 3.4. Changes in nanoscale surface topography after 200°C MWHT modification for up to 40 h. SE images of SLA surfaces after 20 h of MWHT modification in: (a) distilled H2O, (b) an aqueous 2.5 M H2O2 solution, and (c) an aqueous 2.5 M NH4OH solution. Morphometric analyses of the average effective diameters of nanoscale protuberances generated on SLA surfaces (with +1 standard deviation error bars) after MWHT treatment for up to 40 h in: (d) distilled H2O, (e) an aqueous 2.5 M H2O2 solution, and (f) an aqueous 2.5 M NH4OH solution. Data were evaluated by one-way ANOVA, with Bonferroni post-correction p values below 0.05 considered to indicate statistically-significant differences. The symbols *, ^, #, &, and $ refer to p values <0.05 upon comparison to data for control surfaces, MWHT/1 h-treated surfaces, MWHT/4 or 5 h-treated surfaces, MWHT/10 or 12 h-treated surfaces, MWHT/15 h-treated surfaces, respectively.

Influences of MWHT treatments on the water contact angles with, and the chemistries and the phase contents of, PT and SLA titanium surfaces

After exposure of PT surfaces and SLA surfaces to the 200°C/1 hour MWHT treatments with distilled H_2O and with aqueous solutions of H_2O_2 and NH_4OH (followed by overnight drying at room temperature), the contact angles of distilled water droplets on

such modified Ti surfaces were measured. The average contact angles measured for the MWHT-treated PT surfaces were generally lower than for the untreated PT control surfaces (Figures 3.5(a) and (b)). Complete wetting of the water droplet, so as to form a water film, was observed for all MWHT-treated SLA surfaces (indicated as "CW" in Figures 3.5(c) and (d)). Similar results were obtained after more rapid drying with a flowing stream of N_2 for 60 seconds (instead of via overnight room-temperature drying); that is, complete wetting occurred for MWHT-treated surfaces that had been dried in flowing N_2. The same wetting behavior was observed for SLA surfaces after MWHT treatment for 20 hours and 40 hours.

Comparison of SLA specimens exposed to the MWHT/H_2O treatment that were stored under a cover in the as-dried state with those stored in a saline solution (an aqueous solution of 0.9 wt% NaCl) showed that the enhanced wetting achieved after 200°C/1 hour MWHT treatment of the SLA surfaces was maintained over a prolonged time. While the dry samples exhibited a steadily increasing contact angle with time (Figure 3.5(e)), the MWHT/H_2O-treated SLA specimens in the covered saline solution maintained complete wetting through 119 days of storage (Figure 3.5(e)).

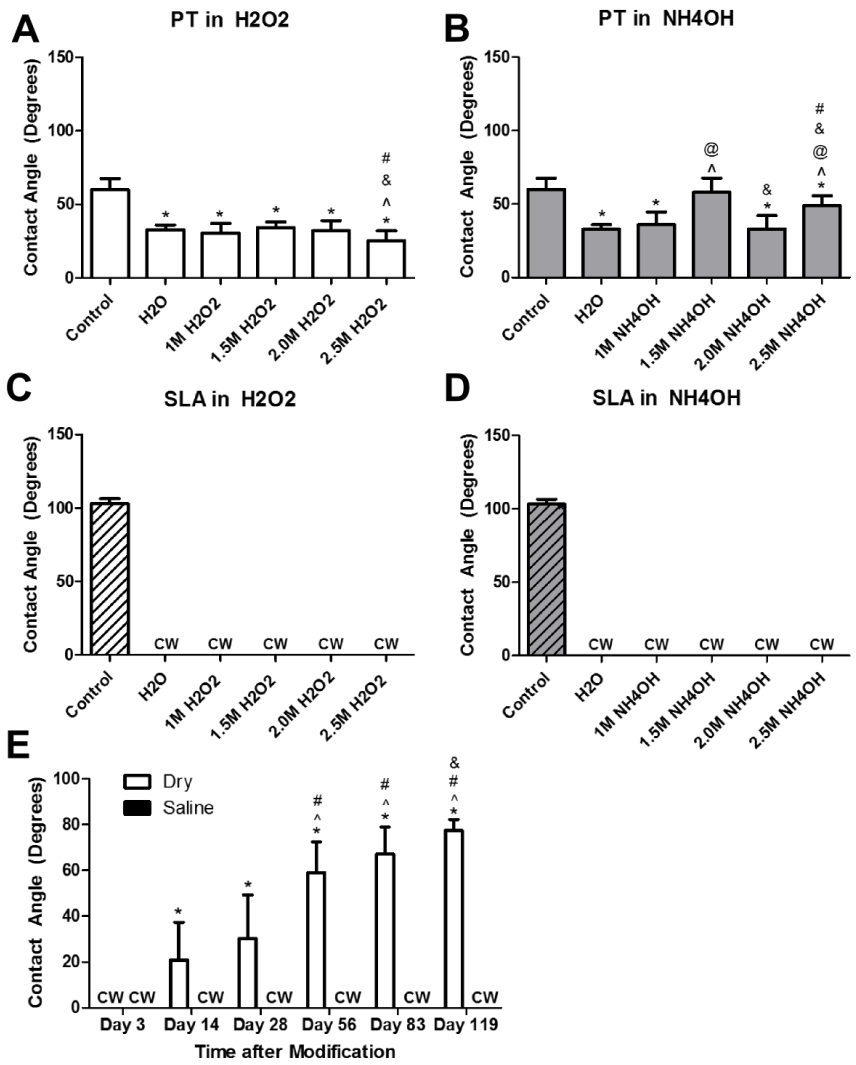

Figure 3.5. Wetting of distilled water on control and MWHT-treated (200°C/1 h) surfaces (after cleaning and drying). Average values of the contact angle of distilled water (with +1 SD error bars) on PT control surfaces and on PT Ti surfaces after MWHT treatment in distilled H2O and in: (a) aqueous H2O2 solutions and (b) aqueous NH4OH solutions. Average values of the contact angle of distilled water (with +1 standard deviation error bars) on SLA control surfaces and on SLA Ti surfaces after MWHT treatment (200°C/1 h) in distilled H2O and in: (c) aqueous H2O2 solutions and (d) aqueous NH4OH solutions. The symbols *, ^, @, &, and # refer to p values <0.05 upon comparison to data for control surfaces, MWHT/H2O-treated surfaces, MWHT-treated aqueous solutions with 1 M H2O2 or 1 M NH4OH, MWHT-treated aqueous solutions with 1.5 M H2O2 or 1.5 M NH4OH, and MWHT-treated aqueous solutions with 2 M H2O2 or 2 M NH4OH, respectively. (e) Average values of contact angle of SLA surfaces after MWHT treatment (200°C/1 h) in distilled H2O and storage either dry (white bar) or in saline solution (black bar) over time. CW refers to complete wetting, where the drop spread across the surface so that a measurement could not be made. The symbols *, ^, # and & refer to p values <0.05 upon comparison to data for 3 days storage, 14 days storage, 28 days storage, and 56 days storage, respectively.

X-ray photoelectron spectroscopy (XPS) of the control and MWHT-treated SLA surfaces indicated the predominant presence of oxygen, titanium, and carbon (Table 2). High resolution Ti2p (Figure 3.6(a)), O1s (Figure 3.6(b)) and C1s (Figure 3.6(c)) spectra revealed increased TiO_2 and reduced C-C species on MWHT-modified SLA samples compared to the control SLA specimens, which was consistent with enhanced oxidation of titanium and carbonaceous species on the SLA surfaces during the MWHT treatments. The specimens stored in the as-dried state also exhibited a higher XPS-measured carbon content after 3 days and 28 days of storage than for the specimens stored in the saline solution for similar times (Table 3.2).

Table 3.2. Chemical composition of surfaces obtained by XPS analysis.

	Element (Average At. % ± Standard Deviation)		
	Carbon	Oxygen	Titanium
SLA Control	24.7 ± 1.6	52.8 ± 0.9	22.5 ± 0.7
SLA H2O	17.2 ± 1.4	58.0 ± 1.1	24.7 ± 0.4
SLA 1M H2O2	18.7 ± 1.0	57.7 ± 0.8	23.6 ± 0.4
SLA 1.5M H2O2	18.8 ± 1.1	58.1 ± 0.7	23.1 ± 0.6
SLA 2M H2O2	17.5 ± 1.1	58.9 ± 0.8	23.5 ± 0.3
SLA 2.5M H2O2	16.6 ± 1.3	58.9 ± 1.1	24.4 ± 0.5
SLA 1M NH4OH	18.2 ± 0.8	57.2 ± 0.7	24.6 ± 0.3
SLA 1.5M NH4OH	18.6 ± 1.3	57.1 ± 0.7	24.3 ± 0.7
SLA 2M NH4OH	16.6 ± 1.1	58.5 ± 0.6	24.9 ±0.6
SLA 2.5M NH4OH	17.0 ± 1.0	58.1 ± 0.6	24.8 ± 0.5
SLA H2O D3 Dry	18.4 ± 0.8	58.0 ± 0.4	23.7 ± 0.6
SLA H2O D3 Saline	15.0 ± 2.1	59.0 ± 1.8	25.1 ± 1.1
SLA H2O D28 Dry	24.6 ± 0.6	53.7 ± 0.5	21.5 ± 0.4
SLA H2O D28 Saline	18.6 ± 1.6	58.3 ± 1.1	20.7 ± 0.5

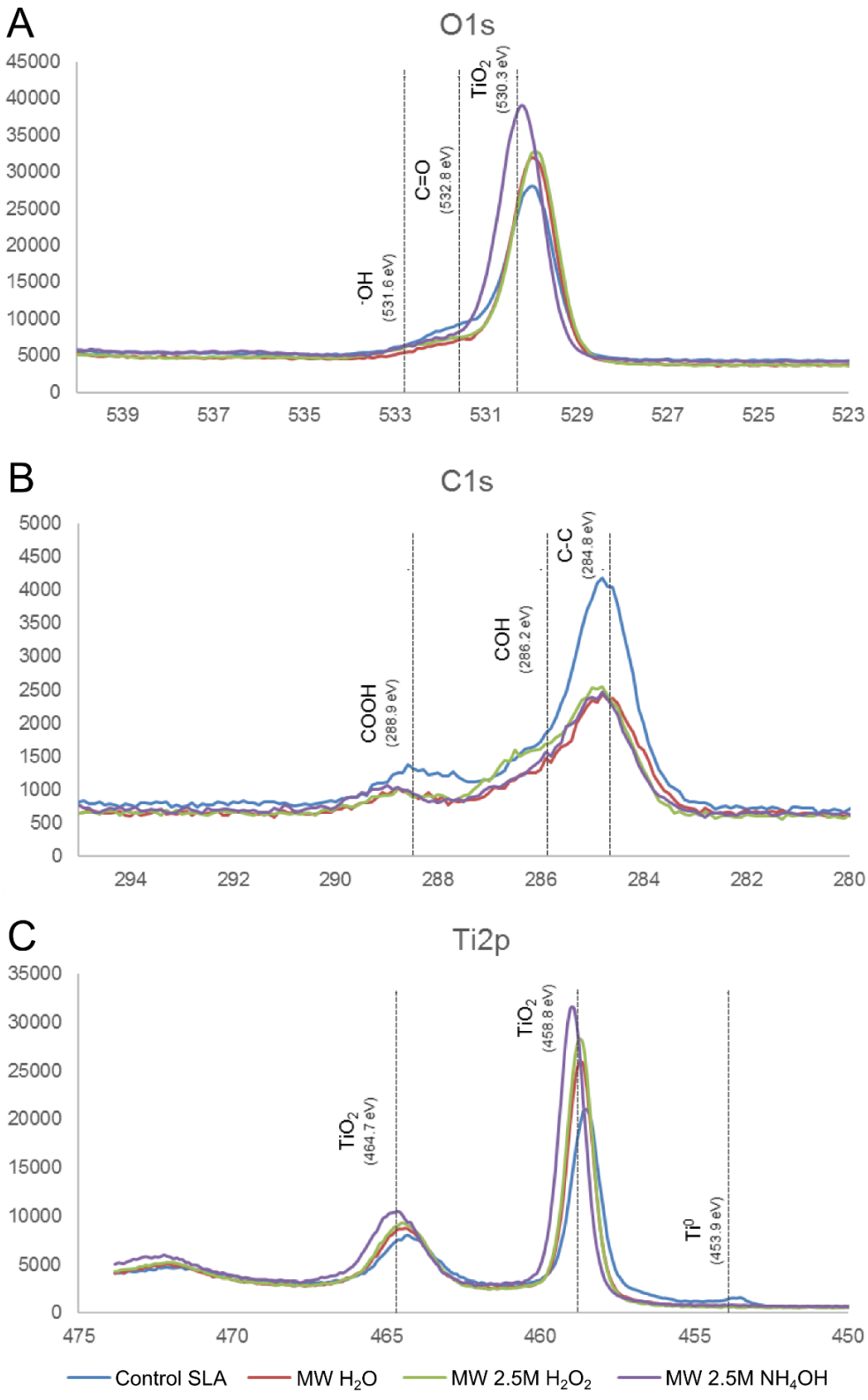

Figure 3.6. XPS high resolution spectra of (a) Ti2p; (b) O1s; and (c) C1s.

Grazing angle XRD analyses were used to evaluate the oxide phase content formed after exposure of the PT Ti specimens to the MWHT treatments (Figure 3.7). Anatase was the only TiO_2 polymorph detected on the PT surfaces after the 200°C/1 hour MWHT treatments in distilled H_2O and in aqueous solutions of 1 M and 2.5 M NH_4OH. The MWHT treatment using an aqueous 2.5 M H_2O_2 solution yielded appreciable rutile titania, along with anatase titania, on the PT surface, whereas a modest amount of rutile titania was detected after exposure to an aqueous 1 M H_2O_2 solution.

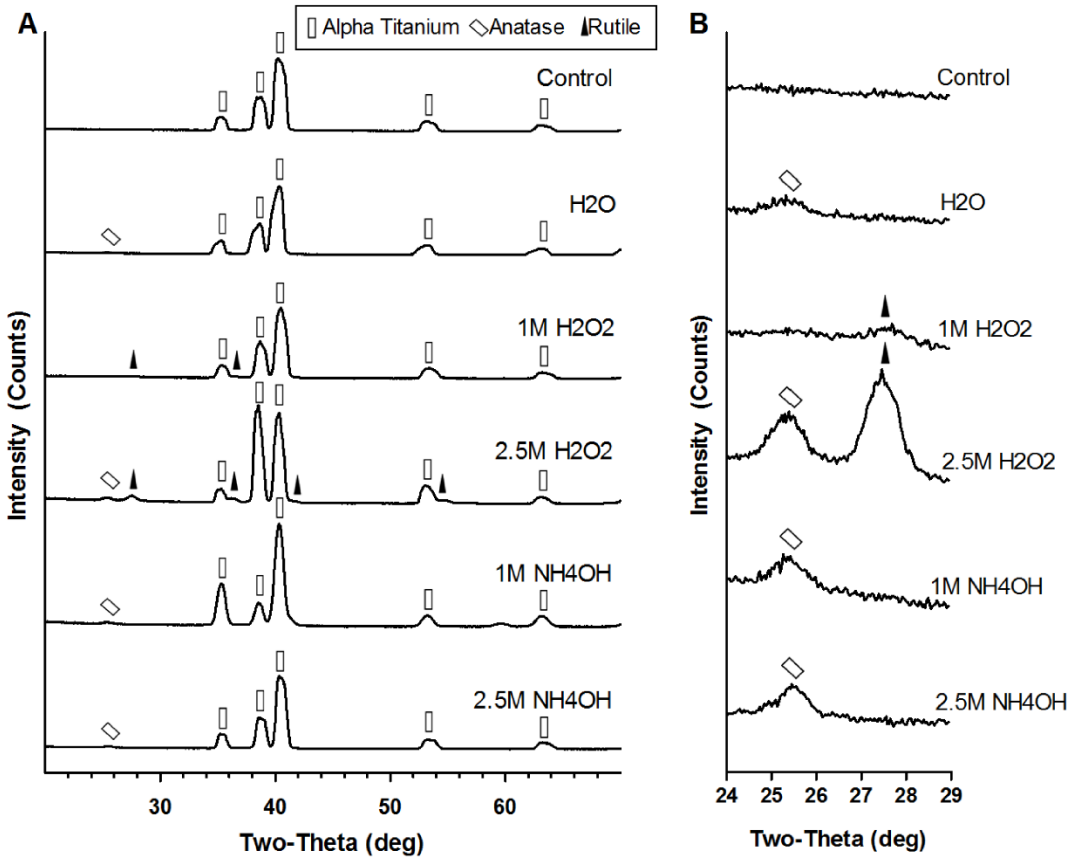

Figure 3.7. XRD patterns revealing TiO2 polymorphs formed on MWHT-treated (200°C/1 h) PT surfaces.

Influences of MWHT treatments on the responses of MG63 and normal human osteoblast cells

Statistical evaluation (one-way analysis of variance, with Bonferroni post-correction p values below 0.05 considered to indicate statistically-significant differences) of whole cell lysate analyses of MG63 osteoblasts (Figures 3.8(a)-(e)) cultured on micro-rough SLA control surfaces yielded lower values for DNA content and ALP, and similar values for osteocalcin, osteoprotegerin, and VEGF, as for cells cultured on smooth PT control surfaces. MWHT modification (200°C/1 hour) of SLA surfaces with the aqueous H_2O_2 and aqueous NH_4OH solutions yielded statistically similar values for DNA content, generally lower values for ALP (although statistically similar values for the MWHT/1 M NH_4OH treatment), statistically similar values of osteocalcin, generally similar values of osteoprotegerin (although statistically lower values for the MWHT/1 M H_2O_2 treatment), and similar or lower values of VEGF depending on the H_2O_2 and NH_4OH concentrations (statistically similar values for the 1 M NH_4OH and 2.5 M H_2O_2 treatments), than for cells cultured on SLA control surfaces (Figures 3.8(a)-(e)).

Statistical evaluation of whole cell lysate analyses of normal human osteoblasts (NHOst) cultured on micro-rough SLA control surfaces (Figures 3.9(a)-(e)) yielded lower values for DNA content, similar values for ALP, higher values for osteocalcin, similar values for osteoprotegerin, and higher values for VEGF than for cells cultured on smooth PT control surfaces. MWHT modification (200°C/1 hour or 20 hours) of SLA surfaces with the aqueous 2.5 M NH_4OH solution yielded higher values for DNA content, similar values for ALP, lower values for osteocalcin, similar values for osteoprotegerin for the 1 h MWHT treatment and lower values for the 20 h MWHT treatment, and statistically similar values for VEGF than for NHOsts cultured on SLA control surfaces (Figures 3.9(a)-(e)).

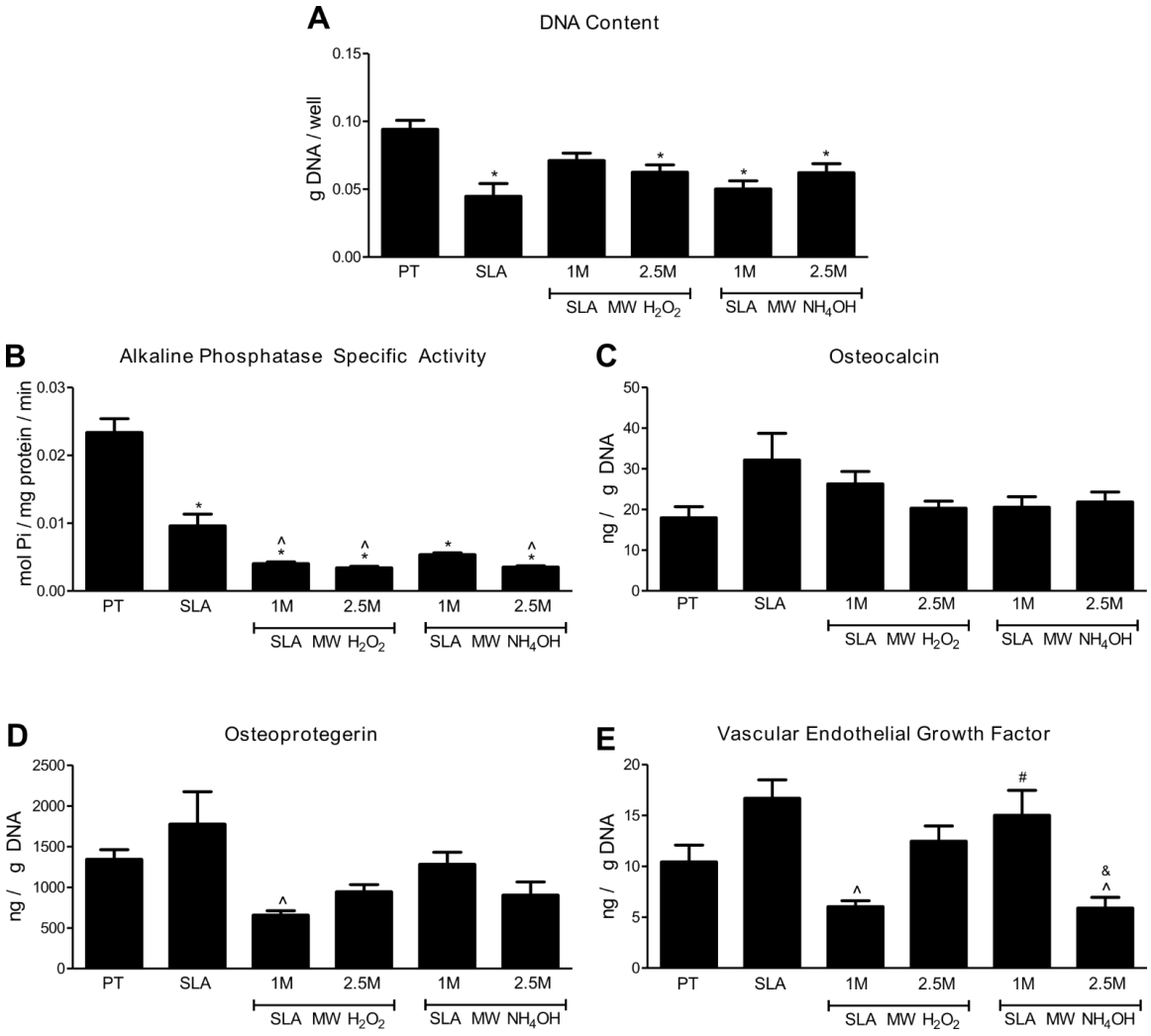

Figure 3.8. MG63 cell responses to MWHT-treated (200°C/1 h) SLA surfaces. Whole cell lysate analyses of the measured levels of: (a) DNA content; (b) alkaline phosphatase specific activity; (c) osteocalcin; (d) osteoprotegerin; and (e) Vascular Endothelial Growth Factor (VEGF). Data were evaluated by one-way ANOVA, with Bonferroni post-correction p values below 0.05 considered to indicate statistically-significant differences. The symbols *, ^, #, and & refer to p values <0.05 upon comparison to data for PT control surfaces, SLA control surfaces, MWHT/1M H2O2-treated surfaces, and MWHT/1M NH4OH-treated surfaces, respectively.

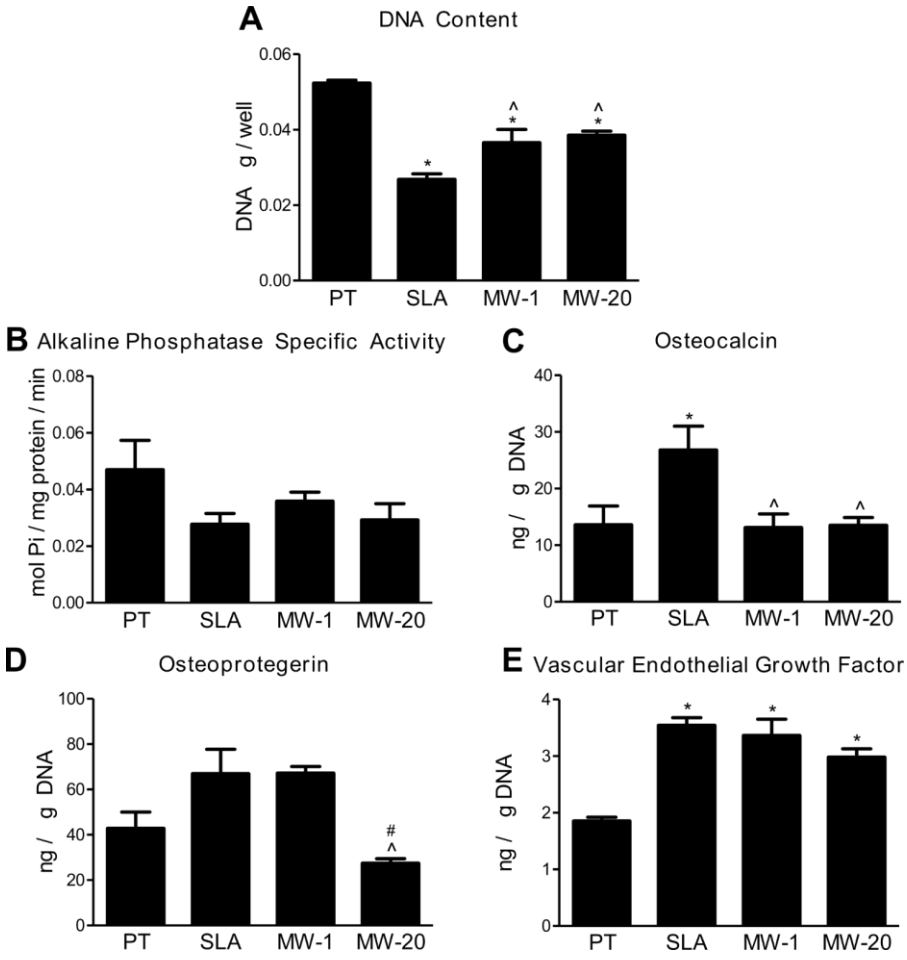

Figure 3.9. NHOst response to MWHT-modified surfaces for 1 and 20 hours in 2.5 M NH4OH. (a) DNA content; (b) alkaline phosphatase specific activity; (c) osteocalcin; (d) osteoprotegrin; and (e) VEGF. 1 way ANOVA with Bonferroni post-correction, $p<0.05$, * vs. PT, ^ vs. SLA, # vs. MW-1.

3.4. Discussion

Prior work has shown that a simple oxidation treatment (740°C in air) can be used to introduce nanoscale rutile TiO_2 protuberances onto micro-rough SLA Ti surfaces that, in turn, can affect wetting behavior and the differentiation, proliferation, and local factor production of MG63 osteoblasts and human mesenchymal stem cells cultured on such surfaces [9]. While this scalable, non-line-of-sight approach was an effective means of superimposing nanoscale protuberances of tailorable size onto SLA surfaces via control of

the oxidation time (i.e., with diameters on PT surfaces ranging from 40-200 nm to 500-1000 nm for oxidation times of 45 min to 180 min, respectively), the use of a 740°C oxidation treatment in air can lead to appreciable oxygen dissolution into titanium (e.g., the solubility of oxygen in titanium at 740°C in air is 33 at. % [86]) and associated alterations in the mechanical properties (strength, ductility, hardness) of titanium implants [87, 88]. An alternative strategy used in the present work was to conduct the oxidation at a much lower temperature via the use of microwave hydrothermal (MWHT) treatments.

Prior work demonstrated that exposure of titanium plates to an aqueous solution of H_2O_2 (an oxidant) for a prolonged time of 72 hours at only 80°C yielded nanorods of titania on the plate surfaces via a dissolution-precipitation mechanism [89]. Nanocrystalline titania particles have also been formed by the precipitation of an aqueous titanium precursor solution upon addition of 4 M NH_4OH at only 70°C [90]. Titania nanoparticles in a variety of morphologies have been synthesized via hydrothermal or microwave hydrothermal reaction of aqueous precursor solutions in the presence of hydrogen peroxide and/or ammonium hydroxide at $\leq$200°C for $\leq$24 hours [91-96]. The present work has focused on evaluating the formation of nanostructured titania on titanium surfaces via low temperature/short time (200°C/1 hour) MWHT treatments in aqueous solutions of hydrogen peroxide or ammonium hydroxide. To our knowledge, this is the first study of the use of such MWHT treatments in H_2O_2 or NH_4OH solutions to generate nanostructured titania surfaces on titanium for evaluation of osteoblast behavior.

In the present work, low-temperature (200°C, 1 h) MWHT treatments in aqueous solutions of H_2O_2 and NH_4OH induced the formation of new nanoscale oxide protuberances on both PT and SLA surfaces. MWHT treatments with H_2O_2-bearing

solutions resulted in the formation of rutile titania, or a mixture of rutile and anatase, on titanium surfaces, whereas MWHT treatments with NH_4OH-bearing solutions yielded only the anatase polymorph of titania. These observations are consistent with prior work indicating that the hydrothermal syntheses of fine anatase nanocrystals is enhanced in basic solutions, whereas rutile nanocrystal formation is promoted in acidic solutions [97-100]. It should be noted, however, that some of the prolonged MWHT treatments with aqueous hydrogen peroxide solutions were terminated prior to the completion of the programmed exposure time due to the buildup of internal pressure (in excess of 2.76 MPa/400 psi) within the sealed Teflon vessels. This pressure buildup was likely due to the decomposition of the peroxide into water and oxygen ($2H_2O_2 \rightarrow 2H_2O + O_2$), which can be accelerated in the presence of nanocrystalline titania [101].

The results presented here differ from previous work where nanomodification of the SLA surface was performed at high temperature (740°C, 1.5 hours, air) [5]. The rutile titania nanoprotuberances that were generated in the earlier study resulted in statistically significant increases in osteocalcin, osteoprotegerin, and VEGF, with similar values of DNA content and alkaline phosphatase activity (ALP) relative to control SLA surfaces, indicating that MG63 osteoblast differentiation was significantly enhanced. In contrast, the results of the present study suggest that osteoblast differentiation was not enhanced by the nanotopography generated by MWHT. Moreover, the specific effects of MWHT treatment varied with cell type and with the surface treatment protocol. MWHT modification (200°C/1 hour) of micro-rough SLA surfaces with aqueous 1 M and 2.5 M NH_4OH solutions yielded anatase nanoprotuberances that, in turn, resulted in MG63 cells producing statistically similar values of osteocalcin, osteoprotegerin, and similar or lower values of

VEGF, with statistically similar values of DNA content and similar or lower values of ALP, than for MG63 cells cultured on SLA control surfaces. NHOst cells cultured on micro-rough SLA surfaces with anatase nanoprotuberances, generated via MWHT modification (200°C/1 hour or 20 hours) with an aqueous 2.5 M NH_4OH solution, yielded lower values of osteocalcin, similar or lower values of osteoprotegerin, and statistically similar values of VEGF, with higher values of DNA content and similar values of ALP than for NHOst cells cultured on SLA control surfaces. MWHT modification (200°C/1 hour) of micro-rough SLA surfaces with aqueous H_2O_2 solutions resulted in nanoprotuberances comprised of rutile or rutile and anatase that resulted in MG63 cells producing statistically similar values of osteocalcin, similar or lower values of osteoprotegerin, and similar or lower values of VEGF, with statistically similar values of DNA content and lower values of ALP than for MG63 cells cultured on SLA control surfaces. Hence, the anatase, rutile, or anatase and rutile nanoprotuberances generated by these MWHT treatments did not result in appreciable consistent changes in MG63 or NHOst cell differentiation. The osteocalcin content of the conditioned media from MWHT-modified surfaces at levels comparable to the PT surface suggests that osteoblast differentiation of NHOst cells may even have been reduced compared to untreated SLA.

There are several explanations for the difference in biological results observed in this study and in our previous work. Both the 200°C/1 hour MWHT treatments with aqueous H_2O_2 solutions of the present work and the 740°C/90 minute oxidation treatment in air by Gittens, et al. [5] yielded rutile-bearing nanoprotuberances on PT and SLA surfaces. However, the MWHT treatments of the present work yielded nanoprotuberances of significantly smaller diameter. Morphometric analyses of the rutile-bearing

nanoprotuberances generated on PT and SLA surfaces via 200°C/1 hour MWHT treatment with 1-2.5 M H_2O_2 solutions yielded average values of effective nanoprotuberance diameter of 32-51 nm. In contrast, the 740°C/90 minutes oxidation treatment in air by Gittens, et al. [5] yielded rutile nanoprotuberances on PT surfaces possessing measured effective diameters of 40-360 nm. The average AFM-measured nanoscale roughness of the rutile-bearing surfaces generated by Gittens, et al. was also greater than for the rutile-bearing surfaces of the present work (i.e., 16 nm vs. less than the tip radius of 7 nm). The significantly enhanced MG63 cell differentiation observed for SLA specimens possessing larger rutile-bearing nanoprotuberances (generated by the 740°C/90 minute/air treatment by Gittens, et al. [5]) relative to the smaller rutile-bearing nanoprotuberances of the present work (generated by the 200°C/1 hour MWHT treatment in H_2O_2 solutions) suggests that there is a preferred nanoprotuberance size range for such enhanced cell behavior.

Dramatic reductions in the water contact angle, so as to result in complete wetting (film formation), were achieved with MWHT-treated SLA surfaces relative to SLA control surfaces. This was also in contrast to the surfaces generated by Gittens, et al., which were hydrophobic [9]. The complete wetting achieved for *all of the MWHT-treated SLA surfaces* indicated that the differences in liquid compositions used for such treatments (H_2O vs. aqueous H_2O_2 solutions of varied H_2O_2 concentration vs. aqueous NH_4OH solutions of varied NH_4OH concentration), and associated differences in the average nanoscale protuberance diameters (over the range of 22-60 nm) or phase contents (relative amounts of anatase and rutile), had little effect on such enhanced wetting behavior. The enhanced wetting was, however, consistent with the observed reduction in XPS-measured carbon content (hydrophobic C-C species) of the MWHT-treated SLA surfaces. Furthermore,

MWHT-treated SLA specimens stored in saline (to avoid direct exposure of the surfaces of such specimens to hydrocarbons from ambient air) retained complete wetting for 119 days, whereas MWHT-treated SLA samples stored in a dry state in ambient air exhibited a steadily increasing contact angle (up to 77 degrees) over the same time period. The specimens stored in the as-dried state also exhibited a higher XPS-measured carbon content after 3 days and 28 days of storage than for the specimens stored in the saline solution for the same times. Other authors have also observed significant increases in water contact angle of titania-bearing Ti or Ti alloy surfaces with exposure time in ambient air, which was attributed to increased adsorption of hydrophobic carbonaceous species [32, 102, 103].

The ability to generate and retain strongly hydrophilic surfaces is highly important for protein adsorption and desired osteoblast cell response [104-106]. The MWHT reaction process of the present work enables hydrophilic micro/nanostructured oxide surfaces to be formed on titanium-based implants with modest temperature/time conditions (200°C/1 hour) so as to avoid degradation of the microscale surface structure and the microstructure and properties of the underlying implant.

3.5. Conclusion

Exposure of clinically relevant micro-rough SLA titanium substrates to MWHT treatments at 200°C for 1 hour with distilled water or with aqueous solutions of 1-2.5 M NH_4OH yielded anatase titania nanoprotuberances with average diameters ranging from 23 nm to 60 nm, whereas exposure to 200°C/1 hour MWHT treatments with aqueous 1-2.5 M H_2O_2 solutions yielded rutile-bearing titania nanoprotuberances with average diameters ranging from 22 nm to 51 nm. MWHT exposure for all solutions examined resulted in

dramatic enhancements in the water contact angle (where a static drop spread to form a film on surfaces), without appreciable degradation in MG63 or normal human osteoblast (NHOst) cell differentiation (as evaluated by whole cell lysate analyses of MG63 and NHOst cells cultured on the surfaces). Enhanced hydrophilicity was retained after 119 days of storage in saline. MWHT oxidation is an effective, non-line-of-sight, low-temperature reaction process for tailoring the nanoscale surface structure and hydrophilicity of titanium implant surfaces, without degrading the microscale surface structure or the microstructure and properties of the underlying bulk implant. The results also indicate that osteoblast behavior is sensitive to nanoscale modification of a micro-rough surface. The nanomodification developed in this study did not impact osteoblast response compared to untreated micro-rough surfaces for most outcome measures, but did reduce osteocalcin production, suggesting that this indicator of osteoblast differentiation is mediated by other surface properties.

CHAPTER 4

CORRELATIVE ANALYSIS OF THE INTERFACE BETWEEN OSTEOBLASTS AND MICRO-ROUGH SURFACES OF LASER-SINTERED TI-6AL-4V CONSTRUCTS USING LASER CONFOCAL MICROSCOPY, SCANNING ELECTRON MICROSCOPY AND TRANSMISSION ELECTRON MICROSCOPY

In [Cheng A, Chen H, Schwartz Z and Boyan BD. Correlative laser confocal, scanning electron and transmission electron microscopy of the cell-material interface. Journal of the Royal Society Interface. 2016. Under review]

4.1. Introduction

Correlative light and electron microscopy (CLEM) has been used in many fields including animal and plant biology, ophthalmology and neuroscience [1-3]. Many of the first applications of high resolution correlative microscopy were in cellular structural biology [4]. Early work employed gridded coverslips, pre- and post-etched sample symbols and even nail polish to serve as fiducial markers for identifying the same physical location [5-7]. Advancements in hardware and software have now lead to automating this process, with sample holders compatible across multiple imaging modalities [8, 9].

Correlative microscopy became more accessible after methods for correlating images with fiducial markers were introduced in ImageJ, a publicly available free software [10]. it was possible to observe bone tissue around titanium dental implants using light microscopy, SEM and TEM, but the tissue-implant interface was only observable in light microscopy [11]. However, the tissue-implant interface was only observable in light microscopy. There was clear sample deterioration after processing for SEM, and implants

had to be completely removed for TEM analysis. TEM images were viewed and referred back to the previous sample area for correlation, rather than areas being pre-determined prior to analysis. Earlier "correlative" light and TEM studies imaged over 2000 TEM lamellas to achieve a comprehensive understanding of the tissue, without any direct information on the tissue-implant interface because implants were removed prior to TEM sectioning [12]. Another semi-correlative study attempted to understand the bone-implant interface by creating light and TEM sections from the same implant, but did not analyze the same section at the same location with both microscopes [13]. Thus, correlative analysis of the tissue-material interface across multiple spatial scales remains a challenge.

High resolution analysis of the biology-material interface is limited by sample preparation and correlation across multiple spatial scales. TEM investigations of the cell-surface interface have mostly been performed on silicon, a popular sensor material that can also be removed by etching or freeze fracture after fixation and resin embedding the cell monolayer in resin [14, 15]. However, removal of the substrate also limits additional TEM diffraction or chemical analyses, which can provide insight into preferred substrate areas of cell attachment. Pioneering work on focal adhesions and the cell-material interface used correlative microscopy of cultured cells on electron-microscopy grids [16, 17]. While useful for mechanistic and structural studies, these surfaces possess neither the chemistry nor the topography of clinically relevant biomaterials. To facilitate clinically relevant studies on the cell-material interface, versatile and high resolution sample preparation techniques must be employed.

Focused ion beams (FIB) have most commonly been employed for materials science applications. Recently FIB has been developed as a powerful imaging and sample

preparation technique for biological specimens [18]. Multiple studies have used FIB to examine cross sections of biological samples, using different sample preparation techniques. Wierzbicki et al. used FIB milling to investigate the cell-material interface of fibroblasts cultured on glass slides with submicron topography [19]. Samples were stained and coated with resin to facilitate FIB milling and viewing of cellular components; however, processing with resin prevented top-down SEM imaging and morphological observations of the cell and surface. We have used an alternate approach, analyzing cell volume and attachment parameters by FIB milling serial cross sections of osteoblasts on smooth and clinically relevant micro-rough titanium substrates [20]. The number of and distance between surface attachments obtained by cross sectional analysis were correlated with quantitative cell morphology obtained by top-down SEM images and with gene expression. Morphological correlations were performed as an average over different experiments. While averaged correlations may be suitable for homogenous cell populations, it can introduce error from other experimental variables. Thus, correlation across the sample or even a specific cell is much more useful for analyzing cell-material interactions.

In this study, we present the first correlative light and electron microscopy analysis of osteoblasts on a clinically relevant, optically opaque biomaterial. We provide examples of multi-scale analysis and flexibility across multiple modalities, each providing unique information about the cell-material interface.

4.2. Materials and Methods

Surface manufacturing

Substrates were disks 15mm in diameter and 1mm in height, which were laser sintered from Ti-6Al-4V powder as described previously [21]. Smooth surfaces were polished with aluminum oxide sandpaper (Norton Abrasive, Paris, France). Surfaces were etched for 90 minutes in a 10% solution of 1:1 maleic acid and oxalic acid (Sigma-Aldrich, Missouri, USA) in distilled water to achieve mesoscale roughness. Surfaces with hierarchical roughness were additionally blasted with calcium phosphate (proprietary, AB Dental, Ashdod, Israel) and acid etched to produce micro-roughness, and then acid etched to achieve mesoscale roughness followed by pickling to produce nano-roughness, as previously described [21].

Cell culture

A diagram of all steps and options for correlative analysis described in this study is presented in Figure 1. Calvarial osteoblasts were isolated from SD-Tg(UBC-EGFP)2BalRrrc transgenic rats (Rat Resource and Research Center, Columbia, Missouri, USA) that express ubiquitous enhanced green fluorescent protein (EGFP) under the human ubiquitin-C promoter with the woodchuck hepatitis virus posttranscriptional regulatory element (WRE). GFP-osteoblasts were plated on disks in 24-well plate at a density of 30,000 cells/cm2 (60,000 cells/well). Full medium (DMEM +10% FBS + 1% PenStrep) was changed 24 hours after plating. Medium was aspirated 48 hours after plating. Wells were rinsed twice with 1mL of pre-warmed 1XPBS, which was then aspirated. Cells were fixed with 1mL of 4% paraformaldehyde in 1xPBS for 15 minutes, then rinsed with 1mL 1xPBS. In order to observe actin filaments and nuclei, cells were incubated in 500µL 1xPBS with 1:80 phalloidin 594 and 1:1000 Hoechst for 20 minutes in the dark,

respectively. Cells were rinsed again three times with 1xPBS.

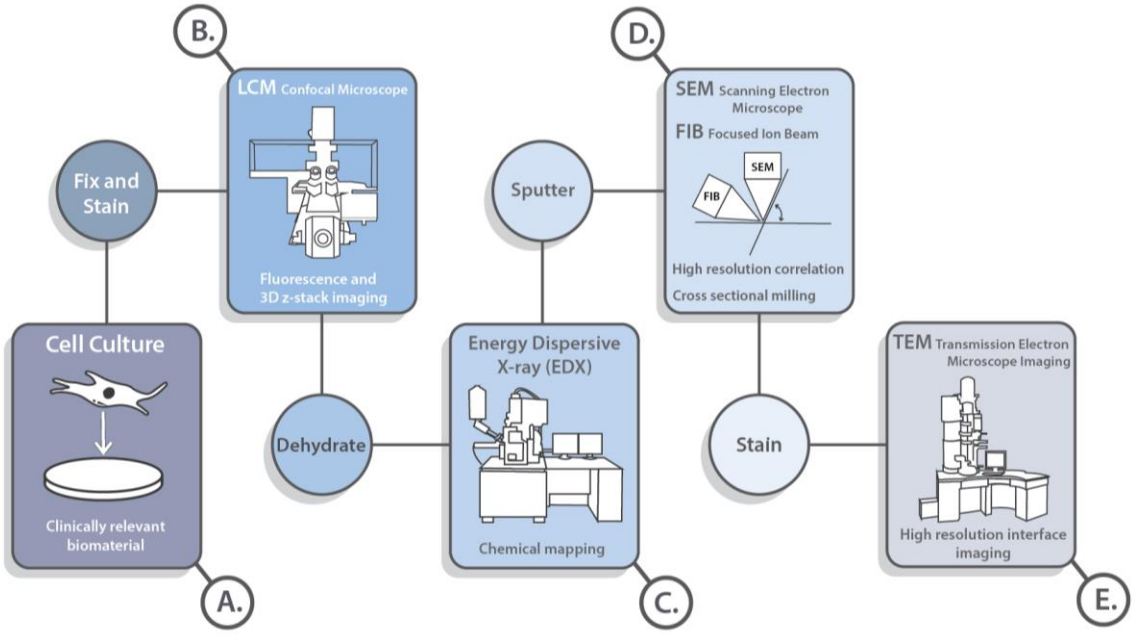

Figure 4.1. Schematic of correlative microscopy workflow. (a) Cells are cultured on a clinically relevant biomaterial of interest, or an implant is placed in vivo. The cells or tissue are fixed and fluorescently stained for proteins of interest before (b) fluorescence and 3D z-stack imaging in LCM. After dehydration, samples are ready for (c) chemical analysis in EDX. Samples are sputter coated to increase conductivity for (d) SEM high resolution correlative imaging and FIB milling of cross sections. Cross sections are stained for (e) high resolution imaging at the biology-material interface in TEM.

Sample fixation

Ti-6Al-4V disks were carefully mounted on 22x22mm glass coverslips (Zeiss, Oberkochen, Germany) with epoxy (Epoxicure 2 epoxy resin and hardener, Buehler, Lake Bluff, Illinois, USA). Epoxy resin was mixed with hardener at a ratio of 4:1. Pressure was applied on the edges of samples to secure them to the glass slide, and samples were allowed to dry overnight to allow the epoxy to cure. A small drop of epoxy was placed at one corner of the glass slide as a marker for orienting the sample during analysis.

Surface roughness and fluorescence imaging

Laser confocal microscopy was used to analyze surface roughness and image GFP fluorescence of cells on the surfaces. Samples were mounted onto a Shuttle and Find sample holder (Zeiss), with orientation noted by the epoxy location. Low magnification z-stacks were taken using a 20x (Plan-Apochromat 20x/0.8 M27), 0.1µm step size, 0.6 zoom and 0.79µs pixel dwell time. High magnification z-stacks were taken using a 40x objective (LD Plan-Neofluar 40x/0.6 M27), 0.1µm step size, 0.6 zoom and 1.58µs pixel dwell time. Four separate tracks were used. Surface roughness was characterized at 405nm in reflection mode, cell GFP was imaged at 488nm, Hoechst staining for the nucleus was imaged at 405nm, and phalloidin staining for actin was imaged at 594nm. Surface roughness was characterized using a 20x objective and analyzed using ZEN Blue software (Zeiss) with a bandpass filter wavelength of 100µm. Average surface roughness (Ra) was analyzed on three regions per sample, with at least two samples per group. Surface roughness values are reported as average ± standard deviation. During confocal imaging, samples were dampened with 1xPBS. A coverslip was secured to the sample with tape, making sure the tape only covered the edges of the coverslip and did not obstruct the sample view.

Preparation for electron microscopy

Samples were dehydrated in increasing concentrations of ethanol for 2 hours each: 15%, 30%, 45%, and then at least 1 hour each in 60%, 75%, 90%, 100%. Samples were immersed two more in fresh 100% ethanol for at least 1 hour, then exchanged in 1:1 100% ethanol and hexamethyldisilazane (HMDS) for 30 minutes in a fume hood. Samples were transferred to 100% HMDS for 30 minutes twice, then transferred to a vacuum dessicator to dry for at least 24 hours prior to electron microscopy.

Energy dispersive x-ray spectroscopy

Samples analyzed with EDX were not sputter coated prior to imaging. Regions of interest (ROI) previously characterized with LCM were relocated after stage calibration using the ZEN Shuttle and Find software package (Zeiss) in the Zeiss Auriga SEM/FIB system. EDX was performed with at a working distance of 9.5mm accelerating voltage of 15kV. EDX maps were performed at a magnification of 260X. Prior to analysis, EDX was calibrated on pure copper tape and aluminum substrates.

Scanning electron microscopy

Prior to scanning electron microscopy, samples were platinum-sputtered at 35µA for 90 seconds. Previously characterized regions of interest were located using the Shuttle and Find sample holder with electron microscopy adaptor in the Zeiss Auriga Zeiss FIB/SEM system. LCM and SEM correlative images were overlaid in Shuttle and Find software. Images were taken at a working distance of 4mm and accelerating voltage of 4kV.

Focused ion beam milling

FIB milling was conducted on a TESCAN LYRA 3 FEG-SEM/FIB system (Brno, Czech Republic) with a working distance of 9mm and 55° tilt. Regions of interest characterized previously by LCM and SEM were located using the Shuttle and Find system using a Zeiss Auriga Zeiss FIB/SEM (Zeiss). To locate regions across multiple SEM and FIB systems without Shuttle and Find, large "X" markers were FIB milled onto some samples. A layer of platinum (Pt) with a thickness of approximately 1µm was deposited at 200pA, 30kV and with a 100µm aperture at the location of interest to provide mechanical stability during FIB milling. Initial milling was performed using a fast stair rectangle template at 5µA and 30kV in front of and behind the Pt-deposited region of interest to

expose the interface. Polishing was performed at 1µA and 30kV to thin sections between 500nm-1µm, and the remaining side area attached to the substrate was milled away. A "U" cut was milled around the sides and bottom of the thin section to prepare for removal, leaving a small area attached for stability. The thin section was attached to a tungsten nano-manipulator using platinum deposition. The thin section was then attached to the TEM grid with Pt deposition on both sides of the sample, and the area attached to the nano-manipulator was removed by milling. Final polishing was performed on thin sections while attached to the TEM grid. This consisted of an initial milling decreasing from 1nA to 200pA to 100pA and at 30kV to mill sections to a thickness of approximately 200nm. Secondary polishing was performed at 100pA to 50pA and at 10kV to further decrease sample thickness to approximately 100nm. Final polishing to prepare for TEM was performed at 20pA and at 5kV and decreasing to 1.5kV to limit sample damage. Samples for electron tomography (ET) were only milled to 200-300nm in thickness.

Thin section contrast staining

Sections were stained to enhance contrast prior to further electron microscopy. Staining was conducted automatically using the Leica EM AC20 (Leica, Wetzler, Germany). Samples were double contrast stained for 20 minutes in 0.5% uranyl acetate, followed by 30 minutes in 3% lead citrate.

Transmission electron microscopy (TEM)

TEM was conducted with a Hitachi H7650 system (Hitachi, Tokyo, Japan) at 80kV and a Zeiss Libra 120 system (Zeiss) at 120kV.

Electron tomography (ET)

ET was conducted with a Titan Krios system (FEI Company, Oregon, USA). The sample holder and section were cooled with liquid nitrogen before transferring to the microscope. Images were taken with a 300kV accelerating voltage using a Falcon direct electron detector at 29kX or 75kX magnification. Manual tracking was used to center each image. The sample tilt angle ranged from ±58°, at 2° when less than 20°, and at 1° for greater angles. Images were taken with exposure time of 1 second, dose of 1.03 electrons per square angstrom (Å2) and pixel size of 2.88 Å at 29kX magnification and 1.11 Å at 75kX magnification. Tomographic reconstruction was conducted using IMOD software (University of Colorado at Boulder, USA) [22].

4.3. Results

Confocal imaging of GFP-cells showed a semi-confluent culture with heterogeneous cell morphology (Figure 4.2A). Cells were elongated and appeared to be nestled between surface features, with filopodia extending out to anchor the cell to the surface. SEM of the same location demonstrated that surface roughness was additionally punctuated by Ti-6Al-4V particles that were partially sintered (Figure 4.2B, C). Higher magnification confocal (Figure 4.2D) and SEM (Figure 4.2E) images were correlated (Figure 4.2F) to show greater detail of the cell and surface. Using this method, we were able to observe specific cell morphology corresponding to surface features.

Confocal imaging of GFP cells (Figure 4.2G) and SEM images of the same location (Figure 4.2H) on unsputtered surfaces were able to assess cell morphology on rough surfaces (Figure 4.2I). A ROI was then selected in SEM (Figure 4.2J) to yield a high magnification light-electron correlated image (Figure 4.2K). This image showed that cells

were generally elongated on the rough surface, but were rounder when attached to specific surface features. Additional analysis of material chemistry using the EDX feature in SEM identified carbon content on surfaces, which correlated with the spatial positioning of cells (Figure 4.2L).

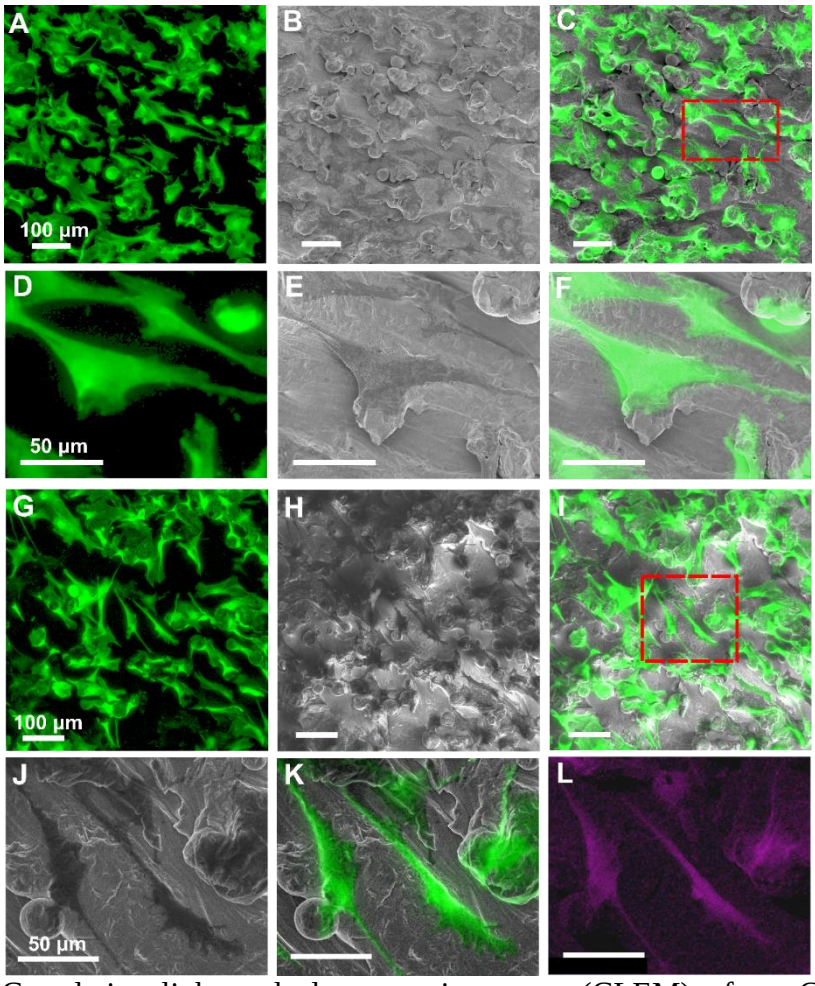

Figure 4.2. Correlative light and electron microscopy (CLEM) of rat GFP calvarial osteoblasts on laser sintered Ti-6Al-4V substrates. Osteoblast were plated on surfaces for 24 hours and imaged with (a) laser confocal microscopy and (b) scanning electron microscopy. (c) GFP fluorescence was superimposed on the correlated scanning electron

micrograph, with a region of interest (ROI) indicated within the red dashed lines. This ROI was enlarged to show the (d) GFP fluorescent osteoblasts, (e) electron micrograph of the surface roughness and (f) correlated. Osteoblasts were plated on surfaces for 72 hours and imaged with (g) confocal and (h) scanning electron microscopy and (i) correlated. An ROI indicated within the red dashed lines was imaged with (j) SEM to produce a (k) correlated light and electron micrograph. Samples were not sputtered prior to SEM, allowing for (l) EDX analysis of carbon content (in purple), which correlated with the presence of cells.

While cell morphology of GFP cells could be seen on CLM and SEM, correlation only provided limited additional information compared to using either method alone. However, by combining the two images it was possible to see how cell morphology related to the material surface. Moreover, LCM enabled identification of internal components of the cell, which were then correlated with SEM top-down images. GFP cells (Figure 4.3A) stained for actin (Figure 4.3B) and nuclei (Figure 4.3C) exhibited aligned actin fibers and normal distribution of nuclei within the cells. High magnification confocal images (Figure 4.3D) were correlated with SEM images (Figure 4.3E) to produce an overlay image (Figure 4.3F) which distinguished individual cells on the polished surface. Analysis of surface roughness using LCM enabled us to assess multi-scale roughness (Figure 4.3G), which showed that the surface possessed a relatively homogeneous micro-roughness with a z-range within 70μm. The same region of interest was correlated with fluorescent cells on the same surface (Figure 4.3H). This provided quantitative information about surface micro-roughness for a typically qualitative SEM image. The images showed a homogeneous distribution of cells attached on rough surfaces, though with less confluence than on polished surfaces.

SEM was also used to further evaluate nano-roughness. Smaller regions of interest were magnified to create correlative LCM-SEM image overlays (Figure 4.3I), with progressive high resolution magnification to desired ROIs (Figures 4.3J, 4.3I) in SEM.

Using this approach, high magnification SEM images of cell filopodia were imaged on surface nano-features (Figure 4.3L). Osteoblasts cultured on rough surfaces exhibited more filopodia than on smooth surfaces. At high magnification, filopodia were observed spreading over the surface nano-roughness, while still adhering to the curvature of the micro-roughness.

The correlative imaging approach was used successfully to examine the interface between osteoblasts and Ti-6Al-4V surfaces produced by laser sintering, a form of additive manufacturing. Smooth surfaces possessed an average surface micro-roughness (Ra) of 0.92±0.3 µm, and rough surfaces possessed a roughness of 7.6±1.1 µm. On smooth surfaces, the location of GFP osteoblasts (Figure 4.4A) correlated with that of EDX carbon mapping (Figure 4.4B). Confocal images were overlaid on SEM images at the same location (Figure 4.4C) to produce a correlative image (Figure 4.4D). A ROI (Figure 4.4D) was located with the FIB detector at a 55° tilt (Figure 4.4E) and a layer of Pt was deposited across the region to be milled (Figure 4.4F) to provide mechanical stability during milling. Trenches were milled around in front of and behind the section (Figure 4.4G). A "U" cut was milled around the section (Figure 4.4I) before attaching to the nano-manipulator (Figure 4.4I) and milling away the remaining section attached to the substrate. The section was attached to the TEM grid (Figure 4.4J) and final polishing was performed to prepare thin sections with approximately 100nm thickness (Figure 4.4K). Final lamellas were stained and imaged with TEM to observe the cell-material interface (Figure 4.4L). Sections were thin enough to view differences between the bottom patterned Ti-6Al-4V substrate, the lighter-colored cell on top of the substrate and the opaque Pt deposited on top of the cell.

After the proof of concept was completed on smooth surfaces, more clinically relevant micro-rough surfaces were used. On rough surfaces, GFP osteoblasts (Figure 4.5A) and SEM images of the same location (Figure 4.5B) were used to create a correlated overlay image (Figure 4.5C). A ROI (Figure 4.5C) was located with the FIB detector (Figure 4.5D) and a thin section was milled (Figure 4.5E). Final milling was performed after the thin section was attached to the TEM grid (Figure 4.5F). After staining, cellular components could be observed, but the section was too thick to observe the titanium substrate in TEM (Figure 4.5G). Higher magnification TEM images showed multiple layers and significant biological sample damage in the form of white semi-circular holes (Figure 4.5H, 4.5I). Unidentified cell organelles were observed as a results of contrast staining in the form of darker oval shapes in the cell. In addition, direct cell attachment was observed on the surface that followed the nano-scale surface contours.

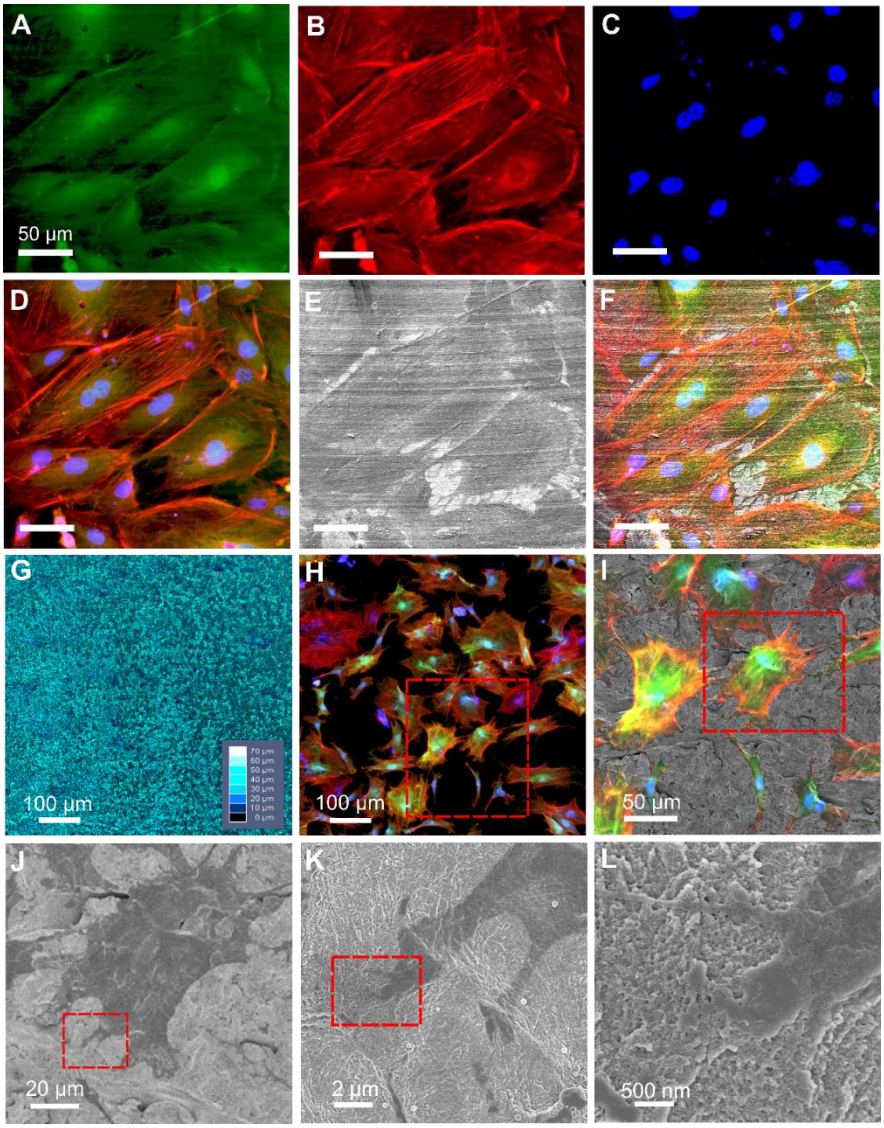

Figure 4.3. Correlative light and electron microscopy of GFP osteoblasts with cytoskeletal staining after 24 hours on smooth and rough Ti-6Al-4V substrates. Cells plated on smooth surfaces were imaged with LCM and show (a) GFP of the entire cell, (b) the actin cytoskeleton and (c) cell nuclei. (d) All three fluorescent tracks were merged with the corresponding (e) scanning electron micrograph in a (f) correlative image. LCM was used to analyze (g) surface micro-roughness of rough Ti-6Al-4V substrates before (h) fluorescence imaging was performed of the cell (green), actin (red) and nucleus (blue). The ROI indicated within the red dashed lines was chosen for (i) correlation with SEM. Each ROI indicated within the red dashed lines in (i, j, k) was imaged at higher magnification in (j, k, l), respectively. A high magnification image obtained with SEM shows the (l) surface nano-roughness that isn't detectable from the micro-roughness map obtained by LCM alone.

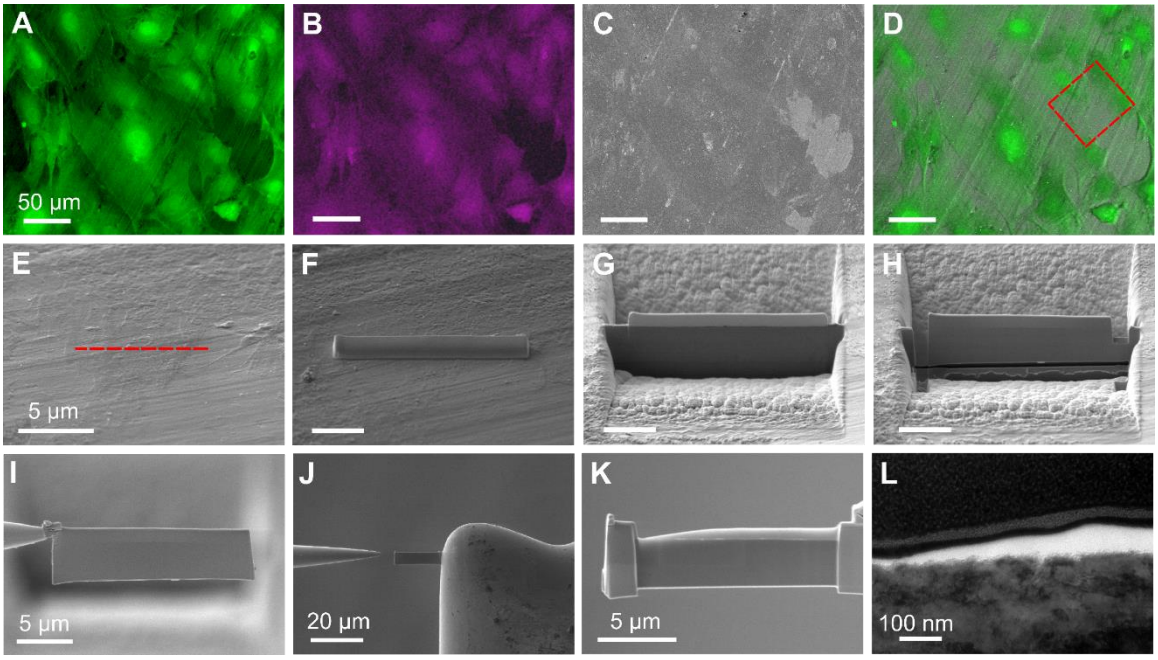

Figure 4.4. Complete correlative light and electron microscopy of osteoblasts on smooth sintered surfaces. (a) LCM of GFP osteoblasts plated on smooth Ti-6AL-4V surfaces, (b) chemical mapping performed in EDX, (d) SEM micrograph after platinum sputtering and (d) a correlated light-electron image. The region of interest indicated within the red dashed lines (e) was identified with the focused ion beam detector at a 52 degree tilt, and a red dashed line indicates the location to be prepared for TEM analysis. (f) Platinum was deposited atop the location to be milled to provide mechanical stability during milling, and (g) a section approximately 500nm thick was milled. (h) The perimeter was milled around the thin section to prepare for detachment, (i) the section was attached to a nanomanipulator by platinum deposition before the remaining edge was milled away. (j) The section was attached to a TEM grid by platinum deposition and (k) final milling was performed to reduce section thickness to less than 100nm. (l) TEM image shows the cell-material interface with high resolution.

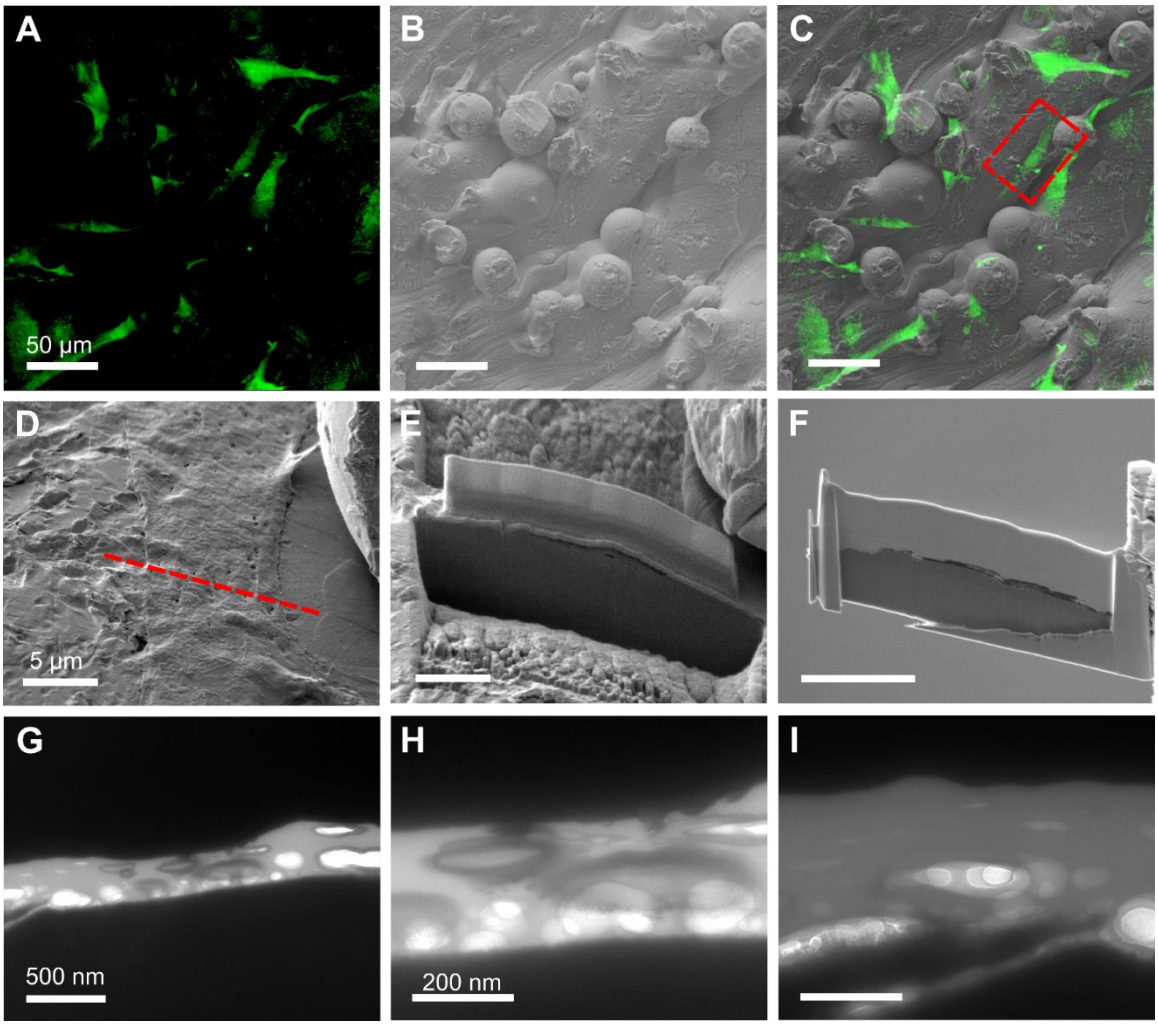

Figure 4.5. Complete correlative light and electron microscopy of osteoblasts on rough sintered surfaces. (a) LCM of GFP osteoblasts plated on smooth Ti-6AL-4V surfaces, (b) SEM micrograph after platinum sputtering and (d) a correlated light-electron image. The region of interest indicated within the red dashed lines (d) was identified with the focused ion beam detector at a 52 degree tilt, and a red dashed line indicates the location to be prepared for TEM analysis. (e) A section approximately 1µm thick was milled. (f) The section was attached to a TEM grid by platinum deposition and final milling was performed to reduce section thickness to less than 200nm. TEM images shows the cell-material interface at (g) lower and (h, i) higher magnification with sample damage induced by the milling process.

To combine the entire process from CLM to electron tomography, GFP osteoblasts were additionally permeabilized and stained for actin and nucleus on rough surfaces (Figure 6A). This showed a heterogeneous cell morphology across the surface. Confocal images were correlated with SEM of the same location (Figure 6B) to produce an image overlay (Figure 6C). This correlation revealed a morphological preference for cells attaching to various surface features. Cells attached on a micro-scale surface feature tended to bridge across the feature, either onto another adjacent feature or onto the bulk surface below. Where there were no adjacent surface features, cells would spread and cover the entire surface feature. Cells attached on the bulk substrate exhibited a smaller but still elongated morphology. A ROI (Figure 6C) was located with the FIB detector, and platinum was deposited at the location to be milled (Figure 6D). A thin section was milled (Figure 6E) and the final section, approximately 300nm in thickness, was attached to the TEM grid (Figure 6F). High voltage electron tomography was used to image the 3D volume of interest (Figure 6G), which was rotated to view depth of the sample and provide higher contrast at certain locations (Figure 6H). A volume of interest was selected at the cell-material interface, and an additional high magnification tomography analysis was used to observe the interface. Individual planes are shown that span through the reconstructed tomogram thickness (Figures 6I-L). Though sample damage was observed (thinner or nonexistent portions of the cell were lighter or white in color, respectively), high magnification tomography was still able to reveal structural changes in cellular organization at the interface (Figures 6I-L, middle portions). Because of increased sample thickness, the Ti-6Al-4V surface was opaque (Figures 6I-L, bottom).

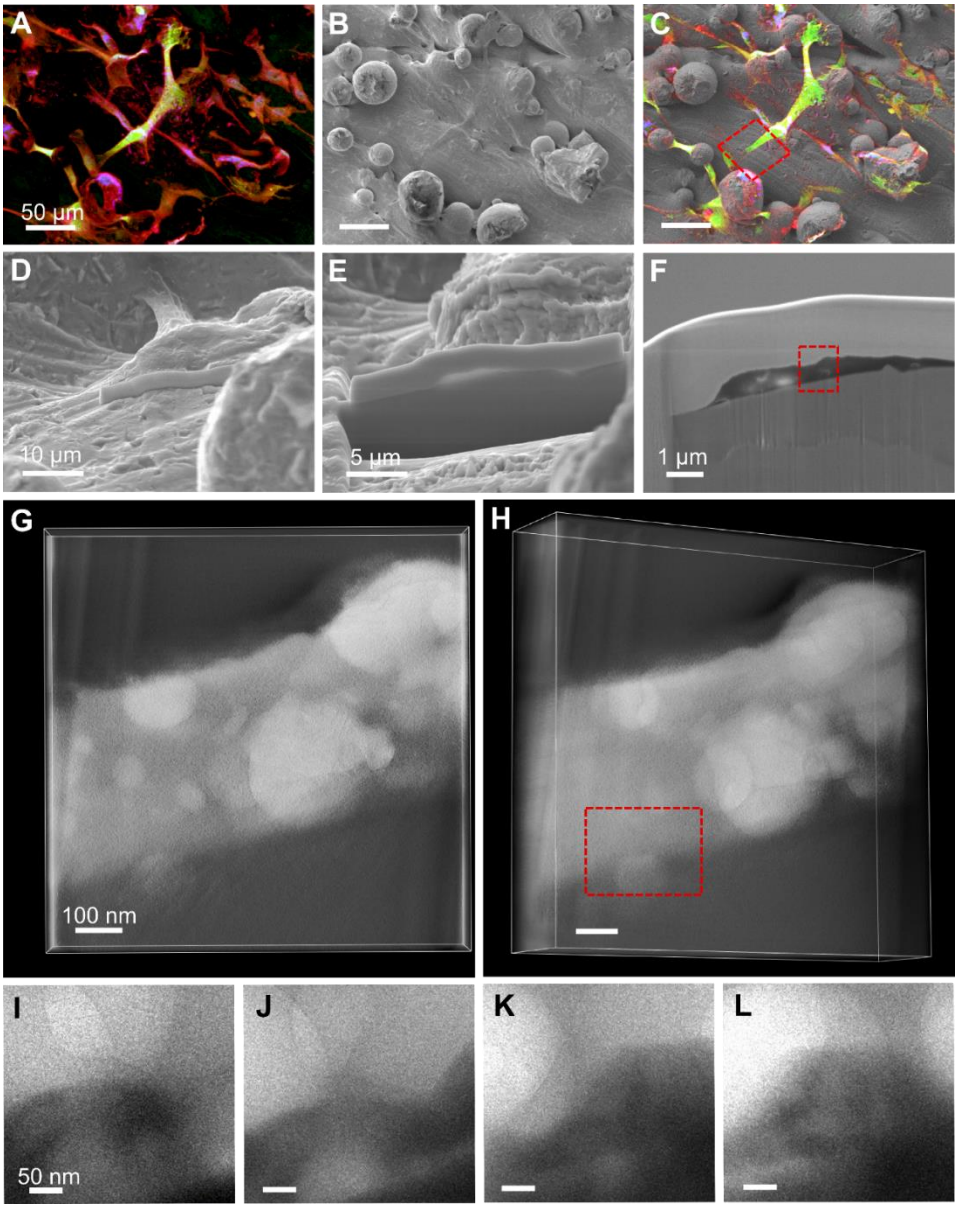

Figure 4.6. Complete correlative light microscopy and electron tomography of osteoblasts on rough sintered surfaces. (a) LCM of GFP osteoblasts plated on smooth Ti-6AL-4V surfaces stained for actin (red) and nucleus (blue), (b) SEM micrograph after platinum sputtering and (d) a correlated light-electron image. The region of interest indicated within the red dashed lines was identified with the focused ion beam detector at a 52 degree tilt, and platinum was deposited on the area to be milled. (e) A section approximately 1µm thick was milled. After attachment to TEM grid, (f) final milling was performed to reduce section thickness to less than 400nm. The region of interest indicated within the red dashed lines was identified as a 3D volume (g) in electron tomography, and (h) could also be tilted for depth perspective. The volume of interest indicated within the red dashed lines was imaged using electron tomography at high magnification to show (i-l) changes in the cell-material interface at different depths of the z-stack.

4.4. Discussion

Our study demonstrates that single-cell correlative analysis can be achieved across multiple imaging modalities. This workflow is especially attractive because it overcomes previous limitations in surface and cell imaging for opaque materials. Initial quantitative surface roughness analyses at the micro-scale can be combined with high resolution imaging of individual filopodia on nano-rough surfaces. For titanium substrates with hierarchical surface roughness, these correlations can provide a glimpse into structural and biological mechanisms regulating osteoblastic differentiation and cell-material interactions. For other biomaterials, this method can be used to elucidate cell preference for specific surface structural or chemical features. This correlative platform method can also be enhanced for future "smart" material analyses.

Because this study highlighted different examples to show versatility and a concept of our novel correlative methods, we did not focus on one particular variable. The most obvious application of this method would be to correlate staining for focal adhesion proteins with attachment morphology and substrate topography. This could be done with the combined use of fluorescent staining and nanoparticle tags that would be observable in both light and electron microscopy [23, 24]. Advancements in high resolution characterization technology may also provide a biochemical map of single cells, which could be correlated with material and morphological information [25, 26]. While we can correlate TEM interface images with an individual cell or even its fluorescently imaged cytoskeletal structure in this study, we cannot definitely identify proteins to correlate with sites of attachment. We chose to section at edges of the cell to focus on these sites of

attachment, which also explains the low cell height and lack of major organelles, such as the nucleus, in our TEM images.

From top-down qualitative images from LCM and SEM, it is clear that morphological differences exist between cells grown on smooth or rough substrates. While exact cell type and surface chemical composition varied from a previous study in our lab that quantified these differences, our results still corroborate that osteoblasts are rounded and more spread out on smooth titanium substrates, and elongated on rougher substrates [20]. This comparison can be observed directly when comparing Figures 3F and 3I (images are presented at the same magnification). These morphological changes on smooth versus rough surfaces are correlated with the degree of osteoblast differentiation [27].

Cross sectional images of osteoblasts in SEM and TEM after FIB milling showed a much thinner osteoblast cross section on smooth compared to rough Ti-6Al-4V surfaces. While osteoblasts on polished smooth surfaces had a cross sectional thickness of approximately 100nm, osteoblasts on micro-rough surfaces had a thickness of approximately 500nm to 1µm, depending on the location of sectioning within the cell. This observation was consistent with previous quantification of FIB-milled osteoblast cross sections on smooth and micro-rough titanium surfaces, which showed that cross sectional osteoblast thickness was much higher for cells cultured on rough titanium surfaces compared to on smooth surfaces [20]. An enhanced presence of cell filopodia was also observed on micro-rough surfaces compared to on smooth surfaces, and cross-sectional images indicated that these projections fully engulfed the surface nano-features. This suggests that while surface micro-roughness may be responsible for osteoblastic

differentiation and maturation, nano-topography can be important for cell attachment and motility.

However, while our previous study noted that cells would "tent" over micro-rough surface features, in this study we observed a differential morphological preference of cells that was feature specific. Cells on partially sintered micro-particles would either tent across to another adjacent particle or the underlying surface, or wrap around the particle almost completely. We believe the site of initial cell attachment as well as the size and spacing between surface features may affect its decision to spread across the feature or remain covering the feature. We have shown this size-specific effect on cell bridging previously, where cells remained within 100µm diameter cavities but would anchor to adjacent cavities when they were reduced in diameter to 30µm [28]. Our laser sintered particles ranged between 25-45µm in diameter with variable spacing between partially sintered surface particles, and this accordingly resulted in a differential response in cell morphology. These observations indicate that cell attachment and morphology are sensitive to distinct micro- and nano-scale surface features.

Sample preparation is very important when imaging at the nano-scale. We chose GFP-cells to optimize the correlative approach because it did not require permeabilization of the cell membrane to stain for cytoskeletal components, which would compromise high resolution electron microscopy analysis. However, we still observed artefacts in the cell membrane. While HMDS has been shown to induce less cell shrinkage than critical point drying, research has also shown that increasing HMDS exposure time correlates with increased cell shrinkage [29]. In addition, handling of samples for confocal imaging, including mounting and creating an orientation marker using epoxy resin and securing a

coverslip with PBS for better optical resolution, may affect cells. Future work should include optimization of fixation and processing protocols to decrease these sample artefacts.

While providing a unique way to observe biological cross sections, FIB milling is still a destructive technique [18]. We chose to use FIB as a sample preparation technique rather than an imaging modality. This technique provides the flexibility to choose between traditional TEM and electron tomographical analysis of cross sections, depending on section thickness. In addition, samples for TEM could be analyzed multiple times (before and after staining, or for chemical or diffraction analyses) for future studies. This is a significant improvement from traditional TEM sectioning, which requires removal of the implant even when sectioning with diamond knives in an ultramicrotome [30].

While ET can be useful for resolving thicker sections, it is also much more time consuming and very data intensive. A high resolution analysis of a nanometer-scale sample can easily take over 24 hours and require over 4 terabytes of data [31]. Even a "slice and view" automated FIB milling and viewing technique of a 90µm x 32µm x 2µm volume can take over 24 hours, though this may be preferable since processing and reconstruction can be completed in the same system [32]. Our method allows the user to analyze across different imaging modalities that would otherwise by incompatible. For example, correlative cryo-EM may require a cryo-light or focused ion beam milling electron microscope to preserve sample temperature [17, 33, 34]. Transportation or reanalysis of samples then also becomes a challenge. By fixing and sectioning samples at room temperature, the user can choose between FIB sectioning, SEM viewing, traditional TEM imaging or ET, without having to keep the sample vitrified during the entire process.

Final milling of thin sections to the desired thickness was challenging due to the inhomogeneous nature of the samples. A curtaining effect can be observed even after fine milling in Figure 6F. While a thicker platinum deposition of approximately 2µm has been shown to decrease curtaining effects, the already existing rough topography of our samples will inadvertently introduce artefacts from an uneven disintegration of platinum during milling [33]. Another way to enhance FIB milling is by ultra-thin resin embedding of the sample, which provides mechanical stability during sectioning [35]. Studies have shown 3D reconstruction of FIB milled cells with resolution as great as 3nm using resin embedding [18]. However, even a thin film of resin will obstruct nanotopographic features of the cell and substrate surface, so this method is recommended only when correlating between confocal and TEM, without consideration of top-down SEM imaging of surface topography.

The applications of this work are vast. First, our study shows the feasibility of evaluating the cell-material interface on almost any biomaterial, regardless of its optical properties. Second, this technique opens the door for dynamic and single cell analyses on these materials, which can provide insight into adhesion, migration and differentiation of wild type of compromised cells. Additional correlative analyses such as AFM, XPS or Raman spectroscopy could provide an even more comprehensive understanding of the surface topography and chemistry or cell differentiation profile.

4.5. Conclusion

We present a correlative microscopy method that spans multiple imaging modalities that allows for multi-scale spatial analysis of the same cells on clinically relevant biomaterial surfaces. Using this method, we evaluated osteoblast morphology and interaction with smooth and micro-rough, laser sintered Ti-6Al-4V surfaces. This platform method can be used to further understanding of the cell-material interface and enhance design of future biomaterial surfaces. Future development of these methods can provide insight into cell-specific interaction mechanisms with different materials.

CHAPTER 5

NOVEL HYDROPHILIC NANOSTRUCTURED MICROTEXTURE ON DIRECT METAL LASER SINTERED TI-6AL-4V SURFACES ENHANCES OSTEOBLAST RESPONSE IN VITRO AND OSSEOINTEGRATION IN A RABBIT MODEL

In [Hyzy SL, Cheng A, Cohen DJ, Yatzkaier G, Whitehead AJ, Clohessy RM, Gittens RA, Boyan BD and Schwartz Z. Novel hydrophilic nanostructured microtexture on direct metal laser sintered Ti-6Al-4V surfaces enhances osteoblast response in vitro and osseointegration in a rabbit model. Journal of Biomedical Materials Research Part A. 2016. 104(8):2086-2098]

5.1. Introduction

Osseointegration of implants into the jaw, hip, spine, or other bone is the ultimate clinical goal for endosseous implants. Titanium (Ti) is commonly used in bone-interfacing implants because of its desirable mechanical properties and ability to create a direct apposition with bone [107, 108]. Ti alloys such as titanium-aluminum-vanadium (Ti-6Al-4V) are also popular and have shown success clinically[109]. The five-year success rate of dental implants has increased from 93.5% to 97.1% within the past decade, with higher survival and lower complication rates [110]. However, in dentistry and other orthopaedic fields, patient and clinical variability affect implant outcomes. High variability in implant survival exists for hip replacements, with an estimated 5 to 20% revision rate for patients with total hip arthroplasty [111]. Osseointegration rates are significantly lower in compromised patients including smokers, diabetics, or those with low bone density [112-114]. In addition, an increasing number of cases require the use of custom or very specific implants. Although implants are made in a variety of shapes and sizes, the production costs

and waste associated with manufacturing a single custom implant can decrease patient desire for implant therapy. Thus, a more cost-effective method of producing orthopaedic and dental implants is necessary for a broad range of clinical cases and patient populations.

Much progress has been made in orthopaedic and dental implant design within the past 20 years. During this time, our lab has focused on developing and characterizing new implant surfaces and understanding the physical parameters of these surfaces on biological response. Recently, the clinical implant research community gained an interest in additive manufacturing, touting it as a "game changer" in the field [115]. Direct metal laser sintering (DMLS) is an additive manufacturing technique that can be used to build custom orthopaedic and dental implants from Ti-6Al-4V powder [116]. Not only does this method save time, material, and money, but it also allows customized implants with micron-scale resolution [117]. Customized implants eliminate the need for further manipulation of the implanted material during surgery or piecing together multiple parts of material. Such advancements in manufacturing technology have shown positive results both *in vitro* and in animal models, and recently, these manufacturing methods have been implemented clinically [38, 116, 118, 119].

From a scientific perspective, manipulating chemical and physical parameters can alter the biological response at the surface. For decades, scientists have tried to understand what factors are needed to optimize the surface for increased cell attachment, osteoblast differentiation, and ultimately osseointegration with the surrounding and new bone. Our lab has shown the importance of wettability, surface micro- and nano-roughness, and implant macro-structure in increasing osteoblast response to implant surfaces [7, 22, 104, 120]. These factors influence protein adsorption and cell response at the implant surface,

but have also been shown to affect osteoblastic differentiation and formation of an osteogenic environment at sites distal to the implant [7, 40]. In addition, various animal models used by our lab and other labs continue to explore osseointegration of new surfaces *in vivo* to translate between mechanistic studies and clinical relevance [65, 118, 121].

Although small rodents are commonly used for preclinical studies due to their low price and availability, implants or surfaces must be designed with smaller dimensions to conform to these models [65]. Rabbits are a larger animal model that can be used with clinically relevant implant sizes, with various studies validating implant placement in rabbit tibias or femurs [122-124]. Rabbits comprise 35% of all animal studies and are the most used model in musculoskeletal research [125].

In this study, we compared the biological response to Ti-6Al-4V surfaces and implants manufactured by either traditional milling using computer numerical control (CNC) technology or DMLS. We first compared osteoblast response to disks fabricated by CNC milling and then polished to yield a smooth surface (CNC-M) with disks fabricated by the laser-sintering technology (LST) followed by processing to generate smooth (LST-M), grit blasted (LST-B), and grit-blasted/acid etched (LST-BE) surfaces. To determine if LST-BE implants were osteogenic *in vivo*, we compared their osseointegration with commercially available CNC-B implants in a rabbit model. We hypothesized that laser sintered surfaces would induce osteoblast differentiation in a roughness-dependent manner and that laser sintered implants with post-fabrication surface roughness would osseointegrate in a manner comparable to, if not better than, clinically used CNC-manufactured and grit blasted implants.

5.2. Materials and Methods

Surface Manufacturing

All disks used for *in vitro* studies were 15mm in diameter and 1mm in height in order to fit snugly into wells in a 24 well plate. Grade 4 Ti-6Al-4V rods were cut using CNC milling and polished using aluminum oxide sandpaper (P240, Norton Abrasive, Paris, France) to yield a smooth surface (CNC-M). LST surfaces were sintered as disks as published previously[38]. Briefly, Ti-6Al-4V particles 24-45μm in diameter were sintered with a Ytterbium fiber laser (EOS, EmbH Munchen, Germany) using a scanning speed of $7ms^{-1}$, wavelength of 1054nm, continuous power of 200W, and laser size of 0.1mm. LST-M surfaces were polished as above to produce a smooth surface. LST-B surfaces were blasted with calcium phosphate particles in a proprietary method (AB Dental, Ashdod, Israel). LST-BE surfaces were laser sintered, blasted with calcium phosphate particles and then acid etched for 90 minutes in 10% of a 1:1 ratio of maleic and oxalic acids (Sigma-Aldrich, St. Louis, MO, USA) in distilled water. All disks and implants were generously provided as a gift from AB Dental.

Scanning Electron Microscopy

Scanning electron microscopy (SEM, Hitachi SU-70, Tokyo, Japan) was used to obtain low and high magnification images of surfaces and implants. Images were taken at an accelerating voltage of 4kV, objective aperture of 30μm, and a working distance of 4mm. Various magnifications were used to image locations across samples and the most representative images chosen for each sample. High magnification images were used to qualitatively assess surface nano-roughness.

X-ray Photoelectron Spectroscopy

The surface chemical composition was determined by X-ray photoelectron spectroscopy (XPS, ThermoFisher ESCAlab 250, Waltham, MA, USA). Survey scans were taken using an Al-Kα X-ray source and a spot size of 500µm. 6 locations were surveyed for each implant, with two implants per group analyzed for a total average across n=12 locations.

X-ray Dispersive Spectroscopy

Chemical analysis was performed by energy dispersive X-ray spectroscopy (EDX, Hitachi SU-70, Tokyo, Japan) at an accelerating voltage of 15kV and a working distance of 15mm. Scans were performed for 50 seconds, and atomic percentages were recorded as the average of 6 scans per group.

Laser Confocal Microscopy

Laser confocal microscopy (LCM, LEXT OLS4000, Olympus, Center Valley, PA) was used to assess average surface micro-roughness (S_a) and peak to valley height (S_z). Scans were taken over a 644µm^2 area with a 20x objective and 0.5µm step size. A cutoff wavelength of 100µm was used to exclude effects of waviness. Three measurements were taken per sample, with two samples per group analyzed (n=6).

Contact Angle and Immersion Analysis

Wettability of surfaces was assessed through sessile drop contact angle. A 4µL drop of distilled water was deposited on surfaces using a goniometer (Rame-hart model 200, Succasunna, NJ) and was analyzed with DROPimage (Rame-hart). For hydrophilic samples, surfaces were dried for 1 minute with flowing nitrogen between measurements. Five drops were analyzed per sample, with two samples per group (n=10). Reported measurements are the mean and standard deviation of the left and right contact angles for

each group. Images of implant immersion into distilled water were captured to evaluate implant wettability qualitatively[69].

Cell Culture

A cell culture model established by our lab for analyzing osteoblast response to clinically relevant surfaces was used to assess cell response to laser sintered surfaces[9, 126]. MG63 osteoblast-like cells (ATCC, Manassas, VA) or normal human osteoblasts (NHOst, Lonza, Walkersville, MD) were plated onto tissue culture polystyrene (TCPS), CNC-M, LST-M, LST-B, and LST-BE surfaces at a density of 10,000 cells/cm^2. MG63 cells were used before passage 15 while NHOsts were between passage 4 and 7. Cells were cultured in Dulbecco's modified Eagle's medium supplemented with 10% fetal bovine serum (Life Technologies, Carlsbad, CA), 50 U/mL penicillin, and 50 µg/mL streptomycin in a 24 well plate. Cells were fed 24 hours after plating and every 48 hours thereafter until cells reached confluence on TCPS (approximately five days after plating for MG63 cells and seven days for NHOsts). The medium was replaced at confluence. All statistical analyses for *in vitro* studies were conducted using one-way analysis of variance (ANOVA) with Bonferroni-post correction and a p value of less than 0.05 indicating significance.

Secreted Factors Analysis

At 24 hours post-confluence, conditioned media were collected, cell monolayers were rinsed twice with PBS and lysed in 0.05% Triton X-100, and both were frozen overnight before analysis. Cell lysates were homogenized by sonication. DNA content (QuantiFluor, Promega, Madison, Wisconsin) and alkaline phosphatase specific activity (*p*-nitrophenol release from *p*-nitrophenyl phosphate at pH 10.25, normalized to the protein content of lysate) were measured.

Culture supernatants were used to quantify protein release by cells. Enzyme-linked immunosorbent assays were used to quantify osteocalcin (Alfa Aesar, Ward Hill, MA), osteoprotegerin (OPG, R&D Systems, Minneapolis, MN), vascular endothelial growth factor A (VEGF, R&D Systems), fibroblast growth factor 2 (FGF2, R&D Systems) and bone morphogenetic protein 2 (BMP2, PeproTech, Rocky Hill, NJ) following manufacturer's instructions. Immunoassay results for each culture were normalized to total cell number.

mRNA Analysis

In a separate set of culture, cells for mRNA analysis were incubated with fresh media for 12 hours after cells reached confluence on TCPS. TRIzol® was used to isolate RNA according to manufacturer's instructions and reverse transcribed into cDNA (High Capacity cDNA Kit, Life Technologies, Carlsbad, CA). The cDNA was used for quantitative real-time polymerase chain reaction (qPCR) with SYBR Green (Life Technologies). Known dilutions of cDNA were used to generate standard curves and mRNA of integrin subunits α2 (F: ACTGTTCAAGGAGGAGAC; R: GGTCAAAGGCTTGTTTAGG) and β1 (F: ATTACTCAGATCCAACCAC; R: TCCTCCTCA TTTCATTCATC), and were normalized to the expression of glyceraldehyde 3-phosphate dehydrogenase (GAPDH, F: GCTCTCCAGAACATCATCC; R: TGCTTCACCACCTTC TTG).

Implant Manufacturing

All implants were 3.7mm in diameter and 8mm in length and manufactured by AB Dental. Commercially available machined implants were fabricated using a traditional CNC manufacturing process and treated with a proprietary bioresorbable blasting method

(AB Dental, Ashdod, Israel) to induce surface roughness (CNC-B). LST implants were laser sintered from Ti-6Al-4V powder as described above, blasted with calcium phosphate, and subsequently acid etched in the same manner used to generate LST-BE disk surfaces. All implants were sterilized with 2.5 Mrad of gamma radiation before use.

Surgical Procedure

Skeletally mature, male New Zealand white rabbits weighing 4±0.25 kg were obtained from Harlan Laboratories (Rossdorf, Germany). Each rabbit received two implants: a CNC-B implant placed in its left femur, and an LST-BE implant placed in its right femur. Rabbits were given full anesthesia through flowing isoflurane. A 3cm skin incision was made laterally at the distal femur, and muscle and soft tissue were separated. Drilling was carried out at low speed and was accompanied by physiological saline irrigation. CNC-B implants were placed transaxially in the distal right femur, and LST-BE implants were implanted into the contralateral (left) femur. Each rabbit received one implant in each femur, with eight animals per time point and analysis. The cover screw remained above bone level, periosteum and muscle was reapproximated, and a simple running suture technique was used to close the surgical site skin incision. Animals were euthanized three or six weeks after implantation. Implants and surrounding bone were harvested for microcomputed tomography (microCT), histomorphometry, and mechanical testing (described below). The Animal Research Committee approved animal protocols at the University of Goethe (Frankfurt, Germany) and guidelines for the care and use of laboratory animals were observed. Statistical analysis of the histologic assessment of bone-implant contact was conducted using one-way ANOVA and Tukey's tests with a p-value of 0.05. Student's t-test, with a p-value of 0.05 indicating significance was used for

comparison between two groups in the histologic assessment, microCT, and mechanical testing.

Histology

Animals were euthanized at each time point, and femurs were harvested and then were fixed in 10% neutral buffered formalin. Eight implants were examined for each condition, and six implants measured for 3 week machined implants. Samples were embedded in methyl methacrylate. Histological sections longitudinal to the implant and transaxial to the animal were obtained from each sample (Histion LLC, Everett, WA, USA). Each section was stained using Stevenel's Blue [127-129].

Slides were imaged using transmitted light bright field on a Zeiss Observer Z1 (Oberkochen, Germany) microscope equipped with a 10x objective and 10x optical zoom. Images were captured by an AxioCam MRc5 camera and were analyzed with Zeiss ZEN Pro Blue Edition software. The trabecular and cortical perimeter of each implant were measured using the curve (polygon) tool; the perimeter of the implant directly adjacent to the cortical bone was measured as cortical perimeter and the remainder as trabecular bone. Bone-implant contact (BIC) was assessed in three measurements: trabecular BIC, cortical BIC, and total BIC. Contact percentage was found by dividing the length of contact in the cortical and trabecular regions by the cortical and trabecular perimeters, respectively. The total BIC was calculated by summing both lengths of contact and dividing by the total perimeter of the implant.

MicroCT Analysis

Micro-computed tomography (microCT, Bruker SkyScan 1173, Kontich, Belgium) was performed on rabbits three and six weeks after implantation. 8 implants were examined

for each condition, and 6 implants measured for 3 week machined implants. Samples were scanned at a resolution of 1120x1120 pixels, using a 1.0mm aluminum filter, a source voltage of 130kV, source current of 61µA, image pixel size of 18.69µm, exposure of 350ms, rotation step of 0.1^{o} and averaging and random movement correction every ten frames. A standard Feldkamp reconstruction was performed on a subset of samples using NRecon software (Bruker, Kontich, Belgium) with a Gaussian smoothing kernel of zero and a beam hardening correction of 12%. Bone-implant contact was determined by analyzing reconstructed scans in CTAn image analysis software (Bruker, Kontich, Belgium). Sagittal cross sections were thresholded to analyze implant volume within a 25µm radius of the inner periphery. The image was then thresholded again to remove the implant by shrink wrapping the region of interest and despeckling the image. The bone volume within a 25µm radius of the outer implant periphery was then analyzed by thresholding and de-speckling the region of interest. The quotient of the bone volume and implant volume, multiplied by 100, was calculated as the total bone-implant contact (BIC).

Mechanical Testing

Pull out testing was performed as a commonly used technique for evaluating mechanical properties of implant osseointegration in a rabbit femur model (MTS Insight 30; MTS Systems Corp., Eden Prairie, MN, USA)[130]. In contrast to evaluating bone contact at the interface with torsional testing, pull out testing evaluates the quality of new bone formation around the implant[131]. A custom abutment fabricated by AB Dental was screwed completely into the implant and then was pulled at a crosshead speed of 5 mm/min according to ASTM standard 543-13. Axial pullout strengths were recorded and the load was monitored for force at failure (N). Three animal-matched pairs of implants were

examined three weeks after implantation and five pairs of implants were examined 6 weeks post-implantation.

5.3. Results

Surface Roughness and Topography

All surfaces showed varying degrees of surface roughness. CNC-M and LST-M surfaces were smooth at both the micro- and nanoscale (Figure 1A, B). Both LST-B and LST-BE surfaces possessed similar micro-roughness and homogenously distributed nanostructures (Figure 1C, D). LCM analysis showed increasing average surface roughness (S_a) for CNC-M (1.42 ± 0.10µm), LST-M (1.71 ± 0.05µm), LST-B (2.39 ± 0.28µm) and LST-BE (2.94 ± 0.32µm) (Table 5.1). In the same manner, peak to valley height (S_z) increased for CNC-M (28.59 ± 3.61µm), LST-M (35.26 ± 11.59µm), LST-B (49.40 ± 8.61µm) and LST-BE (57.66 ± 7.33µm). Though blasting with calcium phosphate and acid etching both resulted in increased S_a and S_z compared to smooth surfaces, the increase of roughness on LST-B surfaces compared to LST-M was larger than the increase in roughness on LST-BE surfaces compared to LST-B surfaces.

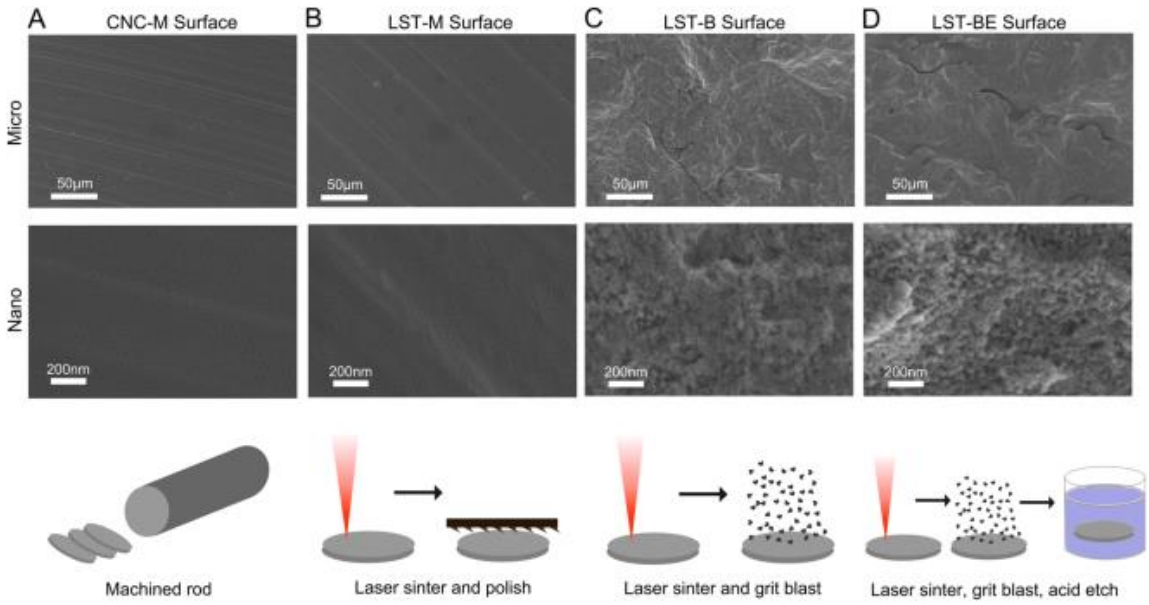

Figure 5.1. SEM micrographs of CNC-M (A), LST-M (B), LST-B (C) and LST-BE (D) surfaces used for in vitro studies. A low magnification view shows micro-roughness (top) and high magnification view shows nano-roughness (middle). CNC-M surfaces were cut from a rod (A bottom), while LST-M, LST-B and LST-BE surfaces were produced by laser sintering with further surface treatment (B-D bottom).

Table 5.1. Average roughness and peak-to-valley heights

Sample	**Average (S_a) [µm]**	**Peak-to-Valley Height (S_z) [µm]**
CNC-M	1.42 ± 0.10	28.59 ± 3.61
LST-M	1.71 ± 0.05	35.26 ± 11.59
LST-B	2.39 ± 0.28	49.40 ± 8.61
LST-BE	2.94 ± 0.32	57.66 ± 7.33

Elemental Analysis

Elemental composition analysis by EDX showed a prominence of Ti, followed by Al and V elements on all surfaces (Table 5.2). Ti, Al, and V were present on CNC-M, LST-M, and LST-BE surfaces at similar levels (Table 5.3). However, LST-B surfaces had reduced Ti, Al and V and a more O compared to other surfaces.

Table 5.2. EDX elemental analysis

Sample	Concentration [Atomic % ± SD]			
	Ti	**Al**	**V**	**O**
CNC-M	86.6 ± 1.1	9.3 ± 1.2	4.0 ± 0.2	--
LST-M	87.1 ± 1.1	8.9 ± 1.4	4.0 ± 0.3	--
LST-B	59.1 ± 1.5	5.8 ± 0.5	2.5 ± 0.1	32.6 ± 1.6
LST-BE	87.8 ± 0.5	8.3 ± 0.7	3.9 ± 0.2	--

Table 5.3. XPS elemental analysis

Sample	Concentration [Atomic % ± SD]						
	Ti	**O**	**C**	**F**	**P**	**Al**	**Si**
CNC-B	14.5 ± 1.2	51.1 ± 2.7	26.3 ± 4.3	2.2 ± 1.9	2.8 ± 1.4	1.7 ± 1.8	1.3 ± 1.4
LST-BE	9.4 ± 1.7	39.1 ± 1.7	39.5 ± 9.1	8.1 ± 4.2	--	--	--

Surface Wettability

Contact angle measurements showed that LST-B had significantly lower contact angle and, therefore, higher surface wettability, compared to all other surfaces (Table 5.4). The contact angles of CNC-M (108±8^o) and LST-M (111±5^o) were not significantly different from each other. However, micro-rough LST-B and LST-BE surfaces were hydrophilic with contact angles of less than 20^o and 25±7^o, respectively.

Table 5.4. Sessile drop contact angle

Sample	Contact Angle (°) ± SD
CNC-M	108 ± 8
LST-M	111 ± 5
LST-B	<20
LST-BE	25 ± 7

In Vitro Cell Response

DNA was higher in MG63 cells cultured on LST surfaces than on CNC-M (Figure 2A). Alkaline phosphatase specific activity (Figure 2B), osteocalcin (Figure 2C), osteoprotegerin (Figure 2D), FGF2 (Figure 2F), and BMP2 (Figure 2G) were higher in MG63 cells on LST-B and LST-BE surfaces than cells on smooth (CNC-M and LST-M) surfaces. VEGF was only higher on LST-BE surfaces in comparison to M and LST-M surfaces (Figure 2E). mRNA levels of ITGA2 (Figure 2H) and ITGB1 (Figure 2I) increased on LST-B and LST-BE surfaces in comparison to CNC-M surfaces, but there was no difference in expression due to the acid etched surface.

While MG63 and NHOst responded similarly on the surfaces examined, the response varied for the specific factors measured. Osteocalcin secreted by NHOst was higher on all LST surfaces in comparison to CNC-M, and was higher on LST-B and LST-BE surfaces compared to LST-M surfaces (Figure 3A). OPG was increased on LST-B and LST-BE in comparison to CNC-M and LST-M surfaces (Figure 3B). VEGF was increased on LST-B and LST-BE surfaces in comparison to CNC-M and LST-M surfaces, and was significantly higher on LST-BE surfaces in comparison to LST-B surfaces (Figure 3C). BMP2 was higher on LST-B and LST-BE surfaces than on M and further increased on LST-BE surfaces in comparison to LST-B surfaces (Figure 3D).

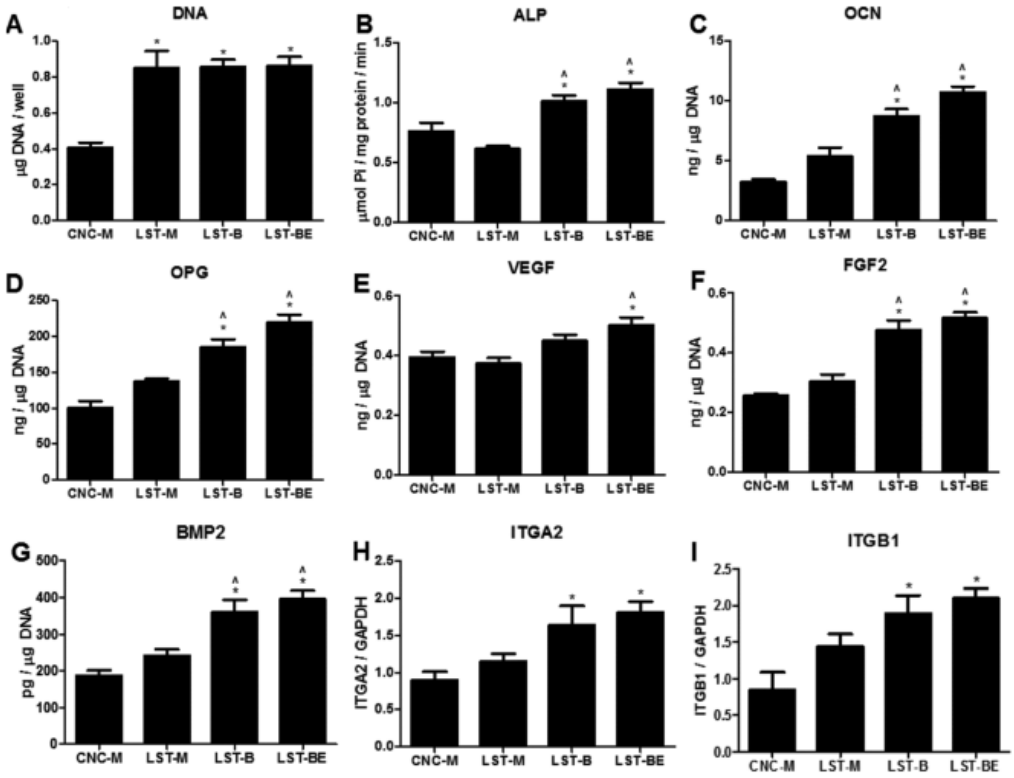

Figure 5.2. MG63 cell response to CNC-M, LST-M, LST-B and LST-BE surfaces. DNA content (A) and alkaline phosphatase specific activity (B) were analyzed in cell lysates. Osteocalcin (C) vascular endothelial growth factor A (D), fibroblast growth factor 2 (E), and bone morphogenetic protein 2 (F) were measured in cell-conditioned media. mRNA levels of ITGA2 (G) and ITGB1 (H) were measured analyzed in cell media 24 hours after confluence. $p<0.05$, * vs. CNC-M, ^ vs. LST-M, # vs. LST-B.

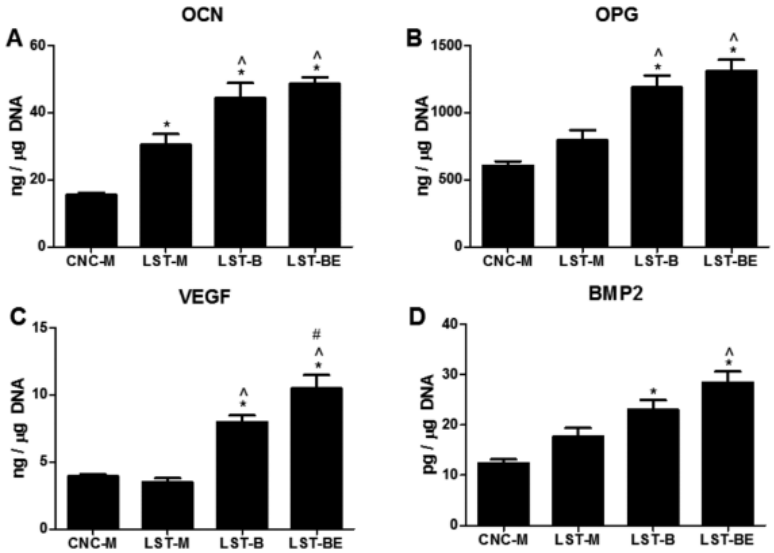

Figure 5.3. NHOst cell response to CNC-M, LST-M, LST-B and LST-BE surfaces. Osteocalcin (A), osteoprotegerin (B), vascular endothelial growth factor (C) and bone morphogenetic proteins (D) were upregulated on LST-B and LST-BE surfaces. $p<0.05$. * vs. CNC-M, ^ vs. LST-M, # vs. LST-B.

Implant Surface Roughness

CNC-B implants were manufactured by a traditional CNC manufacturing process, and LST-BE implants were manufactured via laser sintering. CNC-B and LST-BE implants underwent different surface treatments; however, both implants possessed micro- and nano-roughness (Figure 4A, B). Although micro-roughness was similar for CNC-B and LST-BE implants, nano-roughness was quite different. LST-BE implants possessed distinct nanostructures on the surfaces while CNC-B implants did not have such distinct nanofeatures.

Implant Surface Chemistry

Surface chemistry analysis by XPS showed mainly Ti, O, and C on implant surfaces, with less than 3% of F, P, Al and Si detected on CNC-B implants only (Table 4).

Implant Wettability

Sessile drop contact angle on the coronal, non-threaded portion of the implant showed a relatively more hydrophobic surface on CNC-B implants (85 ± 2^{o}) compared to LST-BE implants ($<20^{o}$) (Figure 4C). Immersion of implants into distilled water showed a similar trend (Figure 4D). Water was drawn up the sides of the LST implant when immersing, indicating a hydrophilic surface. When pulling the implant out of water, more water was retained on the LST-BE implant compared to the CNC-B implant.

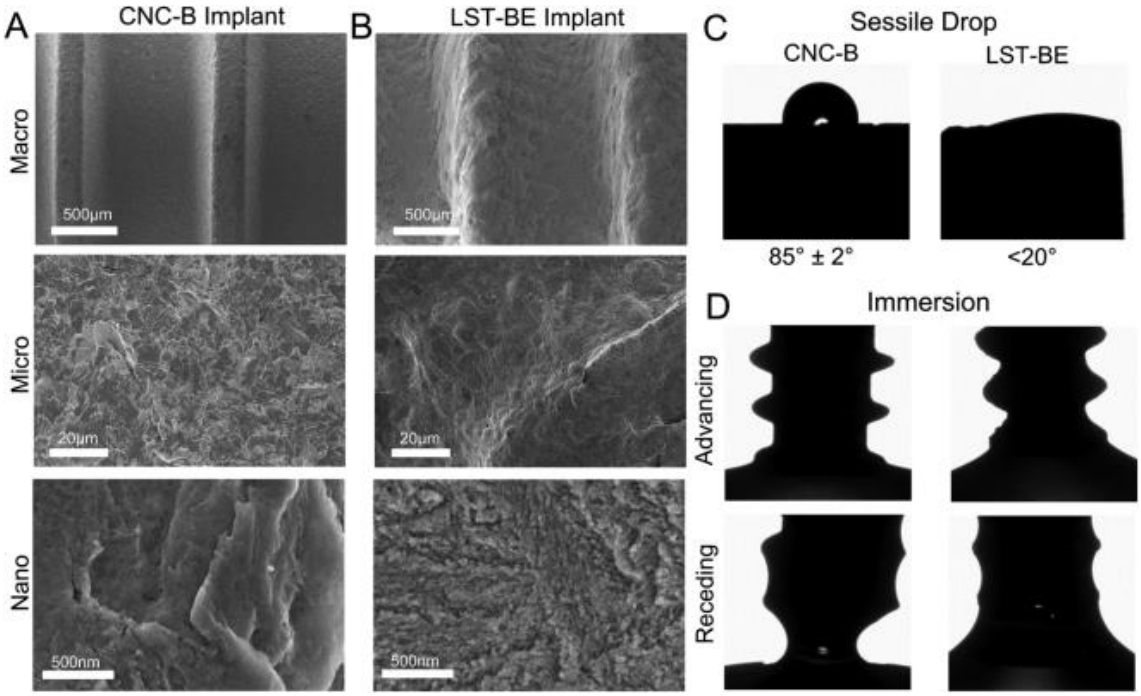

Figure 5.4. Scanning electron micrographs showing macro (top), micro (middle) and nano-roughness (bottom) of CNC-B (A) and LST-BE (B) implants. Sessile drop contact angles of CNC-M (left) and LST-BE (right) implants (C) and immersion analysis of wettability.

Histology

Histological analysis of CNC-B and LST-BE implants at three weeks (Figure 5A) and six weeks (Figure 5B), revealed differences in BIC values for each implant. BIC for LST implants was found to be significantly higher than in the machined implants at both the three week and six week time points (Figure 5C, D). Cortical BIC at three weeks was significantly lower than total or trabecular BIC for both CNC-B and LST-BE implants, although there were no differences in trabecular BIC at three weeks. Total BIC in the LST-BE group was statistically higher than that in the machined group at six weeks. Trabecular BIC of LST-BE implants was significantly lower than total BIC at six weeks but was not significantly different from trabecular BIC of CNC-B implants. Cortical BIC values for both CNC-B and LST-BE implants were lower than total and trabecular BIC values at six weeks.

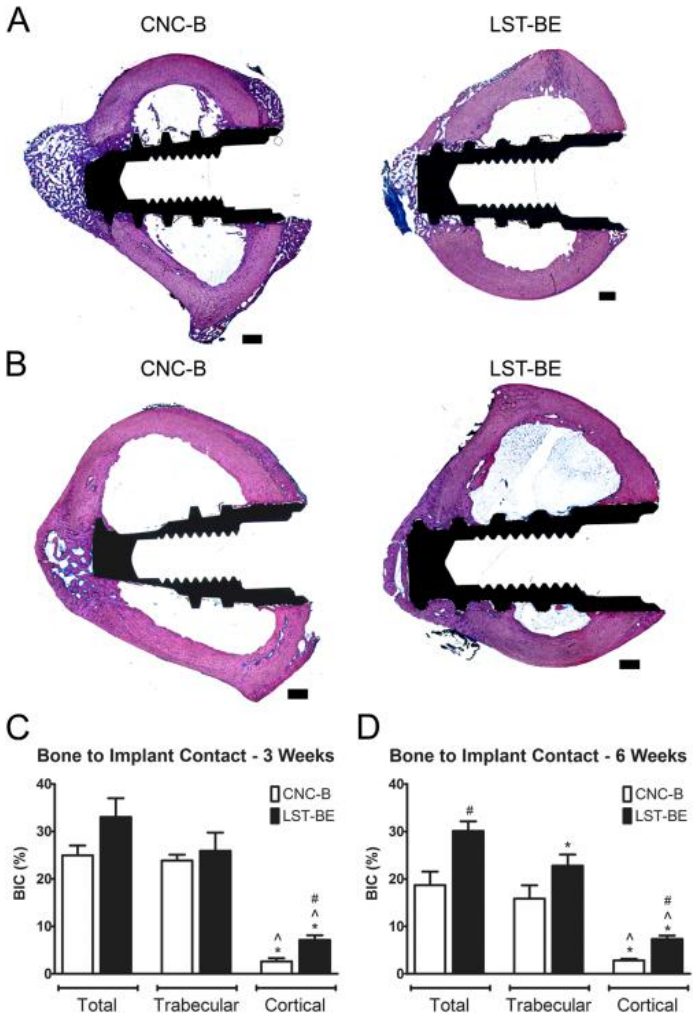

Figure 5.5. Histology stained with Stevenel's Blue of CNC-B implants (left) and LST-BE implants (right) implanted in rabbits after 3 (A, n= 6-8) and 6 weeks (B, n=8). Bone to implant contact analyzed via histology images after 3 weeks (C) and 6 weeks (D) of implantation. Scale bars are 670µm. 1 way ANOVA with Bonferroni correction, $p<0.05$, * vs. Total, ^ vs. Trabecular. Unpaired t-test, $p<0.05$, # vs. CNC-B implant.

MicroCT Analysis

Osseointegration was achieved for both implant groups, and was compared using microCT analysis. BIC values obtained through microCT analysis were not significantly different between machined and LST-BE implants at three and six weeks (Figure 6A-D). Additional analysis conducted on the superior cortical, trabecular, and inferior cortical regions of implants showed no difference in BIC values between CNC-B and LST-BE implants at six weeks (Figure 6E).

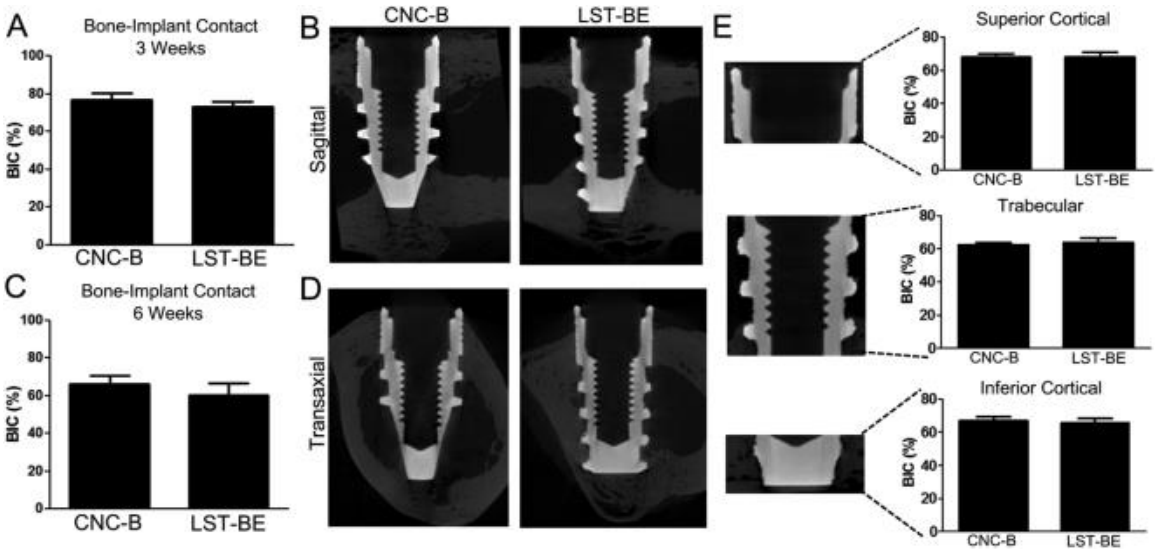

Figure 5.6. Bone to implant contact values after 3 weeks (A, n=6-8) and 6 weeks (C, n=8) of implantation. MicroCT sagittal (B) and transaxial (D) cross sectional images of CNC-B (left) and LST-BE (right) implants after 6 weeks of implantation. Superior cortical (top), trabecular (middle) and inferior cortical (bottom) regions were analyzed for bone to implant contact as well (E).

Mechanical Testing

The femur specimen was fixed in a custom-fabricated test device with the implant aligned to the machine axis to ensure that no bending moment was created during the test (Figure 7A). Pullout mechanical testing revealed no significant differences between failure forces for CNC-B and LST-BE implants after three (Figure 7B) and six (Figure 7C) weeks. Values at three and six weeks for each implant type were comparable, with strong implant to bone stability.

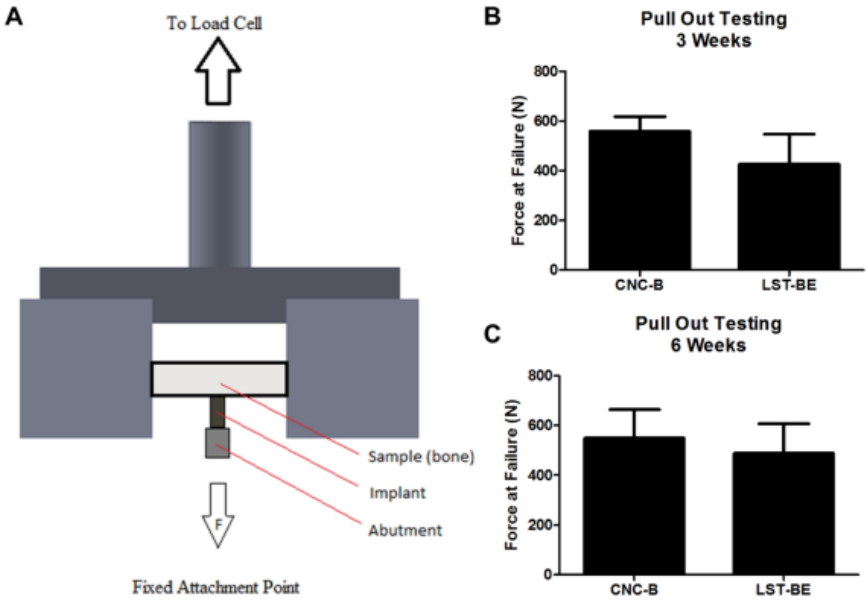

Figure 5.7. A schematic of pull out mechanical testing of implants (A). Force at failure at 3 (B, n=3 implants/type) and 6 weeks (C, n=5 implants/type) after surgery in rabbits. Unpaired t-test showed no difference between CNC-B and LST-BE implants.

5.4. Discussion

Advanced manufacturing technologies such as laser sintering can produce Ti-6Al-4V constructs with potential use in the dental and orthopaedic implant industries. In this study, laser sintering was used in conjunction with surface treatments to produce novel Ti-6Al-4V implant surfaces and implants with hierarchical micro- and nano-roughness and hydrophilicity that increased osteoblast response *in vitro* and osseointegration *in vivo.* Our results indicate that additive manufacturing is a viable method for producing dental implants leading to enhanced biological response, even when compared to a traditionally manufactured, currently used commercial implant.

Surface characterization of disks revealed a unique hierarchical micro-/nano-roughness of LST-BE surfaces with post-processing treatments. Although both blasting (LST-B) and blasting plus acid etching (LST-BE) resulted in this roughness, LCM analysis of roughness values showed higher S_a and S_z values for LST-BE surfaces than LST-B

surfaces. Because surface micro-roughness was beyond the z-limit of currently existing atomic force microscopes, nano-roughness could be observed only qualitatively via SEM images[132]. In this study, all laser sintered surfaces were post-processed to remove any residual particles or debris remaining from the sintering process and to create a more homogeneous surface roughness that has been shown to result in better biological response[38, 116]. The combination of micro- and nano-roughness on titanium and Ti-6Al-4V has been shown to increase osteoblast maturation, differentiation and local factor production *in vitro*, and other studies have shown hierarchical roughness and hydrophilicity to be important for increasing osseointegration in animal models as well[9, 22, 25, 51, 133-135].

LST-B surface contained much higher levels of oxygen than any other surface, indicating an increased oxide layer that was a result of the calcium phosphate blasting process. Studies have shown that oxygen retention can occur during the sintering process, even within an enclosed argon chamber [136]. Though grit blasting may have exposed these oxygen-rich sites, acid etching was able to alter the surface oxide. Traditionally, strong sulfuric and hydrochloric acids have been used to etch titanium surfaces to induce micro-roughness [137]. Additional aging over time in saline solution or a second oxidation processing step was required to overlay nanostructures on existing micro-roughness [9, 27, 133]. In this study, we were able to introduce both micro- and nano- roughness in just one etching step. Maleic and oxalic acids are commonly used to etch human enamel and dentin [138], but this is the first report of the combination used to etch titanium. Although not characterized in this study, material mechanical properties can differ for cast and laser sintered Ti-6Al-4V [117]. As hardness and tensile strength can be directly affected by the

thickness of the oxide layer, differences in mechanical properties may also be implicated in the biological response [139].

In vitro studies suggest that LST-BE surfaces possess unique surface characteristics that increase osteoblast differentiation and maturation at the implant site, contribute to the differentiation of cells distal to the implant surface, contribute to the bone remodeling process by decreasing osteoclast resorption, and enhance blood vessel formation to further bone formation. Our lab has pioneered the MG63 cell line as a model for evaluating osteoblast response to surface topography and wettability, showing enhanced maturation for increasing surface roughness and hydrophilicity [9, 104, 140, 141]. In this study, osteoblasts responded to surfaces in a maturation-dependent manner.

Osteocalcin, a late marker of osteoblast differentiation, has been shown to be regulated by both surface roughness and hydrophilicity in MG63 cells [39]. While immature osteoblast-like MG63 cells increased osteocalcin protein production on micro-/nano-rough, hydrophilic LST-B and LST-BE surfaces than on the smoother CNC-M and LST-M surfaces, the cells were not able to differentiate between the small changes in roughness between the surfaces examined. In contrast, mature NHOsts were more sensitive to small roughness changes in the absence of hydrophilicity, showing increased osteocalcin production on LST-M surfaces compared to slightly smoother CNC-M surfaces. However, NHOst osteocalcin production did not differ on the hydrophilic LST-B and LST-BE surfaces possessing a similar magnitude change in surface roughness.

Surface effects on OPG, a RANKL decoy receptor, for both cells were similar. Increased levels of OPG on rough surfaces suggest that surface roughness by itself can affect bone remodeling. By decreasing RANKL binding, secretion of OPG can inhibit

osteoclast activity for increased net bone formation by osteoblasts. The increase in OPG on rough surfaces has been attributed to a similarity of surface micro-/nano- features with resorption pits in bone, indicating a possible explanation for the response to rough LST surfaces in our study [142].

VEGF production by NHOsts showed a much more robust response to hierarchical surface roughness and hydrophilicity in comparison to VEGF production by MG63 cells. These results suggest that VEGF may play a more active role later in osteoblast maturation, contributing to continued blood vessel formation and bone integration. BMP2 expression in NHOst cells showed a differential response to small changes in roughness on hydrophilic surfaces LST-B and LST-BE while expression of MG63 cells was similar for both hydrophilic surfaces. Expression of these local factors is important for enhancing osteoblastic differentiation of mesenchymal stem cells distal to the implant, as our group has shown previously [7]. Taken together, our *in vitro* results align with previous observations that a more robust response to nanotopography by mature osteoblasts in comparison to undifferentiated mesenchymal stem cells, with this effect able to be modulated by surface wettability [22, 133].

Cell surface integrin receptors mediate cell response to biomaterials. In particular, integrin α2β1 has been shown to play a significant role in the osteoblast and mesenchymal response to titanium surface roughness, though different integrin profiles may play a role depending on cell lineage [7, 34, 56]. In this study, we analyzed mRNA expression of α2 and β1 integrin subunits, showing increased expression of both these subunits on rough LST-B and LST-BE surfaces compared to smooth CNC-M surfaces. The similar expression profiles of α2 and β1 corroborate our theory that α2β1 is responsible for

osteoblast maturation and differentiation on micro-rough surfaces. The presence of hierarchical micro-/nano-roughness on our LST-B and LST-BE suggests that α2β1 mediates cell response to surfaces at the nanoscale as well.

A variety of animal models have been used to study osseointegration of laser sintered implants [121, 143, 144]. We opted to use a rabbit model to compare osseointegration of LST-BE implants with osseointegration of CNC-B implants, which are used clinically. Although rabbits possess differences in bone structure and remodeling in comparison to humans, including a venous plexus within the tibial cortical bone, they have shown similar responses to implant roughness that are seen clinically, and are the most commonly used model for dental implant evaluation [17, 145-148]. Due to faster skeletal change and bone turnover rates in rabbits compared to humans, studies have shown accelerated healing at four weeks [149, 150]. To address the fact that most commonly implants are used in adult humans, we used a fully mature rabbit for the present study.

We evaluated BIC values at three and six weeks to understand the effects of implant manufacturing and differences in surface roughness on early events in osseointegration. Other studies evaluating osseointegration of implants placed in a similar femoral model in rabbits show new trabecular bone formation by four weeks, with continued bone remodeling and growth up to 42 weeks after implantation [151, 152]. Though our study ended at six weeks, other studies have shown predictive osseointegration results in rabbits as early as two weeks after implantation [147]. It is possible that differences may have been observed at earlier time points. As with any small animal model where the implant cannot be placed directly in the jaw, mechanical loading will be different [145]. We believe that our model is valid for comparing osseointegration of endosseous implants and can be

indicative of clinical outcomes. While BIC values showed improvement in osseointegration of LST-BE implants in comparison to CNC-B implants, further studies in disease challenged animal models or at longer time points may be necessary for elucidating the superiority of novel LST implants for improving osseointegration in compromised cases.

Although microCT evaluation of BIC has been compared to histomorphometric analysis with promising results, metal artifacts due to scattering continue to be a confounding factor in accurate microCT analysis [153-155]. We considered BIC values from both sources and found that histomorphometric analysis was more reliable in describing bone formation during the early stages of osseointegration. Although total BIC was not significantly different between CNC-B and LST-BE implants at three weeks, a higher amount of cortical bone was seen in LST-BE implants compared to CNC-B implants. The change in the composition of trabecular and cortical bone between three and six weeks was evident as well, which was observed at the same time points in a similar implantation model [156]. Total BIC values were higher for LST-BE implants compared to CNC-B implants at six weeks, with a significantly reduced trabecular LST BIC compared to total BIC. This reduction was not seen in either implant group at three weeks, suggesting increased bone remodeling of LST-BE implants during the osseointegration process as compared to that of CNC-B implants.

Differences in BIC values can also be attributed to the analysis in different planes. BIC analysis was performed on sagittal cross sections throughout the entire implant for microCT, whereas analysis was carried out on transaxial cross sections for histology. Mechanical testing was performed to verify osseointegration of implants further. Similar

pullout forces for both implants indicate that LST-BE implants achieved good mechanical stability, which was comparable to that of the commercially used CNC-B implant. These results suggest that LST-BE implants are similar to, if not better than traditional CNC-B manufactured implants. The enhanced biological response can be attributed to the LST-BE's unique surface properties and ability to promote osteoblast maturation and differentiation at and distal to the surface, influence bone remodeling and increase blood vessel formation for increased osseointegration.

5.5. Conclusion

Laser sintering is an additive manufacturing technique that can produce Ti-6Al-4V implants. The implants can be further processed to create micro-rough, nano-rough, and hydrophilic surfaces. The resulting surface with combined roughness and wettability enhanced both MG63 and NHOst cell response in comparison to smooth CNC-M and LST-M surfaces. LST-BE implants were compared to commercially available CNC-B implants in a healthy animal model, and cortical BIC was higher at three weeks and total BIC higher at six weeks than CNC implants. LST-BE and CNC-B implants had similar pullout forces at both time points examined, indicating that LST-BE implants are as mechanically stabile as clinically used implants. These results suggest that implants produced by laser sintering with combined micro-/nano-roughness and high surface energy are a suitable alternative to traditionally manufactured endosseous implants, with favorable biological response and ability to osseointegrate.

CHAPTER 6

ADVANCES IN POROUS SCAFFOLD DESIGN FOR BONE AND CARTILAGE TISSUE ENGINEERING AND REGENERATION

In [Cheng A, Li X, Shao Z, Sun M, Ao Y, Schwartz Z, Boyan BD and Chen HF. Advances in porous scaffold design for bone and tissue engineering and regeneration. Tissue Engineering Part B: Reviews. 2016. (In preparation)]

6.1. Introduction

Scientists and the public have long dreamed of the bionic human, complete with artificial organs. Tissue engineering approaches are well underway to regenerate the most complex of tissues. However, most of these technologies have remained in the laboratory. Meanwhile, the clinical need is great: By 2030, 572,000 total hip and 3.48 total knee replacements are expected to occur in the United States alone [157]. In addition, 96,700 hip revisions and 268,200 knee revisions procedures are projected. This indicates not only a need for effective regenerative strategies, but also ones that can remain successful throughout the life of the patient.

Tissue engineering provides a promising way to repair and regenerate damaged tissues by mimicking the structural and functional profile of the natural extracellular matrix (ECM). An ideal scaffold should have the appropriate surface chemistry, biocompatibility, porosity and mechanical properties to integrate with the native host tissue [158]. Though both included under the orthopaedic umbrella, bone and cartilage are very different, and require different approaches to regenerate. Bone is highly vascularized, with most blood vessels located within 100μm of the bone surface [159]. Thus, most tissue engineering approaches for bone attempt to increase vascularization. In contrast, cartilage is avascular,

and requires a vastly different approach to regeneration [160]. Though two quite different tissues, development of bone and cartilage is still inter-related. For example, Sox9 has been recently found to negatively regulate both bone and cartilage regeneration [161]. Thus, orthopaedic tissue engineering strategies should also consider their impacts on neighboring tissues.

A tissue engineering approach not only includes the physical properties of the scaffold, but also the biological factors that can enhance regeneration. Instead of building a one-size-fits all solution in the laboratory, successful functional scaffold design harnesses the natural regeneration abilities of the human body. These include peptides for cell homing and attachment, proteins for creating a favorable microenvironment, and cells to facilitate early ECM formation (Figure 5.1). Though challenges still exist for bone and cartilage regeneration, progress in these methods highlight advances in our understanding of biology and biomaterial response. In this review, we highlight advances in two major approaches for manufacturing porous scaffolds, surface roughness and functionalization, the use of exogenous factors, and finally the use of biological models for scaffold evaluation.

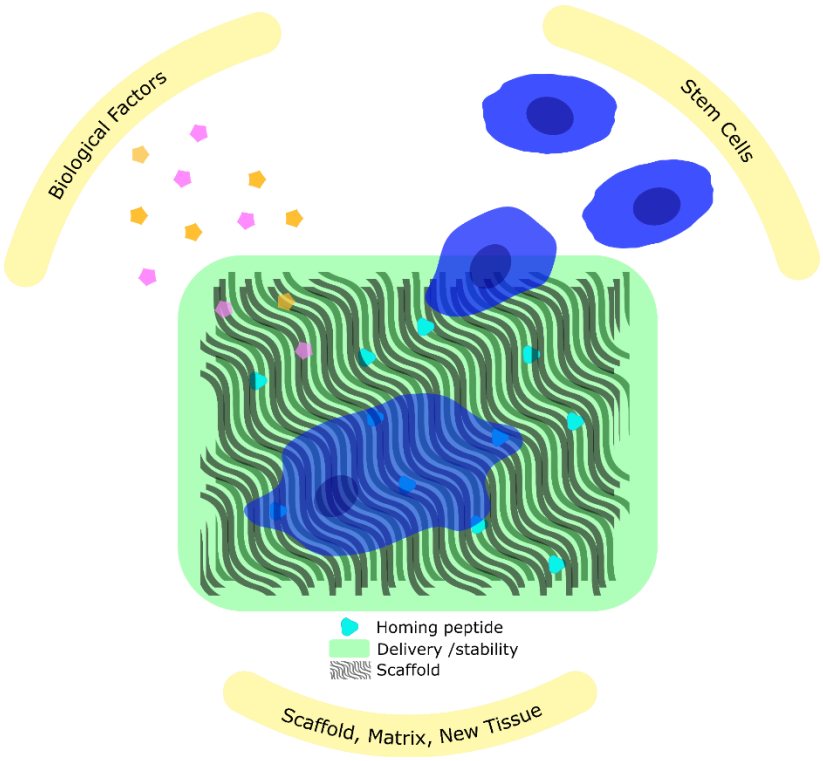

Figure 6.1. Scaffolds that harness the natural regeneration processes of the body to recruit endogenous stem cells and biological factors for tissue regeneration.

6.2. Scaffold Composition and Geometry

Scaffolds for bone and cartilage tissue engineering are composed of a variety of materials. Synthetic polymers are low in cost, abundant and have low variation among batches. These include polyglycolide (PGA), polylactide (PLA), polylactic-co-glycolic acid (PLGA) and polycaprolactone (PCL), among others [162, 163]. Varying ratios and combinations of these biodegradable polymers can be used to customize mechanical and structural properties. These materials can be designed to degrade up to years after implantation, which make them ideal for delivering drugs or growth factors, and serve as structural scaffolds that are eventually replaced with new tissue [164]. Nondegradable synthetic polymers such as polycaprolactone-dimethacrylate are also attractive for their ability to control the scaffold shape and potentially cell fate after implantation [165].

Organic polymers include those found in humans, as well as in other natural organisms. Collagen is most commonly used to mimic the structure and composition of the natural extracellular matrix. Decellularized matrices also attempt to provide a more natural environment for cell infiltration and tissue growth, although require optimization and a standardized decellularization process [166]. Polysaccharides such as chitosan and polypeptides such as silk fibroin are other naturally derived polymers that have been used for bone or cartilage tissue engineering scaffolds [167, 168]. Silk fibroin scaffolds have shown promise for cartilage tissue engineering due to their mechanical properties and versatility. Silk hydrogels, porous sponges and electrospun silk are also approaches to support cartilage regeneration through a tissue engineering scaffold [168-170]. Additionally, hydrogels can be composed of a variety of polymers to provide substantially different mechanical and structural properties.

Ceramic scaffolds such as calcium phosphate, bioglass and titanium are used heavily in bone tissue engineering applications, where mechanical strength is important. Hydroxyapatite scaffolds resemble the natural composition of bone, and can be manufactured with varying porosities to enhance bone ingrowth [171]. For bone tissue engineering scaffolds, metals and ceramics are preferred for their mechanical properties and biological compatibility. Titanium and its alloys are attractive because of a naturally occurring TiO_2 oxide layer that increases corrosion resistance and contributes to hardness at the surface. Silicon-based bioglass is a ceramic that is defined by the formation of hydroxyapatite-like surface layer upon immersion in simulated body fluid [172]. However, use of bioglass is limited by its degradation properties and manufacturing into porous scaffolds.

At the most basic level, the function of tissue engineering scaffolds is to serve as a mechanical support for regeneration of tissue, especially in load bearing areas. However, the macro structure of scaffolds must also allow for cell and tissue infiltration, as well as blood vessel and nerve growth [173]. Thus, the size scale and structure of pores within the scaffold must be considered for optimal biological response. Pore diameters over 100μm have been considered necessary for cell attachment, and pore diameters over 300μm for tissue growth [174, 175]. Porosity can also indirectly affect cell response by altering the fluid shear forces on the cell. While it is difficult to recapitulate the *in vivo* environment exactly in cell culture, studies have shown that cells are indeed influence by mechanical forces resulting from fluid flow, and that these flows are altered based on scaffold porosity [176, 177]. Additional studies have shown the importance of smaller micropores and the role of morphology in facilitating protein adsorption [178]. With little consensus on the ideal pore diameter or morphology, perhaps the best option is to create scaffolds with porosity gradients to serve specific functions throughout the regeneration process [175].

As scaffold design becomes more sophisticated, multiple parameters of characterizing porosity should be considered. Simple parameters such as total percent porosity and pore diameter are now being supplemented with more descriptive characteristics, such as channel tortuosity and surface area to volume ratio (Table 6.1). Characterization of pores has also advanced to include pore shape and curvature. It is important to fully characterize scaffolds based on standardized parameters in order to reproduce and evaluate results across biological studies.

Parameter	Definition	Biological Response

Total porosity	Percentage of total void space	Total porosity also affects mechanical strength of the scaffold, which is especially important for load bearing applications. An ideal scaffold would mimic the Young's modulus of 3-20 GPa for bone and 10MPa for cartilage [13, 179].
Open porosity	Percentage of pores that are interconnected	Interconnected pores can affect cell permeability and tissue infiltration, as well as growth factor diffusion. For bone, open porosity is necessary to increase vascularization and can be measured in scaffolds via microCT or mercury intrusion porosimetry [175, 180].
Tortuosity	Quantification of twists and turns through a connected channel, expressed as the length of the entire channel divided by the shortest distance between starting and ending points.	In addition affecting surface area, tortuosity of scaffold channels can also affect cell migration and delivery and removal of nutrients and waste, respectively [181].
Surface area to volume ratio	Ratio of total scaffold surface volume to total scaffold volume	Surface area to volume should e considered when choosing cell seeding density and concentration of functionalized factors on scaffolds for *in vitro* studies. Degradation rates may also be affected in degradable scaffolds, impacting drug release [182].
Pore diameter	Diameter of largest sphere that fits within pore channel	The size of pores has been investigated extensively for facilitating bone growth, with no clear consensus on the optimal pore diameter. While pores over 100μm are generally preferred for cell infiltration and bone ingrowth, recent studies suggest that smaller pores may be preferable during later stages of growth [183, 184].
Strut thickness	Also known as "trabecular thickness," the thickness of structural supports within the scaffold	Strut thickness is typically inversely correlated with porosity and pore diameter, thus affecting cell penetration tissue growth into the scaffold [177].
Pore curvature	Radius of curvature	The degree of concave or convex surface curvature can affect cell contraction and focal adhesion formation [181].
Pore circularity	Though not a standard definition, pore circularity refers to the similarity of pore channel cross sections to circles	Circular, triangular, square and hexagonal pore cross sections influence cell growth and ECM deposition differently [181].
Pore gradient	Difference in pore diameter, total porosity or other porosity parameter. This is not standardized and can be expressed in multiple ways.	Localized and gradient porosity have been proposed to increase tissue specific growth during the regeneration process. This allows nutrient transport throughout the scaffold based on the scaffold and tissue architecture [185].
Stiffness	Mechanical property commonly expressed in units of kPa.	Stiffness of a substrate can affected MSC differentiation int osteoblasts, which is mediated by integrin signaling [186]. Stiffness is typically inherent in a material's composition, but may also change over time for degradable scaffolds or shape memory polymers. Dynamic hydrogels also provide a model for understanding cell resposne to changes in ECM stiffness during disease and development [187].
Swelling ratio	The ratio of wet mass or volume to dry mass or volume of a hydrogel	Swelling can affect delivery of growth factors or oxygen diffusion, leading to changes in cell response [188]. Rate of swelling may also affect cell attachment and proliferation [189].

Table 6.1. Parameters for porous scaffold characterization

6.3. Scaffold Manufacturing

Traditional methods for manufacturing porous scaffold manufacturing techniques include foam processing, solvent casting and freeze drying [158]. However, these methods allow limited control over scaffold chemistry, macro-structure and porosity. Other methods have been proposed to address issues in scalability, sustainability and spatial control (Table 2, Figure 2). Advances in manufacturing have allowed for the development of two main technologies for producing tunable scaffolds for tissue engineering, electrospinning and additive manufacturing.

Table 6.2. Porous scaffold manufacturing techniques

Technique	Applications
Freeze casting	Ceramic slurries are most commonly freeze cast, where water from the slurry is sublimated and results in pores with the morphological characteristics of ice crystals [190].
Freeze drying / lyophilization	A relatively simple technique that can be used with natural materials such as collagen, gelatin or silk fibroin, the porosity can be modified based on changes in freezing temperature and material concentration [191, 192].
Solvent casting and particulate leaching	For three dimensional scaffolds, molds must be created for casting the polymer solution. Though leaching requires additional processing time, the use of organic solvents facilitates addition of drugs or growth factors to scaffolds [193].
Gas foaming	Carbon dioxide at high pressure is used to expand the polymer instead of using temperature or other solvents. Varying pressure can also produce scaffolds with a gradient porosity [194].
Phase separation	Thermally induced phase separation can be used to separate polymers into their solvent and solid polymer, resulting in homogenous and interconnected porosity throughout the scaffold that can be tunable based on cooling rates during processing [195].
Electrospinning	Electrosprun fibers can vary from nanoscale to micro-scale, with alignment and chemical opmosition based on processing parameters. Previously restricted to polymers, recent advances have also allowed for electrospinning of titanium for bone tissue engineering [196].
Sol gel	Traditionally used colloidal metal oxides, the sol gel method results in a scaffold with tunable porosity and chemistry. Biphasic chitosan scaffolds with an affinity peptide have shown the ability to recruit stem cells for cartilage regeneration [197].
Additive manufacturing	Extrusion methods are mostly polymer based. Solid freeform via sintering can be applied to both polymers and metals, while laser melting is restricted to metals [38, 119].

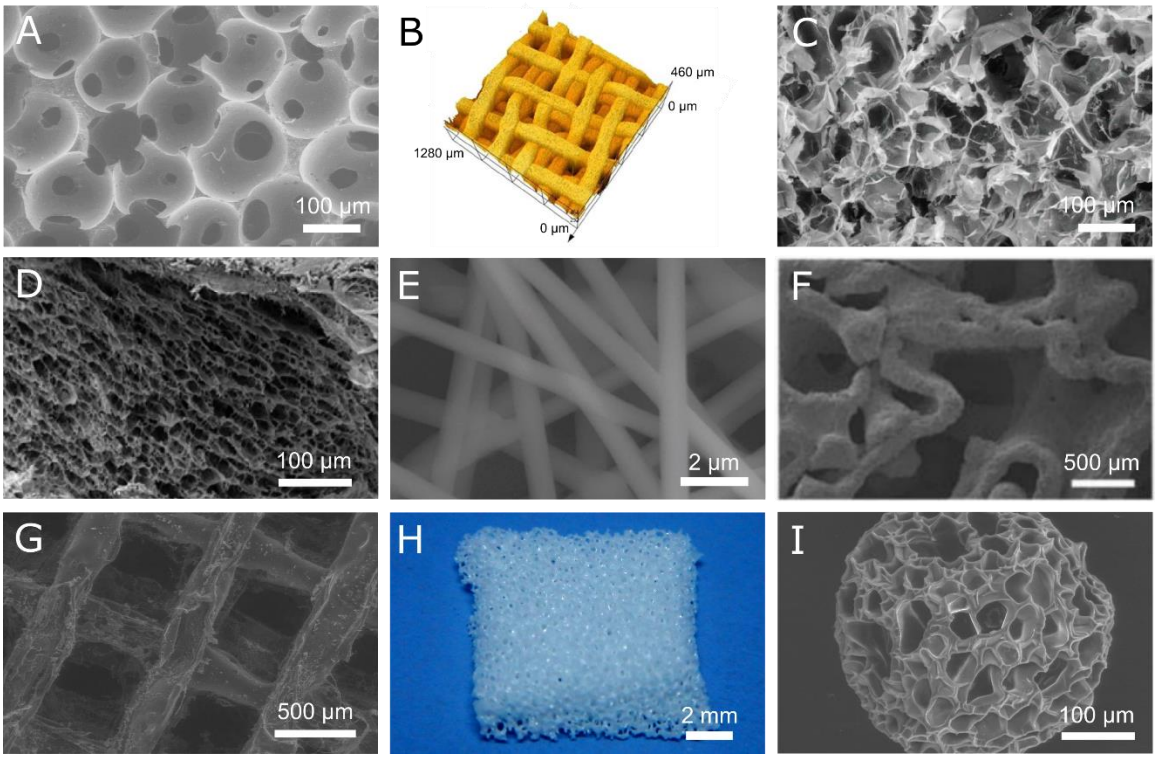

Figure 6.2. Different manufacturing techniques for porous scaffolds. Freeze dried polyurethane scaffold (A), pressed TiO2 scaffolds (B), thermal polymerizable alginate-glycidyl methacrylate freeze dried hydrogen scaffold (C), demineralized bone matrix coated with a chitosan thermogel (D), electrospun PEO/PPy conductive scaffolds (E), direct metal laser sintered Ti-6Al-4V scaffold from human trabecular bone template (F), fibroin-gelatin mixture poured into 3D printed, dissolvable polystyrene mold (G), zirconia slurry poured into freeze dried and dissolvable polyurethane scaffold to achieve porous, fully zirconia scaffold (H), agarose-gelatin microbead produced via a microfluidic system (I). Adapted from [37, 198-202].

Electrospinning

Electrospinning is a technique which is able to produce micro- and nano-scale fibers from polymers and composite materials with tunable diameter, porosity, surface morphology and fiber alignment [203, 204]. Due to a large surface area and high porosity, electrospun scaffolds can be used for tendon-to-bone and cartilage tissue engineering applications [205, 206]. The use of coaxial and other electrospinning techniques has also allowed for the development of composite electrospun scaffolds.

Electrospinning has been vastly applied to polymers and ceramic materials [207, 208] Natural polymers like collagen [209] and silk fibroin [210] have been proposed to avoid inflammation and foreign body reaction when implanted *in vivo*. While the main organic ECM component of bone is collagen type I, the presence of collagen type II dominates in cartilage; both have been employed in electrospinning scaffold applications [209, 211]. However, synthetic polymers are also commonly used, which are less expensive and have more consistency across batches. The most commonly used synthetic polymers consist of poly(ε-caprolactone) (PCL), polylactic acid (PLA) and ploy(lactic-co-glycolic) acid (PLGA) [212-214]. For cartilage tissue engineering, polymer electrospinning has been combined with hydrogels through various processing techniques that provides both structure and function [215].

The morphology of electrospun nanofibers can be manipulated by controlling the parameters for electrospinning. By using a rotating mandrel as the collector, it is possible to produce aligned to mimic the parallel bundles of collagen fibrils [205], and tunable crimped nanofibers [213] to vary mechanical strength. Besides mimicking the ECM, the alignment of electrospun nanofibers can also guide cell attachment migration. Initial work on electrospinning PLGA scaffolds for cartilage tissue engineering sought to mimic the native structure of collagen fibrils, and resulted in electrospun fibers ranging from 500 to 800 nm in diameter [216]. However, recent works suggests that chondrocytes may prefer larger micro-scale fiber diameters on electrospun scaffolds over nano-scale fiber diameters [217]. These mimic the natural range of collagen fibrils, which vary based on zone and patient age [218].

Composite electrospun scaffolds have also been produced that combine advantages of the biological performance of natural polymers and the mechanical properties of synthetic polymers. Ceramic scaffolds using hydroxyapatite [219] or TiO_2 [196] have also been manufactured as bone graft substitutes for bone repair. Electrospinning of TiO_2 nanofiber mats resulted in nanofiber diameters of mostly 100-300nm with 6% PVP and 300-500 with 10% PVP [33]. MG63 osteoblasts on larger diameter TiO_2 scaffolds made with 10% PVP also exhibited higher levels of osteocalcin compared to smaller diameter scaffolds. In addition, osteocalcin, osteoprotegerin (OPG) and vascular endothelial growth factor (VEGF) were higher on the patterned side of the scaffold compared to the flat side for scaffolds made with 10% PVP. Osteocalcin and VEGF were not higher for patterned scaffolds made with 6% PVP compared to smooth scaffolds of the same composition, indicating that the response to surface characteristics was also dependent upon nanofiber diameter (Figure 3). 3D titanium mesh scaffolds with microroughness induced by acid etching were also evaluated for their effects on osteoblast differentiation [37]. Compared with the 2D group, 3D scaffolds with a submicron-scale texture showed higher levels of osteoblast differentiation markers, and these effects were mediated by integrin $\alpha 2\beta 1$. In follow-up studies, silica-titania nanofiber scaffolds also exhibited the ability to positively affect osteoblast differentiation *in vitro* [196].

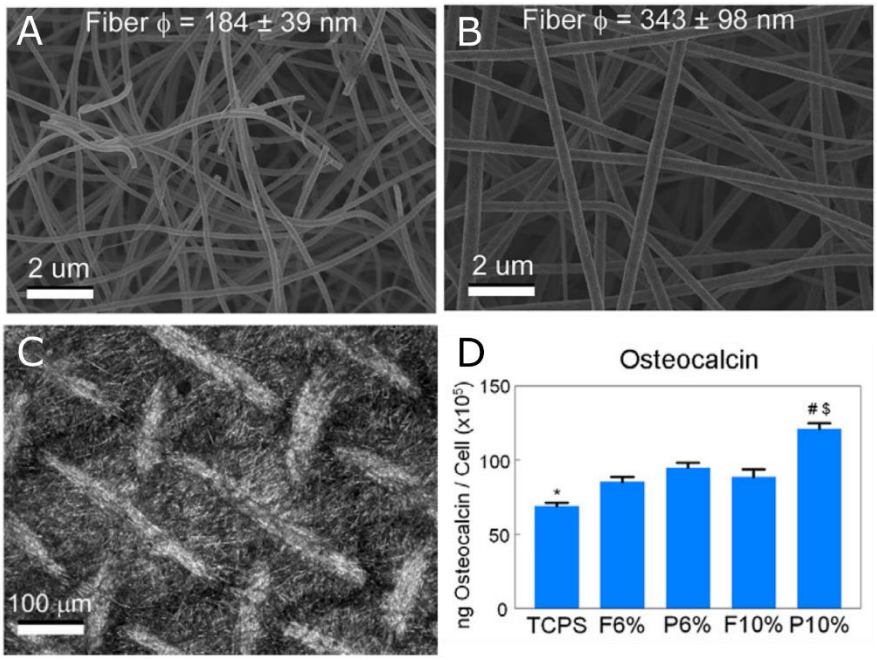

Figure 6.3. The effect of electrospun nanofiber diameter and scaffold microstructure on biological response. TiO2 scaffolds with 6% PVP (A) had smaller fiber diameters than TiO2 scaffolds with 10% PVP (B). TiO2 scaffolds with 10% PVP that were additionally micro-patterned (C) induced the highest osteocalcin levels by osteoblasts (D). Adapted from [33].

Additive Manufacturing

Additive manufacturing has paved the way for patient specific biomaterials, and holds much promise within the maxillofacial and orthopaedic implant fields [220, 221]. Additive manufacturing also provides advantages in cost, scale and flexibility over traditional manufacturing methods [222]. The American Society for Testing and Materials has classified 7 different additive manufacturing processes based on deposition and bonding: photopolymer vat, material jetting, material extrusion, powder bed infusion, directed energy deposition, sheet lamination and binder jetting [223]. These have all been methods used for biomedical applications. For bone applications, powder bed fusion is most promising and includes selective laser sintering, selective laser melting, electron beam

melting and selective mask sintering. These methods can all employ metals such as Ti-6Al-4V, which have the mechanical ability to withstand the loads experienced by bone.

Tissue regeneration is dependent in part upon the macro-scale scaffold architecture. For large bone defects, full vascularization into scaffolds has yet to be achieved and remains a challenge in scaffold design [224]. While bone regeneration favors interconnected micro-porous scaffolds, cartilage regeneration is more prevalent on nanoporous scaffolds with less interconnectivity that lead to hypoxic conditions [225]. While topological design studies suggest that bone interfacing scaffolds should mimic the mechanical properties of the native bone, they have not yet offered an ideal porosity configuration that leads to the best biological response [226, 227]. Instead of homogenous porosity across the scaffold, recent studies have used additive manufacturing to create Ti-6Al-4V constructs with trabeculae-inspired porosity to enhance vascularization and osseointegration [38] (Figure 4). Further work shows that while the MG63 osteoblast-like cell line and normal human osteoblasts (NHOsts) exhibit increase osteoblast differentiation maturation markers on 3D porous constructs compared to 2D surfaces manufactured with the same method, NHOsts were less sensitive to changes in the percent porosity compared to MG63 cells [201]. This corroborates other studies on hydroxyapatite scaffolds indicating that percent porosity may matter less than pore distribution, size and surface parameters [228]. These studies showcase the importance of using biologically inspired porosity with the potential to be personalized to the patient, rather than pre-defined porosity with a homogenous pore distribution. Additional work has been conducted on 3D printing of PLGA, PCL and hydroxyapatite scaffolds for bone tissue engineering [229].

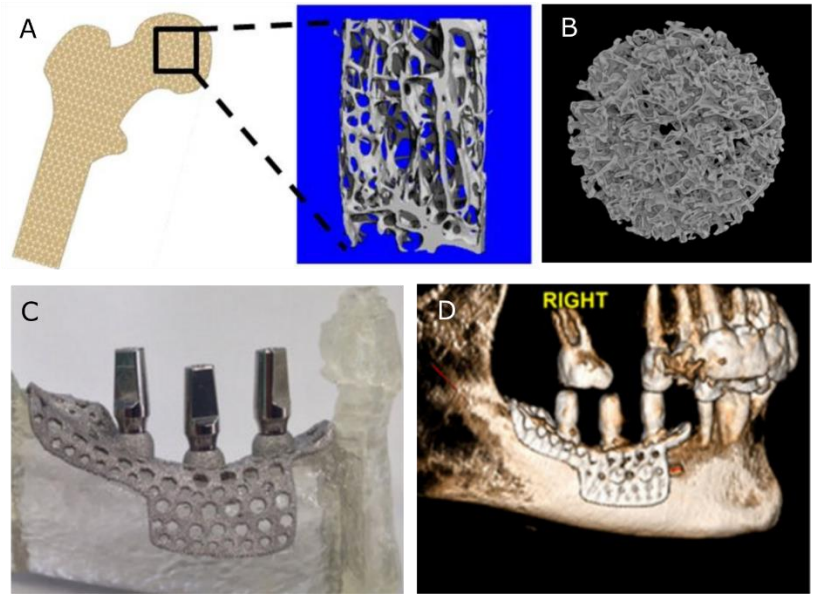

Figure 6.4. Direct metal laser sintering is a form of additive manufacturing that can use a human trabecular bone template (A) to produce constructs with similar porosity (B). DMLS can also be used to produce patient-specific implants (C) that have been used clinically with patients with severe jaw atrophy (D). Adapted from [38, 119].

One of the challenges of cartilage regeneration is that the tissue itself is heterogeneous, with gradients in cells, matrix composition and mechanical properties. Biofabrication or bioprinting methods that combined additive manufacturing of both the scaffold material and biological factors of cells are attractive for their ability to provide spatial and temporal control within a single manufacturing step [230-232]. Bioprinting using ECM components and cells is a promising strategy for providing an appropriate environment for cartilage regeneration that mimics the native tissue [233]. However, unlike sintering, which requires high temperature or energy to bond a bed of powder, most biofabrication processes are low in temperature and extrusion-based so as to not harm the biological components of the scaffold. Extrusion and inkjet printing remain the most popular methods for biofabrication [223]. However, these methods are limited by their material specifications and lower resolution.

Because bulk mechanical properties of layer-by-layer sintered powdered are different than that of cast or forged metals, post-processing treatments are necessary for ensuring mechanical compatibility and functionality with the host tissue [234]. Studies have shown dramatic improvements in elongation at failure and yield strength for additively manufactured Ti-6Al-4V parts after thermal post-processing [235]. In addition, build orientation should also be considered for optimizing mechanical properties of additively manufactured Ti-6Al-4V [236].

Endochondral bone formation, requiring first the formation of cartilage before bone, is favored when mechanical forces are present at the site [237]. Scaffolds for cartilage regeneration can use this to their advantage by incorporating dynamic mechanical properties into their design. While the magnitude of loading for bone and cartilage are different, the ability for scaffolds to transfer these forces to cells is pertinent for both applications. Particularly for bone, scaffolds with mechanical properties mimicking the host bone are desirable for both osseointegration via endochondral ossification and prevention of stress shielding once osseointegrated.

6.4. Surface Roughness

While scaffold macro-structure and geometry can be easily customized and influence later stages of tissue regeneration, micro- and nano-scale features can more directly impact biological response. Surface micro-roughness of solid orthopaedic implants has been shown to enhance osseointegration in comparison to smooth implants, which tend to favor soft tissue formation [23]. Recent studies suggest that surface micro-roughness is just as important for osseointegration and bone regulation in porous scaffolds [38, 238]. From

studies of osteoblasts on rough titanium surfaces, we know that roughness alone is able to alter cell morphology and induce osteoblastic differentiation [55]. This occurs based solely on the surface roughness, without the use of exogenous factors, and in fact through a different mechanistic pathway than the canonical Wnt3A pathway [44]. The Wnt5A pathway has been implicated in osteoblast response to surface roughness, which is also integrated with integrin response [21]. Specifically, integrin α2β1 has been found responsible for osteoblast response to titanium surface microtopography [56], which is important for understanding both the direct and indirect effects of surface roughness on bone growth. A recently published review highlights the role surface roughness on MSC response on bone interfacing titanium implant surfaces [239]. Beyond cell response, surface roughness also provides structural nucleation sites for hydroxyapatite precipitation [240].

In addition to micro-scale topography, the nanotopography of biomaterials also can shape stem cell destiny, and may affect the adhesion and differentiation of stem cells [241, 242]. Oxidized nanostructures on titanium are typically achieved through thermal or electrochemical treatments. Thermal and hydrothermal treatments occur at high temperatures, although at longer time scales spontaneous nanostructures have formed on pure titanium surfaces stored in saline at room temperature [27]. Additively manufactured Ti-6Al-4V scaffolds anodized to produce 70nm diameter nanotubes showed significantly greater new bone volume compared to scaffolds without surface processing [243]. Acid etching followed by treatment with H_2O_2 / NaOH and pickling can also generate a combined micro- / nano-topography on additively manufactured 3D Ti-6Al-4V scaffolds [38].

More recently, the addition of nano-roughness to micro-roughness to create a hierarchical surface topography has become attractive for increasing biological response on titanium surfaces [9]. This also mimics the natural structure of native bone. Individual hydroxyapatite plates are 25-50nm in diameter, and collagen molecules are 1.23nm in diameter and 300nm in length [244]. Though cell response to nanotopography is not completely understood, emerging reports suggest that it may also occur through a different pathway than response to microtopography [57]. The nanotopographical features of biomaterials have been identified as able to influence cell behaviors by affecting the conformation of integrin-binding proteins, changing the availability of binding sites, and modifying integrin signaling [245]. Evaluation of MSC proliferation and osteogenic differentiation on non-woven and patterned PLLA nanofibrous mashes fabricated by electrospinning showed that nanofibrous meshes were able to direct cell morphology through their nanotopographical features and nanofiber orientation. A nano-textured surface presented by patterned nanofibrous meshes provided a more effective microenvironment for osteoblastic differentiation of MSCs when compared to non-woven nanofibrous meshes. This topography-driven commitment was found to be related in part to the RhoA-ERK signaling pathway, as well as the regulation of Runx2 gene expression [246].

Surface roughness can be difficult to homogeneously achieve across surfaces of a 3D scaffold. Physical line-of-sight methods such as grit blasting or spray coating are not always able to reach internal pore surfaces [38, 247]. Even clinically used coatings such as hydroxyapatite are not always stable, and can lead to mechanical failure after repeated loading [248]. Etching and oxidation remain two surface processing methods that, when

performed in a controlled environment, can affect all surfaces of a 3D scaffold. While alkali treatments can alter the mechanical properties of titanium scaffolds, acid etching is used for surface roughness of implants that are currently in clinical use [238]. For many scaffolds, a combination of acid etching and direct surface oxidation has been used to induce hierarchical micro- and nano-roughness. Studies have shown osteoblasts tend to favor the sharp peaks generated by acid treatment, while a superimposed oxidized nano-roughness can enhance this response [9].

6.5. Surface Functionalization and Exogenous Factors

Currently, bone tissue engineering involves use of a bone graft either from a cadaver (allograft) or directly from the patient (autograft). Allografts can cause major inflammation and potential host rejection [249]. Though autografts are considered the most popular and preferred bone graft, they often require an additional surgery with potential complications, and are limited by the patient's availability [250]. Therefore, natural and synthetic bone grafting substitutes have become an alternative method for regenerating bone [250, 251]. For large defect areas, a structural scaffold may not be enough to support complete regeneration. In these cases, exogenous factors and peptides can be functionalized to the scaffold surface to enhance regeneration. Indeed, functionalized growth factors on scaffold surfaces may present a more controlled mode of delivery compared to soluble delivery. Incorporating both VEGF and BMP2 in layer-by-layer assembled polylelectrolyte films increased bone formation 33% compared to films with BMP2 alone [252]. Use of functionalized scaffolds may better mimic the natural presentation of growth factors by the ECM, in contrast to soluble factors secreted by cells. Therefore, tissue engineering

strategies should consider endogenous growth factor presentation when optimizing local factor delivery [253].

Tissue Engineering has evolved to include the combination of a scaffold matrix with cells and biologically active molecules to form a construct that promotes tissues repair and regeneration. All these three basic components work together to establish an appropriate niche for tissue regeneration [254]. While scaffolds and biomaterials were originally designed as a substitute to organs, scientists are starting to design scaffolds that integrate with and enhance the natural regeneration processes of the human body. Recent work suggests that anatomically correct scaffolds combined with growth factor delivery can regenerative articular cartilage without cells [255]. A major challenge for establishing this niche is to recruit and facilitate cell differentiation to the site of repair. Current work has focused on the use of autologous cells, which require harvest from the patient, expansion in culture and finally implantation back into the patient. Complications can result at each step, and often the number of endogenous cell is not sufficient for use [256, 257].

Instead of implanting cells with the scaffold, an alternate strategy is to recruit MSCs directly to the site after implantation. Arginine-glycine-aspartic acid (RGD), a peptide derived from fibronectin in ECM, is best known for cell adhesion on synthetic material surfaces [258-261]. The E7 MSC-homing peptide has been developed using phage display and conjugated to PCL electrospun meshes, which have shown the ability to attract MSCs *in vivo*. In addition, the E7-conjugated PCL electrospun meshes are specific for MSC recruitment, compared to the RGD-conjugated PCL electrospun meshes that attract

multiple cell types [206]. These approaches recruit the body's existing population of stem cells, which is attractive for saving time and decreasing immune response.

Other scaffolds have also utilized chemotactic and peptide functionalization for cell homing [255, 262-264]. Modification of coaxial PCL electrospun scaffold with co-delivery of MSC-affinity peptide (E7) and rhTGF-β1 for cartilage regeneration has also shown success in targeting MSCs in tissues of interest with high efficiency [265]. The scaffolds not only enhanced BMSC adhesion and growth, but also promoted their chondrogenic differentiation *in vitro* (Figure 5). This was due to the combination of nanoscale fibers that mimicked the physical structure of the ECM [266] and supported BMSC growth; recruitment of BMSCs by E7 on the PCL shell of the coaxial fibers and controlled release of rhTGF-β1 encapsulated in the core of coaxial fibers to BMSC chondrogenic differentiation.

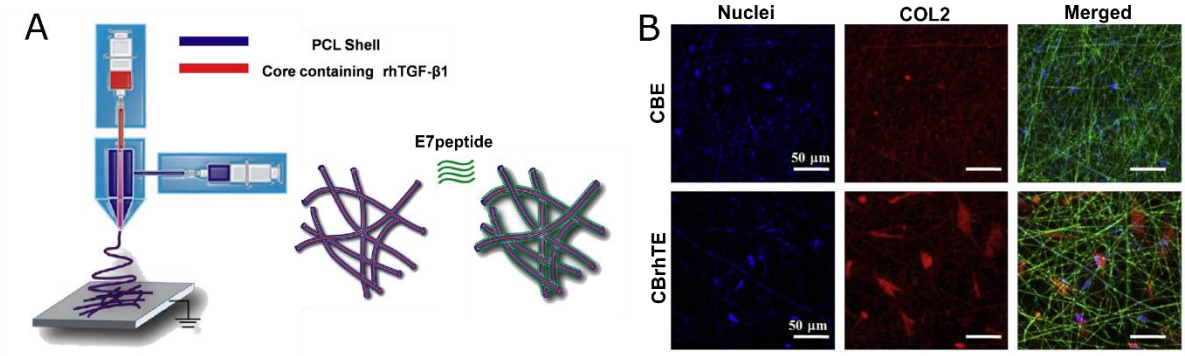

Figure 6.5. Electrospun co-axial PCL fibers with rhTGF-b1 were surface-modified with an MSC homing E7 peptide (A). BMSCs attached on both CBE and CBrhTE scaffolds with E7, but produced more COL2 on CBrhTE scaffolds with release of rhTGF-b1 (B). Adapted from [265].

MSC-affinity peptide has also been conjugated onto the surface of demineralized bone matrix (DBM) and delivered within a chitosan (CS) hydrogel as a single functional biomaterial for *in vivo* cartilage repair with a one-step surgical procedure [197]. The biofunctional scaffold was able to sustain a large number of cells within the microfracture

clot during the sol-gel phase transition of chitosan, with mechanical support provided by the solid matrix to enable neo-cartilage formation and maturation. Additionally, conjugation of the affinity peptide to the scaffold facilitated the recruitment and homing of additional BMSCs from the subchondral marrow and peripheral blood to enhance cartilage regeneration and integration within the host tissue (Figure 6).

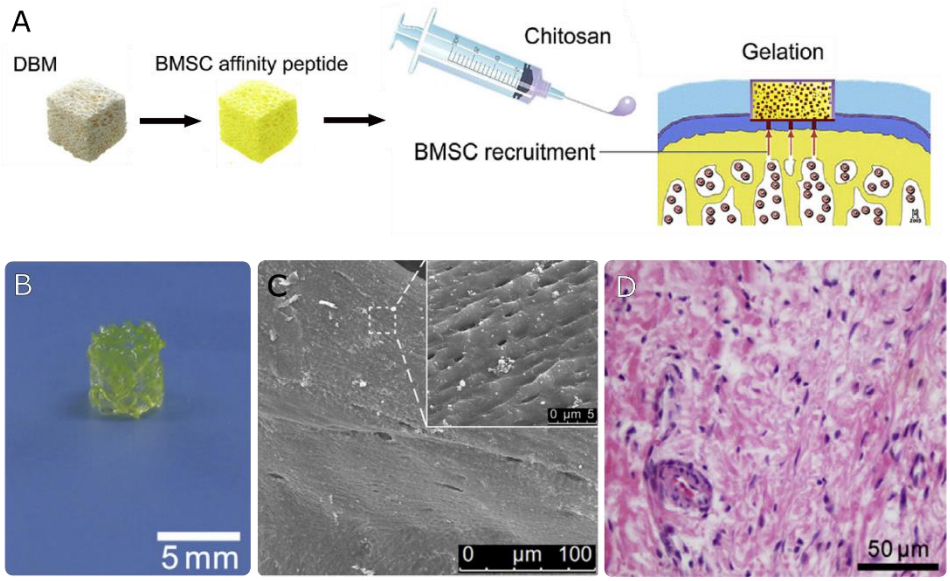

Figure 6.6. MSC affinity peptide functionalized to surface of biphasic DBM scaffolds with chitosan (A). Manufactured scaffolds (B) possessed a rough topography and porosity (C) and were able to attract cells to cartilage when implanted (D). Adapted from [197].

rh-BMP2 and BMP7 is approved for clinical use in certain spinal, long bone and maxillofacial procedures, and has shown positive results when used with scaffolds *in vitro* [229, 267-271]. However, up to 85% of BMP use is off-label [272]. Studies show that BMPs can be detrimental when used in high concentrations or for off-label indications [273]. *In vitro* studies show that BMP2 induces apoptosis in a cell-type dependent manner, with osteoblasts more sensitive to increasing concentrations of BMP2 compared to MSCs [274]. Additionally, it is challenging to evaluate growth factor release profiles after implantation, especially for scaffolds with multiple growth factors [275]. Therefore, care should be taken to use the appropriate dose of BMP, especially for non-FDA approved

indications. Other growth factors commonly used for bone regeneration include VEGF, FGF and TGF-β. While trials are ongoing, none of these have been clinically approved for use [276, 277].

For cartilage regeneration, efforts have focused on increasing matrix production. Though microfracture procedures are still commonly performed, the resulting fibrocartilage does not have the properties of native cartilage and can deteriorate over time [278]. While autologous cells have become more popular in cartilage repair compared to in bone repair, biomaterials are still being studied to facilitate tissue regeneration. Hydrogels are preferable for this application because they are degradable. Recent work functionalizing degradable PEG hydrogels with TGF-β1 and delivered with a mixed population of chondrocytes and MSCs shows promising results for new cartilage growth and remodeling [279].

Nanoparticles developed for bone bone tissue engineering can be used to deliver drugs, vaccines and growth factors with tunable release profiles [280]. Carrier particles include bioglass, PLLA, hydroxyapatite, cobalt ferrite, where the molecule of interest is conjugated to the surface of the nanoparticle for delivery. Additional work shows that electrospun composite scaffolds sprayed with HA nanoparticles enhanced mineralization and ALP specific activity of hFOB cells compared to TCPS; scaffolds without these nanoparticles did not perform statistically better than the control [281]. To monitor new bone growth and scaffold integration, a variety of noninvasive imaging and mechanical techniques have been introduced. Lanthanide apatite particles with fluorescence have been used to distinguish new bone tissue from the implanted scaffold, which can be tracked noninvasively over time [282] (Figure 7).

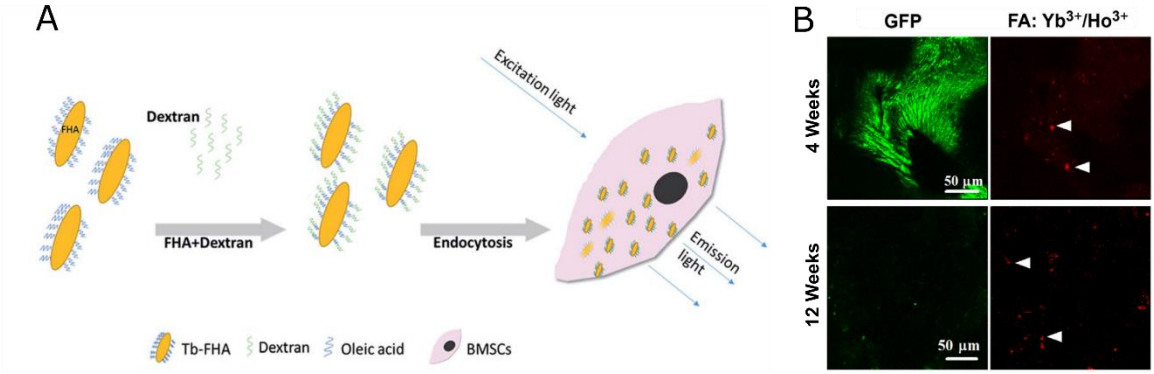

Figure 6.7. Fluorapatite nanorods doped with lanthanides can be endocytosed by and used to track cells over time (A). GFP-labeled BMSCs on DCCBM scaffolds in nude mice with 50 ug/mL FA:Yb3+/Ho3+ after 4 (top) and 12 (bottom) weeks after transplantation (B). Two photon imaging shows that while GFP intensity decreased with time, upconversion nanoparticles retained a strong fluorescent signal. Adapted from [283].

In contrast to nanoparticles, larger microbeads can be used to encapsulate and deliver cells to bone and cartilage requiring regeneration. For cell delivery, carriers must ensure cell viability and, for stem cells, maintain a certain state of differentiation or stemness. MSCs are attractive for both bone and cartilage regeneration. *In* vitro culture of chondrocytes has proved challenging, and cell therapies based on chondrocyte delivery fail to regenerate cartilage due to dedifferentiation of cells after extraction [284]. Alginate microbeads serve as one delivery mechanism for MSCs that allows for controlled degradation by use of alginate lyase [285]. Using microextrusion, alginate hydrogels have been shown to maintain cell viability up to two weeks after manufacturing [286]. Larger alginate hydrogel scaffolds have also been printed with separate compartments for chondrocyte and progenitor cell delivery [287].

An interesting aspect to consider in the development of "smart" biomaterials is the ability to stop the effects of functionalized molecules on the scaffold surface. Degradable scaffolds must have consistent and controllable degradation rates, especially if release of growth factors occurs with degradation. These scaffolds also need to ensure they maintain

sufficient mechanical properties conducive to cell growth and ECM deposition during degradation [175, 288]. As an example, though Mg2+ can be favorable for bone formation and exists as an element within the human body, fast degradation of Mg2+ in also causes air pockets to form that may negatively impact healing. Thus, alloying elements and scaffold materials must be chosen and designed with care that continue to serve their purpose throughout the lifetime of the scaffold. Even nondegradable scaffolds should consider stability of functionalized factors, coatings or surface nanofeatures.

6.6. Biological Evaluation

Though new manufacturing approaches for tissue engineering scaffolds offer increased structural flexibility and resolution, challenges still exist in commercializing these materials for clinical use. Functionalized scaffolds or those with cells must be properly packaged, stored and implanted correctly by the physician [289]. Quality control that fails at any of these steps can be lead to catastrophic consequences. To reduce infection in implanted scaffolds, the addition of silver, copper and zinc ions to metallic implant scaffolds have shown favorable antibacterial effects [290]. These can be incorporated via the native oxide layer, through deposition or as part of the alloy prior to fabrication. Graphene has also been shown to reduce biofilm formation when functionalized on scaffold surfaces [291].

Preliminary *in vitro* investigations on biological response to scaffolds often use immortalized cell lines or mature primary cells. However, there are an increasing number of studies that choose to instead focus on the response of mesenchymal stem cells to the biomaterial surface. Because MSCs are one first cells to the wound site and have the

potential to differentiate into osteoblasts, chondrocytes and fibroblasts, altering their fate can lead to successful integration or fibrous capsule encapsulation and ultimately scaffold failure. Studies have also shown the ability of MSCs to distally affect cells near the implant through release of growth factors. However, the use of MSCs, and in fact many primary cells, can result in differential responses based on donor gender, age and health. Osteoblasts from a female donor, for example, secrete lower levels of osteocalcin compared to osteoblasts from a male donor [292]. Osteoblasts from 11 month old mice displayed a reduced response to titanium surface micro-roughness and $1\alpha,25(OH)_2D_3$ compared to osteoblasts isolated from 1 month old mice [65]. Differences exist even among the source of MSCs. Bone marrow derived MSCs had higher proliferation and matrix production on scaffolds used for cartilage repair compared to adipose derived MSCs [293]. Though the use of primary cells is more clinically relevant, it can be cost-prohibitive to screen across multiple donors to account for variation during preliminary biomaterial evaluation. Primary cells also have a finite number of passages, and especially in the case of chondrocytes, can lose phenotype very quickly when cultured *in vitro [284, 292, 294]*.

Though small animal models are convenient for *in vivo* screening of orthopaedic scaffolds due to their cost convenience and short lifespans, they do not physiologically mimic the human musculoskeletal system. Therefore, larger animals are preferable for evaluating scaffolds on a larger spatial and longer temporal scale closer to that of humans. Larger animals such as primates, dogs, sheep and pigs possess bone architecture more comparable to that of humans. Small rodents, for example, do not have fully developed Haversian systems, an important component of human cortical bone [295]. In addition, larger animals may have other properties similar to humans that can affect bone

regeneration. An increasing number of studies have focused on sex differences and the role of estrogen deficiency or supplementation on bone regeneration [296]. For these studies, it is important to choose an animal model that mimics an estrous cycle similar to humans. While many models for osteoarthritis exist for mice and rats, they do not recapitulate all the systemic effects of the disease as observed in humans [297, 298]. In contrast, horses have naturally occurring osteoarthritis that may be a more suitable model for regenerative scaffold therapies [299].

Once an animal has been chosen, the implantation site must also be considered. Studies have indicated higher BIC and osseointegration of implants placed in cortical bone compared to trabecular bone [300]. In humans, it takes 3-6 months for trabecular bone to remodel, and 6-12 months for cortical bone to remodel [301]. When evaluating bone or cartilage regeneration, it is also important to establish a critically sized defect for each animal model. Not only is the defect size important, but appropriate negative controls that are currently available should be used for comparison, not just a void space [302].

Advanced as biofabrication methods are, experts do not expect a musculoskeletal tissue engineered substitute to be available clinically anytime in the immediate future. Biomaterial design today faces challenges in vascularization and necrosis, the same problems that the biomedical community has faced over the past 50 years [223]. Additional challenges in maintaining cell viability require continued optimization of manufacturing temperature, mechanical extrusion strain and the use of crosslinking agents [232, 303, 304]. In addition, standard are still lacking for characterization of materials, degradation products or evaluation of tissue regeneration after implantation [239, 305]. Even biomaterials that are engineered in the lab and work in *in vitro* and *in vivo* systems do not always translate

to successful clinical use. The term “regenerative medicine” has been defined to include both cell therapy and regenerative surgery, or a combination of biology and human skill [306]. Thus, it is imperative that scientists, engineers and orthopaedic surgeons work collaboratively when developing new materials for bone and cartilage regeneration.

Although over 1400 articles have been published between 2003 and 2013 on “smart” scaffolds for bone tissue engineering, there were only 23 clinical trials evaluating the use of bone scaffolds [307, 308]. One reason for this dichotomy is the continued controversy over classification of these scaffolds by the United States Food and Drug Administration (FDA). Currently, the FDA provides three types of regulatory pathways for new products entering the market: biologic, device or combination product. Scaffolds as a structural support, similar to orthopaedic implants, are most easily regulated through the device pathway, which requires a 510K if the manufacturer can claim similarity to a product previously approved. As scaffolds for tissue engineering become more advanced, they may require a different regulatory pathway for approval. A clear pathway for evaluating and regulating safety and efficacy of scaffolds will also advance clinical progress in bone and cartilage tissue engineering.

6.7. Conclusion

Many advances have been made in scaffold design and manufacturing for bone and cartilage tissue engineering. New manufacturing techniques including additive manufacturing are paving the way to personalized materials. Processing at the macro,

micro and nano-scales also contribute to biological response and clinical success. Finally, we see an integration of functional scaffold design and the innate regeneration potential of patients, rather than relying on the material alone. While still in development, these materials show great promise for clinical translation within the next decade.

CHAPTER 7

ADDITIVELY MANUFACTURED 3D POROUS TI-6AL-4V CONSTRUCTS MIMIC TRABECULAR BONE STRUCTURE AND REGULATE OSTEOBLAST PROLIFERATION, DIFFERENTIATION AND LOCAL FACTOR PRODUCTION IN A POROSITY AND SURFACE ROUGHNESS DEPENDENT MANNER

In [Cheng A, Humayun A, Cohen DJ, Boyan BD and Schwartz Z. Additively manufactured 3D porous Ti-6Al-4V constructs mimic trabecular bone structure and regulate osteoblast proliferation, differentiation and local factor production in a porosity and surface roughness dependent manner. Biofabrication. 2014. 6(4):045007]

7.1. Introduction

Over two million dental implants are placed annually, and over four million hip and knee replacement surgeries are expected by the year 2030 [157]. The orthopaedic implant market is projected to exceed $46 billion by the year 2017, in part due to an increasing number of elderly patients as well as increased quality of life expectations of younger patients [309]. Titanium and its alloys are still widely used in dental and orthopaedic metal implants, based on the ability of bone to form in tight apposition to implants fabricated from these materials [107, 310, 311]. Titanium and titanium-aluminum-vanadium (Ti6Al4V) have a naturally occurring passive oxide layer on their surface that is biologically preferable and resists corrosion, while still maintaining strong mechanical properties and a high strength to weight ratio [312].

Implant surface roughness is one factor that has been shown to successfully increase cell response *in vitro* and osseointegration *in vivo*, and micro-rough surfaces are currently used as the industry standard in dental and many bone-interfacing orthopaedic

implants [142, 313]. Previous studies in our lab confirm that the combined presence of micro-/submicron-scale roughness contributes to increased osteoblast response [9, 31]. By altering only the surface microtopography and without exogenous factors in media, osteoblast differentiation can be increased on titanium surfaces [7]. This may be due in part to the protein-material interaction at the surface, which affects downstream cell response. Changes in the cytoskeleton, including integrin expression and signaling, have also been implicated in this effect [56, 314].

Although dental implant success is achieved in over 95% of healthy patients, certain risk factors still inhibit osseointegration. Osseointegration rates for diabetics and smokers are reduced tremendously [315, 316]. In addition, low bone density or osteoporosis most commonly seen in the increasing elderly population can also decrease osseointegration. Most orthopaedic implants have a lifetime of only 12-15 years, requiring revision surgery that can be fatal for older patients [310, 317]. These factors contribute to the need for improving both osseointegration rates and implant longevity. Therefore, there is an existing need for implants that have the ability to increase bone formation and enhance the regeneration process.

Titanium also has desirable mechanical properties due to its low modulus of elasticity and high strength to weight ratio [318]. However, solid titanium still exceeds the stiffness of cortical bone by more than threefold, causing stress shielding and bone loss downstream of the implant [319]. 3D porous coatings and implants have been proposed to decrease stress shielding via porosity-dependent mechanical properties and increased bone interlocking, making these a promising treatment for at risk patients or younger patients who need an extended implant lifetime [320, 321].

Additive manufacturing techniques provide a layer-by-layer approach to building porous or patient-specific implants that have tailored macro structural and mechanical properties [322]. Selective laser sintering (SLS) has the ability to create high resolution, porous metal constructs with positive results in both *in vitro* and *in vivo* studies [323]. There have been many studies that observe the effect of controlled porosity on *in vitro* or *in vivo* response. However, porosity in these studies was created using homogeneous strut and pore sizing, without a biological template and limited surface modification [323-326]. Trabecular bone in the human body does not have the same pore shape, size or surface roughness. In studies where surface modification was used to induce micro-roughness, bulk porosity was limited to a user designed template [116, 118]. Thus far, the combination of macro structural parameters integrated with micro-scale surface treatment has not been studied. The purpose of this study was to replace the traditional man-made structural template with a biological template.

In this study, we used human trabecular bone as a template to laser sinter Ti6Al4V with varying porosity, and additionally modified the surfaces to obtain a combined micro-/nano- roughness. The resulting constructs were characterized for their surface, structural and mechanical properties. Cellular response to constructs with varying porosity was also performed, with the hypothesis that osteoblast response would increase on 3D constructs with increasing porosity.

7.2. Materials and Methods

Manufacturing

Material Manufacturing

A computed tomographic (CT) scan was taken of a human femoral head retrieved from a hip replacement (µCT 40, Scanco Medical, Bassersdorf, Switzerland) with a 16 µm voxel size. A template was created using Scanco software (Scanco Medical, Bassersdorf, Switzerland) and rotated and superimposed on itself 12, 24, or 36 times to create constructs with low (3DLP), medium (3DMP) and high porosity (3DHP), respectively (Figure 1A). Generated 3D renderings were manufactured into Ti6Al4V disks 15mm in diameter and 5mm in height. Each disk included a 1mm solid base upon which the remaining porous material was sintered in order to ensure mechanical stability during sintering. 2D surfaces were 15mm in diameter and 1mm in height (Figure 1B). Laser sintering was performed using an Ytterbium fiber laser system (EOS, EmbH Munchen, Germany) with Ti6Al4V (grade 5) particles 25-45um in diameter (Advanced Powders & Coatings, Quebec, Canada) in an argon atmosphere. Laser scanning speed was 7m/s with a wavelength of 1054nm, continuous power of 200W and laser spot size of 0.1mm.

Surface Modification

After manufacturing, disks were blasted with calcium phosphate particles using proprietary technology (AB Dental, Jerusalem, Israel) and then acid etched by ultrasonicating in 0.3N nitric acid (HNO_3) once for five minutes at 45^{o}C and twice for five minutes at 25^{o}C. Disks were rinsed in 97% methanol for five minutes. Final pickling treatment was performed by ultrasonicating disks thrice for 10 minutes in ultrapure distilled water, immersing for 30 minutes in 1:1 20 g/L NaOH to 20 g/L H2O2 for 30 minutes at

80°C and ultrasonicating in water for 10 minutes. Constructs were then placed in a degreaser for 12 minutes, immersed in 65% aqueous HNO3, and ultrasonicated thrice in water for 10 minutes. Surfaces were blotted with lint free tissue and allowed to dry for at least 24 hours in order to stabilize the oxide layer before characterization and cell culture.

Material Characterization

Surface Chemistry

Surface chemistry was analyzed using x-ray photoelectron spectroscopy (XPS, K-Alpha, ThermoFisher Scientific, Boston, MA). Samples were transferred to the analysis chamber at a pressure of 1e-8 mbar. An XR5 gun was used with a 500µm spot size at 15kV to perform survey scans with 20ms dwelling time and 1eV energy step size. Bulk chemistry was analyzed using energy dispersive x-ray spectroscopy (EDX, Hitachi SU-70, Tokyo, Japan).

Contact Angle

Sessile drop contact angle was used to assess surface energy and surface wettability (Ramé-Hart goniometer, Succasunna, NJ). 2D solid laser sintered surfaces that received the same post-processing treatment as 3D constructs (Figure 2E, F) were used as a proxy for contact angle measurements due to difficulty in obtaining accurate contact angle measurements for porous constructs. 4µl drops of distilled water were deposited on five predetermined locations per disk, with two disks per group (n=10). Videos of these drops were taken and still images were used in conjunction with DROPimage software (Ramé-Hart goniometer, Succasunna, NJ) to determine the average left and right contact angle of each drop.

Surface Topography

Surface topography was qualitatively assessed using scanning electron microscopy (SEM, Hitachi SU-70, Tokyo, Japan). Disks were secured on imaging stubs with carbon tape and imaged with 56µA ion current, 4kV accelerating voltage and 4mm working distance. Three locations per disk were imaged to ensure homogeneous assessment, with at least two disks per group imaged.

Roughness

Macro- and micro-roughness were analyzed with confocal laser microscopy (LEXT OLS4000, Olympus, Center Valley, PA). Macro roughness was analyzed with a 10x objective, and micro-roughness was analyzed with a 20x objective and additional 5x optical zoom. After a 3 point correction, a cutoff wavelength of 100µm was used to analyze average roughness (R_a) and surface area.

Porosity

3D constructs were analyzed for porosity using micro-computed tomography (micro CT) (SkyScan 1173, Micro Photonics, Inc., Allentown, PA). A volume of interest of 469mm^3, or approximately 66% of each construct's porous volume, was analyzed for total percent porosity, open porosity, pore diameter, strut size, and surface area to volume (SA/V) ratio. Scans were taken using an Al 1.0mm filter, 100kV voltage, 80µA current, 1120x1120 camera pixels, 0.2^o rotation step, frame averaging of 10, random movement of 10. Post-processing included a global threshold of 100-255 and despeckling black and white speckles less than 10 voxels. We verified the validity of micro CT analysis by comparison of total porosity analyzed through a traditional method based on size and mass (Figure 1C).

Mechanical Testing

Compressive moduli of 3D constructs were determined using the MTS Insight 30 testing machine (MTS Systems, Minnesota, USA). A pre-load of 0.01kN was applied at 0.025 mm/s, then a test speed of 0.02 mm/s was used until failure or the maximum load of 30kN was applied. Data acquisition rate was 500Hz, and the compressive modulus was taken as the slope output of the resulting stress/strain curve. Testing was performed on 6 constructs group (total n=6).

Biological Response

Cell Viability

The MG63 human osteoblast-like cell line was used as a model for osteoblast viability, proliferation and differentiation on sintered surfaces. These cells have been characterized and are used by our lab as a model for osteoblast response to titanium surfaces with varying topography [23, 141]. Surfaces were sterilized in UV for 20 minutes in a biosafety cabinet prior to cell culture. Cells were cultured in tissue culture polystyrene (TCPS) flasks until confluence, then centrifuged and resuspended to yield a plating density of 30,000 cells per cm^2 on TCPS, or 60,000 cells per surface in a 24-well plate. Dulbecco's modified Eagle medium (DMEM) with 10% fetal bovine serum (FBS) and 1% penicillin/streptomycin was used to feed cells 24 hours after plating and treat at confluence according to the TCPS control. 24 hours after confluence, cells were treated with 5 µM calcein-AM and 4 µM ethidium homodimer-1 (LIVE/DEAD, Life Technologies, California, USA) in 1x Dulbecco's phosphate buffered saline (D-PBS, Life Technologies) for 20 minutes. Surfaces were imaged using the Zeiss LSM 710 confocal microscope (Zeiss, Oberkochen, Germany). Individual images were taken of 2D disks, while 550um z-stacks were taken of 3D disks. Green (live) and red (dead) channel thresholds were

optimized for each group in order to better distinguish cells. Three images were analyzed and averaged per z-stack, with at least n=6 total areas (z-stacks) analyzed for at least two constructs per group (total n=12).

Osteoblast Proliferation and Maturation

Surfaces were gamma irradiated prior to cell culture. MG63 cells were cultured as described above. Media were changed at confluence, and cells were harvested 24 hours after confluence, rinsed twice with 1xPBS, then stored at -20^{o}C overnight for biological assays. Cell lysate was assayed for DNA content (P7589, Invitrogen) and total protein content (23225, Pierce). Alkaline phosphatase specific activity was measured as a function of *p*-nitrophenol production from *p*-nitrophenylphosphate at pH 10.2 and normalized to total protein. Media were assayed for osteocalcin (OCN, BT-480, Biomedical Technologies, Inc.), VEGF (DY293B, R&D Systems), OPG (DY805, R&D Systems), BMP2 (900-K255, PeproTech) and BMP4 (DY 314, R&D Systems). Data were normalized to total DNA content. Experiments were performed at least twice to ensure validity of the results.

Sample Preparation for Scanning Electron Microscopy

One disk from each group was UV-treated for 20 minutes in a biological hood and plated with 60,000 MG63 cells and cultured as described above. Media were changed at confluence, and cells were fixed 24 hours after confluence with 4% paraformaldehyde (Electron Microscopy Sciences). Constructs were rinsed three times in 1xPBS, then dehydrated in a series of increasing ethanol concentrations: 15%, 30%, and 45% for two hours, then 60%, 75%, 90% and thrice in 100% for at least one hour. Samples were then exchanged in 1:1 100% ethanol and hexamethyldisilazane (HMDS, Sigma Aldrich) for 30

minutes in a chemical safety hood, then twice in 100% HMDS for 30 minutes. Samples were dried 24 hours in a desiccator before being platinum sputtered and imaged with SEM as described above (Hitachi SU-70, Tokyo, Japan).

Statistical Analysis

Surface characterization data are presented as mean ± one standard deviation (SD) of all measurements performed across samples in the same group. Cell viability is presented as the mean of all measurements performed across samples in the same group. Cell proliferation and differentiation data are presented as mean ± standard error of the mean (SEM) for six independent cultures. All experiments were repeated at least twice to ensure validity of observations, with results from individual experiments shown. Statistical analysis among groups was performed by analysis of variance, and significant differences between groups were compared using Bonferroni's modification of Student's t-test. A p value of less than 0.05 was considered statistically significant.

7.3. Results

Surface Characterization

Laser sintered 3DLP, 3DMP and 3DHP constructs had 16.2±2.9%, 38.5±3.9%, and 70.0±3.5% total porosity and 15.0±2.9%, 37.9±4.0%, 70.0±3.5% open porosity, respectively (Table 7.1). Total porosity and open porosity were not significantly different, showing complete interconnectivity between pores (Figure 7.1D). Average pore diameter was 177±22 μm for 3DLP, 383±15 μm for 3DMP and 653±22 μm for 3DHP constructs. Average strut thickness was 628±150 μm for 3DLP, 454±57 μm for 3DMP and 305±26 μm for 3DHP. The ratio between the analyzed construct surface area to volume ratio was 23.5 ± 7.4 for 3DLP, 36.1 ± 5.4 for 3DMP, and 56.9 ± 5.8 for 3DHP disks. For all porosity

parameters (total porosity, open porosity, pore diameter, strut thickness and SA/V ratio), all groups were significantly different from each other. Pore diameter, strut thickness and SA/V ratio all increased with increasing construct porosity.

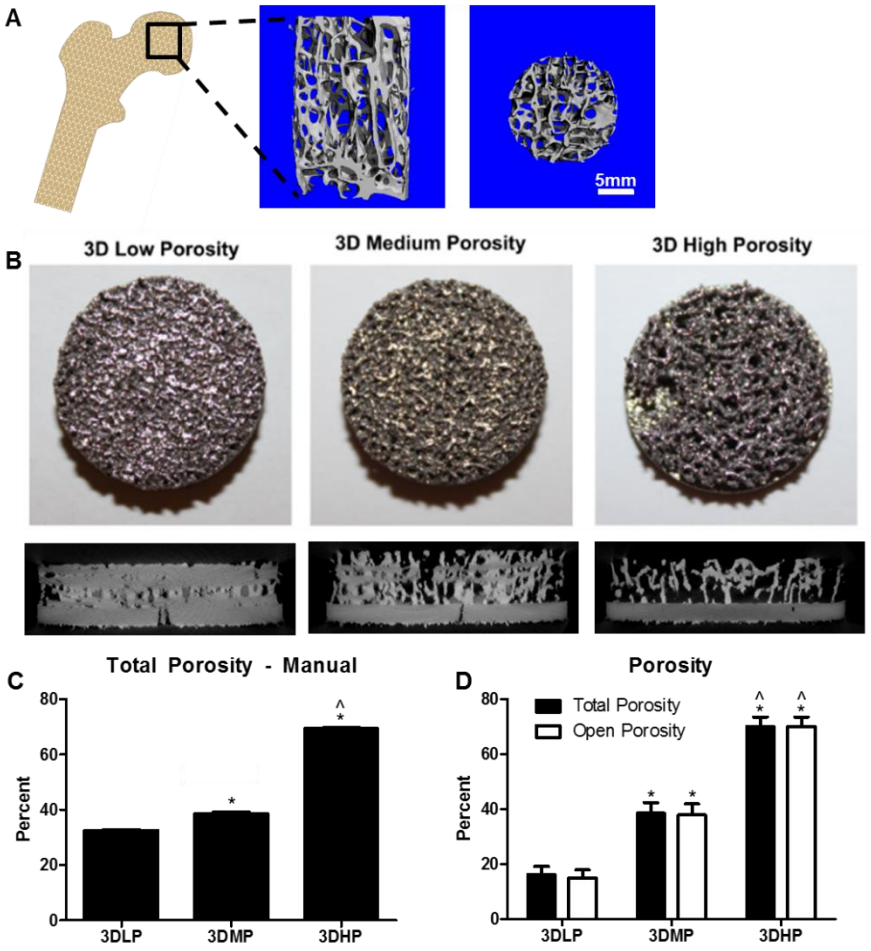

Figure 7.1. (Left to right) Laser sintered disks were created from a CT scan conducted of human trabecular bone from the femoral head after a hip replacement. Original CT scans showing bone porosity through transverse and axial cross sections were used as a template for porous, laser sintered disks (A). Top-down camera images and micro CT cross sections of laser sintered 3D disks with (from left to right) low, medium and high porosity (B). Total porosity was calculated using a traditional method based on mass (C). Total and open porosity was calculated with micro CT (D). 1 way ANOVA with Bonferroni's correction was performed separately for total porosity or open porosity. $p<0.05$ is indicated by * vs. 3DLP and ^ vs. 3DMP. Unpaired t-test between total and open porosity showed no significance between groups.

Surface chemistry performed by XPS showed mostly C, O and Ti in the oxide layer, with small amounts of N, P and Ca due to processing, and Al present on 2D surfaces (Table 7.2). EDX allows for higher penetration past the oxide layer and showed Ti, Al and V as the bulk surface composition, with a small amount of C present on 3DLP surfaces (Table 7.3). Contact angle of 2D proxy surfaces was 92 degrees with a standard deviation of 8 degrees. Compressive modulus decreased in a porosity-dependent manner (Table 7.4). 3DLP had a modulus of 2954±21, 3DMP a modulus of 2818±42 MPa and 3DHP a modulus of 2063±85.

Table 7.1. Porosity Parameters

Porosity Parameters (Average ± SD)					
	Total Porosity (%)	Open Porosity (%)	Pore Diameter (μm)	Strut Thickness (μm)	SA/V Ratio
3DLP	16.2 ± 2.9	15.0 ± 2.9	177 ± 22	628 ± 150	23.5 ± 7.4
3DMP	38.5 ± 3.9 (*)	37.9 ± 4.0 (*)	383 ± 15 (*)	454 ± 57 (*)	36.1 ± 5.4 (*)
3DHP	70.0 ± 3.5 (*^)	70.0 ± 3.5 (*^)	653 ± 22 (*^)	305 ± 26 (*^)	56.9 ±5.8 (*^)

Significance * vs. LP, ^ vs. MP $p<0.05$.

Table 7.2. Surface Chemistry (XPS): Elemental Composition

Element (Atomic % Average ± SD)							
	O	C	Ti	N	P	Ca	Al
2D	41.6 ± 3.7	41.8 ± 5.4	12.6 ± 1.5	1.3 ± 0.6	--	--	2.5 ± 0.5
3D-LP	44.9 ± 4.4	36.6 ± 7.9	6.3 ± 1.7	5.6 ± 1.5	3.3 ± 3.9	2.6 ± 1.9	--
3D-MP	54.5 ± 1.9	20.5 ± 20.4	6.9 ± 1.7	4.9 ±0.9	9.7 ± 1.6	3.6 ± 1.0	--
3D-HP	51.7 ± 3.1	29.5 ± 2.8	13.4 ± 1.1	3.2 ± 0.8	1.6 ± 1.8	--	--

Does not include trace elements less than 1%

Table 7.3. Surface Chemistry (EDX): Elemental Composition

Element (Weight % Average ± SD)				
	Ti	Al	V	C
2D	89.8 ± 0.6	7.1 ± 0.8	3.1 ± 0.2	--
3D-LP	87.3 ± 4.7	6.7 ± 1.6	3.0 ± 0.2	2.4 ± 3.8
3D-MP	88.9 ± 2.2	7.0 ± 1.1	3.1 ± 0.2	--
3D-HP	89.0 ± 1.8	7.5 ± 1.4	3.2 ± 0.2	--

Does not include trace elements less than 1%

Table 7.4. Compressive Modulus (MPa)

Compressive Modulus (Average MPa ± SD)	
3D-LP	3693 ± 27
3D-MP	3522 ± 52 (*)
3D-HP	2579 ± 106 (*^)

Significance $p<0.05$. * vs. LP, ^ vs. MP

After manufacturing the surfaces had a very grainy topography at the macro scale, but smooth topography at the micro scale (Figure 7.2A,B). Blasting and acid etching induced micro roughness on surfaces while maintaining macro structure (Figure 7.2C,D). Pickling overlaid fine and homogenous nanofeatures on the macro surface (Figure 7.2E,F). Cross sectional, low magnification SEM images show internal pore surfaces looking similar to pretreated constructs, indicating the inability of grit blasting treatment to affect internal construct pores (Figure 7.3). Surface roughness results revealed increasing surface roughness and area at the macro level for increasing porosity (Figure 7.4A,B). Surface micro roughness showed no difference between groups except an elevation in 3DHP surfaces, and no difference between groups for surface area at the micro level (Figure 7.4C,D).

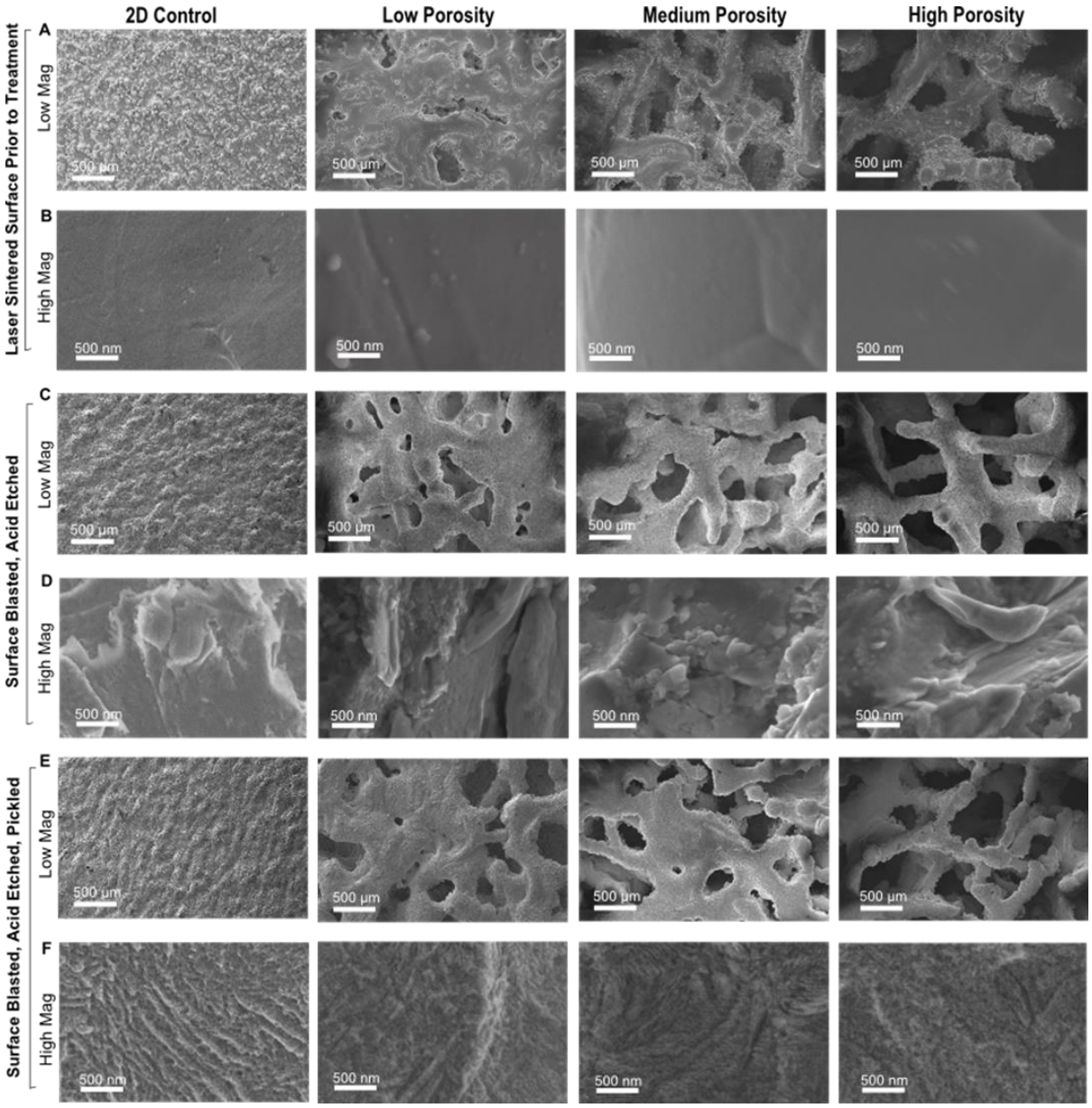

Figure 7.2. SEM images of (columns from left to right) 2D, 3D low, medium and high porosity disks. Low magnification images showing trabecular structure after production (A), after blasting and acid etching (B), and after picking (C). High magnification images showing smooth surfaces after production (B), micro-roughness after blasting and acid etching (D), and nano-roughness after pickling (F).

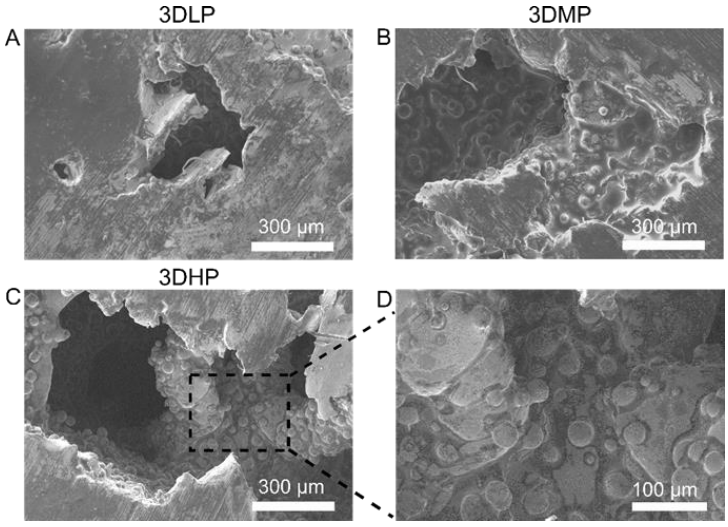

Figure 7.3. Cross sectional SEM images of 3DLP (A); 3DMP (B); and 3DHP (C) constructs. An enlarged image of 3DHP (D) shows an absence of surface roughness induced by grit blasting.

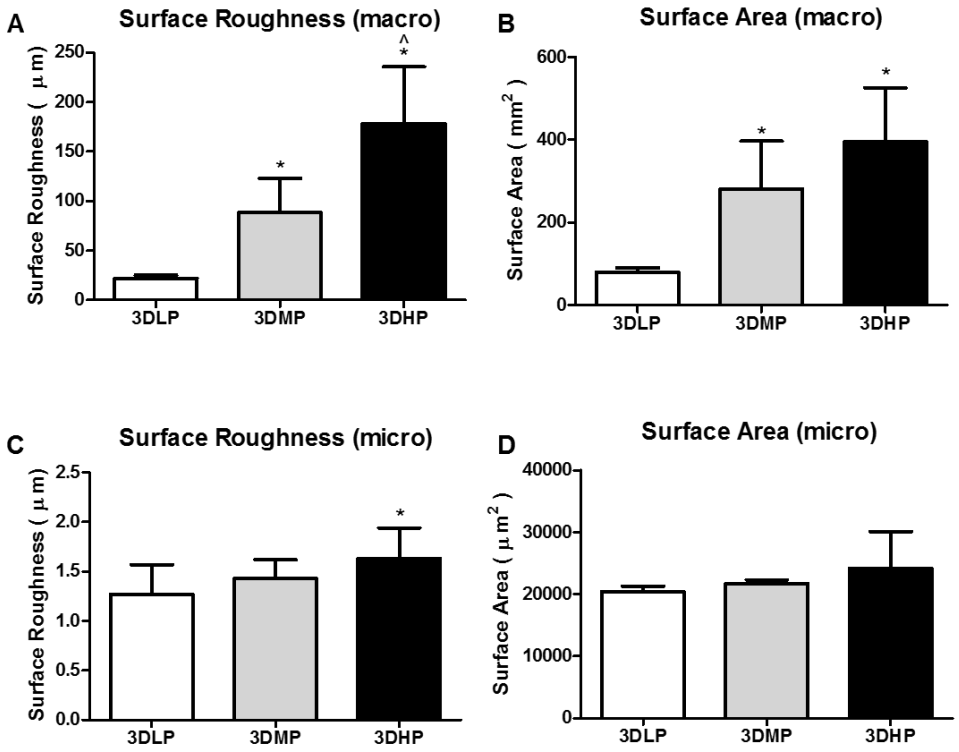

Figure 7.4. Macro surface roughness (A), macro surface area (B), micro surface roughness (C) and micro surface area (D) analyzed with laser confocal microscopy. 1 way ANOVA with Bonferroni's correction shows significance of $p<0.05$ for * vs. 3DLP and ^ vs. 3DMP.

Biological Response

Live/dead analysis indicated that cells on all surfaces had high viability. No significant differences in osteoblast viability were observed across constructs with varying porosity (Figure 7.5A). 2D surfaces had the highest percent viability at 99.9%. 3DLP, 3DMP and 3DHP constructs had 94.9%, 98.1% and 91.6% cell viability, respectively. A noticeable decrease in number of cells was seen on 2D surfaces cultured under continuously shaking conditions. Representative SEM micrographs of cells cultured on disks showed cells spread evenly across surfaces (Figure 7.5B).

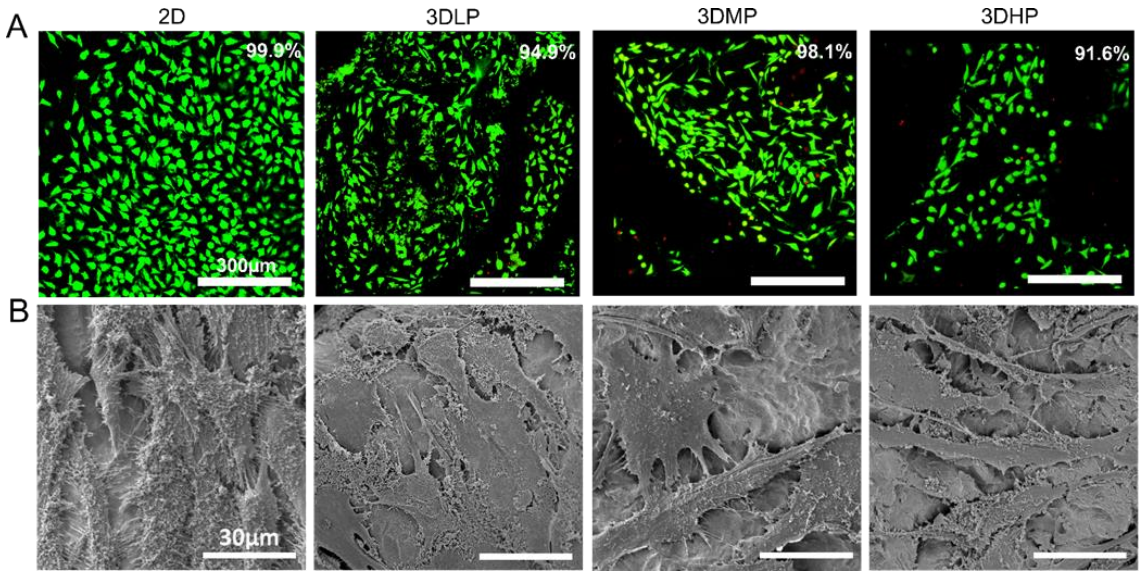

Figure 7.5. MG63 cell viability (live=green, dead=red) after culturing until confluence on TCPS (A). No differences were found among groups using 1 way ANOVA with Bonferroni's correction, $p<0.05$. SEM micrographs revealing well-spread cell morphology on surfaces (B).

DNA was highest on TCPS and decreased as porosity increased (Figure 7.6A). ALP, a marker of early osteoblastic differentiation, was elevated on 3DLP compared to TCPS, then decreased on 3DMP and 3DHP compared to 3DLP, and decreased significantly on 3DHP compared to TCPS (Figure 6B). OCN increased significantly on 3DHP compared to TCPS (Figure 7.6C). OPG increased on 3DMP and 3DHP compared to TCPS and 3DLP,

and was also significantly higher on 3DHP compared to 3DMP (Figure 7.6D). BMP2 on 3DLP, 3DMP and 3DHP was significantly higher than on TCPS, and 3DMP and 3DHP constructs had higher BMP2 levels compared to 3DLP (Figure 7.6E). BMP4 was elevated on 3DHP compared to TCPS only (Figure 7.6F). VEGF was elevated on 3DMP and 3DHP compared to TCPS and 3DLP, and was also significantly higher on 3DHP compared to 3DMP (Figure 7.6G).

7.4. Discussion

Increased implant failure due to lack of osseointegration is a problem in compromised patients, which creates the need for better bone integration and mechanical properties of Ti and Ti alloy implants [316]. Although studies have pointed toward 3D porous implants as a possible solution, these surfaces have not been optimized for porosity or combined with desired surface roughness features.

Various additive manufacturing methods such as direct beam melting and laser sintering have come to the forefront of customized and porous implant manufacturing. The sintering system we use in this study has a theoretical resolution of 100 microns according to the laser size; however, limited studies have been performed on the homogeneity of laser strength within that diameter. Scan speed and wavelength can all have an effect on the manufactured structure's density and therefore mechanical properties, but with higher resolution comes increased time of production.

Previous studies have observed increased sintering density of over 97% with decreasing scan speeds to 50 mm/s [324]. Our qualitative evaluations using SEM and quantitative analysis using micro CT point toward a close approximation of our construct

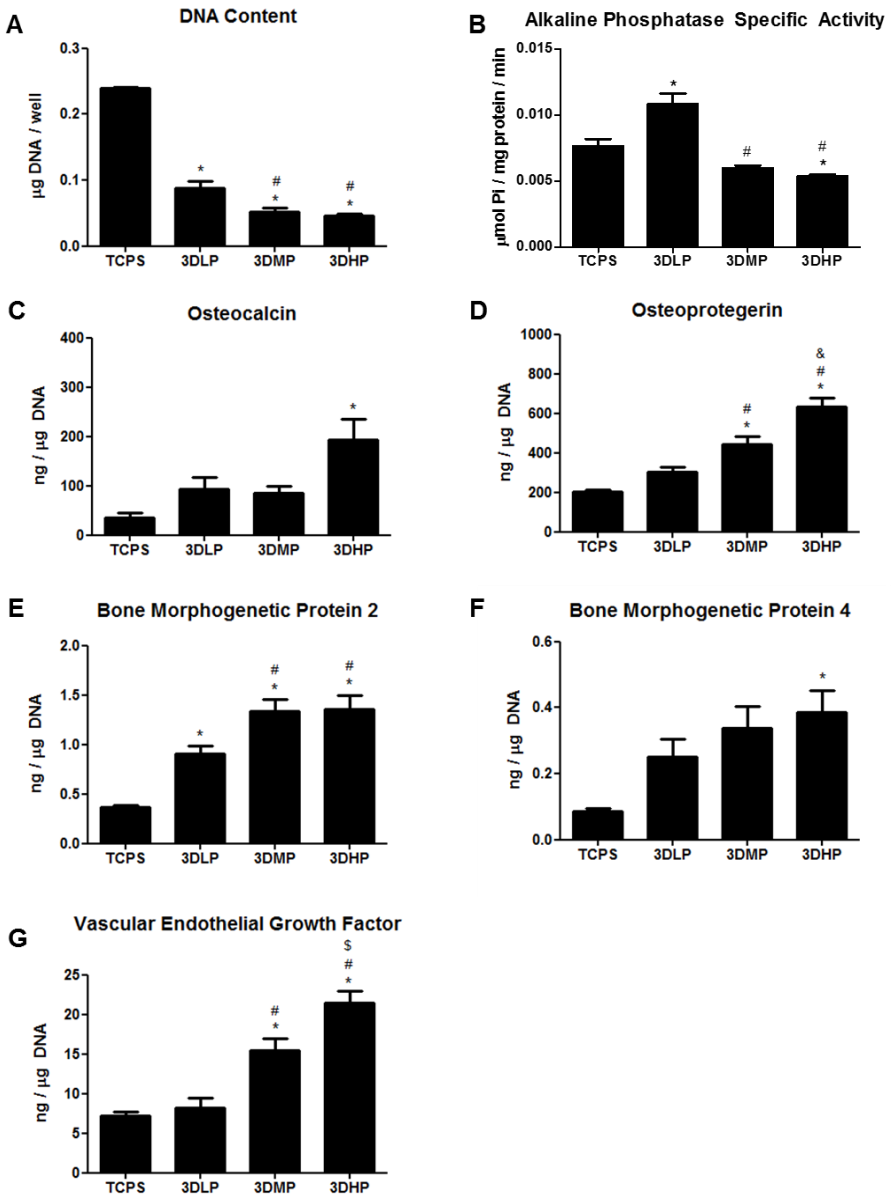

Figure 7.6. MG63 cell response to laser sintered, porous surfaces 24 hours after confluence. DNA content (A), alkaline phosphatase specific activity (B), osteocalcin (C), osteoprotegerin (D), bone morphogenetic protein 2 (E), bone morphogenetic protein 4 (F), and vascular endothelial growth factor (G). Significance determined with 1 way ANOVA with Bonferroni's post- correction, $p<0.05$ for * vs. TCPS, ^ vs. 2D, # vs. 3DLP and $ vs. 3D-MP.

structure with that of human trabecular bone, even at high density. Although the optimal pore diameter for porous implants has been debated in literature, most studies observe increased cell infiltration or bone ingrowth for pores larger than 100µm in diameter [175,

327, 328]. Pore sizes of 200-400μm have been thought to increase osteoblast attachment, migration and proliferation via activation of mechanoreceptors [329]. We observed pore sizes upwards of 300μm in our disks, which has been suggested as a minimum for new bone and capillary formation [175]. Pore diameter has been suggested to have higher influence on bone ingrowth when compared to total percent porosity alone, although we were not able to isolate these two variables in our constructs [330].

Similar processing methods have previously been shown to successfully manufacture surfaces with stable mechanical properties and good *in vitro* results [116]. The effect of roughness at both the micro- and nano-scales on osteoblast differentiation has been well documented [9, 140, 141], and our results show that traditional methods such as blasting and acid etching are effective at inducing a homogeneous combined micro-/nano-roughness on additively manufactured surfaces. Due to the high interconnectivity between pores, acid treatment and pickling solutions were able to access the entire surface area of constructs to create a unique, homogenous nanostructured surface. However, our results show that blasting was not able to significantly alter the internal pores of the constructs. Despite this, cell response still increased significantly for high porosity constructs, suggesting that macro-structural effects of 3D porous constructs may play a larger role in cell response compared to surface roughness alone.

Human trabecular bone from the mandible has a porosity range of 70-90%, which varies with location and patient factors [331-333]. In this study, we created porous structures ranging from 20-70% to determine the optimal percent porosity for cells. Our compressive moduli decrease with increasing porosity, which has been corroborated for both synthetic constructs and human bone [320, 332]. Compressive testing on human

trabecular bone has shown a compressive modulus of 1.08 GPa [334]. A study encompassing 160 human trabecular bone samples with compressive moduli ranging from approximately 300-900 MPa showed that bone-volume fraction (density), surface-to-volume ratio, trabecular thickness (strut thickness) and spacing (pore diameter) all contributed significantly to differences in mechanical properties [335]. The direction of loading can also impact mechanical output, which is especially true due to the anisotropic properties of bone [325]. In this study, we performed testing on porous constructs with a 1mm solid base, which may have contributed to a higher modulus than just the porous component alone.

Surface chemistry of disks with varying porosity contained mainly elements of Ti, O and C, although bulk chemistry confirmed the presence of Ti, Al and V in the alloy. Previous surface analysis of Ti6Al4V surfaces has also shown the presence of Al in the oxide layer, which may have been masked by Ca and P after blasting [133]. Contact angle on 2D proxy surfaces was neither super-hydrophilic nor hydrophobic. These 2D surfaces underwent the same surface treatment as 3D constructs, although the effect of strut curvature and differences in internal surface roughness on wettability for 3D constructs could not be determined. Surface roughness and area at the micro level were not different among groups except for an elevated roughness on 3DHP, which may have been due to the decreased strut thickness and increased curvature at sites of analysis.

Cell viability was high and not significantly different among surfaces. A qualitative observation of a decrease in cell number with increasing porous constructs suggests that cells had infiltrated pores and distributed over a larger surface area. Previous studies on additively manufactured porous surfaces also showed high cell viability and cell infiltration

into pores [336], which were confirmed by our SEM images. We assume high cell viability exists for cells that have infiltrated to the pores; however, we were not able to visualize all the way to the bottom of the disks to fully verify cell infiltration. Viability results were limited to the first 550μm, a limitation of the imaging equipment.

The decrease in ALP specific activity and the increase in OCN point toward a porosity-dependent maturation response. Previous reports of ALP activity on roughened surfaces noted a significant difference in cell layer activity versus isolated cells, suggesting increased matrix vesicle production [337]. These results also correspond to the decreased DNA content on 3DHP constructs, indicating a preference toward osteoblast maturation instead of proliferation. OPG, a decoy receptor for RANKL and involved in the bone remodeling process, was increased on 3DMP and 3DHP constructs. This increase in OPG blocks osteoclast differentiation in a protective effect to enhance bone growth, and has been implicated in osteoblast-osteoclast communication [338]. An increase of BMP2 and BMP4, especially on 3DHP surfaces, corroborates previous studies that observe increased BMP production on constructs with 300-400μm pore diameters [339]. Although our pore diameters are larger, the irregular porosity of trabecular bone may contribute differently to local factor production than in other studies with user-defined geometries. The increase of BMP local factor production indicates that our porous constructs have the potential to regulate the induction of bone inside the construct, as well as induce bone distally. The Increased levels of VEGF on 3DHP constructs also point toward this trend, indicating that highly porous constructs of trabecular bone structure are inductive for blood vessel formation as part of supporting new bone formation and bone regeneration.

As percent porosity increased, so did the surface area to volume ratio, indicating an increased surface area for cell interaction. It has previously been shown that rough titanium surfaces enhance osteoblastic differentiation and increase local factor production, so the increased cell response in this study may well be attributed to the varying material properties of our surface [23]. In this study, the combination of the three dimensional macro-structure, increase in surface area and combined micro-/nano- surface modification enhanced the osteoblast phenotype. Increased curvature on 3D surfaces with higher porosity may exert higher mechanical forces on a cell, which has been shown to direct cells toward osteoblast differentiation [340]. This response could be mediated by cell-surface integrin proteins. In particular, α5 has been implicated in osteoblast attachment and proliferation, and α2β1 in osteoblast morphology and differentiation via its binding to collagen in the extracellular matrix [55, 56].

The role of confluence may contribute to cell response, and has been previously discussed with regard to TCPS versus rough titanium surfaces [54]. Although decreased DNA was shown on Ti6Al4V surfaces compared to TCPS controls, previous studies on pre-confluent cultures have also shown a different maturation profile of osteoblasts on the Ti alloy surfaces compared to TCPS, suggesting that our resulting cell response was also surface specific and not confluence dependent [329].

Increased bone growth in response to additively manufactured implants has been shown in various animal models, including rats and sheep [118, 341]. Previous work has shown highest calcium content and *in vivo* response to materials with 75% porosity compared to higher porosities [13]. Further work in an animal model will be essential to

assess the success of bone growth into individual pores and osseointegration capability of the entire porous construct.

7.5. Conclusion

In this study, we used additive manufacturing to produce Ti6AlV materials with varying porosity that structurally mimicked human trabecular bone, and further created a desirable surface for osteoblasts by inducing combined micro-/nano-roughness. Our results indicate that a high porosity construct mimicking trabecular bone structure is capable of stimulating osteoblast differentiation when compared to 2D and low porosity constructs. Additive manufacturing is a scalable manufacturing method that has the potential to create structurally complex, patient-specific orthopaedic and dental implants and scaffolds for increased osseointegration. Although trabecular orientation may vary across individuals and locations in the body, this study suggests that osteoblast cells actually do prefer one type of porosity and structure. In addition, this study reveals the possibility for creating patient-specific implants, which may accelerate the fields of dental and orthopaedic implants.

CHAPTER 8

ENHANCED OSTEOBLAST RESPONSE TO POROSITY AND RESOLUTION OF ADDITIVELY MANUFACTURED TI-6AL-4V CONSTRUCTS WITH TRABECULAE-INSPIRED POROSITY

In [Cheng A, Humayun A, Boyan BD and Schwartz Z. Enhanced osteoblast response to porosity and resolution of additively manufactured Ti-6Al-4V constructs with trabeculae-inspired porosity. 3D Printing and Additive Manufacturing. 2016. 3(1):10-21]

8.1. Introduction

Additive manufacturing in the biomedical space has traditionally been limited to polymer printing through a deposition style method [342]. In contrast, methods such as laser sintering and electron beam melting manufacture from a bed of powder [322]. These methods allow a bottom up approach of manufacturing for metals, opening up vast opportunities for engineering implants and devices with improved mechanical strength.

Titanium and its alloys are commonly used materials for orthopaedic and dental implants due to their corrosion resistance, high strength to weight ratio and ability to osseointegrate with the body [107, 311]. Until recently, these implants have been manufactured through a reductive process to produce a solid implant body. While the implant body has not changed much over the last few decades, advances in surface technology have introduced micron scale, submicron scale and nanoscale roughness as well as increased wettability on implant surfaces. These changes at the surface have helped to increase early osseointegration and implant success in patients [19, 343]. However, osseointegration rates still vary widely, especially for patients with diabetes, smokers and the elderly [316, 344, 345]. Additionally, mechanical mismatch in orthopaedic implants

between the implant bone and host bone can cause stress shielding, leading to repercussions including increased fracture rate occurring distal to the implant[321, 346]. These factors all contribute toward a need for implants that enhance clinical success.

The introduction of porous implants by additive manufacturing has sought to address these issues. This solution is attractive not only for its ability to manufacture materials with less time and waste, but also to design custom implants for patients[144, 347, 348]. Laser sintering is one form of additive manufacturing that has been used to create bone-interfacing Ti-6Al-4V implants [144]. Already, these laser sintered solid implants have shown promise in clinical studies [349]. Surface processing methods have been used to achieve similar surface roughness and wettability for additively manufactured Ti-6Al-4V implant materials as traditional implants [116]. Previous studies have shown increased osteoblast-like response to trabecular bone-like constructs based on porosity [38]. Enhanced cell response at the surface can lead to favorable clinical responses. Other porous TI-6Al-4V implants have shown success via increased bone to implant contact and mechanical integration compared to solid implants in animal studies [121, 350]. However, as porosity of an irregular bone like trabecular environment can be difficult to define, cell response may depend on more than just how much void space is available within the construct. The combination of well-known surface parameters such as roughness and hydrophilicity with variations in trabecular detail and porosity has not yet been explored.

In this study, we characterize and evaluate biological response to laser sintered Ti-6Al-4V constructs with a 3D trabecular bone inspired porosity. We hypothesize that osteoblastic response will be enhanced on 3D compared to 2D solid constructs, and that this response is porosity and resolution dependent.

8.2. Materials and Methods

Material manufacturing and post-fabrication surface processing

2D disks and 3D constructs were manufactured using laser sintering (EOS GmbH, Krailling, Germany) from Ti-6Al-4V powder as described previously[38]. 2D disks were 15mm in diameter and 1mm in height. A CT template scan was taken of human femoral trabecular bone (µCT40, Scanco Medical, Bassersdorf, Switzerland) with a 16µm voxel size. Scanco software was used to rotate the template on itself 12, 24 or 36 times to create low, medium or high porosity constructs 15mm in diameter and 5mm in height, including a 1mm solid base. In this study, resolution is defined as the amount of trabecular detail captured from the original CT scan. In this study, "high resolution" constructs are those that captured more detail from the CT template due to higher thresholding within the capture software. "Low resolution" constructs are those with a lower data capture threshold, and resulted in less detail incorporated into the final manufactured construct. Disks and constructs were blasted with $CaPO_4$ particles, followed by acid etching once in 0.3N HNO_3 at 45^oC and twice at 25^oC for five minutes. Materials were rinsed in 97% methanol before ultrasonicating three times for 10 minutes in ultrapure distilled water at room temperature. Materials were then immersed for 30 minutes at 80^oC in a 1:1 solution of 20 g/L NaOH to 20 g/L H_2O_2 and ultrasonicated again in water at room temperature. Materials were finally immersed in 65% HNO_3 for 30 minutes before ultrasonicating in water at room temperature. All materials were allowed to dry for at least 24 hours to stabilize the oxide layer, then sterilized via gamma irradiation before characterization and cell culture.

Material characterization

Scanning electron microscopy (SEM) was used to evaluate surface topography at the macro-, micro- and submicro/nano-scales (Zeiss AURIGA, Oberkochen, Germany). Images were taken with a 4kV accelerating voltage, 30µm aperture, InLens detector and 4mm working distance.

Micro-computed tomography (microCT) was used to evaluate porosity of 3D constructs (SkyScan 1173, Bruker Corporation, Billerica, Massachusetts, USA). An accelerating voltage of 100kV, current of 80µA, 1.0mm aluminum filter and pixel size of 20.1µm were used to image constructs. Files were reconstructed in NRecon software with 100% beam hardening. Reconstructed files were analyzed in CTAn software to determine total porosity (percent of void space within construct), surface area to volume ratio, pore diameter (average spherical diameter between metal struts) and strut thickness. The average ± standard deviation (SD) of porosity parameters was calculated for 6 samples per group.

Laser confocal microscopy (LCM) was used to image and quantify surface roughness (Zeiss LSM 710). Z-stacks were obtained with a Plan Apochromat 20x/0.8 M27 objective with a 5x optical zoom, 0.39µs pixel dwell, 25µm pinhole, 85µm x 85µm image size and z-step of 1µm. A 405nm laser with 50% strength was used in reflection mode. 3D z-stack images were captured of 2D and 3D constructs at 10X magnification to show differences in macro-scale features. To evaluate surface roughness, z-stacks were taken at 40X magnification with a 5X optical zoom to eliminate interference from curvature. Average surface roughness (Sa) was defined as the average absolute distance in the z-plane, and peak-to-valley height (Sz) was defined as the average sum of the highest peak and the

lowest valley in the z-plane. Roughness values were obtained using ZEN software (Zeiss) and shown as an average ± SD of 6 samples per group.

X-ray photoelectron spectroscopy (XPS) was used to analyze surface chemistry (ThermoFisher ESCALab 250). Analysis was conducted using an XR5 gun at 15kV with a 20ms dwell time and 1eV energy step size. A spot size of 500µm was used, with average values taken from two survey scans.

Sessile drop contact angle analysis was used to determine surface wettability on 2D disks (Ramé-Hart Instrument Co., Succasunna, New Jersey, USA). A 4µL drop of distilled water was placed on disks, and the average of left and right angles were averaged every 5 seconds for 20 seconds after drop placement. A total n=10 drops was analyzed across two disks.

Mechanical properties of samples were evaluated through compression testing of porous constructs (MTS Insight 30, MTS Systems Corporation, Eden Prairie, Minnesota, USA) at room temperature. Testing was conducted with a speed of 0.02 mm/s, data acquisition rate or 500hz/s, pre-load of 0.01kN, pre-load speed of 0.025mm/s and strain endpoint of 80%. Testing was conducted until failure or a 30kN maximum load was applied.

Biological response

MG63 osteoblast-like cells (ATCC, Manassas, Virginia, USA) and normal human osteoblasts (NHOst Donor 25433, Lot 336963, Lonza, Walkersville, MD, USA) were cultured to confluence in T75 flasks before plating. 2D disks and 3D constructs were designed to fit snugly in the bottom of a 24-well plate. Cells were plated at a density of 30,000 cells/cm^2 according to surface area on tissue culture polystyrene (TCPS), which

was used as an optical control for confluence. Cells were fed with full medium (DMEM + 10% FBS + 1% penicillin/streptomycin) 24 hours after plating. At confluence at approximately day 3, cells were treated with fresh medium and harvested 24 hours afterward for analysis of cell layer lysate and conditioned medium.

DNA content was analyzed by fluorescence using the Quant-iT kit (Thermo Fisher Scientific, Waltham, Massachusetts, USA). Alkaline phosphatase specific (ALP) activity of cell lysates was determined by analyzing release of para-nitrophenol from para-nitrophenolphosphate at pH 10.2. ALP was normalized to total protein content as determined by bicinchoninic acid assay (Thermo Fisher Scientific). Enzyme-linked immunosorbent assays were used to evaluate expression of osteocalcin (OCN, Alfa Aesar, Ward Hill, Massachusetts, USA), osteoprotegerin (OPG, R&D Systems, Inc., Minneapolis, Minnesota, USA), vascular endothelial growth factor (VEGF, R&D Systems, Inc.) and bone morphogenetic proteins 2 and 4 (BMP2, PeproTech, Rocky Hill, New Jersey, USA and BMP4, R&D Systems, Inc.).

Statistics

All material characterization results are shown as average and standard deviation (SD), while biological results are shown as average and standard error of the mean (SEM). The differences between groups was measured by one way analysis of variance (ANOVA) was performed with a Bonferroni post-hoc analysis to analyze groups of 3 or more. $P<0.05$ was considered statistically significant.

8.3. Results

Material characterization

SEM images of sintered constructs showed varying macro-scale topography but similar micro-/submicro-/nano-scale topography after surface processing. 2D controls possessed pronounced peaks observed at low magnification, while a micro-roughness with nano-features was evident at high magnification (Figure 8.1A). Macro-scale features of 3D constructs with low resolution (Figure 8.1B) were significantly different than those with high resolution (Figure 8.1D). 3D constructs with high resolution contained smaller pores and struts within larger features. However, high magnification images of all 2D and 3D constructs across porosities and resolutions indicated similar micro-roughness, which included submicron and nano-features (Figure 8.1C and 8.1E).

MicroCT analysis showed total porosity ranged was 41.0%, 56.6% and 76.1% for LP-LR, MP-LR and HP-LR constructs, respectively. Total porosity was 52.5%, 57.3% and 70.9% for LP-HR, MP-HR and HP-HR constructs, respectively (Table 8.1). Total porosity values were not significantly different than open porosity values for the same constructs (Figure 8.2A). Cross-sectional images of constructs showed finer detail in high resolution constructs compared to low resolution constructs that was evident throughout the bulk of the construct (Figure 8.2B). MicroCT analysis also showed that SA/V ratio and pore diameter increased and strut thickness decreased with increasing porosity within each resolution (Table 8.1). Surface area to volume ratio ranged from 5.1 to 8.1 for LR constructs and 10.2 to 11.5 for HR constructs. Pore diameter ranged from 641 to 1096 μm for LR constructs and 461 to 872 μm constructs. Strut thickness ranged from 475 to 673 for LR constructs and 267 to 311 for HR constructs.

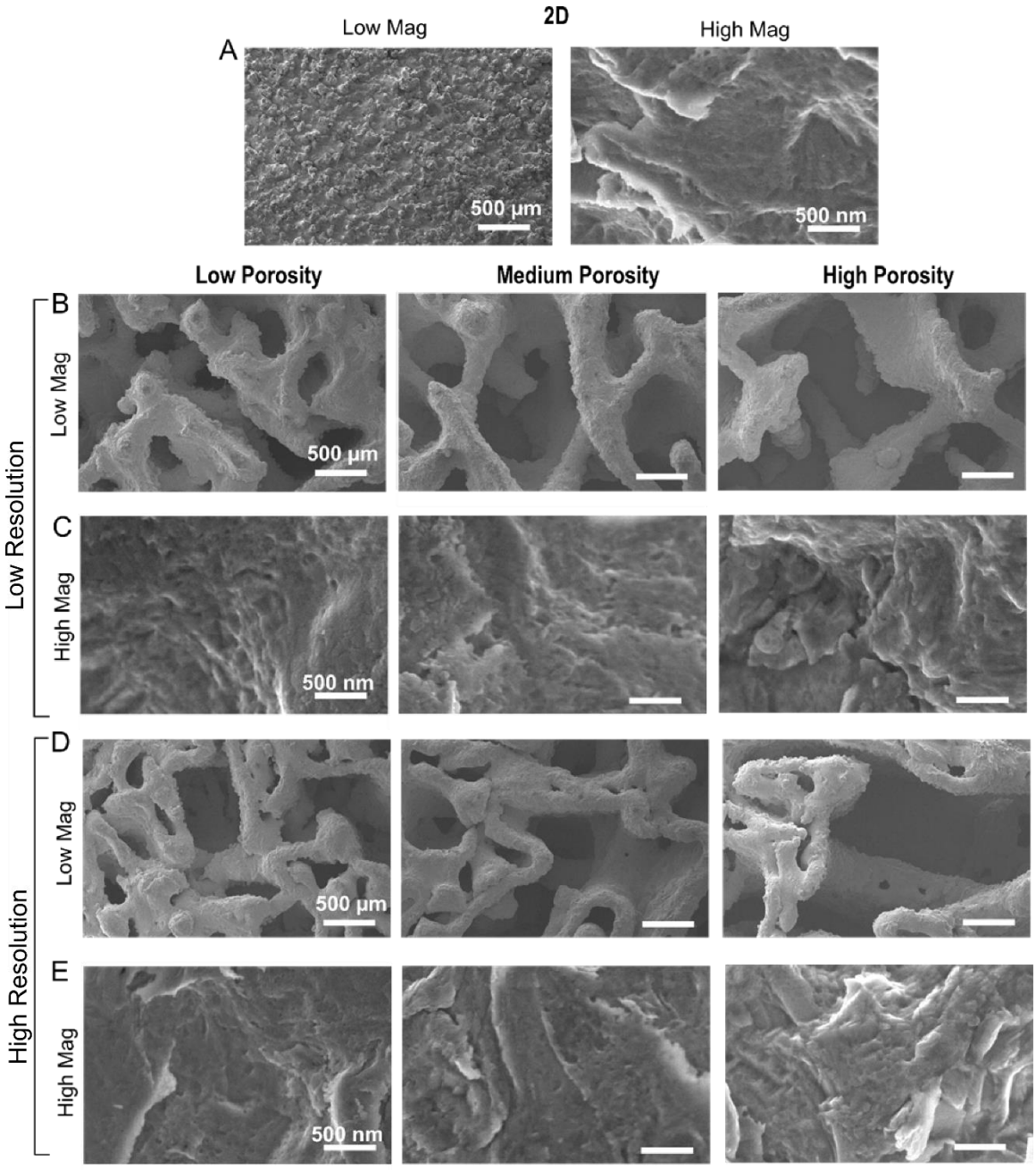

Figure 8.1. Scanning electron micrographs of 2D (A), low resolution 3D (B,C) and low resolution 3D (D,E) constructs. Low magnification (A left, B, D) shows macro-structure of constructs, while high magnification (A right, C, E) shows micro- and nano-roughness of surfaces.

Table 8.1. Porosity Parameters Obtained by MicroCT (Average ± Standard Deviation)

Group		Total Porosity (%)	SA/V Ratio	Pore Diameter (µm)	Strut thickness (µm)
Low Resolution	3DLP	41.0 ± 0.3	5.1 ± 0.1	641 ± 9	673 ± 10
	3DMP	56.6 ± 2.4 (*)	6.5 ± 0.3 (*)	785 ± 15 (*)	572 ± 18 (*)
	3DHP	76.1 ± 0.8 (*^)	8.1 ± 0.1 (*^)	1096 ± 31 (*^)	475 ± 7 (*^)
High Resolution	3DLP	52.5 ± 2.1 (*^#)	10.2 ± 0.2 (*^#)	461 ± 9 (*^#)	311 ± 6 (*^#)
	3DMP	57.3 ± 0.8 (*#&)	10.8 ± 0.3 (*^#&)	563 ± 2 (*^#&)	288 ± 8 (*^#&)
	3DHP	70.9 ± 0.4 (*^#&$)	11.5 ± 0.1 (*^#&$)	872 ± 6 (*^#&$)	267 ± 3 (*^#&$)

1 way ANOVA with Bonferroni correction, $p<0.05$. * vs. LPLR, ^ vs. MPLR, # vs. HPLR, & vs. LPHR, $ vs. MPHR

Surface roughness was evaluated by laser confocal microscopy (Figure 2C-E). Average surface roughness was not significantly different for any of the 2D or 3D construct surfaces. Peak-to-valley height values did not differ for any surfaces except for 3DHP-HR, which was higher than 3DMP-LR.

XPS showed that a majority of elements present on the surface of 2D and 3D low resolution constructs were oxygen (O), carbon (C) and titanium (Ti). The levels of these three main elements did not vary significantly between 2D and 3D constructs (Figure 3A). Differences were exhibited for lower concentration elements nitrogen (N) and sulfur (S). Contact angle analysis yielded a contact angle of 62±18º for 2D surfaces (Figure 3B).

Compression testing showed a nonlinear decrease in compressive modulus with increasing construct porosity, with different trends for changes in porosity in low and high resolution constructs (Figure 3C). Average compressive moduli of 3.6±0.083, 3.4±0.080 and 2.6±0.078 GPa decreased significantly as porosity increased for LP-LR, MP-LR and

HP-LR constructs, respectively. A similar trend was observed for LP-HR, MP-HR and HP-HR constructs with respective compressive moduli of 4.1±0.024, 3.8±0.058, and 2.4±0.15 GPa.

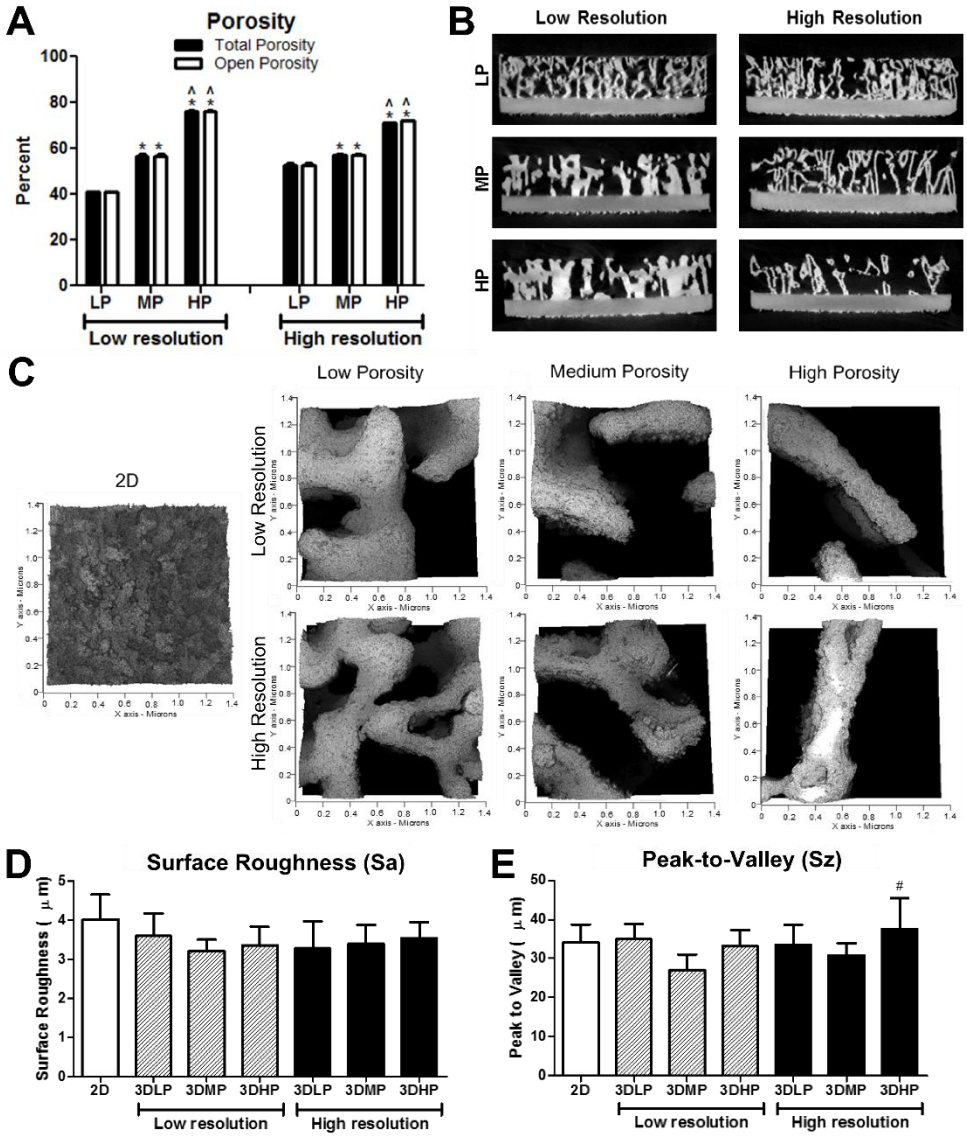

Figure 8.2. Total (black) and open (white) porosity values (A) and cross sectional views (B) of 3D constructs obtained by microCT imaging. 1 way ANOVA with Bonferroni correction, $p<0.05$, * vs. LP, ^ vs. MP within low and high resolution groups. Student's t-test comparing total and open porosity for each group was not significant. Surface roughness images (C) and average surface roughness (D) and peak-to-valley height values (E) for 2D surfaces and 3D constructs. 1 way ANOVA with Bonferroni correction, $p<0.05$, # vs. 3DMP-LR.

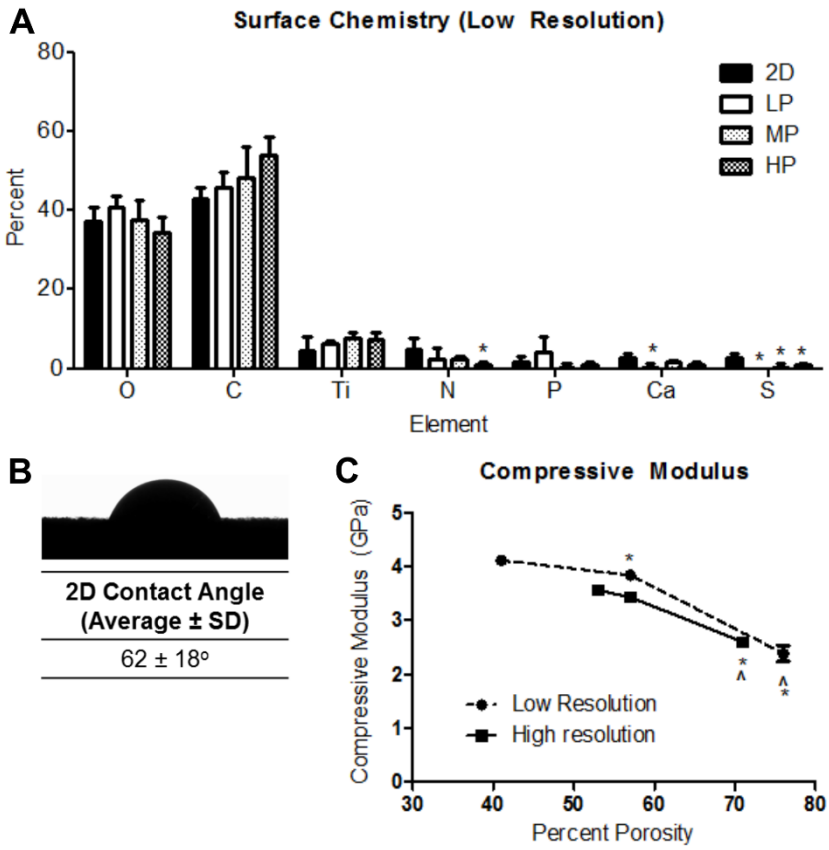

Figure 8.3. Surface chemistry of 2D and 3D high resolution constructs (A). 1 way ANOVA with Bonferroni correction, $p<0.05$, * vs. 2D. Contact angle of 2D surfaces (B). Average and standard deviation of compressive modulus values for low resolution (circles, dotted line) and high resolution (squares, solid line) 3D constructs (C). 1 way ANOVA with Bonferroni correction, $p<0.05$, * vs low porosity, ^ vs. medium porosity for each type of resolution.

Cell response

MG63 cells exhibited differential responses to 2D and low and high resolution 3D constructs. MG63 cells exhibited porosity and resolution dependent responses to 3D constructs. DNA content decreased for all 3D constructs compared to 2D surfaces (Figure 4A). DNA content was further decreased for LP-HR and MP-HR constructs compared to all LR constructs, and increased for HP-HR constructs compared to LP-HR and MP-HR constructs. OCN was elevated on HP-LR, LP-HR and MP-HR constructs compared to 2D surfaces and LP-LR constructs (Figure 4B). OCN for LP-HR and MP-HR constructs was

additionally increased compared to MP-LR and HP-LR constructs. OPG was elevated on LP-HR and LP-HR compared to 2D surfaces, and LP-HR compared to LP-LR and MP-LR constructs (Figure 4C). OPG was decreased on MP-HR and HP-HR constructs compared to LP-HR constructs. VEGF was increased on HP-LR and MP-HR constructs compared to 2D surfaces and LP-LR and MP-LR constructs, and VEGF on MP-HR was also increased compared to on HP-LR and LP-HR constructs (Figure 4D). BMP2 was increased on HP-LR, LP-HR and MP-HR constructs compared to 2D surfaces, LP-LR and MP-LR constructs, and decreased on HP-HR constructs compared to HP-LR, LP-HR and MP-HR constructs (Figure 4E).

NHOst response to 2D versus 3D constructs confirmed the MG63 cell results. Therefore, effects of porosity were only analyzed on HR constructs. NHOsts grown on high resolution constructs exhibited less robust differences to porosity on high resolution constructs compared to MG63 cells. DNA content and ALP activity was decreased on all 3D constructs compared to 2D surfaces (Figure 5A, B). Osteocalcin was significantly higher on LP-HR and MP-HR constructs compared to 2D surfaces, while OPG, VEGF and BMP4 were elevated on all 3D constructs compared to 2D surfaces (Figure 5D, E, G). BMP2 was elevated on all 3D constructs compared to 2D surfaces, but decreased on HP-LR constructs compared to MP-HR constructs (Figure 5F).

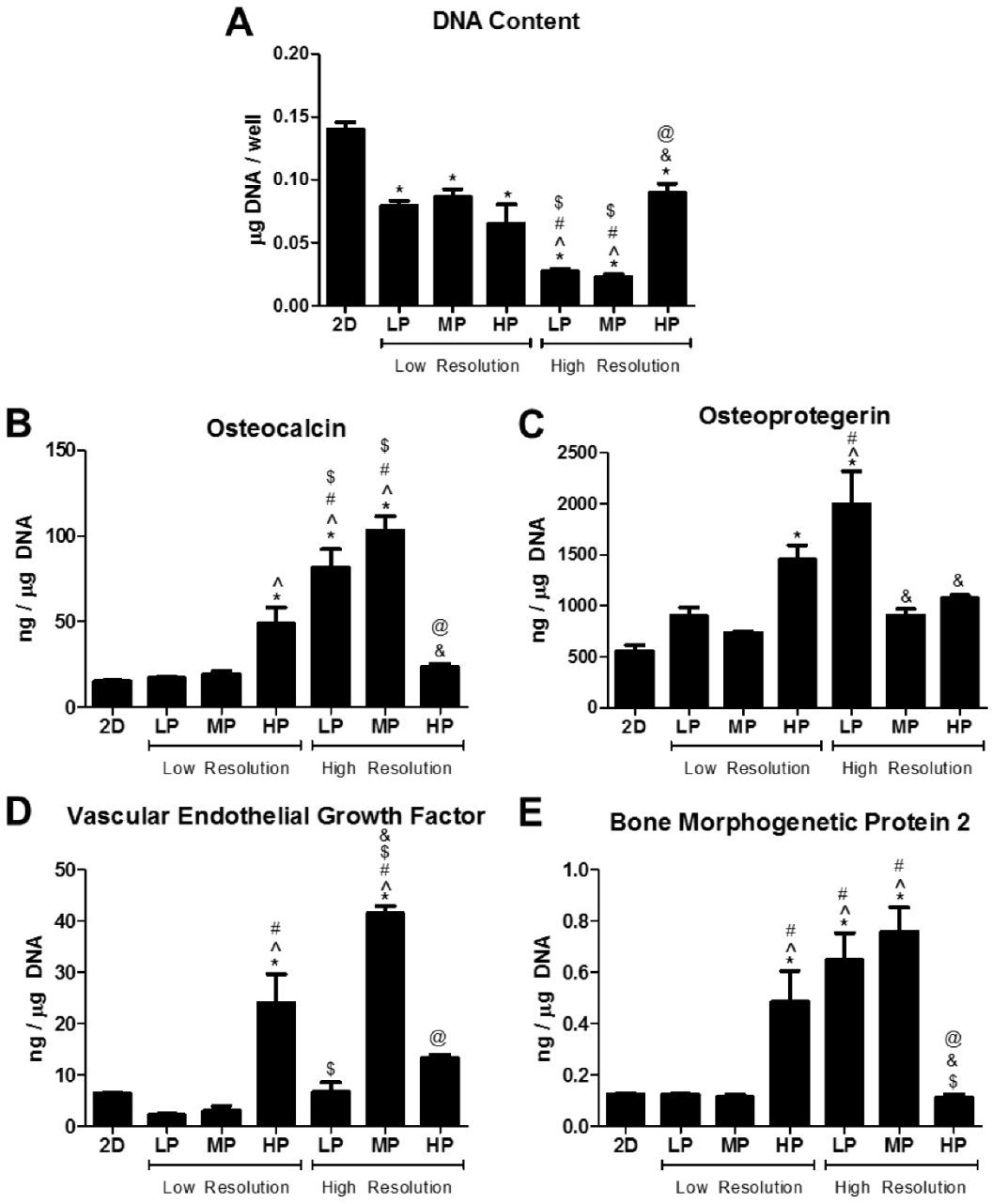

Figure 8.4. MG63 cell response to 2D and low and high resolution 3D constructs. DNA content (A), osteocalcin (B), osteoprotegerin (C), vascular endothelial growth factor (D) and bone morphogenetic protein 2 (E). 1 way ANOVA with Bonferroni correction, $p<0.05$, * vs. 2D, ^ vs. 3DLP-LR, # vs. 3DMP-LR, $ vs. 3DHP-LR, & vs. 3DLP-HR, @ vs. 3DMP-HR.

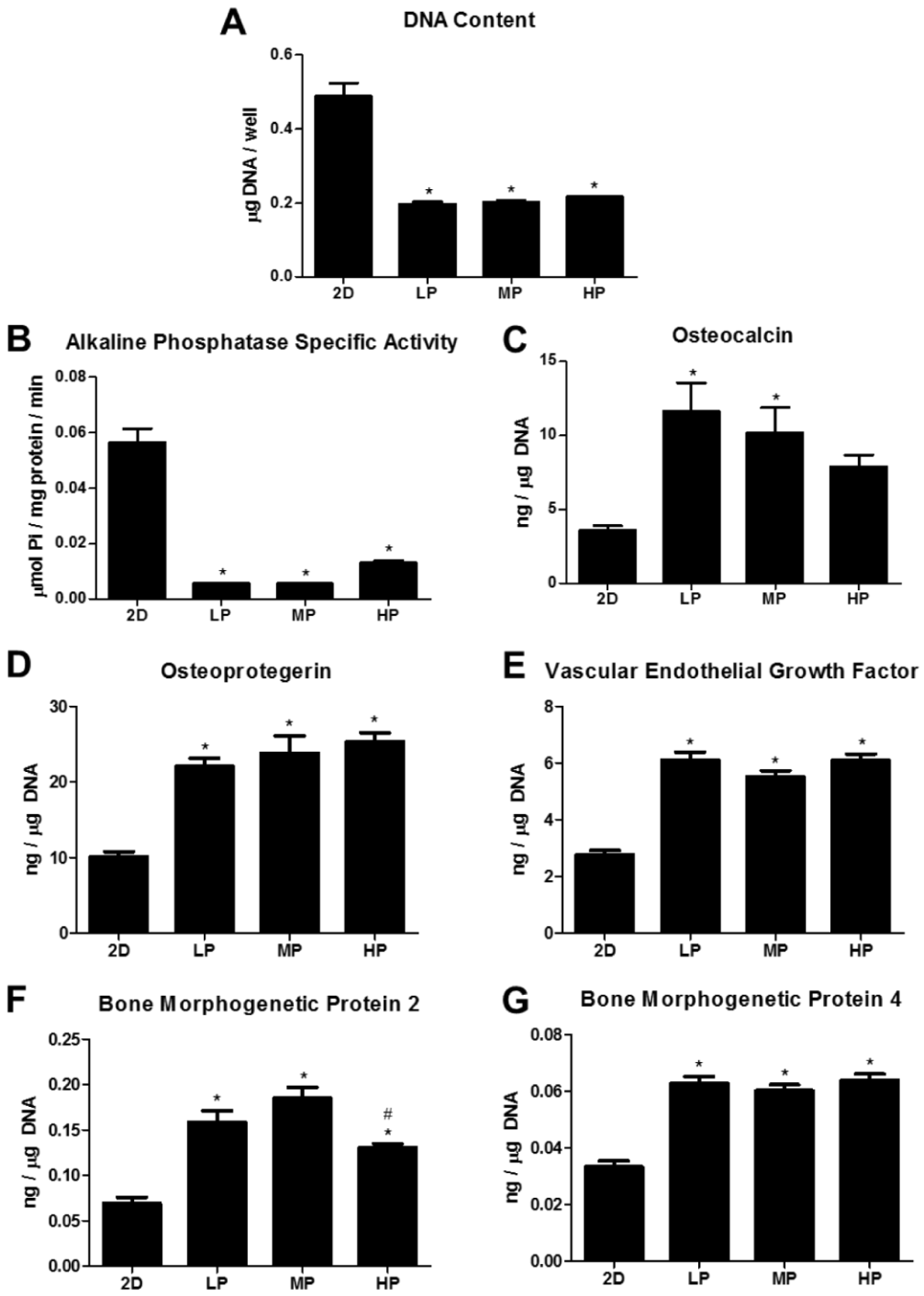

Figure 8.5. Normal human osteoblast response to 2D and high resolution 3D constructs. DNA content (A), alkaline phosphatase specific content (B), osteocalcin (C), osteoprotegerin (D), vascular endothelial growth factor (E), bone morphogenetic protein 2 (F) and bone morphogenetic protein 4 (G). 1 way ANOVA with Bonferroni correction, $p<0.05$, * vs. 2D, ^ vs. LP, # vs. MP.

8.4. Discussion

Total and open porosity of 3D constructs did not differ, indicating that all pores were interconnected. microCT results corroborated qualitative SEM observations. Although MP-LR and MP-HR constructs did not have significantly different total porosity values, MP-HR constructs had a significantly higher SA/V ratio and smaller pore diameter and smaller strut thickness compared to 3DMP-LR constructs. This could also be observed in SEM images, and was due to the incorporation of higher detail into 3DMP-HR constructs.

Although average surface roughness (Sa) did not differ for constructs, peak-to-valley heights did vary for some. This may have been due to the inability of line-of-sight surface processing techniques to evenly affect and penetrate all parts of the constructs. While acid etching may be able to penetrate the entire construct, blasting by calcium phosphate may have been limited to certain exposed sites at the surface. Cross sectional SEM images shown in a previous study corroborate this[38].

While high concentration Ti, O and C elements did not vary across constructs, the presence of low concentration elements did differ. Variations in nitrogen may be a result of time spent during manufacturing and surface processing, as nitrogen is used in the laser sintering process as well as during etching in HNO_3. The presence of Ca and P could be attributed to trace elements left behind during blasting with $CaPO_4$. Although XPS analysis was averaged across 6 different areas and multiple constructs, differences in one area may contribute to a larger standard deviation for low concentration elements.

Contact angle analysis could not be performed on 3D constructs due to the large pores. Although contact angle was performed on 2D surfaces as a proxy, the surface

roughness may have contributed to higher standard deviation in contact angle values [22]. Additional methods for wettability analysis may need to be evaluated in the future to gain a better understanding of surface energy on 3D constructs.

Optimal bone substitution materials should have similar mechanical properties to natural bone and integrate well with the surrounding tissue. In addition to their ability to osseointegrate, titanium alloys are attractive for implant materials due to their high fracture toughness and strength [310]. However, the high elastic modulus of titanium compared to that of bone can cause significant clinical problems for orthopaedic implants. Elastic moduli for bone has been reported to range from 0.5 to 30 GPa based on trabecular or cortical areas, which differs from an elastic modulus of up to 115 GPa for titanium alloys [351-353]. This difference in bulk material properties can lead to insufficient loading on bone distal to the implant, resulting in stress shielding and bone resorption [346, 352]. For hip implants in particular, reduced stem stiffness by incorporating porosity can decrease bone atrophy due to stress shielding[321].

All 3D constructs presented in this study had compressive moduli ranging from 2.4 to 4.1 GPa, which are within the lower range of moduli for bone [352]. Other studies have indicated similar mechanical properties for laser sintered porous Ti-6Al-4V[38, 354]. Differences in mechanical properties of constructs and the non-linear correlation with percent porosity can also be attributed to differences in structural parameters such as strut size and tortuosity [320, 355]. These results indicate that porosity can be tailored to alter mechanical properties for patient- and application-specific applications, with the potential to reduce stress shielding. In this study, compression testing was performed to evaluate the elastic modulus. Although tensile modulus is typically reported for materials, previous

studies have shown that compressive and tensile analysis of bone yields comparable modulus values [356]. In addition, the load-bearing nature of bone-interfacing implants makes compression testing more clinically relevant. Because compression testing was performed on constructs including a 1mm solid base, modulus values may be higher than for completely porous constructs. However, the values presented here may be more clinically relevant for solid implants coated with a porous exterior.

Various studies have shown increased osseointegration via volume of bone ingrowth and mechanical stability of porous implants compared to solid implants [350, 357, 358]. Our hope is that porosity inspired by nature would yield a better biological response than human-designed porosity. We have seen this concept to be true in previous studies of surface roughness, where osteoblasts exhibit higher factor production on acid-etched and grit blasted titanium surfaces with a more natural distribution of peaks and valleys compared to micro-patterned substrates with predefined features [142]. Other studies have shown the effectiveness of combined micro-/nano-roughness on titanium substrates, mimicking the natural hierarchical surface roughness of bone, for improving osteoblast response [9, 25]. Through characterization data, we showed that our constructs had similar surface chemistry and multi-scale roughness but differences in 3D porosity. Based on the differential biological response to our materials, we propose that osteoblast response is sensitive to and dependent upon changes in pore diameter and structure in 3D Ti-6Al-4V constructs.

Osteoblasts showed increased differentiation, maturation and local factor production on 3D constructs compared to 2D solid surfaces. In this study, we first used the MG63 cell line to screen for differences in biological response to 2D versus 3D constructs

with low and high resolution. The MG63 osteoblast-like cell line is commonly used to evaluate cell response to titanium surfaces. Although immortalized cell lines are attractive for their ease of culture and reduced biological variability, they cannot serve as a substitute for using primary cells. MG63 cells in particular, although acceptable for pilot testing of biomaterials, still exhibit increased proliferation, RUNX2 and osteocalcin gene expression and decreased alkaline phosphatase and collagen 1 gene expression compared to normal human osteoblasts [359]. Due to the clear preference of MG63 cells for HR constructs, we then chose NHOsts as a primary osteoblast to validate MG63 results to changes in porosity on the HR constructs. Although both MG63 and NHOst cells significantly favored 3D porous constructs over 2D solid surfaces, NHOsts exhibited less of a porosity-dependent response on HR constructs compared to that of MG63 cells.

This cell-dependent response to titanium surfaces has been shown previously with respect to surface roughness [22, 133]. We propose that this response is also dependent on the stage of osteoblast maturation. A heightened response to varying porosity from immature osteoblast-like MG63 cells contrasts a decreased response from NHOsts at a potentially different stage of maturation. Our results showed 6.9, 6.5 and 6.1 fold increases in OCN, VEGF and BMP2 for MG63 cells on MP-HR constructs compared to 2D controls, respectively, while NHOsts on the same constructs exhibited 2.9, 2.0 and 2.7 fold increases, respectively. We have previously observed shown that mature osteoblasts exhibit a reduced response to surface roughness as well as to 1,25-dihydroxyvitamin D3 treatment [360]. Age and sex are important considerations when evaluating response of primary cells, and have been shown to significantly affect response to titanium substrates [63, 65]. In this study, the NHOst donor was a 2 year old Caucasian male. It is possible that the young age

of this donor resulted in favorable responses to all 3D constructs regardless of porosity, and that an older or more compromised donor would show a more differential response based on porosity. Further studies on primary osteoblast response based on donor age, sex and potentially health will be necessary to understand if and how porous constructs can be tailored to certain populations.

Few studies have shown such a clear preference of osteoblasts to 3D porous Ti-6Al-4V constructs compared to 2D surfaces. Because all materials in this study were manufactured and processed in the same way to achieve similar roughness and chemistry, we propose that the 3D constructs provide a distinct structural advantage over 2D surfaces that increases osteoblast response. It is unclear what specific material parameter drives differentiation of osteoblasts on 3D constructs, if one at all. Previous studies by our lab suggest that the enhanced osteoblast response to surface roughness and 3D substrate morphology is dependent upon the α2β1 integrin, a surface receptor for collagen [37, 56]. Indeed, changes in porosity may lead to variations in cell attachment and orientation, affecting extracellular matrix production and mineralization [361]. Characterization by microCT shows that total porosity, surface area to volume ratio, pore diameter and strut size all vary based on construct design and resolution. However, due to the trabeculae inspired design of porosity, each of these parameters may change depending on the exact location of characterization. In addition, it is unclear how interconnected porosity affects cell-cell communication. Not only can open porosity facilitate paracrine signaling, but parameters such as size, shape and tortuosity have also been shown to influence the shear stress on cells [362]. Although mechanical transduction is not well understood in porous constructs, it is well known that changes in the mechanical stimulus of a cell or its substrate

can lead to downstream effects [363]. In fact, it is suggested that fluid forces contribute more to osteoblast response than strain from the substrate or extracellular matrix [364]. While our characterization provides information on the average porosity parameters for these constructs, cells may experience a different micro-scale environment based on their location within the construct. Future studies may examine location-specific biological response to understand how response within individual pores contributes to overall biological response.

8.5. Conclusion

Porous Ti-6Al-4V implants have great potential in the dental and orthopaedic fields. With additive manufacturing, implant porosity can be customized for the patient. In this study, laser sintered constructs were manufactured with varying porosity and resolution inspired by human trabecular bone structure. Biological response by human osteoblasts showed increased differentiation, maturation and local factor production on 3D compared to 2D solid constructs. Osteoblasts exhibited cell-type dependent responses to construct porosity. MG63 cells produced higher local factor production on HR compared to LR constructs, which incorporated finer detail from trabecular bone. NHOst cells also exhibited an enhanced response to 3D porous constructs compared to 2D solids surfaces, though the response to changes in porosity was less evident than that of MG63 cells. These results suggest that incorporating trabecular-inspired porosity into bone-interfacing implants may enhance cellular response and implant osseointegration.

CHAPTER 9

LASER SINTERED CONSTRUCTS WITH BIO-INSPIRED POROSITY AND SURFACE MICRO/NANO ROUGHNESS ENHANCE MESENCHYMAL STEM CELL DIFFERENTIATION AND MATRIX MINERALIZATION IN VITRO

In [Cheng A, Cohen DJ, Boyan BD and Schwartz Z. Laser sintered constructs with bio-inspired porosity and surface micro/nano roughness enhance mesenchymal stem cell differentiation and matrix mineralization in vitro. Calcified Tissue International. 2016. In press]

9.1. Introduction

Additive manufacturing of metals, the industrial term for "3D printing," has been credited with huge potential for the future of orthopaedic and dental implants; implants can be customized and fabricated to be porous for mechanical and biological fixation. The use of additive manufacturing to develop materials with non-traditional architecture can reduce material waste with potential financial savings [365, 366]. Large animal studies point toward the success of these implants for clinical use [341, 367]. A recent study by researchers in Italy showed a 97.4% 3-year implant clinical survival rate for direct metal laser sintered dental implants used to support maxillary overdentures, the first long-term clinical study of its kind [368]. Varying porosity of three dimensional (3D) implants also offers the ability to increase surface area for bone-to-implant contact, promote blood vessel formation and tailor a mechanical modulus that more closely mimics bone than conventional solid implants [175, 369-371].

Our lab previously manufactured 3D titanium-aluminum-vanadium (Ti-6Al-4V) constructs with porosity approximating that of human trabecular bone, with additional surface processing to create micro- and nano- surface roughness [38]. Surface roughness at the micro- and nano-scale has been shown to positively influence osteoblast differentiation and clinical responses to titanium and its alloys [9, 34, 133, 135, 142, 372]. Until recently, however, biological responses to surface treatments were evaluated in vitro on two-dimensional implant surfaces. We reported that MG63 osteoblast-like cells responded in a porosity-dependent manner on 3D constructs with hierarchical surface roughness, with changes in factors promoting osteoblast differentiation, maturation and local factor production [38].

While osteoblasts are necessary for bone formation, they are only one of many cell types present during bone regeneration in response to implant placement. Mesenchymal stem cells (MSCs) are multipotent cells that have the ability to differentiate into various cells, including osteoblasts, chondrocytes and adipocytes [373]. More importantly, they are one of the first cells to arrive at the implant site, where they secrete factors that can influence cell recruitment, differentiation and the inflammatory micro-environment [374, 375]. Studies from our lab have also shown that MSC response can be altered on titanium surfaces with varying micro- and nano-roughness [329]. Moreover, MSCs can differentiate into osteoblasts on the appropriate surface without the need for exogenous factors, such as bone morphogenetic protein 2 (BMP2), dexamethasone, or beta-glycerol phosphate [21, 22, 65, 133].

Few studies have examined the response of human marrow derived MSCs to porous titanium constructs, and even fewer have taken into consideration the variable of surface

roughness [376, 377]. Yavari *et al.* examined the effect of varying surface roughness of additively manufactured porous constructs on the response of human periosteum-derived cells, revealing differential *in vitro* and *in vivo* bone forming capabilities in response to different surface treatments [118]. Thus, both surface roughness and porosity can play an important role in MSC response and ultimately bone growth into these constructs, and are important parameters to be considered when designing orthopaedic and dental implant materials.

In this study, we considered MSC response to our previously reported additively manufactured Ti-6Al-4V constructs with varying porosity and combined micro-/nano-surface roughness. These constructs were designed with porosity ranging from 52.5% to 70.9% based on a computerized tomographic (CT) template of human trabecular bone [201]. We examined the effects of porosity and 3D construct environment on cell response, and analyzed osteogenic factor production after 3, 6, and 9 days, and mineralization after 8 weeks to test the following hypotheses. (i) MSCs can be directed more effectively toward osteoblastic differentiation on 3D porous constructs than on 2D surfaces. (ii) The ability of MSCs on these 3D porous constructs to produce and respond to osteogenic factors is sustained longer than on 2D surfaces. (iii) The MSCs on 3D porous constructs are able to mineralize their extracellular matrix.

9.2. Materials and Methods

Manufacturing

Constructs were laser sintered (EOS, Krailling, Germany) from Ti-6Al-4V powder and surface treated as described previously and with a higher level of detail ("high

resolution" constructs) captured from original bone CT scans than first generation "low resolution" constructs according to software capability. In short, constructs were manufactured as 15mm diameter disks with a total height of 5mm (including a 1mm solid base) in low, medium and high porosity by overlaying the software template 12, 24 or 36 times over itself to achieve the 52.5% (LP), 57.3% (MP) and 70.9% (HP) porosity, respectively [201]. 3D construct pore diameters ranged from 461 to 872μm and strut thicknesses ranged from 267 to 311μm. 2D solid disks were manufactured 15mm in diameter and 1mm height to serve as a control in materials characterization and biological evaluation. After laser sintering, all constructs were blasted with calcium phosphate particles using a proprietary method and acid etched in 0.3N HNO_3, then in a 1:1 solution of 20 g/L NaOH and H_2O_2 and finally in 65% HNO_3. This treatment resulted in micro- and nano-scale surface roughness, with minimal impact on surface chemistry (<3% Ca and <4% P detected by x-ray photoelectron spectroscopy analysis) [201]. All constructs were sonicated in ultrapure distilled water, after which they were dried and sterilized with gamma radiation prior to characterization and cell culture.

Materials Characterization

Scanning electron microscopy

An AURIGA SEM (Zeiss, Oberkochen, Germany) was used to evaluate surface topography of constructs. The In-Lens detector was used with an accelerating voltage of 4kV, working distance of 4mm and aperture of 30μm. Images were captured at varying magnifications to observe macro-, micro- and nano- features of constructs.

Contact Angle

Surface wettability was examined on 2D disks using sessile drop contact angle. A 4µL drop of distilled water was placed on five predetermined locations per disk, with two disks analyzed (n=10, where each drop is n=1) [22, 378]. The average of left and right contact angles of each drop were analyzed over 4 measurements taken every 5 seconds for 20 seconds after drop deposition.

Cell culture

Human mesenchymal stem cells (hMSCs) (Donor 1F4287, 22 year old black male) were obtained from Lonza (Walkersville, MD) and were cultured in MSC growth medium (Lonza) in T75 flasks until confluent, then plated on 2D surfaces and LP, MP and HP constructs at a density of $6x10^4$ cells/construct. For confluence analysis, medium was replaced 24 hours after plating and at confluence (approximately the third day). For time course analysis, only TCPS (tissue culture polystyrene), 2D disks and MP constructs were plated with cells. Medium was replaced 24 hours after plating, then every 48 hours or at 3, 6 and 9 days. Medium was aliquotted for analysis 24 hours after final medium exchange. Cells were rinsed twice with 1xPBS (EMD Millipore, Billerica MA) and lysed by overnight storage at -80°C in 0.05% Triton-X 100 (Sigma Aldrich, St. Louis, MO), followed by sonication for 10 seconds per sample. Whole cell lysates were analyzed for DNA content, alkaline phosphatase specific activity (ALP) and total protein. DNA content was analyzed by a fluorescent assay (Quant-iT DNA Assay kit, Life Technologies, Carlsbad, CA). ALP was determined by cleavage of para-nitrophenylphosphate to para-nitrophenol at pH 10.2 after 45 minutes. ALP was normalized to total protein content, which was determined using a BCA Protein Assay kit (ThermoFisher Scientific). Osteocalcin (OCN, Alfa Aesar, Ward

Hill, MA), osteoprotegerin (OPG, R&D Systems, Minneapolis, MN), vascular endothelial growth factor-A (VEGF, R&D Systems), bone morphogenetic protein 2 (PeproTech, Rocky Hill, NJ) and BMP4 (R&D Systems) were analyzed by enzyme-linked immunosorbent assays (ELISA) using harvested conditioned medium. ELISA results were normalized to DNA content.

Extracellular Matrix Mineralization

Sample preparation and cell seeding techniques were adapted from previous studies with minor alterations [379, 380]. Only MP constructs were used in this study, in three experimental groups: osteogenic medium (OM group); OM plus BMP2 (BMP2 group); and COL1-coated constructs treated with OM plus BMP2 (COL1 group) as described below.

To coat MP constructs with type I collagen, rat tail collagen type I (>95% purity, Sigma Aldrich) was diluted to 1.5 mg/ml in 0.05% acetic acid and neutralized with 1M sodium bicarbonate under sterile conditions. 1mL of collagen solution was pipetted onto disks in the COL1 group and placed at -80^{o}C for 1 hour, then lyophilized overnight before being placed into 24-well plates. Remaining disks for each group were also placed into wells.

hMSCs were cultured in MSC growth medium until confluent, and plated on constructs at a density of $2x10^{6}$ cells/200µL and allowed to attach for 1 hour. 1.8mL of additional media were added slowly to the wells. Growth medium was changed after 24 hours, and then every 48 hours for 6 days. On day 7 and until harvest, all groups were fed with OM (α-MEM [Life Technologies, Carlsbad, CA] supplemented with 16% fetal bovine serum [Life Technologies], 1% penicillin–streptomycin [Life Technologies], 50 µg/mL

ascorbic acid 2-phosphate [Sigma Aldrich], 50 ng/mL thyroxine [Sigma Aldrich], 6 mM beta-glycerophosphate [Sigma Aldrich] and 1 nM dexamethasone [Sigma Aldrich]). The BMP2 group was supplemented with an additional 50 ng/ml human recombinant BMP2. Media were replaced three times weekly for the duration of the experiment. A set of control MP constructs were cultured without any cells and media were changed with the same frequency as all other groups. Each group contained an n of 6 independent cultures.

After 8 weeks of culture, media were aspirated and constructs were rinsed twice in 1xPBS and then were fixed overnight in 4% paraformaldehyde for analysis. Constructs were dehydrated in a series of ethanol concentrations for at least 2 hours each: 15%, 30%, and 45%, then for at least 1 hour each: 60%, 75%, 90% and twice in 100%. Constructs were exchanged in 1:1 100% ethanol to hexamethyldisilazane (HMDS, Sigma Aldrich) for 30 minutes in a fume hood, then immersed fully in 100% HMDS twice for one hour. Constructs were further dried in a vacuum dessicator for 24 hours before characterization.

Rabbit tibial bone was used as a control for EDX analysis. A New Zealand white male rabbit approximately 11-14 weeks of age was euthanized was ear vein injection of sodium pentobarbital. The tibia was harvested and then was stored in 10% formalin overnight before dehydrating for SEM.

In Vivo Primary Bone Formation

Mineralization of cells on constructs was compared to primary bone formation in femoral bone marrow and on the surface of calvarial implants in a Sprague-Dawley rat. Bone marrow ablation was performed in the femoral bone cavity of a 10-week old male rat under an Institutional Care and Use Committee approved protocol at Virginia Commonwealth University, as described previously [381]. Rectangular calvarial implants

were manufactured 6.5mm by 3.5mm and 2mm using the medium porosity template. The rat was anesthetized and the periosteum was elevated to expose the calvarium. Pilot holes were drilled to allow stem cell infiltration into the implant. After implant placement, the periosteum was closed with a purse-string suture, and the skin was sutured closed. The rat was euthanized by CO_2 after 7 days to observe primary bone formation at both sites. The femur and implant were isolated and fixed in 10% formalin, then dehydrated in a series of increasing ethanol concentrations and HMDS. Samples were sputter coated with platinum prior to imaging.

Characterization of Mineralization

Micro-computed Tomography (MicroCT)

Constructs were analyzed with microCT (Bruker SkyScan 1173) before culture and after harvest to quantify construct porosity and volume of mineralization. Scans were performed with a Hamamatsu 130/300 x-ray source at a source voltage of 130 kV, source current of 60µA, exposure time of 400ms pixel size of 20µm (8e-6mm^3 voxel size) and 0.25mm brass filter. Scans were taken over 360 degrees with a rotation step of 0.2 degrees and averaging across 10 frames. NRecon software version 1.6.9.8 was used to analyze porosity and volume.

X-ray Diffraction

X-ray diffraction scans were performed on the Xpert Pro Panalytical system with a Cu Kα radiation source. A continuous single scan was performed with a 2θ angular range of 20-60 degrees with a step size of 0.026, 400 seconds per step and scan speed of 0.017 degrees per second. A soller slit of 0.04 radians was used with a ½ degree fixed divergence slit and 10mm fixed mask. Reference JCPDS 74-0565 was used as a control for

hydroxyapatite, and JCPDS 44-1294 as a control for alpha titanium (International Centre for Diffraction Data, Newton Square, PA, USA) .

Laser Confocal Microscopy (LCM)

Constructs were stained with OsteoImage Mineralization (Lonza) fluorescent stain according to assay instructions. Constructs were imaged on a Zeiss LSM 710 laser confocal system at 10x magnification with an EC Plan – Neofluar 10x/0.3 M2.7 aperture at 488nm laser to detect green fluorescence. Z-stacks captured the first 550µm of constructs using a step size of 5µm over a 850x850 µm field of view. Imaging parameters also included a pixel size of 0.83 µm, average of 1, bit depth of 8 and pixel dwell time of 0.64µs. 3D images were generated from superimposed z-stacks for analysis. ImageJ was used to analyze penetration of mineralization into constructs. A cross sectional area of constructs was analyzed using the "Plot Profile" function to quantify amount of mineralization at different depths.

Scanning Electron Microscopy (SEM)

Constructs and animal samples were prepared for SEM analysis by dehydrating in a series of ethanol concentrations: 15%, 30%, 45% for at least 2 hours each, then 60%, 75%, 90% and 100% twice for at least 1 hour each. Samples were then exchanged in a 1:1 ratio of hexamethyldisilazane (HMDS) and 100% ethanol for 30 minutes, then twice in 100% HMDS for 1 hour before drying overnight in a vacuum dessicator. All samples used for SEM analysis were sputter coated with platinum for 90 seconds at 30 mA using the Denton Vacuum Desk V system (Denton Vacuum, Moorestown, NJ). The Zeiss AURIGA system (Zeiss) was used to image constructs at a working distance of 4mm with an accelerating voltage of 4kV.

Energy Dispersive X-ray (EDX)

EDX analysis was conducted at 1kx on the Zeiss AURIGA SEM with an accelerating voltage of 20kx, working distance of 10.5mm, aperture of 60um at high current, SE2 detector, amp time of 3.84 seconds, 50 second collection time and dead time of approximately 30%. Analysis was performed by TEAM (Texture and Elemental Analysis Microscopy) software with a 30 second pre-scan survey. Maps were taken with 100x256 pixel and standard resolution, with each scan taking approximately 6 minutes. Ca/P ratios were analyzed from overlaid elemental analysis of maps. Samples for EDX were not previously sputter coated. The femur from a New Zealand rabbit was used to indicate a typical bone sample. A 3DMP construct immersed in OM medium without cells for 8 weeks was used as a control.

ICP-OES Analysis

ICP-OES analysis was performed on Vista-MPX CCD Simultaneous ICP-OES system using Varian ICP-Expert Version 4.1.0 software. 10 standards of Ca and P diluted in 2% HNO_3 ranging from 0 to 500ppm were fit to a second order polynomial using Graphpad Prism software, and sample values were interpolated. Constructs were decalcified overnight in 2mL 0.1N HCl and diluted to 15mL with 2% HNO_3 for analysis.

Statistics

One way analysis of variance (ANOVA) with a Bonferroni post-correction was used to determine significance across groups. A p value of less than 0.05 indicated a statistical significance.

9.3. Results

Material Characterization

Materials were characterized after laser sintering and surface processing to examine the macro-, micro- and nano- features. SEM micrographs show differing macro-structure of 2D control substrates and 3D constructs possessing a trabeculae-inspired porosity (Figure 9.1, top panel). Surface processing resulted in a fine nano-roughness that was distributed homogeneously across micro-rough surfaces after blasting (Figure 9.1, bottom panel). Contact angle of 2D surfaces was 60±6 degrees, indicating a relatively hydrophilic surface.

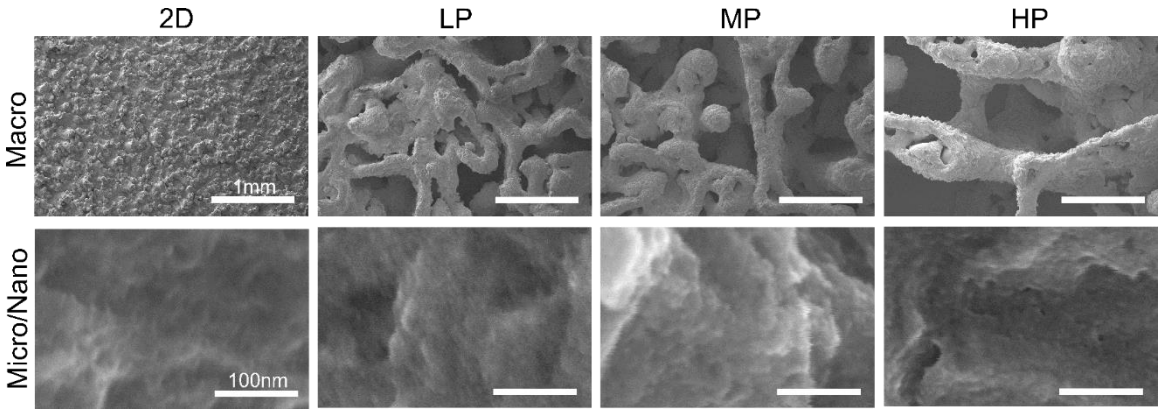

Figure 9.1. SEM images showing macro-scale and micro-/nano-scale roughness of 2D surfaces and LP, MP and HP constructs

Cell Response

hMSCs were analyzed after confluence (which occurred approximately 3 days after plating), or after time (3, 6 or 9 days). 24 hours after confluence, hMSCs exhibited significantly lower DNA content on all 3D constructs compared to TCPS and 2D sintered solid control disks (Figure 9.2a). Alkaline phosphatase specific activity (ALP), an early marker of osteoblast differentiation, was significantly reduced on 2D sintered disks compared to TCPS, and reduced on all 3D constructs compared to both TCPS and 2D surfaces (Figure 9.2b). Osteocalcin, a later marker of osteoblast differentiation, was increased on all 3D constructs compared to TCPS, LP constructs compared to 2D surfaces, and decreased on MP and HP constructs compared to LP constructs (Figure 9.2c). OPG

was significantly increased on HP constructs compared to TCPS, 2D and LP constructs (Figure 9.2d). VEGF was increased on all 3D constructs compared to TCPS and 2D controls (Figure 9.2e). Although the levels of BMP2 were increased on 2D and 3D constructs compared to TCPS, this difference was not statistically significant (Figure 9.2f). BMP4 was significantly increased on all 3D constructs compared to TCPS and on MP and HP constructs compared to 2D sintered controls (Figure 9.2g).

Time course studies showed that the effect of this trabecular 3D construct environment could be sustained over 9 days. DNA content was decreased on 2D and MP constructs compared to TCPS, and MP was decreased on MP compared to 2D constructs after 3 days (Figure 9.3a). The same trend was observed after 6 days. After 9 days, DNA content was reduced on MP constructs compared to TCPS and 2D controls only. ALP specific activity was reduced on 2D and MP constructs compared to TCPS, and MP constructs compared to 2D sintered controls after 3 days (Figure 9.3b). After 6 days, MP had significantly lower ALP specific activity than TCPS and 2D controls. After 9 days, ALP specific activity was increased on 2D compared to on TCPS, and was decreased on MP constructs compared to both TCPS and 2D controls. OCN was increased on MP constructs compared to both TCPS and 2D controls after 3 days and 9 days. At 6 days, OCN was higher on both 2D and MP constructs compared to TCPS, and MP constructs compared to 2D controls (Figure 9.3c). OPG was not significantly different after 3 or 6 days, but was elevated on MP constructs compared to 2D controls on day 9 (Figure 9.3d). VEGF was increased on 2D and MP compared to TCPS, and MP compared to 2D for 3

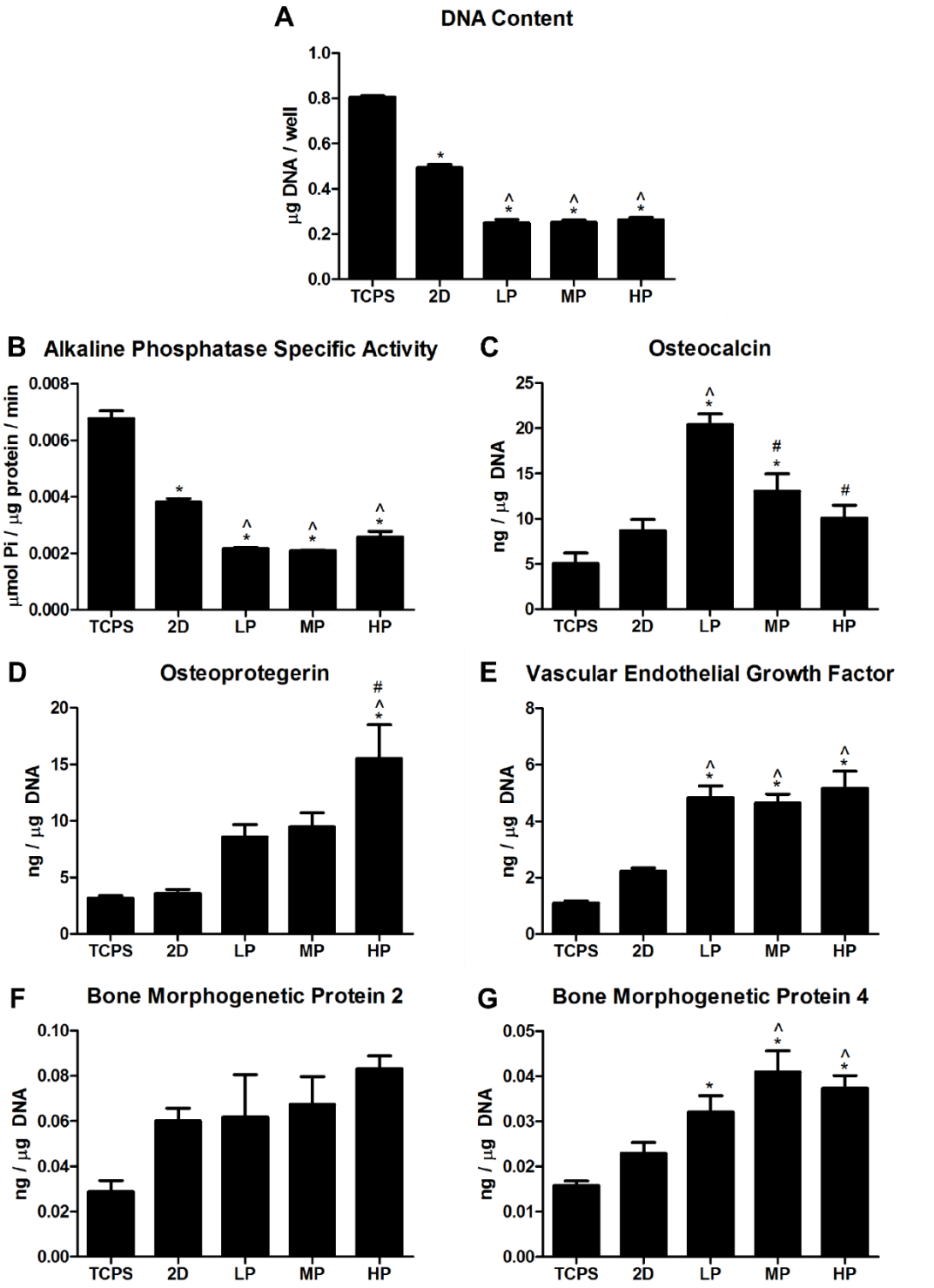

Figure 9.2. hMSC response to TCPS, 2D surfaces, and LP, MP and HP constructs at confluence (A). DNA content (B), alkaline phosphatase specific activity (B), osteocalcin (C), steoprotegerin (D), vascular endothelial growth factor (E), bone morphogenetic protein 2 (F) and bone morphogenetic protein 4 (G). 1 way ANOVA with Bonferroni correction, $p<0.05$, * vs. TCPS, ^ vs. 2D, # vs. LP, $ vs. MP

6, and 9 days (Figure 9.3e). BMP2 was increased on 2D, MP constructs compared to TCPS, and MP compared to 2D after 3 days (Figure 9.3f). No differences were observed for BMP2 at 6 days, and at 9 days BMP2 was increased on MP constructs compared to both TCPS and 2D. BMP4 was increased on 2D and MP constructs on day 3 compared to on TCPS (Figure 9.3g). On days 6 and 9, only MP constructs had increased BMP4 compared to both TCPS and 2D controls.

Extracellular Matrix Mineralization

MicroCT analysis showed an increase in overall construct volume for BMP2 and COL1 constructs compared to control disks prior to culture, but the difference was not statistically significant (Figure 9.4a). XRD showed peaks corresponding to the hydroxyapatite reference for COL1 constructs, but only peaks corresponding to the titanium reference for OM and BMP2 constructs (Figure 9.4b). OsteoImage qualitatively showed that most mineralization occurred on surfaces of COL1 group constructs (Figure 5a). However, cross sectional images showed that this mineral was constrained to only the surface of the constructs, without penetrating into the pores (Figure 9.5b, c). By contrast, semi-quantitative observations showed mineral formation deeper into the construct pores for constructs in both OM and BMP2 groups.

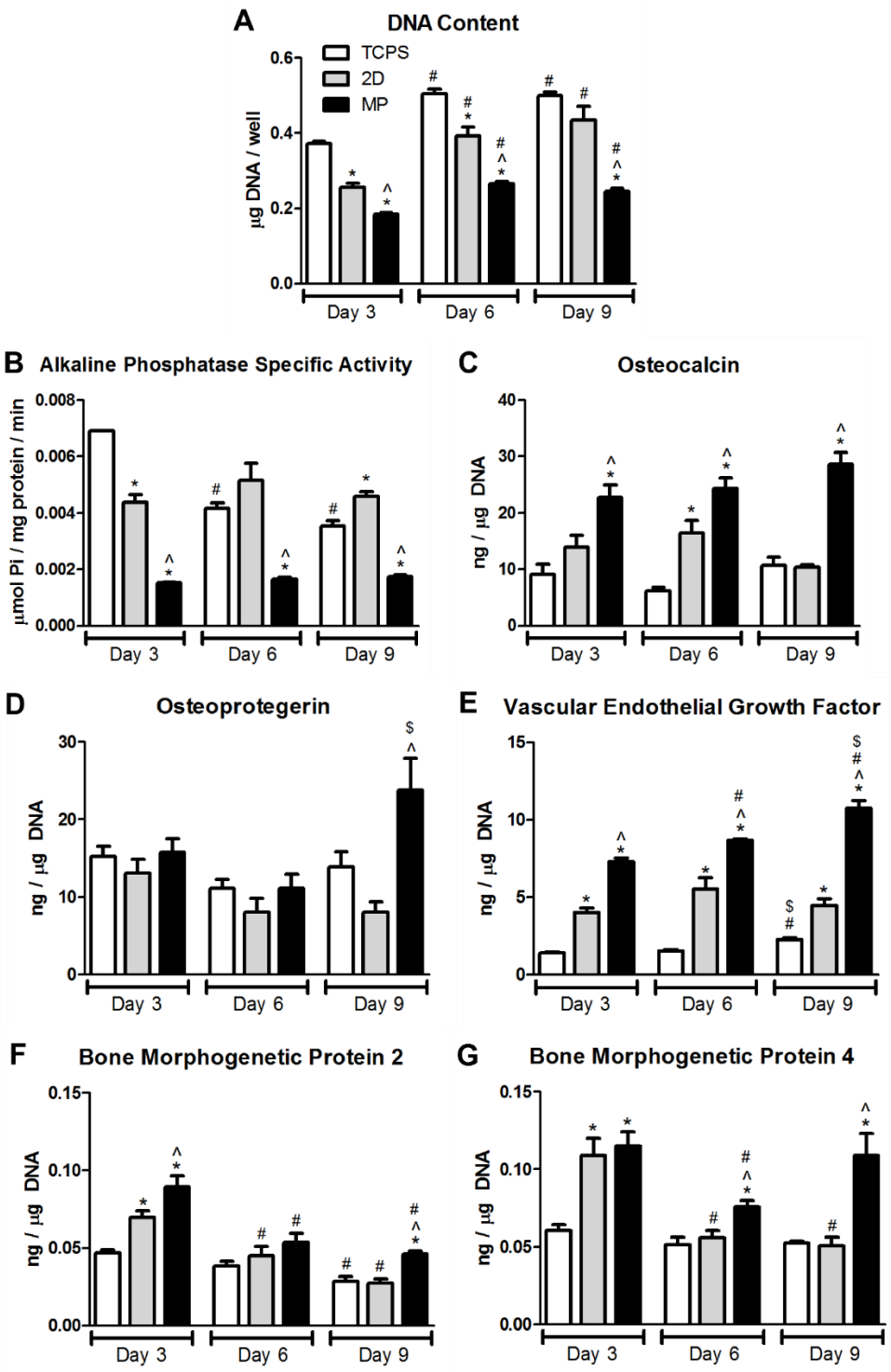

Figure 9.3. hMSC response on TCPS (white bar), 2D surfaces (gray bar) and MP constructs (black bar) 3, 6 and 9 days after plating. DNA content (A), alkaline phosphatase specific activity (B), osteocalcin (C), osteoprotegerin (D), vascular endothelial growth factor (E), bone morphogenetic protein 2 (F) and bone morphogenetic protein 4 (G). 1 way ANOVA with Bonferroni correction, $p<0.05$. Comparisons by day, * vs. TCPS, ^ vs. 2D. Comparisons by group, # vs. Day 3, $ vs. Day 6

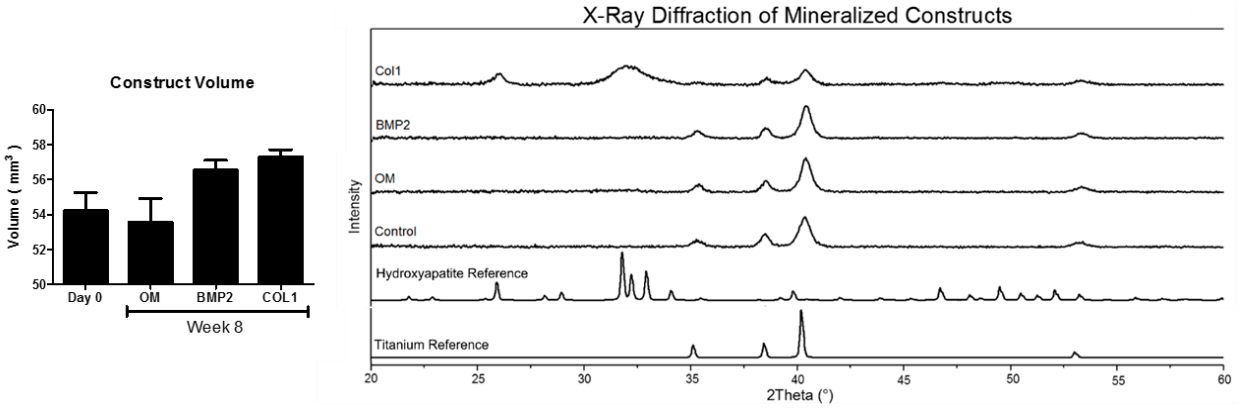

Figure 9.4. Total construct volume obtained by microCT of constructs before culture (Day 0) and after 8 weeks of culture for OM, BMP2 and COL1 groups (A). 1-way ANOVA with Bonferroni correction, $p<0.05$, no significance. XRD results of constructs after 8 weeks of culture (B). Hydroxyapatite reference was taken from JCPDS 74-0565 and titanium reference was taken from JCPDS 44-1294.

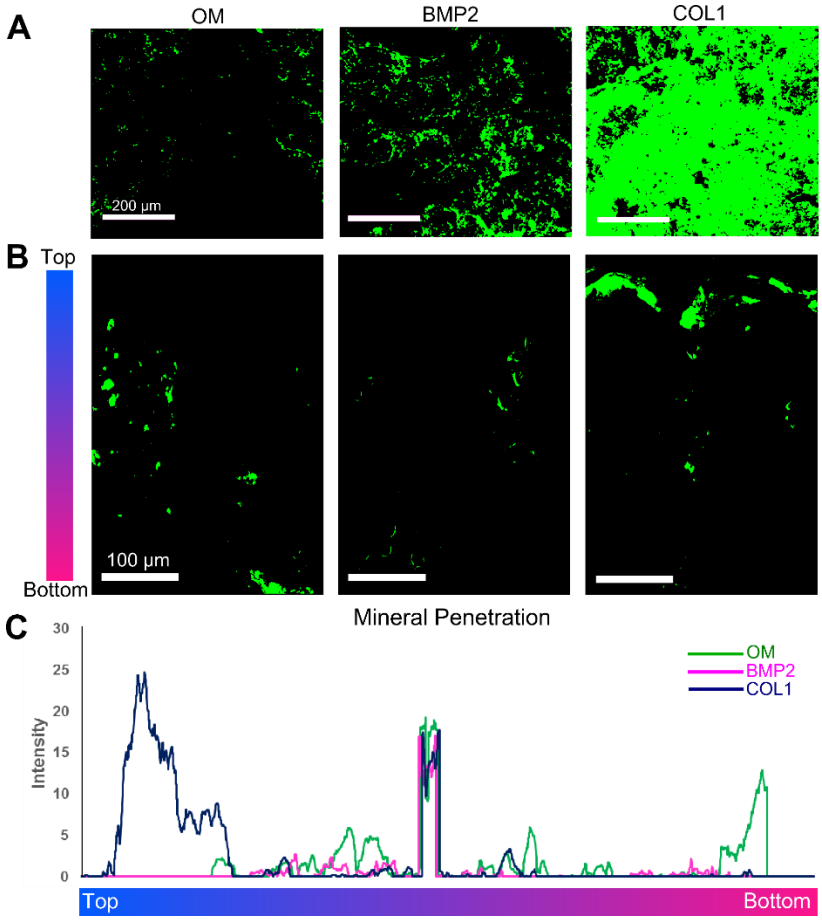

Figure 9.5. Top-down view of OsteoImage staining of hydroxyapatite on OM, BMP2 and COL1 constructs (A). Cross-sectional view of OsteoImage staining of hydroxyapatite on OM, BMP2 and COL1 constructs (B). Quantification of mineral penetration into constructs based on cross-sectional images (C)

EDX analysis of mineralized areas revealed the presence of C, O, P and Ca (Figure 9.6). The Ca:P ratio quantified on the surface of constructs by EDX was similar for OM and BMP2 constructs, while COL1 constructs exhibited a lower ratio. Ca:P atomic ratios were 1.7±0.1 for OM constructs, 1.5±0.2 for BMP2 constructs, and 1.4±0.1 for COL1 constructs, compared to theoretical Ca:P ratio values for crystalline hydroxyapatite of 1.67 (Table 9.1).

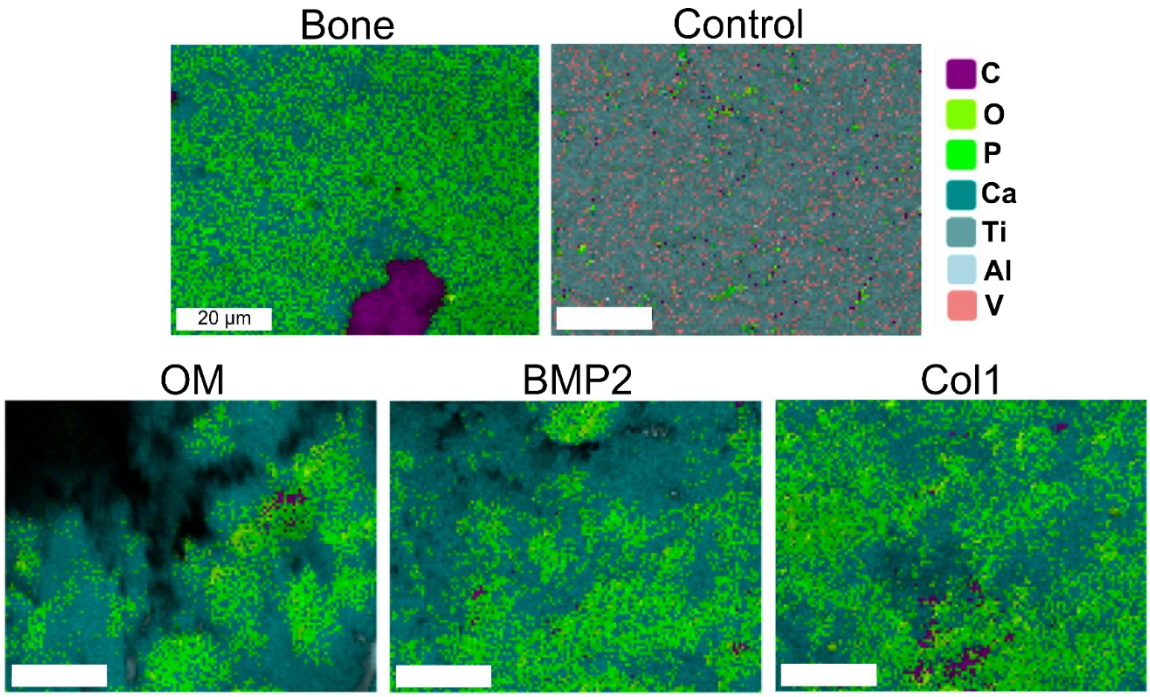

Figure 9.6. EDX chemical mapping of New Zealand rabbit femur (bone), control construct cultured in OM for 8 weeks without cells (control), OM, BMP2 and COL1 constructs cultured for 8 weeks

Table 9.1. EDX Quantification of Ca:P Atomic Ratio for 3D cultures

Group	Ca:P Atomic Ratio
OM	1.7 ± 0.1
BMP2	1.5 ± 0.2
COL1	1.4 ± 0.1

ICP-OES was also used to quantify Ca:P weight ratios after decalcifying constructs, and revealed ratios of 1.27 for OM constructs, 1.37 for BMP2 constructs and 1.43 for COL1 constructs in comparison to a theoretical Ca:P weight ratio value of 2.1 (Table 9.2).

Table 9.2. ICP-OES Quantification of Ca:P Weight Ratio for 3D cultures

Group	Ca (ug/ul)	P (ug/ul)	Ca:P Weight Ratio
OM	32.5	25.7	1.27
BMP2	53.2	38.8	1.37
COL1	68.6	47.9	1.43

Scanning electron micrographs showed the presence of nodules on constructs from all groups except the control group without cells (Figure 9.7a-c). COL1 constructs qualitatively showed the most mineral formation, and high magnification of mineral nodules revealed similar structure across constructs (Figure 9.7a-c, lower panel). This was in contrast to control constructs that underwent the same culturing conditions without the presence of cells (Figure 9.7d).

We observed structures *in vivo* on a construct placed subperiosteally on a rat calvarium at 7 days that were morphologically similar to the nodules present in the mineralized constructs at high magnification (Figure 9.7e, f, bottom panel). Comparable structures were present within the ablated femur.

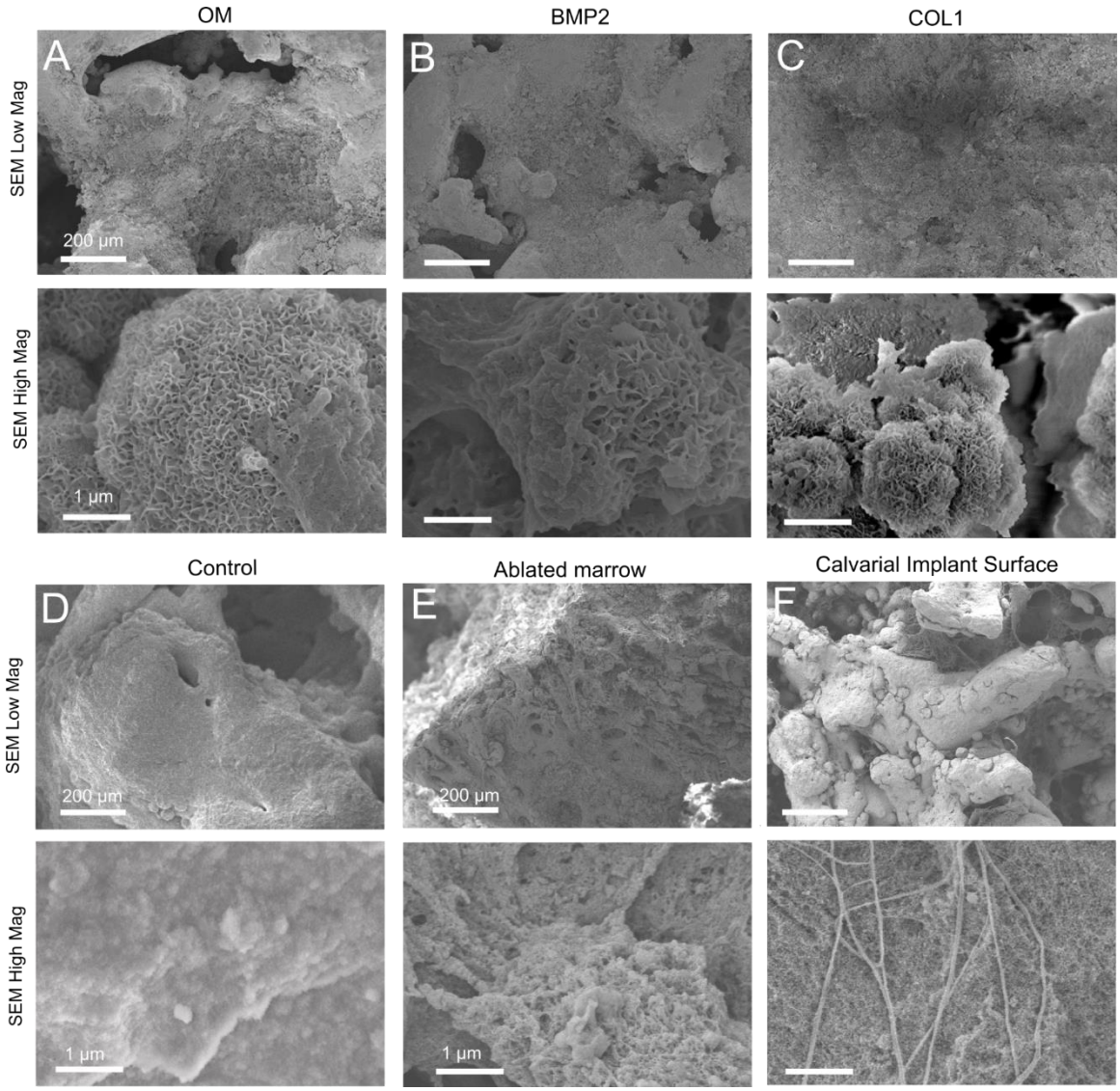

Figure 9.7. SEM low and high magnification images of hMSC mineralization on OM, BMP2 and COL1 constructs after 8 weeks in culture (A, B, C). SEM low and high magnification images of control construct placed in OM for 8 weeks without cells (D). SEM low and high magnification images of bone marrow 7 days after ablation in Sprague Dawley rat (E). SEM low and high magnification images of construct after 7 days of implantation on calvarium of Sprague Dawley rat (F)

9.4. Discussion

In this study, we analyzed the temporal response of hMSCs after 3, 6, 9 and 56 days to additively manufactured Ti-6Al-4V constructs with a trabeculae-inspired 3D architecture. We developed a unique culture system and parameters to evaluate mineralization in a 3D environment, as compared to traditional standard cell culture experiments using 2D surfaces. Our results showed that hMSCs respond to a 3D compared to a 2D environment with enhanced differentiation and matrix mineralization.

A previous study using similar constructs published by our lab showed that MG63 osteoblast-like cells were responsive to constructs in a porosity-dependent manner [38]. The effects of the Ti-6Al-4V 3D porous constructs on cell response were significant compared to a 2D TCPS surface. In this study, we included a 2D control Ti-6Al-4V surface manufactured using the same methods as our 3D constructs, with comparable chemistry and surface roughness [201]. Inclusion of this control shows that hMSC differentiation into an osteoblast phenotype is increased based on a 3D implant architecture, with up to a 2.8-fold increase in osteocalcin and 2.4-fold increase in VEGF on day 9 of culture. However, the hMSCs were less sensitive to changes in percent porosity across different 3D constructs than noted previously for MG63 cells [201]. This phenomenon has also been observed with normal human osteoblasts, which showed lower sensitivity to construct porosity when compared to MG63 cells [201]. Other studies have shown that MSCs were less sensitive to surface roughness at the nano-scale compared to MG63 cells [22]. It is not clear if this is a difference in the state of the two cell types in the osteoblast lineage or other differences between the two cell types. Regardless of percent porosity, the presence of a 3D trabecular

architecture had an effect upon most of the factors analyzed compared to both the 2D TCPS and laser sintered Ti-6Al-4V surfaces.

In a previous time course study of hMSC response to rough 2D surfaces conducted by our group, no difference in RUNX gene expression was observed after 2 days. However, after 4 and 6 days, RUNX gene expression remained elevated for cells cultured on both hydrophobic and hydrophilic rough titanium surfaces compared to TCPS or smooth titanium surfaces [21]. Alkaline phosphatase specific activity is a time sensitive early marker of osteoblast differentiation and typically peaks sooner for cells on rough titanium and titanium alloy surfaces compared to smooth surfaces [23, 31, 382, 383]. Our results also suggest that ALP activity peaks before day 3 for 3D constructs when compared to TCPS or 2D surfaces. While ALP activity for TCPS is reduced after 6 and 9 days compared to after 3 days, ALP remains steady for 2D and 3D constructs. An earlier peak in ALP activity on TCPS compared to other studies may be due to the high initial seeding density used in this study [384]. Because surface roughness has been shown to increase ALP activity on titanium substrates compared to TCPS, we believe that the reduced ALP activity observed on 2D and 3D constructs is a product of an earlier peak in ALP activity on these constructs compared to TCPS. This is also corroborated by elevated levels of osteocalcin over 3, 6 and 9 days, suggesting that hMSCs on our 3D constructs are later along the osteoblastic differentiation pathway. Previous studies showing MG63 osteoblasts cultured on 3D electrospun titanium meshes indicate that osteocalcin remains elevated compared to a 2D smooth titanium surface up to 12 days after confluence, suggesting that cells on our constructs will continue to differentiate and mature as osteoblasts over time [37].

In this study, we used bone marrow-derived MSCs from a young adult, black male. Variations in differentiation potential can exist among the physiological source of MSCs, be it from adipose tissue or bone marrow, with differences in cell response based on donor age, gender and body mass index [385]. Even for the same donor, responses differ based on passage number once cells are cultured *in vitro* [60]. Unfortunately, many studies do not identify the source of cells, or describe donor characteristics. Despite these differences, however, all MSCs show osteogenic potential, with alkaline phosphatase specific activity correlating well with *in vivo* bone formation potential. We suggest that future studies include multiple donors in order to gain a more complete understanding of biological response to these 3D constructs.

To examine the potential of our 3D environment possessing surface roughness to support bone formation, an *in vitro* mineralization assay was conducted. It is well known that surface roughness can enhance osteoblast response and accelerate bone formation *in vivo* [23, 25]. MicroCT was unable to resolve differences in density, and thus mineralization, between pre- and post-culture constructs. This may be due to the relatively low mineral content present only on the surface of constructs. Although the average construct volume was higher for COL1 constructs compared to that of other groups, error resulting from x-ray scatter when imaging titanium could not prove this observation to be statistically significant.

We could not detect mineral via microCT; therefore, the presence of mineral was established using three alternative methods for characterizing mineralization. The OsteoImage mineralization assay (Lonza) is a fluorescent assay for quantifying the amount of hydroxyapatite present. However, it is unclear whether the assay is able to bind to the

very small mineral particles present on our constructs, as was suggested by the limited detection of mineral content by XRD analysis. Hydroxyapatite was detected throughout OM and BMP2 constructs, but only on the surface of COL1 constructs, suggesting that the collagen coating prevented cell infiltration through the porous construct.

Von Kossa staining only identifies phosphate and Alizarin Red identifies divalent cations; these methods are not sufficient to determine hydroxyapatite formation [386]. Therefore, we used alternative methods to characterize any mineral present in the cultures. Our data support the interpretation that mineral quality varies at the surface versus the bulk of the construct. EDX analysis was performed on the nodules as identified qualitatively by SEM. EDX analysis is surface and feature specific while ICP-OES analysis considers the Ca and P present everywhere in the construct; we used both techniques. Although a theoretical weight ratio of 2.15 was not achieved for samples, our ICP-OES results are similar to the lower Ca:P ratios found in *in vitro* cultures [387]. Indeed, physiological Ca:P weight ratios differ from theoretical values due to differences in phosphorous content in different locations of the cell and matrix [388, 389]. Higher Ca:P ratio values suggest dystrophic calcification, where calcium phosphate precipitation occurs without collagen matrix deposition [390]. This has also been corroborated in the literature by atomic Ca:P ratios of less than the theoretical 1.67 value resulting from EDX analysis of native bone [391]. EDX detected the presence of Ca and P from the culture medium on control constructs, but these surfaces were starkly different than mineralized surfaces from the OM, BMP2 and COL1 groups. Our findings also support previous work showing that mineral deposition in OM can involve dystrophic calcification and that physiologically

normal calcification results in a Ca:P ratio similar to the 1.4 we observed for the COL1 cultures [387].

Although we did not observe apatite formation on our control constructs in the absence of cells, we did observe topographical changes on the surface in comparison to constructs before culture. In particular, smaller nano-structures as observed on pre-experimental constructs were amplified after 8 weeks in culture medium. This has been observed previously as spontaneous nanostructures have formed on titanium substrates after immersion in saline solution; however, the exact mechanism leading to this surface change is unknown [27]. Other studies have even shown changes at the micro-scale of titanium surfaces soaked in simulated body fluid for only 3 weeks [392]. Our control results are in contrast to other studies that have reported apatite formation on surface-treated titanium surfaces immersed in simulated body fluid. These surfaces were typically altered to achieve a surface composition that included an amorphous alkali titanate to facilitate apatite formation [393, 394]. These results indicate that the mineral content formed on these 3D constructs with trabecular porosity is indeed a product of the hMSCs.

Bone formation *in vivo* occurs in two stages following implantation. During the first week, primary bone forms across the implant site and on the implant surface. Thereafter, secondary bone is formed via resorption and remodeling of primary bone [395]. Because our constructs were cultured only in the presence of hMSCs and for eight weeks, mineralization from this study could not directly be compared to primary mineralization *in vivo*. Because of this closed culture system without osteoclasts, we chose to observe implants in rats after one week to compare mineralization during the primary mineralization phase. However, qualitative similarities, combined with enhanced

osteoblastic differentiation factors, suggest that constructs may osseointegrate well in the body. Future studies of interest might include understanding how implant surface changes in culture and upon implantation affect downstream cell response, matrix production and bone formation.

9.5. Conclusion

Additive manufacturing has great potential within the medical field. In this paper, we show that additively manufactured, porous Ti-6Al-4V constructs with human bone architecture and micro-/nano- surface roughness can enhance osteoblast differentiation of MSCs, including their ability to mineralize their extracellular matrix compared to 2D surfaces. These positive results lay a foundation for future *in vivo* studies with 3D porous constructs, and eventual clinical application within the orthopaedic and dental fields.

CHAPTER 10

LASER SINTERED POROUS TI-6AL-4V IMPLANTS STIMULATE VERTICAL BONE GROWTH

In [Cheng A, Cohen DJ, Kahn A, Clohessy RM, Sahingur K, Newton JB, Hyzy SL, Boyan BD and Schwartz Z. Laser sintered porous Ti-6Al-4V implants stimulate vertical bone growth. Journal of Dental Research. 2016. Under review]

10.1. Introduction

Dental implant success remains a challenge for the elderly, smokers, diabetics and patients undergoing irradiation therapy of the head and neck. [316]. Implants with porosity are now being introduced as a way to enhance bone formation in compromised patients [396]. Histological studies in the rabbit have also indicated blood vessel formation in concavities of implants, suggesting that porosity may also enhance vascularization [397].

Titanium and its alloys are still the preferred materials for bone interfacing implants based on their ability to osseointegrate, as well as their corrosion resistance and mechanical properties [351, 398]. Though tantalum-coated porous implants have been introduced into the market, they have shown only comparable but not superior performance to solid implants [399]. In addition, these and other porous implants made using traditional manufacturing techniques cannot be manufactured in one piece, requiring additional processing.

Selective laser sintering (SLS) is a form of additive manufacturing that is able to create high resolution, patient-specific Ti-6Al-4V constructs and bone-interfacing implants in one step. Previous studies have shown a clear preference of human osteoblasts for a 3D porous over a 2D solid environment, with higher expression of factors favoring osteoblastic

differentiation and maturation, including osteocalcin, vascular endothelial growth factor (VEGF) and bone morphogenetic proteins (BMPs) [38, 201]. In addition, animal studies have indicated that SLS Ti-6Al-4V implants support vertical bone growth when equally spaced through-pores are included [119, 378]. These studies suggest that SLS implants that are fabricated to have bioinspired porosity will support osteoblast differentiation in vitro and osseointegration in vivo. To test this hypothesis, we used SLS technology to generate implants with porosity based on trabecular bone and examined their effectiveness at supporting vertical bone growth in a rabbit cranial onlay model with and without the use of demineralized bone matrix putty (DBX) to stimulate osteogenesis.

10.2. Materials and Methods

Materials Manufacturing

All constructs were laser sintered from Ti-6Al-4V powder from a "medium porosity, high resolution" template based on human trabecular bone and processed to obtain micro-/nano- surface roughness as previously described [38, 201]. Implants for histology had a solid or porous base 3.5mm in width and 5mm in length between two 0.75mm solid supports on either side, and were 2mm in height (Figure 10.1A). Implants for mechanical testing included an additional arch 2.5mm in height connected to the solid side supports (Figure 10.1B). Constructs for cell studies were manufactured with the same porosity as implants, but were 15mm in diameter and 5mm in height (including a 1mm solid base) to fit snugly within wells of a 24-well plate.

Material Characterization

Material characterization was performed for implants only; material characterization of constructs used for *in vitro* studies was previously performed and published [201]. Surface chemistry was determined using x-ray photoelectron spectroscopy (XPS, ESCAlab 250, ThermoFisher, Waltham, MA). Aluminum clips were sonicated in acetone for 10 minutes prior to use in securing samples. Analysis was conducted using an XR5 gun, 500µm spot size, 20ms dwelling time and 1eV energy step size. Six spots were analyzed per implant, with two implants per group (n=12).

Sessile drop contact angle was performed on solid implants (Ramé-Hart, Succasunna, NJ). A 1µL drop of distilled water was placed on implants. The average of left and right contact angles of the drop were calculated every 5 seconds for 20 seconds using DROPImage software (Ramé-Hart). Three drops were placed per implant for two implants (n=6).

Implants were imaged using scanning electron microscopy (SEM, Zeiss AURIGA, Zeiss, Oberkochen, Germany). Imaging was conducted in Inlens mode with an accelerating voltage of 4kV and working distance of 4-6mm.

Micro-computed tomography (microCT, Skyscan 1173, Bruker, Kontich, Belgium) was used to analyze implant porosity. Implants were scanned at a resolution of 1120x1120 pixels, using a brass 0.25mm filter with a voltage of 120 kV, current of 60µA, image pixel size of 20.13µm, exposure time of 300ms and rotation step of 0.2 degrees. A standard Feldkamp reconstruction was performed with a Gaussian smoothing kernel of zero and a beam hardening correction of 20% using NRecon software version 1.6.9.17 (Bruker) and analyzed in CT-Analyser version 1.14.4.1 (Bruker). Constructs were binarized and total porosity was calculated within a fixed VOI averaged over n=3 constructs.

Cell Response

Male (donor 27625, 32yo white) and female (donor 28014, 20yo white) normal human osteoblast (NHOst) cells (Lonza, Walkersville, MD) were plated on tissue culture polystyrene (TCPS), or solid or porous constructs at a density of 60,000 cells per well. Cells were fed with Dulbecco's modified Eagle medium (DMEM) supplemented with 10% fetal bovine serum (FBS) and 1% penicillin/streptomycin 24 hours after plating. At confluence according to TCPS, medium was exchanged. Cells were harvested 24 hours after confluence by rinsing twice with phosphate buffered saline (1xPBS). Media were analyzed for osteocalcin, osteoprotegerin (OPG), vascular endothelial growth factor (VEGF) and bone morphogenetic protein 2 (BMP2), and these were normalized to DNA content. Whole cell lysates were used to analyze DNA content, alkaline phosphatase activity (ALP) and total protein content. ALP was normalized to total protein content.

For imaging, cells were fixed in 4% paraformaldehyde, then dehydrated in a series of increasing ethanol solutions and hexamethyldisilazane (HMDS) as reported previously [38]. Samples were sputtered with platinum prior to SEM imaging.

Cranial Onlay Model

Methods for the cranial onlay model and subsequent characterization were adapted from a previously published study [119]. Eight-week old 250-300g male athymic nude rats (Hsd:RH-Foxn1^{rnu}, Harlan Laboratories, Indianapolis, IN) were anesthetized with 1.2 L/min of flowing isoflurane and 0.2% oxygen. Hair was removed from the head with depilatory cream. A 2cm incision was made on the calvarium to the right of the sagittal suture, and the periosteum was elevated. A dental burr was used to perforate the calvarium 10-15 times at the site of implant placement in order access the marrow space and allow

for stem cell infiltration [400]. A solid or porous implant was placed on top of the calvaria. For one group of porous implants, demineralized bone matrix putty (DBX, Musculoskeletal Transplant Foundation, Edison, NJ) was placed on the bottom surface of implants in contact with the calvaria. Each group (Solid, Porous, and Porous+DBX) had n=8 rats for histology and an additional n=8 rats for mechanical testing. Implants were secured to the calvarium using a purse-string suture to close the periosteum around the implant, and the skin was sutured closed. Rats were euthanized after 10 weeks. All animal procedures were approved by and carried out in accordance with the Virginia Commonwealth University Institutional Animal Care and Use Committee.

Mechanical Testing

Rat calvaria harvested for mechanical testing were stored overnight at 4^{o}C without formalin. The head was loaded into a custom testing device with the implant aligned to the testing machine axis to minimize bending during the test (MTS Insight 30; MTS Corp., Eden Prairie, MN, USA). A stainless steel wire (0.02 in diameter, Malin Co., Cleveland, OH, USA) was threaded through the support loop of the implant and pulled at a crosshead speed of 5mm/min. Axial pull-out strengths and force at failure (N) were recorded.

MicroCT

Rat calvaria harvested for microCT and histology were stored in 10% formalin. MicroCT scans and reconstructions were performed as described above. After binarization, a volume of interest (VOI) was applied along the 5mm porous or solid length of implants (not including the solid sides) and extending 500µm in the z-direction. The VOI was shrink-wrapped around the implant and then dilated to include an 80µm border to minimize error from image scattering. The implant was subtracted from the VOI, and

the remaining bone in contact with the void space within a 20 μm perimeter where the implant had been subtracted was shrink-wrapped, thresholded and quantified. Basal bone-implant contact was calculated by taking the volume of bone measured in the VOI divided by the volume of implant measured in the VOI. To calculate total bone volume in porous implants, bone was binarized and quantified after thresholding from the implant. To calculate bone volume as a percentage of total porous implant volume, the total bone volume was divided by the implant porous volume within the VOI.

Histology

Calvaria were prepared for histological sectioning by setting in poly (methyl methacrylate) (Histion, LLC, Everett, WA). Sections were stained using Stevenel's Blue [127]. The Zen 2012 Blue Edition software with an AxioCam MRc5 camera and Axio Observer Z.1 microscope (Carl Zeiss Microscopy, Oberkochen, Germany) was used to image slides using an N-Achroplan 10x/0.25 Ph1 M27 objective. Calculation of bone area below the implant was performed as a modification of previously published analysis method for expected bone-to-implant contact (BIC) [401]. Bone area was quantified 0.5mm below a straight line connecting the outer boundaries of the implant. Bone ingrowth into the implants was calculated by dividing the total area of bone within the implant by the total porous area of the implant. The porous area was calculated between the upper and lower boundaries of each implant. The total area of the bone in the implant was then calculated by finding the area of the bone present within the boundaries of the implant.

Statistical Analysis

A one-way analysis of variance (ANOVA) was performed to compare across three or more groups, with Bonferroni post-hoc analysis to determine significance between

individual groups. All statistical analyses were conducted using GraphPad Prism software (GraphPad, La Jolla, CA).

10.3. Results

Material Characterization

SEM images show the macro-, micro- and nano- features produced after surface treatment on both solid and porous implants (Figure 10.1C). MicroCT analysis of porous constructs revealed an interconnected porosity of 67% ± 3%. XPS analysis showed that both solid and porous implants possessed oxygen, carbon, titanium, nitrogen and calcium on their surfaces (Figure 10.1D). Porous implants additionally had a small percentage of phosphorous present. Solid implants possessed a contact angle of $47^{o} \pm 17^{o}$ (Figure 10.1E).

Cell Response

NHOst cells plated on solid disks (Figure 10.2A, top) and porous constructs (Figure 10.2A, bottom) showed elongated morphology with extended filopodia. Cells were observed suspended across struts and crevasses on porous constructs. Less cells were observed on porous constructs compared to on solid disks. DNA content was decreased on solid and porous constructs compared to TCPS and solid constructs (Figure 10.2B), confirming the morphological observations.

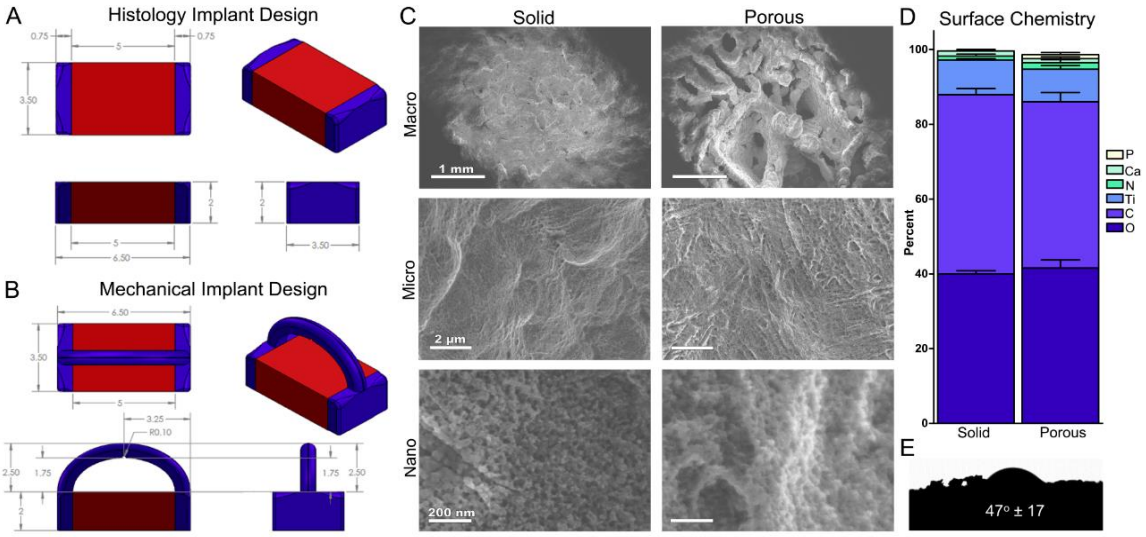

Figure 10.1. Implants for histology (A) and mechanical testing (B). Blue indicates solid side support and arch for mechanical testing; red indicates either solid or trabecular porosity based on experimental group. SEM images of solid (left) and 3D porous (right) implants showing macro, micro and nano-surface topography (A); implant surface chemistry (B); and contact angle of solid implant surfaces (C).

Osteoblast differentiation was sensitive to implant porosity. Alkaline phosphatase specific activity was significantly lower on solid and porous constructs compared to TCPS for female NHOst cells only (Figure 10.2C). In contrast, osteocalcin was significantly increased on porous constructs compared to TCPS and solid disks for both female and male NHOsts (Figure 10.2D). Moreover, male NHOsts exhibited significantly higher levels of osteocalcin than female NHOsts on TCPS and solid disks. Osteoprotegerin was significantly increased on porous constructs compared to TCPS and solid disks for both female and male NHOsts (Figure 10.2E). Male NHOsts had significantly higher levels of osteoprotegerin on TCPS and porous constructs compared to female NHOsts. Vascular endothelial growth factor (VEGF) was significantly increased on solid disks and porous constructs compared to TCPS, and porous constructs compared to solid disks for both male and female NHOsts (Figure 10.2F). VEGF was higher for male NHOsts on TCPS compared to female NHOsts. Bone morphogenetic protein 2 (BMP2) was significantly

increased on porous constructs compared to TCPS and solid disks for both male and female NHOsts, and was increased for male NHOsts on TCPS compared to female NHOsts (Figure 10.2G).

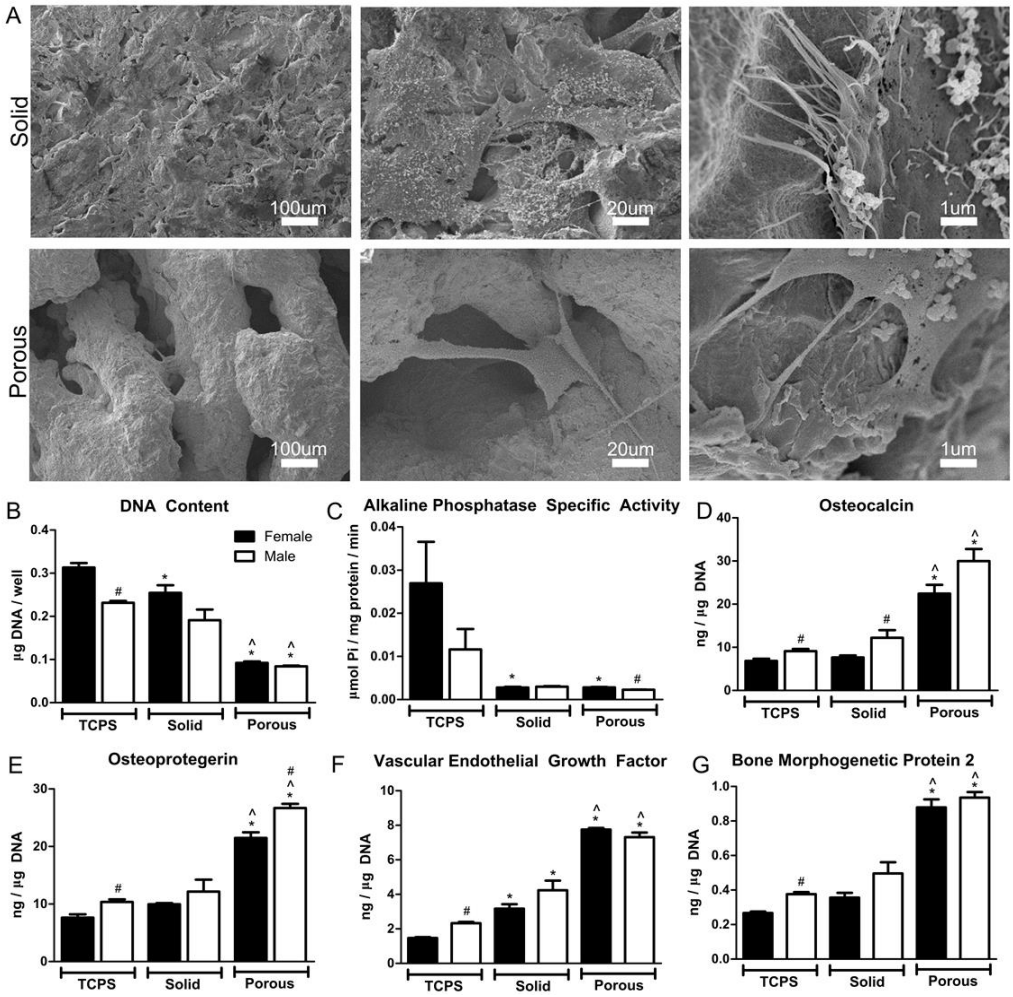

Figure 10.2. NHOst cells on solid (top) and 3D porous (bottom) constructs (A); DNA content (B); alkaline phosphatase specific activity (C); osteocalcin (D); osteoprotegerin (E); vascular endothelial growth factor (F); and bone morphogenetic protein (G) of male and female NHOst cells on 2D and 3D porous constructs. 1 way ANOVA with Bonferroni post-hoc test, $p<0.05$, *vs. TCPS ^ vs. 2D. Unpaired t-test, $p<0.05$, # vs. Female. Scale bars represent 100um.

10.3.3. MicroCT analysis

We used a calvarial onlay implantation procedure for this study, which allowed us to correlate bone-to-implant contact measured histologically with mechanical strength

(Figure 10.3A). MicroCT images contrasted bone growth below Solid implants (Figure 3B) with vertical bone growth into Porous (Figured 10.3C) or Porous+DBX implants (Figure 10.3D). These qualitative observations were corroborated by quantitative analysis. BIC across the base of the implant was higher for Porous+DBX implants compared to Solid implants, but was not significantly different between Porous and Porous+DBX groups (Figure 10.3E). Solid implant BIC was 20% ± 3.6 for Solid implants, 25% ± 1.4% for Porous implants and 33% ± 2.7% for Porous+DBX implants. Bone growth expressed as total volume (Figure 10.3F) or percentage of porous construct void volume (Figure 10.3G) was also not significantly different for porous implants with or without DBX. Total bone volume within pores was 3.1±0.60 mm^3 for Porous and 2.5 ± 0.18 mm^3 for Porous+DBX implants. This constituted 6.2 ± 0.76% of the porous volume of implants for Porous implants, and 4.8 ± 0.46% of the porous volume for Porous+DBX implants.

Mechanical Testing

Pull-out values of implants were significantly higher for Porous and Porous+DBX compared to Solid implants, but the use of DBX did not contribute to a significant increase in pull-out force for porous implants (Figure 10.4A). Optical (Figure 10.4B) and SEM (Figure 10.4C) images of rat calvaria after pull-out testing show a relatively smooth surface for calvaria with solid implants, while calvaria with porous implants showed rough locations of bone growth and breaking points during testing. Optical (Figure 10.4D) and SEM (Figure 10.4E) images of implants after mechanical testing show limited periosteum and bone on solid implants, while large portions of bone and periosteum were integrated inside pores of porous implants.

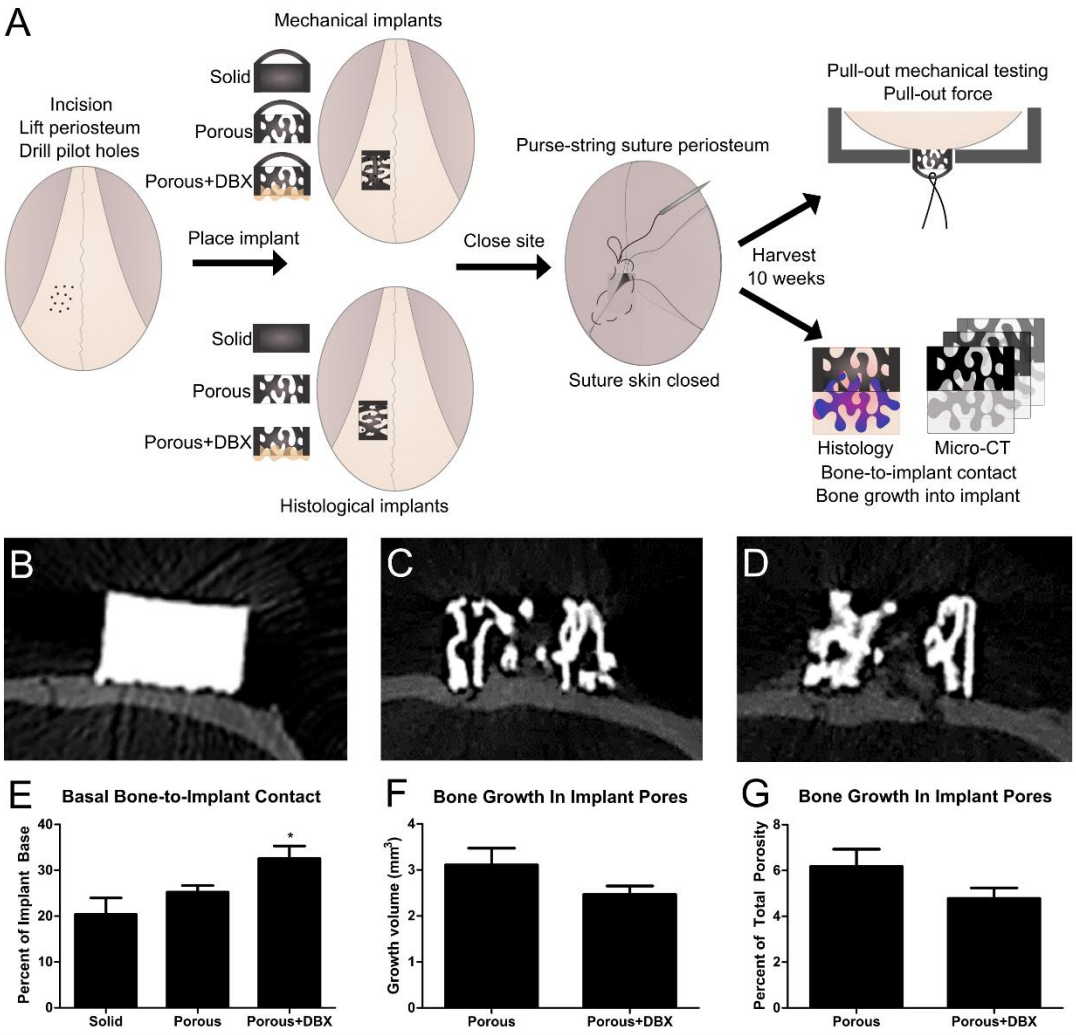

Figure 10.3. Surgery schematic. An initial incision was made and the periosteum was lifted. 15-20 pilot holes were drilled to allow for stem cell infiltration before implant placement. Implants were placed atop the calvarial bone and secured by a purse-string suture of the periosteum around the implant. Animals were harvested after 10 weeks for pull-out testing or microCT followed by histology. MicroCT cross-sectional images of 2D (B), 3D (B) and 3D with DBX implants (C) on rat calvaria 10 weeks after implantation. Bone to implant contact (D), volume of bone growth into implant pores (E) and percent volume of bone growth into implant pores (F) as analyzed by microCT analysis. 1 way ANOVA with Bonferroni post-hoc test, $p<0.05$, *vs. 2D. Unpaired t-test, $p<0.05$. No significance.

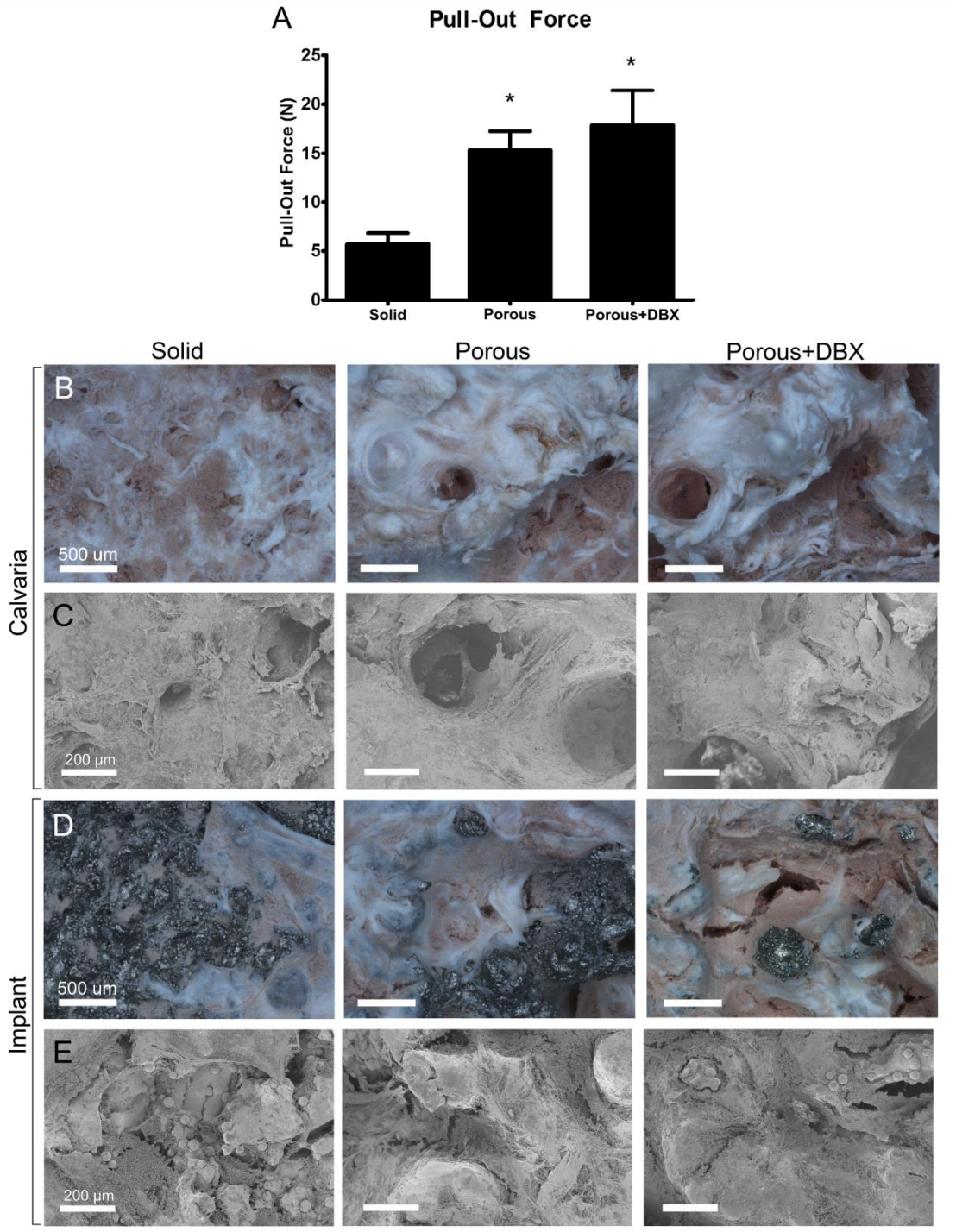

Figure 10.4. Pull-out force 10 weeks after implantation (A), with corresponding optical (B, D) and SEM (B, E) images of calvaria (B, C) and implant (D, E) after mechanical testing.

Histology

Histological cross-sections of solid implants (Figure 10.5A) showed BIC occurring near the middle of implants. In contrast, Porous (Figure 10.5B) and Porous+DBX implants (Figure 10.5C) showed bone ingrowth into pores and all along the base of the implant. Bone area calculated 0.5mm below the implant base was 2.97±0.23, 2.52±0.14 and 2.61±0.14 mm^2 for Solid, Porous and Porous+DBX implants, respectively (Table 10.1). These values were not significantly different among implant groups (Figure 10.5D). New bone growth into porous implants was 1.62±0.21 mm^2 for Porous implants and 1.52±0.34 mm^2 for Porous+DBX implants, which were not significantly different from each other (Table 10.1). This constituted 21% ± 2.4% of the area for Porous implants and 20% ± 4.8% for Porous+DBX implants (Figure 10.5E). Porous+DBX had an additional 1.29±0.27 mm^2 of DBX remaining within the implant pores, or 16% ± 3.0% of the porous area (Table 10.1, Figure 10.5E).

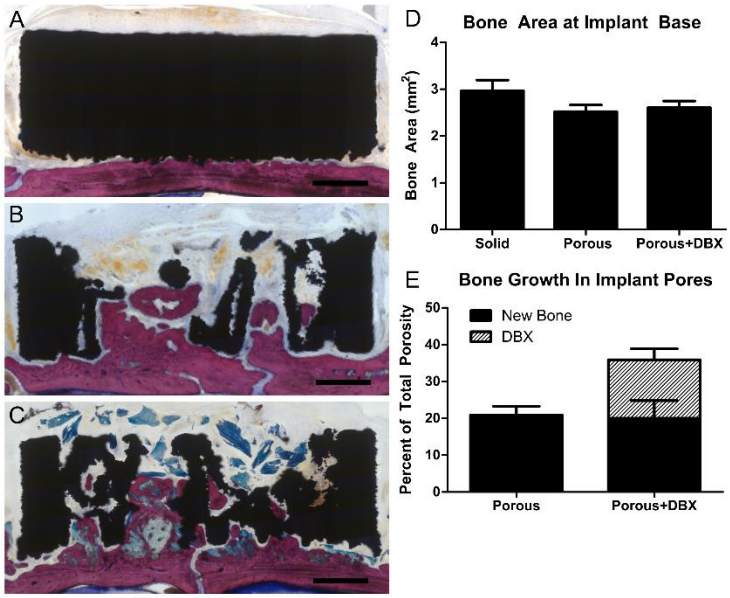

Figure 10.5. Histological sections of 2D (A), 3D (B) and 3D with DBX (C) implants 10 weeks after implantation. Bone area 0.5mm below the implant base (D) and percent growth of bone into implant pores (E) determined from histological analysis (E). Scale bars represent 1mm.

Table 10.1. Histological analysis of total bone and new bone growth into 3D implants.

Histological Analysis (Average ± SEM)			
	Solid	Porous	Porous + DBX
Bone 0.5mm Below Implant Base (mm^2)	2.97 ± 0.23	2.52 ± 0.14	2.61 ± 0.14
New bone (mm^2)	--	1.62 ± 0.21	1.52 ± 0.34
DBX (mm^2)	--	--	1.29 ± 0.27

10.4. Discussion

This objective of this study was to examine the influence of a trabecular-inspired porosity on cell response and bone ingrowth. While sex-dependent differences did exist for some factors, in general both male and female osteoblasts in our study responded more favorably to porous constructs compared to solid substrates. The effect of a 3D trabecular porosity was also observed *in vivo*, where porous implants were able to induce vertical bone growth even without the addition of exogenous factors.

Studies on sex differences have traditionally focused on gender-specific diseases, but a recent report by collaborators at the National Institutes of Health and the American Academy of Orthopaedic Surgeons has pushed for inclusion of sex differences in musculoskeletal health [61]. Previously, our lab investigated the effect of surface roughness on male and female cells isolated from rats, showing that male cells were more responsive to 1α,25(OH)2D3 on titanium surfaces than female cells [64]. Other studies evaluating biological effects of additively manufactured titanium aggregated the responses of male and female cells from humans for analysis [402]. In this study, only one donor from each sex was examined. Because osteoblast response can vary across experimental conditions and with donor age, we suggest that future studies continue to consider sex

differences and use multiple donors when evaluating primary cell response to implant materials [65, 292].

Our results indicate that bone-to-implant contact is correlated positively with mechanical strength of the interface. Pull-out force values supported microCT results, indicating enhanced osseointegration for porous compared to solid implants, regardless of DBX use. Optical and electron images showing bone nodules on calvaria and new bone in implant pores, combined with microCT observations and pull-out force values, indicate that bone was strongly osseointegrated within surfaces of porous implants and that failure at the base of the implant contributed more to pull-out force. This also indicates that new bone quality was similar for porous implants with or without DBX, and superior to that of solid implants.

Surprisingly, the use of DBX did not significantly enhance mechanical pull-out testing force or total vertical bone volume growth into porous implants. A review on ridge augmentation procedures suggests that implant success in augmented areas is a function of the residual bone and less a function of the grafted bone [403]. Our results corroborate this finding. Although 16% of DBX still remained in implants after 10 weeks, this had no discernable effect on the mechanical functionality of implants. This also points to the importance of supporting natural bone growth, in contrast to using large bone block substitutes. Previous work by our lab also showed DBX remaining when using the same cranial onlay model [119]. A study of three different types of demineralized bone matrix (DBM) in rat spines showed varying amounts of residual DBM after 8 weeks, indicating that the formatting of DBM is also an important factor to consider [404].

Because our study ended after 10 weeks, it is possible that bone would continue to form over longer time periods. A previous dental implant study in humans without the use of bone substitutes showed that there was still coronal bone formation occurring even at 9 months after implant placement with a non-resorbable membrane [400]. Although longer term and larger animal studies are necessary for evaluating implant survival, our results suggest that porous implants can be successfully placed in areas with insufficient bone to induce vertical bone regeneration.

10.5. Conclusion

Most clinical procedures for implant placement in patients with insufficient bone volume still require the use of a bone substitute or sophisticated surgical techniques to achieve vertical bone growth [405]. Our study suggests that implants with a natural inspired porosity may be better able to leverage the regenerative potential of patients, which may be useful for challenging clinical cases. Laser sintered trabeculae-inspired porosity implants may also achieve superior long-term clinical outcomes over traditional solid implants in compromised patients. It should be noted that both solid and porous Ti-6Al-4V implants used in this study had microscale and nanoscale surface texture, which has been shown previously to enhance osteogenic differentiation of mesenchymal stem cells in vitro and osseointegration in vivo [378, 406]. Thus, the enhanced bone-to-implant contact and mechanical stability noted with porous implants is a reflection of their increased surface area resulting from their porosity, and not due to differences in surface processing alone.

CHAPTER 11

EVALUATING PERFORMANCE OF AND BONE GROWTH INTO LASER SINTERED TI-6AL-4V IMPLANTS WITH TRABECULAR POROSITY IN A RABBIT FEMORAL MODEL

In [Cheng A, Cohen DJ, Sahingur K, Clohessy RM, Hopkins L, Boyan BD and Schwartz Z. Evaluating performance of and bone growth into laser sintered Ti-6Al-4V implants with trabecular porosity in a rabbit femoral model. Acta Biomaterialia. 2016. Under review]

11.1. Introduction

The long term success and osseointegration of bone-interfacing implants continues to be a challenge. Success rates of titanium (Ti) and titanium-aluminum-vanadium (Ti-6Al-4V) alloy dental implants can vary from over 90% in healthy patients to less than 70% in compromised patients [316]. The lifespan of many orthopaedic implants is limited to 15 years, requiring costly and potentially fatal revision procedures for continued functionality [317, 351]. In addition, an increasing life expectancy and demand for total joint replacements will require better performing implants with longer lifespans [407].

Osseointegration of implants can be affected by physical properties at the surface including chemistry, wettability and micro-/nano-roughness. Implants that are Ti based have a passive TiO_2 layer that resists corrosion and can directly osseointegration with bone. High surface energy has been shown to increase cell attachment as well as the rate of implant mechanical stability in animal studies [39]. While implants with micro-roughness show superior clinical performance compared to smooth implants, surfaces possessing hierarchical micro-/nano-roughness are now being explored and have been shown to enhance biological response compared to micro-roughness alone [9, 22, 133]. All these

factors contribute to creating a desirable interface for cell attachment, differentiation and ultimately bone formation for successful implant ossoeintegration.

Macro-scale properties such as porosity also play an important role in enhancing bone formation and osseointegration [175]. Laser sintered implants with through-pores showed enhanced osseointegration and vertical bone growth in a rat calvaria onlay model as evidenced by increased pull-out values when compared to solid implants [119]. No differences in mechanical testing results or vertical bone ingrowth were observed between porous implants placed with or without the use of an osteogenic bone graft, suggesting that implant surface and porosity alone were able to induce bone growth. However, this earlier study evaluated cortical bone growth only, without considering the response of trabecular bone that is in contact with implants under many clinical conditions.

While porous implants have been introduced to match the mechanical properties of bone and increase integration, a clear consensus on the ideal properties of pores has not yet been reached. Instead of optimizing pore geometry, our group has taken a different approach and incorporated porosity inspired by nature. Previous studies have shown that laser sintered Ti-6Al-4V constructs with trabecular bone-inspired porosity have shown increased osteoblast response [38, 201]. These *in vitro* results combined with *in vivo* studies demonstrating the ability of laser sintered implants to perform as well as implants manufactured with conventional techniques in animal models [378, 406], suggest that laser sintered implants with trabecular porosity may be superior to solid implants and enhance osseointegration in challenging clinical cases.

Until now, osseointegration of implants with trabecular porosity has not yet been analyzed in a clinically relevant orthopaedic or dental animal model. The objective of this

study was to evaluate and compare osseointegration of laser sintered Ti-6Al-4V implants with a solid or a trabecular bone-inspired porous exterior in a rabbit model that includes both cortical and cancellous bone. We hypothesized that micro-/nano-rough laser sintered implants with a three-dimensional, trabecular porosity would increase new bone formation and enhance osseointegration compared to solid sintered implants with the same surface roughness.

11.2. Materials and Methods

Implant manufacturing

Implants were manufactured from Ti-6Al-4V powder with laser sintering (EOS GmbH, Kralling, Germany). Implants were 3.8mm in diameter and 8mm in length. Both solid and porous implants possessed similar internal abutment connections and only differed in their solid or porous exterior. Porous implants were designed from a "medium porosity, high resolution" microCT template as described previously [201]. After manufacturing, implants were blasted with calcium phosphate particles and pickled to remove impurities, as described previously [201]. All implants were sterilized with gamma irradiation prior to characterization and implantation.

Implant characterization

Scanning electron microscopy

Scanning electron microscopy (SEM, Zeiss AURIGA, Oberkochen, Germany) was used to qualitatively evaluate implant macro-structure and surface roughness. Implants were secured on stubs with carbon tape and imaged with an accelerating voltage of 4kV, 30µm aperture and working distance of between 4-6mm. An SE2 detector was used to image samples.

Laser confocal microscopy

Laser confocal microscopy (LCM, Zeiss LSM 710) was used to quantitatively evaluate surface micro-roughness as described previously [201]. A Plan Apochromat 40x / 0.95 Corr M27 objective was used with an additional 5x optical zoom. Scan areas were 42.5µm x 42.5µm and imaged using the 405nm laser in reflection mode, with a 0.04µm pixel size and 1.60µs pixel dwell time. Z-stacks were performed using a step size of 1µm. Primary average roughness (Ra) and peak to valley roughness (Rz) were averaged over 3 scans per implant, with two implants per group (total n=6).

Micro-computed tomography

Micro-computed tomography (microCT, SkyScan 1173, Bruker, Kontich, Belgium) was used to evaluate implant porosity. A 0.25mm brass filter was used with a voltage of 120kV, current of 60µA, exposure of 300ms, pixel size of 40µm and rotation step of 0.2°. Scans were reconstructed in NRecon (Bruker) and analyzed in CT-Analyser (Bruker). A cylindrical volume of interest (VOI) was defined for only the lower half of implants to avoid analysis of the internal screw. This VOI was binarized and then thresholded to determine total implant porosity.

XPS

Surface chemistry of implants was evaluated with x-ray photo-electron spectroscopy (XPS ThermoFisher ESCAlab 250, Thermo Scientific, Waltham, Massachusetts, USA). Averages were taken over two survey scans per 500µm spot, using an XR5 gun and AlKα x-ray source at 15kV. Scans were taken with a 20ms dwell time and

1eV step size. Four locations per implant for two solid and two porous implants (n=8) were analyzed.

Contact angle

Surface wettability of solid implants was evaluated by sessile drop contact angle analysis (Ramé-hart Instrument Co, Succasunna, New Jersey, USA). A 1µL drop of distilled water was placed on the body of implants and analyzed with DROPImage software (Ramé-hart Instrument Co). Left and right contact angles were averaged every 5 seconds for 20 seconds per drop, with 4 drops placed per implant for two implants (n=8).

Surgical procedure

A schematic of the surgical procedure and harvest is provided in Figure 11.1A. Male New Zealand White Rabbits 13-16 weeks of age (7.0-7.9 pounds, late adolescent) were obtained from Robinson Services Inc (Mocksville, North Carolina, USA). Anesthesia was induced with an intramuscular injection of 35 mg/kg ketamine and 5 mg/kg xylazine, followed by a subcutaneous injection of 0.12 mg/kg buprenorphine SRLab for post-operative analgesia. Anesthesia was maintained using isoflurane gas delivered by v-gel supraglottic airway in 3-4% Oxygen to effect. The greater trochanter of the femur was palpated and a 5cm vertical incision was made distal to this landmark. The muscles were separated and the posterior surface of the proximal femur was localized. The periosteum was elevated and increasing drill bit diameters were used (1.9, 2.0, 2.5, 3.2, 3.65, and 3.80mm) to create a 3.80mm defect by drilling transaxially through the cortical and cancellous portions of the femur to a depth of 8mm Solid or porous implants were press fit into the defects flush with the cortical surface, and capped with a cover screw. The periosteum and muscle were re-approximated, and the skin incision was closed with a

running technique. Rabbits were euthanized after 10 weeks with a 0.22ml/kg intravenous injection of euthanasia solution, and the implants were harvested for pull-out testing (n=10) or microCT and histological analysis (n=10). Approval was obtained from the Institutional Animal Care and Use Committee at Virginia Commonwealth University. All experiments were carried out in accordance with approved procedures and reported according to ARRIVE guidelines [408].

Tissue analysis

Mechanical testing

Pull out testing was performed using a MTS materials test system (MTS Insight 30; MTS Systems Corp., Eden Prairie, MN, USA) as published previously [119]. The femur specimen was fixed in a custom fabricated test device with the implant aligned to the testing machine axis to ensure that no bending moment was created during the test. A custom abutment fabricated by AB Dental was joined to the implant and then pulled at a crosshead speed of 10 mm/min. Axial pull-out strengths were recorded and the load was monitored for force at failure (N) on nineteen implants (11 M, 8 LST).

MicroCT

Bone growth in and around implants was evaluated by microCT (Figure 1B). Fixed samples were imaged with a voltage of 130 kV and current of 60uA. High resolution scans were conducted using a 10µm pixel size, 1500ms exposure time and 0.4° rotation step. After reconstruction, shrink-wrapping was performed to isolate an initial VOI containing the implant. The VOI was dilated 10 pixels (100 µm) to account for new bone formed around the outside of implants and in order to provide a comparison between solid and porous implants. This final VOI was thresholded to subtract the implant, leaving only the

bone remaining. The VOI was reloaded and the bone was thresholded, binarized and quantified as the total bone volume. Total bone as a percentage of VOI was calculated by dividing the total bone volume by the final VOI. Total bone as a percentage of pore volume was calculated by diving the total bone volume by the pore volume from control implants as described above. Apical bone volume values were calculated by restricting the VOI to only the lower half of implants below the internal hex connector.

Histology

Samples were commercially processed (Histion, Everett, WA). Femurs were embedded in methyl methacrylate, and one ground section from each specimen was stained with Stevenel's blue/van Gieson. Sections were imaged with an AxioCam MRc5 camera and Axio Observer Z.1 and analyzed using ZEN 2012 Blue Edition software (Carl Zeiss Microscopy, Oberkochen, Germany).

The total bone-to-implant contact (BIC) was determined by dividing the length of bone touching the exterior of the implant by the total length of the exterior of the implant. The cortical region was set as the region from the two uppermost points of the implant, one on either side of the implant, down 2mm along the exterior of the implant. The total base length was calculated by finding the length of the horizontal component of the implant at its bottom. Some samples maintained an unbroken base, which resulted in a base measurement across the full length. Because porous implants did not retain a solid base across the full length of the implant, the implant base of these samples was calculated as the combined lengths of the fragmented pieces that appeared at the bottom of the implant closest to the bone. The BIC was calculated based on the bone touching these fragments.

The total bone ingrowth of the implant was calculated by dividing the total area of bone within the implant by the total area within the implant without bone (Figure 11.1C). A horizontal line was drawn across the two highest points on either side of the implant, the total area of the bone in the implant was was analyzed within these boundaries.

Statistics

Average and standard error of the mean values are presented for all analyses. Comparisons between solid and porous implants were made using a student's unpaired t-test, with $p<0.05$ indicating significance.

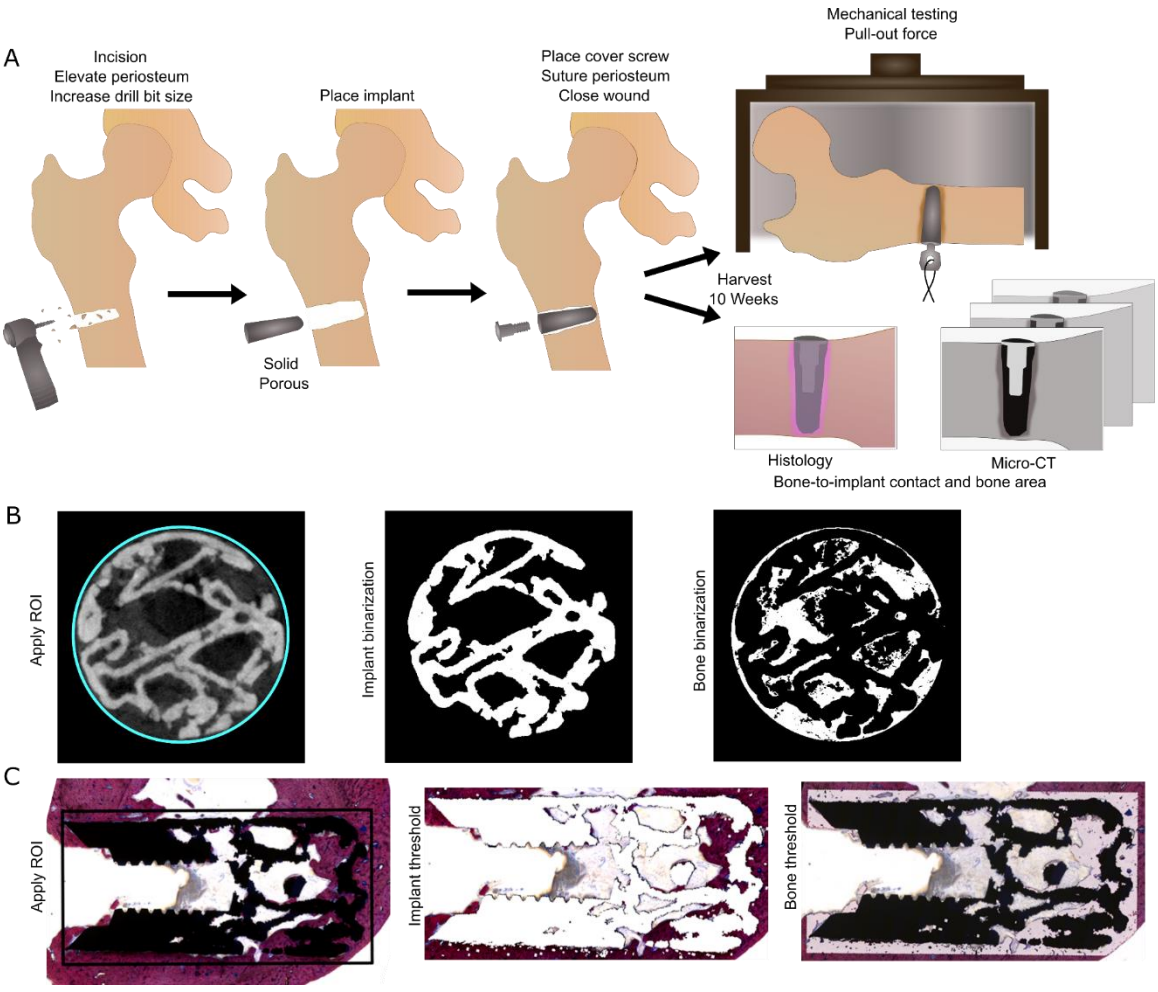

Figure 11.1. Surgery schematic (A). After incision at the femur, the periosteum was lifted and increasing drill bit diameters were used to drill transaxially into the femur. Solid or porous implants were placed and capped with a cover screw. The periosteum and skin was

sutured closed. Rabbits were harvested after 10 weeks. One group was used for pull-out testing, while the second group was used for microCT and histological analysis. MicroCT (B) and histological (C) methods for bone volume analysis.

11.3. Results

Implant characterization

SEM images were taken of implant macrostructure and surface roughness (Figure 11.2). Solid and porous implants were manufactured with the same dimensions. After surface processing, roughness at the micro- and nano-scale was present and similar on both solid and porous implants. Average and peak to valley surface micro-roughness were quantitatately evaluated by LCM; these values were not statistically different between solid and porous implants (Table 11.1). Solid implants of MicroCT analysis revealed that porous implants possessed a total and open porosity of 68.6% ± 0.8%. XPS analysis of surface chemistry showed mostly O and C present on implant surfaces, with smaller amounts of Ti, N, Ca, Al and Na also present (Table 11.2). Contact angle of solid implants was $85^{o}\pm11^{o}$.

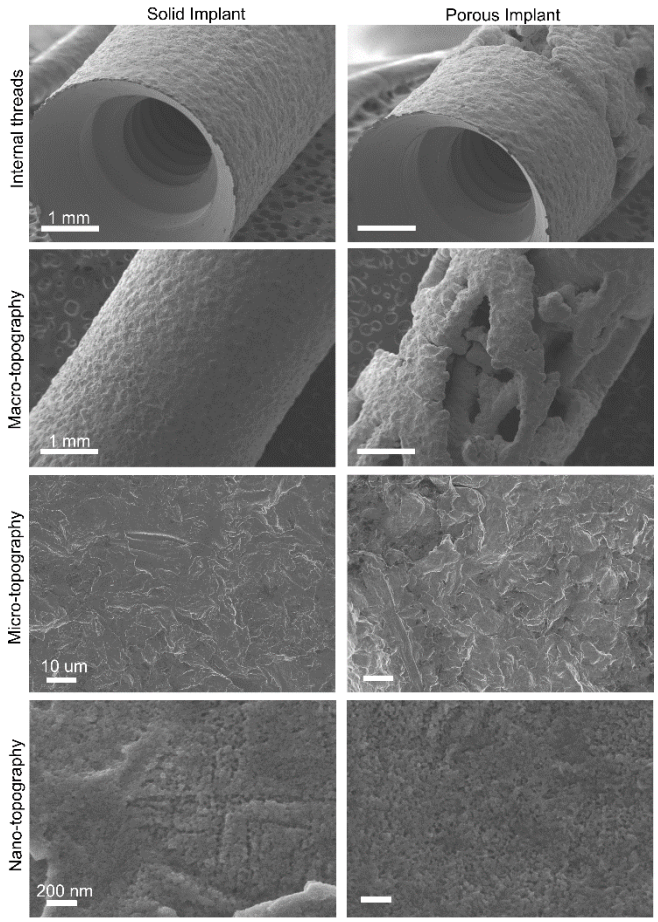

Figure 11.2. Scanning electron micrographs of solid (left) and porous (right) implants showing the macro- (top panel), micro- (middle panel) and nano-topography (bottom panel) after manufacturing and surface processing.

Table 11.1. Surface chemical composition of solid and porous implants obtained from x-ray photoelectron spectroscopy analysis.

Element	**Solid**	**Porous**
	Atomic Percent (Average ± Standard Error)	
C	59.3 ± 1.8	56.6 ± 3.1
O	29.9 ± 0.9	29.0 ± 1.9
Ti	3.4 ± 0.4	0.62 ± 0.2
N	3.1 ± 0.5	5.4 ± 0.7
Ca	2.4 ± 0.4	2.7 ± 0.1
Al	1.5 ± 0.7	2.9 ± 0.7
Na	0.2 ± 0.2	1.2 ± 0.2

Table 11.2. Surface roughness of solid and porous implants obtained from laser confocal microscopy analysis.

Element	Solid	Porous
	Roughness (Average ± Standard Error)	
Ra	2.66 ± 0.03	2.47 ± 0.10
Rz	24.22 ± 0.86	25.72 ± 1.32

Mechanical testing

Mechanical pull-out testing values for solid and porous implants after 10 weeks were 441.2±64.03 N and 501.5 ± 47.55 N, respectively (Figure 3A). These values were not significantly different. SEM images of the surface (Figure 3B) and microCT reconstructed (Figure 3C) images of implants after mechanical testing showed bone formation on both solid and porous implants. Bone was also observed in pores of porous implants.

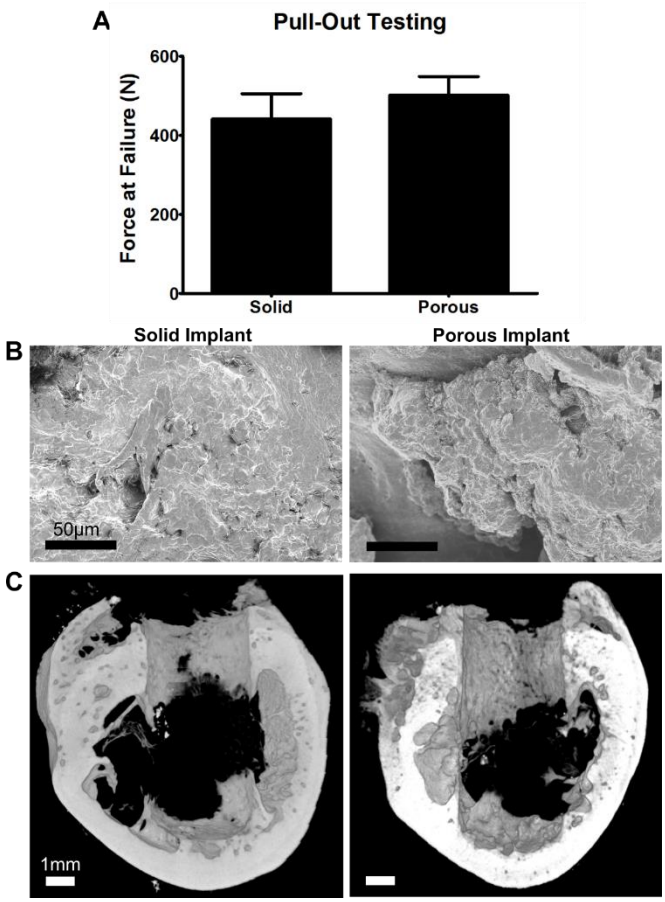

Figure 11.3. Pull-out testing force at failure (A); scanning electron micrographs (B) and microCT reconstructions (C) of implants after mechanical testing.

MicroCT

Axial and sagittal microCT reconstructions of solid and porous implants show bone growth around both implant groups (Figure 4). A view of the implant alone, bone around the implant a merged view show differences in bone growth around solid and porous implants. While mostly solid bone growth was achieved around solid implants, an interconnected network of trabecular-like bone was observed around and penetrating through porous implants.

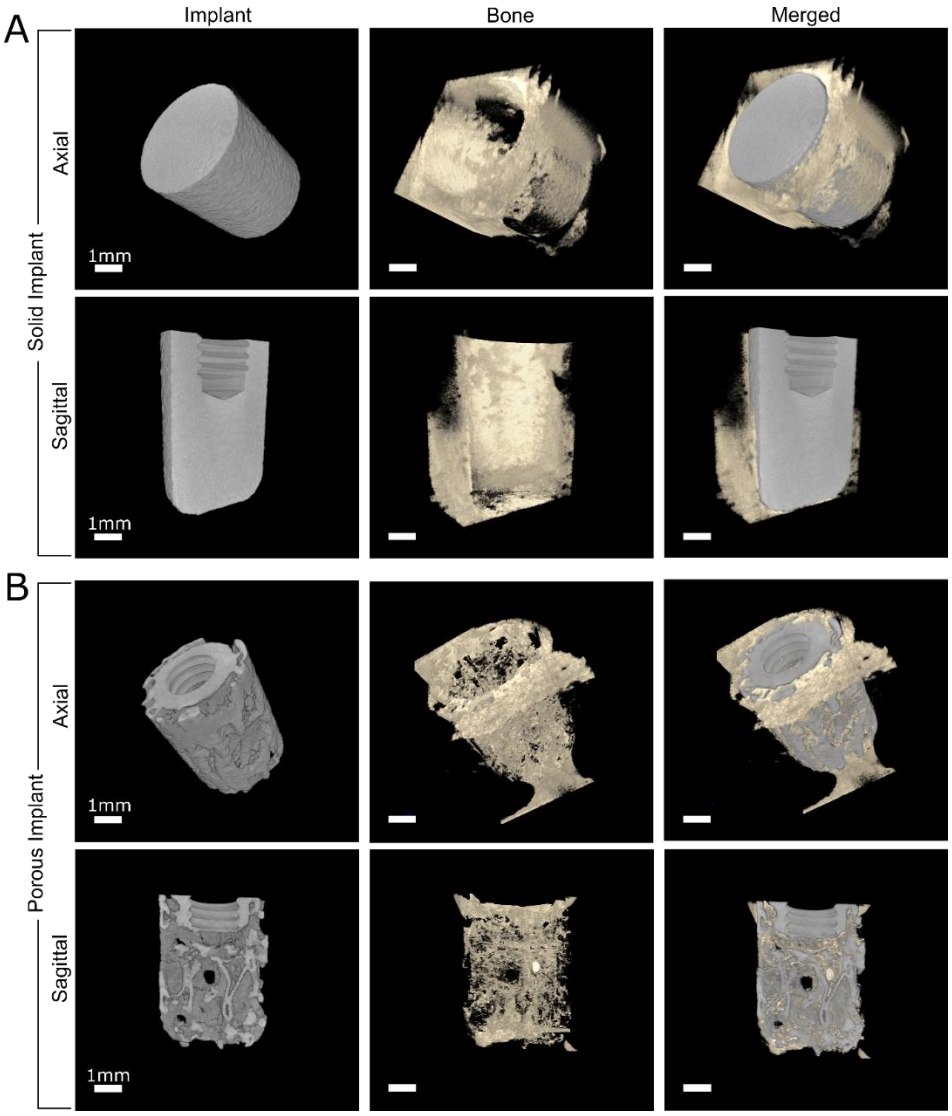

Figure 11.4. MicroCT three-dimensional reconstructions of solid (A) and porous implants (B) after 10 weeks in rabbit femurs. For each implant group, top panel shows axial cross section and bottom panel shows sagittal cross section.

MicroCT 3D reconstructions of implants in femurs showed bone formation around both solid and porous implants (Figure 5A). While dense bone formed around the outer cortex of solid implants, a porous bone network penetrated and formed throughout porous implants. Total bone volume within a VOI around porous implants was 20.7±1.2% of the entire implant volume, which was significantly higher than the 14.8±0.7% for solid implants (Figure 5B, Table 3). When isolated to just the apical portion of the implant, the

percentage of bone volume over implant volume was 17.9±1.8% (Figure 5C). This value was also significantly higher than the percent of bone analyzed within the same VOI for solid implants, which was 4.6±0.3%.

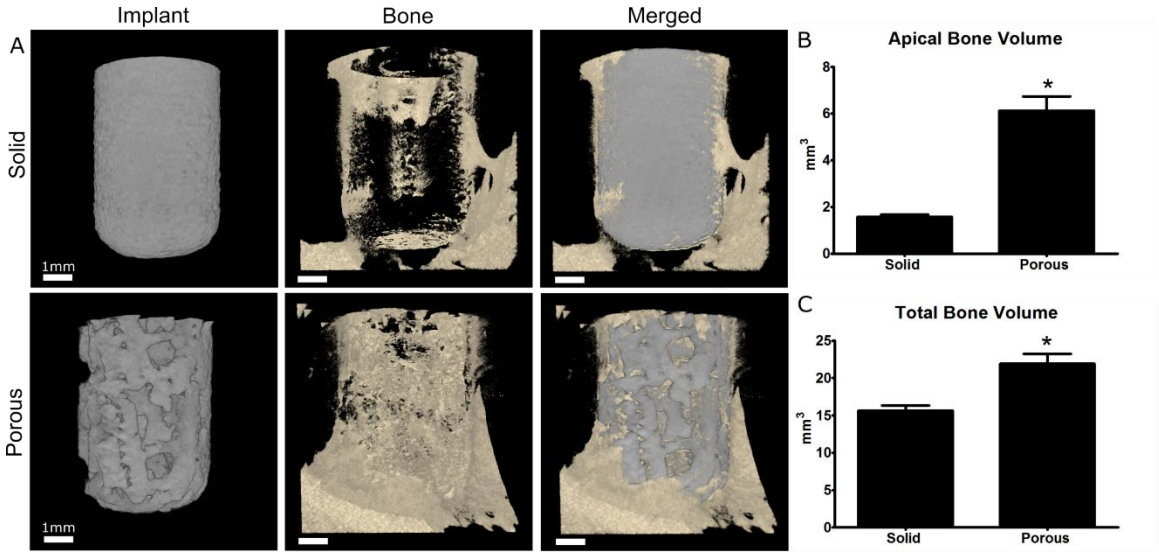

Figure 11.5. MicroCT three-dimensional reconstructions of solid and porous implants after 10 weeks in rabbit femurs (A). Total new bone volume within a defined volume of interest including on the lower apical portion of the implant (B) and for the entire implant (C).

Table 11.3. MicroCT and histological analysis of bone growth in and around solid and porous implants after 10 weeks of implantation in rabbit femora.

		Solid	**Porous**
		Average ± Standard Error	
MicroCT	Total bone volume	15.6 ± 0.72	21.9 ± 1.3
	Total bone volume / VOI (%)	14.8 ± 0.68	20.7 ± 1.2
	Total bone volume / pore volume (%)	--	46.2 ± 2.7
	Apical bone volume	1.6 ± 0.1	6.1 ± 0.6
	Apical bone volume / VOI (%)	4.6 ± 0.3	17.9 ± 1.8
Histology	Total bone area (mm^2)	3.7 ± 0.2	5.0 ± 0.5
	Total bone area / ROI (%)	16.4 ± 1.0	33.5 ± 4.0
	Total bone to implant contact	43.2 ± 5.8	39.5 ±5.6
	Total bone area / pore area (%)	--	20.1 ± 2.9
	Cortical bone to implant contact	66.8 ± 6.8	55.4 ± 10.0
	Marrow bone to implant contact	37.3 ± 6.9	34.7 ± 6.1
	Apical bone to implant contact	43.9 ± 10.0	44.6 ± 9.5

Histology

Histological sections of solid (Figure 11.6A) and porous (Figures 11.6B) implants provide a more detailed view of bone growth around implants. Bone was observed interfacing along the body of solid implants, while bone was observed both around inside pores of porous implants. Total BIC calculated the perimeter was not significantly different between solid and porous implants (Figure 11.6C). Total bone area within a fixed VOI containing the entire implant was significantly higher for porous compared to solid implants (Figure 11.6D). Bone area calculated within a fixed VOI near the apex of implants was also greater for porous compared to solid implants (Figure 11.6E).

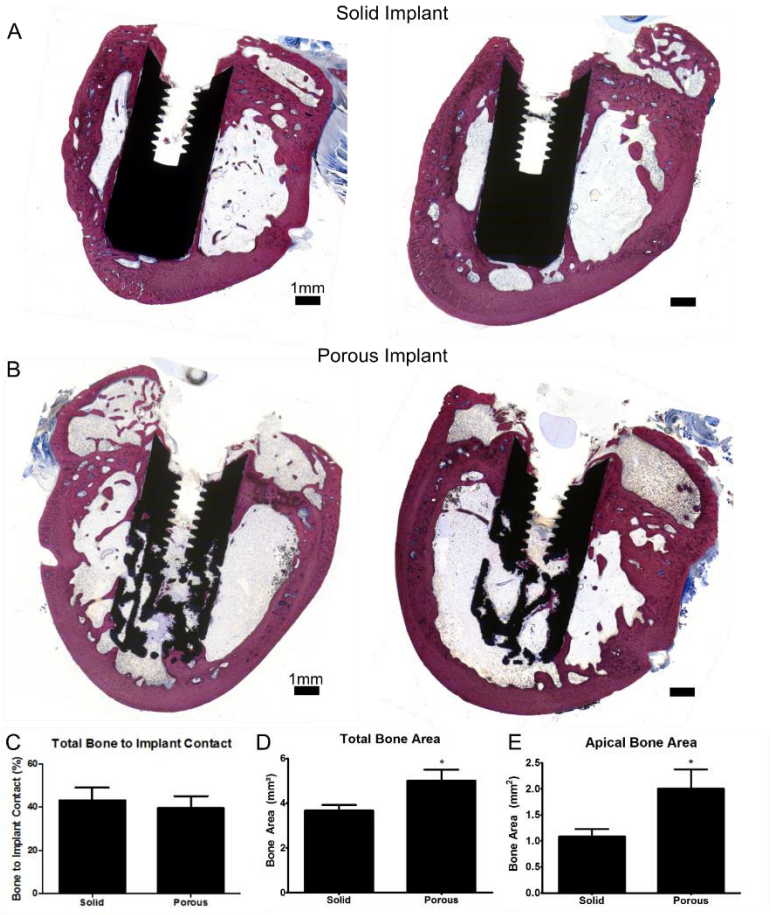

Figure 11.6. Histological cross sections of solid (A) and porous implants (B) in rabbit femurs after 10 weeks stained with Stevenel's Blue. Bone to implant contact values along the entire implant (C). Bone area within a defined region of interest encompassing the entire implant (D) and just the apical portion of the implant (E).

11.4. Discussion

Additive manufacturing has already shown great potential in the field of biomaterials, with laser sintering of Ti-6Al-4V already being implemented for bone-interfacing implants. However, in many cases, post-build surface modification was not used to enhance osseointegration. In this study, we used a rabbit femoral bone model to evaluate the osseointegration of laser sintered Ti-6Al-4V implants with micro-/nano-rough surfaces and trabecular bone-inspired porosity in comparison to solid implants with the same surface roughness. Implant characteristics were comparable to previously manufactured constructs used for *in vitro* studies [201]. The higher total porosity observed for the implants may be attributed to the use of a different VOI size and location analyzed in our implant geometry compared to our previous construct geometry, though pores were interconnected for both constructs. Our results confirmed that surface roughness was comparable across solid and porous implants, showing the versatility of surface treatments for different construct geometries.

Our group has shown that laser sintered Ti-6Al-4V solid implants placed in rabbit tibia cortical bone perform better than traditional implants manufactured with computer numerical control [378]. We have also shown in previous studies that porous implants with or without the use of an osteogenic agent (DBX, Musculoskeletal Transplant Foundation, Edison, New Jersey, USA) on rat calvaria did not show significant differences in mechanical pull-out testing or new bone volume analyzed by microCT [119]. However, histological analysis showed 16% of the implant pores still contained DBX, suggesting the potential for enhanced bone growth over time in DBX-treated sites. We did not use DBX or another osteogenic agent in this study in order to evaluate the comparative effects of

solid and 3D porous implants. However, we suggest that use of a bone graft substitute should still be considered for clinical cases requiring large volumes of bone regeneration.

Optimal pore size for osseointegration may vary with time, implant location, and surface treatment. A study comparing pore diameters of Ti implants in the rabbit tibia concluded that a 600μm pore diameter resulted in the most bone ingrowth and bone-material fixation compared to implants with 300μm and 900μm diameter pores over the 8 weeks of the experiment [409]. A study in the rabbit calvaria showed greater bone ingrowth into Ti scaffolds with a maximum pore size of 600μm after 3 weeks, while implants with a maximum pore size of 100μm showed superior bone growth after 20 weeks [184]. Early studies on porous hydroxyapatite implants in rabbit femora showed the presence of osteoclasts as early as 2 weeks, and continued remodeling up to 4 months after implantation [171]. In vitro data using 3D Ti mesh scaffolds suggest that bone growth and remodeling within the pores occur in cycles [37]. Thus, as new bone forms and remodels, changes will occur around the implant microenvironment that affect the rate and extent of bone formation, and these are influenced by the physical properties of the implant.

While our study suggests that additively manufactured implants with trabecular bone-inspired porosity can achieve superior results to solid implants, there are still limitations to our animal model and analysis. We chose the rabbit femur for implant placement because it better mimics the clinical placement of a dental or orthopaedic implant through both cortical and trabecular bone. This model is also more relevant than the calvarial onlay model, providing the ability to evaluate response to an implant size that could be used clinically. While vertical cortical bone formation had been previously observed in a cranial onlay model in rats, it was unclear how osseointegration would occur

horizontally within the trabeculae [119]. For orthopaedic implants and dental implant placement in the mandible, the ratio of cortical to cancellous bone contributes to primary stability and long term success [410, 411]. Our rabbit femoral implant model does not account for uniaxial mechanical loading, which is a major consideration when placing dental implants. Reports also indicate that bone remodeling in the mandible occurs more rapidly than in the femur, with distinct regeneration properties [412]. This may be due to mechanical forces experienced by the implant, as well as a different local microenvironment or system effects induced by implantation.

In addition, solid and porous implants used in this study both possessed a solid portion at the top of the implant for internal screw fixation. Because implants were inserted transaxially into the femur, the cortical shell came into contact with both the solid and porous portions of the porous implant. Thus, pull-out testing could not completely isolate the effects of a porous implant on mechanical strength. Analysis of apical portions of implants in both groups via histology and microCT show that more bone is present in and around porous compared to solid implants, suggesting that mechanical strength is enhanced in porous areas.

Finally, this study only evaluated osseointegration of implants at one time point, 10 weeks after implantation. Previous studies have shown differences in bone healing around hydroxyapatite implants placed in rabbits up to 6 months after implantation [171]. Work from our group has also shown varied response to additively manufactured implants at 5 weeks compared to 10 weeks [119]. It may be possible that differences in healing occurred at an earlier time point, but stabilized for both implants after 10 weeks.

Not only did new cortical and trabecular bone form in porous implants and around both solid and porous implants, but the presence of new bone was also observed above and covering the implant. This was particularly obvious in histological sections, which showed another layer of trabecular bone, marrow and cortical bone above the originally existing cortical bone. Previous studies have observed similar vertical bone growth along titanium implants placed in rabbit mandibles [413, 414]. However, the implants were placed with at least 2mm exposed above the mandible to support supracrestal bone formation. In contrast, we observed vertical bone growth in this study over the implant and cover screw, without a physical implant presence to guide bone formation.

This phenomenon was also distinctly different than a bony callus, which has shown to result in cortical union by day 28 after fracture in the rabbit tibia [415]. The presence of an additional cortical and cancellous bone layer above the implant in our study after 10 weeks indicates that the bone was no longer in the callus stage of healing. Early studies of porous-coated intramedullary implants placed in beagle femurs showed that cortical bone formation occurred near the endosteal cortex, but also when placed up to 2mm away from the endosteum [416]. While multipotent stem cells and progenitor cells may contribute to trabecular bone formation within the medullary canal, our results suggest the cortical bone formation may be influenced first by cells from the endosteal cortex. This corroborates other findings that suggest cortical bone contributes to distant osteogenesis [417].

11.5. Conclusion

Porous Ti-6Al-4V constructs with surface roughness have shown enhanced cell response and mineralization *in vitro*. In this study, we observe osseointegration of these

implants in a clinically relevant size with the rabbit femur. While both solid and porous implants were osseointegrated, porous implants allowed significantly more bone growth in some applications. This study suggests that additive manufacturing of porous Ti-6Al-4V implants may enhance osseointegration clinically compared to solid implants, and may be used to improve long term clinical outcomes.

CHAPTER 12

CONCLUSIONS AND FUTURE DIRECTIONS

This thesis has presented multiple studies that indicate the clinical potential of bone interfacing titanium implants with hierarchical structural features at the macro-, micro- and nano-scales. Starting at the two dimensional micro- and nano-scales and moving to include macro-porosity, these studies validate the enhanced in vitro and in vivo results of titanium implant materials designed with hierarchical structural features.

A novel low-temperature nano-modification method was first developed on a clinically micro-rough, solid titanium substrate that is an established model in the literature. While improving wettability, nano-modification did not result in appreciable differences in osteoblast surfaces. This first study was essential to understanding that not all nano is good nano, which has been an ongoing controversy in biomaterials research. In order to further elucidate differences in cell response to smooth and micro-/nano-rough substrates, a correlative microscopy method was developed that allowed for characterization of the cell-material interface across multiple imaging modalities and spatial scales. As a proof of concept, this platform method was used to characterize smooth and rough Ti-6Al-4V substrates that were additively manufactured by laser sintering. Clear morphological differences were observed for cells on smooth compared to rough substrates. These results lead to a more in depth study on osteoblast differentiation and maturation on smooth and rough laser sintered surfaces, which also showed that laser sintered implants can be used as a replacement for conventionally manufactured implants.

After micro- and nano-scale surface roughness was evaluated on laser sintered substrates, porosity was introduced to create constructs with unique bio-inspired trabecular

bone porosity. An osteoblast cell line, primary human osteoblasts and human mesenchymal stem cells were used to evaluate the effect of combined surface roughness and porosity on osteoblastic differentiation and maturation. These results indicated that biological response to three-dimensional environments may be maturation, donor and cell-type dependent. Medium porosity constructs were chosen for further evaluation of human MSC mineralization, indicating that constructs were effective in stimulating bone formation in vitro. Implants placed on the rat calvaria indicated the potential of a 3D architecture to stimulate vertical bone growth even with demineralized bone matrix, which is rarely achieved clinically. Implants placed through the rabbit femur corroborate the good osseointegration achieved in rats, with newly formed trabecular and cortical bone penetrating into pores. These studies present the clinical relevance of a novel implant macro-architecture with hierarchical surface roughness.

This work has also identified specific structural features that contribute to biological response. Future rational design of titanium biomaterials should take into consideration the macro-porosity, micro- and nano-scale surface roughness, hydrophilicity, crystinallinity and surface chemistry for optimal osseointegration (Table 12.1).

Because this work was conducted in the laboratory, the next step in translating these implants to clinical use is to work with the FDA on a 501(k) device clearance. Depending on the implant novelty, a clinical trial may be required. Additional implant characterization may also be required to show similarity to a predicate device. Though dental implants were manufactured in this study, application to orthopaedic implants may require a separate approval process.

Table 12.1. Variables for future rational design of titanium bone-interfacing implants

Variable	Conclusions from this work
Macro-scale porosity	Interconnected porosity with >60% total porosity contributes to bone ingrowth
Bio-inspired implant design	Osteoblast differentiation and maturation factors increase on constructs with a porosity that captures that of human trabecular bone with high fidelity and micro-/nano-scale surface roughness
Micro-topography	Micro-scale roughness increases osteoblast differentiation and maturation
Nano-topography	Nano-scale roughness has variable effects on production of factors for osteoblastic differentiation, bone remodeling and blood vessel formation. Nano-topography increases osteoblast filopodia and may affect attachment and spreading.
Surface chemistry	Titanium surfaces stored under ambient conditions will accumulate hydrocarbon contamination, which can be reduced by hydrothermal processing
Surface energy	Hydrophilicity of hydrothermally modified substrates can be preserved by storage in saline
Titanium oxide crystallinity	Factors for osteoblast differentiation and maturation increase on monocrystalline rutile compared to anatase or polycrystalline rutile/anatase titanium oxide

Once approved for human use, further studies can analyze the effects of porosity personalized to each patient's trabecular bone architecture. Included in this future work should also be a control with a randomized porous architecture to compare biological response to specific trabecular porosity with a control porosity. This would have clinical application to patients with low bone density, placement of dental implants in different locations of the mouth corresponding to a different quality of bone, and for orthopaedic implants placed in areas receiving different load orientations. These studies would be performed in various established animal models in our lab and that are found in literature.

In addition, the effect of trabecular porosity on compromised patients, such as smokers or those with osteoporosis, could be investigated in disease model animals.

In addition, mechanisms of enhanced cell response on 3D compared to 2D environments should be investigated with respect to the mechanical and fluid stresses experienced by cells. Fluid shear stress, surface curvature and material stiffness are all variables that cells experience and can modulate behavior. While we performed cell studies in static culture, the availability of oxygen and nutrients throughout the scaffold may still exist as a gradient. These differences would be amplified in the body, where bodily movement, mechanical forces and blood flow exist. This may create different microenvironments within the pores for cells, where signaling could exist in a positive or negative feedback loop. In addition, hardness of the underlying bulk substrate, elastic modulus and flexural strength should be additionally characterized to correlate with changes in construct design. Understanding the effects of mechanical forces could provide great insight into the biological consequences of the designed structural components.

Finally, cellular signaling in response to curvature and porosity should be studied. The strength and weakness of using a trabeculae-inspired porosity is that it contributes to a combined effect on cell response, and is therefore difficult to isolate and test specific variables of the scaffold. While the correlative analysis presented in this thesis can be used to analyze single cell response to surfaces, limits in imaging technology prevent analysis of cells more than 500μm in porous constructs. However, further investigation into specific cellular mechanisms using averaged gene expression and protein studies over time can contribute to a better picture of the events leading to enhanced osteoblast response. Preliminary studies should focus on the expression of integrins, which are cell receptors

required for attachment to proteins adsorbed on any biomaterial surface. Attached integrins typically organize into larger focal adhesions, which can provide mechanical stability and transmit forces via the cytoskeletal network. Though our lab has shown that specific integrins also contribute to downstream response of cells on rough titanium substrates, this profile may be different when a 3D environment is introduced.

Additively manufactured personalized implants, once a concept in science fiction, is quickly becoming reality. These advancements in healthcare are made possible by open communication, collaboration and innovation at the intersection of medicine and engineering. As technology progresses at an increasing pace, it is important to remain unbiased, curious and to always keep the patient in mind.

REFERENCES

[1] Orthopedics data compendium: use, cost, and market structure for total joint replacement. Oakland, CA: Integrated Healthcare Association; 2006.

[2] The 2005-06 Survey of dental services rendered. Chicago, IL: American Dental Association; 2007.

[3] Hadi S, Ashfaq N, Bey A, Khan S. Biological factors responsible for failure of osseointegration in oral implants. Biol Med. 2011;3:164-70.

[4] Scully C, Hobkirk J, Dios P. Dental endosseous implants in the medically compromised patient. J Oral Rehabil. 2007;34:590-9.

[5] Anner R, Grossmann Y, Anner Y, Levin L. Smoking, diabetes mellitus, periodontitis, and supportive periodontal treatment as factors associated with dental implant survival: a long-term retrospectivce evaluations of patients followed for up to 10 years. Implant Dent. 2010;19:57-64.

[6] Raines AL, Olivares-Navarrete R, Wieland M, Cochran DL, Schwartz Z, Boyan B. Regulation of angiogenesis during osseointegration by titanium surface microstructure and energy. Biomaterials. 2010;31:4909-17.

[7] Olivares-Navarrete R, Hyzy SL, Hutton DL, Erdman CP, Wieland M, Boyan BD, et al. Direct and indirect effects of microstructured titanium substrates on the induction of mesenchymal stem cell differentiation towards the osteoblast lineage. Biomaterials. 2010;31:2728-35.

[8] Sjostrom T, Fox N, Su B. Through-mask anodization of titania dot- and pillar-like nanostructures on bulk Ti substrates using a nanoporous anodic alumina mask. Nanotechnology. 2009;20:135305.

[9] Gittens RA, McLachlan T, Olivares-Navarrete R, Cai Y, Berner S, Tannenbaum R, et al. The effects of combined micron-/submicron-scale surface roughness and nanoscale features on cell proliferation and differentiation. Biomaterials. 2011;32:3395-403.

[10] Bjursten LM, Rasmusson L, Oh S, Smith GC, Brammer KS, Jin S. Titanium dioxide nanotubes enhance bone bonding in vivo. Journal of biomedical materials research Part A. 2010;92A:1218-24.

[11] Cheng H-C. Titanium nanostructural surface processing for improved biocompatibility. Appl Phys Lett. 2006;89:173902--3.

[12] Ogawa T, Saruwatari L, Takeuchi K, Aita H, Ohno N. Ti nano-nodular structuring for bone integration and regeneration. J Dent Res. 2008;87:751-6.

[13] Bandyopadhyay A, Espana F, Balla VK, Bose S, Ohgami Y, Davies NM. Influence of porosity on mechanical properties and in vivo response of Ti6Al4V implants. Acta Biomater. 2010;6:1640-8.

[14] Buser D, Schenk RK, Steinemann S, Fiorellini JP, Fox CH, Stich H. Influence of surface characteristics on bone integration of titanium implants. A histomorphometric study in miniature pigs. Journal of biomedical materials research. 1991;25:889-902.

[15] Claes L, Recknagel S, Ignatius A. Fracture healing under healthy and inflammatory conditions. Nature reviews Rheumatology. 2012;8:133-43.

[16] Bianco P, Cao X, Frenette PS, Mao JJ, Robey PG, Simmons PJ, et al. The meaning, the sense and the significance: translating the science of mesenchymal stem cells into medicine. Nat Med. 2013;19:35-42.

[17] Coelho PG, Granjeiro JM, Romanos GE, Suzuki M, Silva NRF, Cardaropoli G, et al. Basic research methods and current trends of dental implant surfaces. J Biomed Mater Res Part B Appl Biomater. 2009;88B:579-96.

[18] Schwartz Z, Kieswetter K, Dean DD, Boyan BD. Underlying mechanisms at the bone-surface interface during regeneration. J Periodontal Res. 1997;32:166-71.

[19] Wennerberg A, Albrektsson T. Effects of titanium surface topography on bone integration: a systematic review. Clinical oral implants research. 2009;20 Suppl 4:172-84.

[20] Cochran DL, Schenk RK, Lussi A, Higginbottom FL, Buser D. Bone response to unloaded and loaded titanium implants with a sandblasted and acid-etched surface: a histometric study in the canine mandible. Journal of biomedical materials research. 1998;40:1-11.

[21] Olivares-Navarrete R, Hyzy SL, Park JH, Dunn GR, Haithcock DA, Wasilewski CE, et al. Mediation of osteogenic differentiation of human mesenchymal stem cells on titanium surfaces by a Wnt-integrin feedback loop. Biomaterials. 2011;32:6399-411.

[22] Gittens RA, Olivares-Navarrete R, Cheng A, Anderson DM, McLachlan T, Stephan I, et al. The roles of titanium surface micro/nanotopography and wettability on the differential response of human osteoblast lineage cells. Acta Biomater. 2013;9:6268-77.

[23] Schwartz Z, Raz P, Zhao G, Barak Y, Tauber M, Yao H, et al. Effect of micrometer-scale roughness of the surface of Ti6Al4V pedicle screws in vitro and in vivo. J Bone Joint Surg Am. 2008;90:2485-98.

[24] Mansoori GA, Soelaiman TAF. Nanotechnology — an introduction for the standards community. JAI. 2005;2.

[25] Gittens RA, Olivares-Navarrete R, Schwartz Z, Boyan BD. Implant osseointegration and the role of microroughness and nanostructures: Lessons for spine implants. Acta Biomater. 2014;10:3363-71.

[26] Mendonça G, Mendonça DBS, Aragão FJL, Cooper LF. Advancing dental implant surface technology – From micron- to nanotopography. Biomaterials. 2008;29:3822-35.

[27] Wennerberg A, Svanborg LM, Berner S, Andersson M. Spontaneously formed nanostructures on titanium surfaces. Clinical oral implants research. 2013;24:203-9.

[28] Olivares-Navarrete R, Rodil SE, Hyzy SL, Dunn GR, Almaguer-Flores A, Schwartz Z, et al. Role of integrin subunits in mesenchymal stem cell differentiation and osteoblast maturation on graphitic carbon-coated microstructured surfaces. Biomaterials. 2015;51:69-79.

[29] Park JH, Wasilewski CE, Almodovar N, Olivares-Navarrete R, Boyan BD, Tannenbaum R, et al. The responses to surface wettability gradients induced by chitosan nanofilms on microtextured titanium mediated by specific integrin receptors. Biomaterials. 2012;33:7386-93.

[30] Park JH, Olivares-Navarrete R, Wasilewski CE, Boyan BD, Tannenbaum R, Schwartz Z. Use of polyelectrolyte thin films to modulate Osteoblast response to microstructured titanium surfaces. Biomaterials. 2012;33:5267-77.

[31] Zhao G, Raines AL, Wieland M, Schwartz Z, Boyan BD. Requirement for both micron- and submicron scale structure for synergistic responses of osteoblasts to substrate surface energy and topography. Biomaterials. 2007;28:2821-9.

[32] Rupp F, Scheideler L, Olshanska N, de Wild M, Wieland M, Geis-Gerstorfer J. Enhancing surface free energy and hydrophilicity through chemical modification of microstructured titanium implant surfaces. Journal of biomedical materials research Part A. 2006;76A:323-34.

[33] Wang X, Gittens RA, Song R, Tannenbaum R, Olivares-Navarrete R, Schwartz Z, et al. Effects of structural properties of electrospun TiO2 nanofiber meshes on their osteogenic potential. Acta Biomater. 2012;8:878-85.

[34] Olivares-Navarrete R, Hyzy SL, Berg ME, Schneider JM, Hotchkiss K, Schwartz Z, et al. Osteoblast lineage cells can discriminate microscale topographic features on titanium–aluminum–vanadium surfaces. Annals of biomedical engineering. 2014;42:2551-61.

[35] Vandrovcova M, Hanus J, Drabik M, Kylian O, Biederman H, Lisa V, et al. Effect of different surface nanoroughness of titanium dioxide films on the growth of human osteoblast-like MG63 cells. Journal of biomedical materials research Part A. 2012;100:1016-32.

[36] Pae A, Kim SS, Kim HS, Woo YH. Osteoblast-like cell attachment and proliferation on turned, blasted, and anodized titanium surfaces. The International journal of oral & maxillofacial implants. 2011;26:475-81.

[37] Wang X, Schwartz Z, Gittens RA, Cheng A, Olivares-Navarrete R, Chen H, et al. Role of integrin α2β1 in mediating osteoblastic differentiation on three-dimensional titanium scaffolds with submicron-scale texture. Journal of biomedical materials research Part A. 2015;103:1907-18.

[38] Cheng A, Humayun A, Cohen DJ, Boyan BD, Schwartz Z. Additively manufactured 3D porous Ti-6Al-4V constructs mimic trabecular bone structure and regulate osteoblast proliferation, differentiation and local factor production in a porosity and surface roughness dependent manner. Biofabrication. 2014;6:045007.

[39] Gittens RA, Scheideler L, Rupp F, Hyzy SL, Geis-Gerstorfer J, Schwartz Z, et al. A review on the wettability of dental implant surfaces II: Biological and clinical aspects. Acta Biomater. 2014;10:2907-18.

[40] Kopf BS, Ruch S, Berner S, Spencer ND, Maniura-Weber K. The role of nanostructures and hydrophilicity in osseointegration: In-vitro protein-adsorption and blood-interaction studies. Journal of biomedical materials research Part A. 2015;103:2661-72.

[41] Urist MR. Bone: formation by autoinduction. Science. 1965;150:893-9.

[42] Wozney JM, Rosen V, Celeste AJ, Mitsock LM, Whitters MJ, Kriz RW, et al. Novel regulators of bone formation: molecular clones and activities. Science. 1988;242:1528-34.

[43] Esposito M, Grusovin MG, Kwan S, Worthington HV, Coulthard P. Interventions for replacing missing teeth: bone augmentation techniques for dental implant treatment. The Cochrane database of systematic reviews. 2008:CD003607.

[44] Olivares-Navarrete R, Hyzy SL, Hutton DL, Dunn GR, Appert C, Boyan BD, et al. Role of non-canonical Wnt signaling in osteoblast maturation on microstructured titanium surfaces. Acta Biomater. 2011;7:2740-50.

[45] Olivares-Navarrete R, Hyzy S, Wieland M, Boyan BD, Schwartz Z. The roles of Wnt signaling modulators Dickkopf-1 (Dkk1) and Dickkopf-2 (Dkk2) and cell maturation state in osteogenesis on microstructured titanium surfaces. Biomaterials. 2010;31:2015-24.

[46] Baksh D, Boland GM, Tuan RS. Cross-talk between Wnt signaling pathways in human mesenchymal stem cells leads to functional antagonism during osteogenic differentiation. J Cell Biochem. 2007;101:1109-24.

[47] Doroudi M, Olivares-Navarrete R, Hyzy SL, Boyan BD, Schwartz Z. Signaling components of the 1α,25(OH)2D3-dependent Pdia3 receptor complex are required for Wnt5a calcium-dependent signaling. Biochim Biophys Acta. 2014;1843:2365-75.

[48] Boyan BD, Batzer R, Kieswetter K, Liu Y, Cochran DL, Szmuckler-Moncler S, et al. Titanium surface roughness alters responsiveness of MG63 osteoblast-like cells to 1 alpha,25-(OH)2D3. Journal of biomedical materials research. 1998;39:77-85.

[49] Olivares-Navarrete R, Hyzy SL, Pan Q, Dunn G, Williams JK, Schwartz Z, et al. Osteoblast maturation on microtextured titanium involves paracrine regulation of bone morphogenetic protein signaling. Journal of biomedical materials research Part A. 2015;103:1721-31.

[50] Hyzy SL, Olivares-Navarrete R, Hutton DL, Tan C, Boyan BD, Schwartz Z. Microstructured titanium regulates interleukin production by osteoblasts, an effect modulated by exogenous BMP-2. Acta Biomater. 2013;9:5821-9.

[51] Olivares-Navarrete R, Hyzy SL, Slosar PJ, Schneider JM, Schwartz Z, Boyan BD. Implant materials generate different peri-implant inflammatory factors: poly-ether-ether-ketone promotes fibrosis and microtextured Titanium promotes osteogenic factors. Spine. 2015;40:399-404.

[52] Schwartz Z, Olivares-Navarrete R, Wieland M, Cochran DL, Boyan BD. Mechanisms regulating increased production of osteoprotegerin by osteoblasts cultured on microstructured titanium surfaces. Biomaterials. 2009;30:3390-6.

[53] Bonewald L, GR M. Role of transforming growth factor-beta in bone remodeling. Clin Orthop Relat Res. 1990;250:261-76.

[54] Kieswetter K, Schwartz Z, Hummert TW, Cochran DL, Simpson J, Dean DD, et al. Surface roughness modulates the local production of growth factors and cytokines by osteoblast-like MG-63 cells. Journal of biomedical materials research. 1996;32:55-63.

[55] Lai M, Hermann CD, Cheng A, Olivares-Navarrete R, Gittens RA, Bird MM, et al. Role of α2β1 integrins in mediating cell shape on microtextured titanium surfaces. Journal of biomedical materials research Part A. 2015;103:564-73.

[56] Olivares-Navarrete R, Raz P, Zhao G, Chen J, Wieland M, Cochran DL, et al. Integrin α2β1 plays a critical role in osteoblast response to micron-scale surface structure and surface energy of titanium substrates. Proc Natl Acad Sci U S A. 2008;105:15767-72.

[57] Gittens RA, Olivares-Navarrete R, Hyzy SL, Sandhage KH, Schwartz Z, Boyan BD. Superposition of nanostructures on microrough titanium–aluminum–vanadium alloy surfaces results in an altered integrin expression profile in osteoblasts. Connect Tissue Res. 2014;55:164-8.

[58] Clover J, Dodds RA, Gowen M. Integrin subunit expression by human osteoblasts and osteoclasts in situ and in culture. Journal of cell science. 1992;103 (Pt 1):267-71.

[59] Bianco P, Robey PG, Simmons PJ. Mesenchymal stem cells: Revisiting history, concepts, and assays. Cell Stem Cell. 2008;2:313-9.

[60] Siddappa R, Licht R, van Blitterswijk C, de Boer J. Donor variation and loss of multipotency during in vitro expansion of human mesenchymal stem cells for bone tissue engineering. J Orthop Res. 2007;25:1029-41.

[61] Tosi LL, Boyan BD, Boskey AL. Does sex matter in musculoskeletal health? A workshop report. Orthop Clin North Am. 2006;37:523-9.

[62] Lohmann CH, Tandy EM, Sylvia VL, Hell-Vocke AK, Cochran DL, Dean DD, et al. Response of normal female human osteoblasts (NHOst) to 17β-estradiol is modulated by implant surface morphology. Journal of biomedical materials research. 2002;62:204-13.

[63] Olivares-Navarrete R, Hyzy SL, Chaudhri RA, Zhao G, Boyan BD, Schwartz Z. Sex dependent regulation of osteoblast response to implant surface properties by systemic hormones. Biology of sex differences. 2010;1:4.

[64] Olivares-Navarrete R, Hyzy SL, Boyan BD, Schwartz Z. Regulation of osteoblast differentiation by acid-etched and/or grit-blasted titanium substrate topography is enhanced by 1,25(OH)2D3 in a sex-dependent manner. BioMed research international. 2015;2015:365014.

[65] Olivares-Navarrete R, Raines AL, Hyzy SL, Park JH, Hutton DL, Cochran DL, et al. Osteoblast maturation and new bone formation in response to titanium implant surface features are reduced with age. J Bone Miner Res. 2012;27:1773-83.

[66] Zhao L, Mei S, Chu PK, Zhang Y, Wu Z. The influence of hierarchical hybrid micro/nano-textured titanium surface with titania nanotubes on osteoblast functions. Biomaterials. 2010;31:5072-82.

[67] Martínez E, Engel E, Planell JA, Samitier J. Effects of artificial micro- and nano-structured surfaces on cell behaviour. Ann Anat. 2009;191:126-35.

[68] Frase CG, Buhr E, Dirscherl K. CD characterization of nanostructures in SEM metrology. Meas Sci Technol. 2007;18:510.

[69] Rupp F, Gittens RA, Scheideler L, Marmur A, Boyan BD, Schwartz Z, et al. A review on the wettability of dental implant surfaces I: theoretical and experimental aspects. Acta Biomater. 2014;10:2894-906.

[70] Karoussis IK, Salvi GE, Heitz-Mayfield LJ, Bragger U, Hammerle CH, Lang NP. Long-term implant prognosis in patients with and without a history of chronic periodontitis: a 10-year prospective cohort study of the ITI Dental Implant System. Clinical oral implants research. 2003;14:329-39.

[71] Steinemann SG. Titanium — the material of choice? Periodontol 2000. 1998;17:7-21.

[72] Boyan BD, Lossdorfer S, Wang L, Zhao G, Lohmann CH, Cochran DL, et al. Osteoblasts generate an osteogenic microenvironment when grown on surfaces with rough microtopographies. European cells & materials. 2003;6:22-7.

[73] Buser D, Nydegger T, Oxland T, Cochran DL, Schenk RK, Hirt HP, et al. Interface shear strength of titanium implants with a sandblasted and acid-etched surface: a biomechanical study in the maxilla of miniature pigs. Journal of biomedical materials research. 1999;45:75-83.

[74] Wennerberg A, Galli S, Albrektsson T. Current knowledge about the hydrophilic and nanostructured SLActive surface. Clin Cosmet Investig Dent. 2011;3:59-67.

[75] Divya Rani VV, Vinoth-Kumar L, Anitha VC, Manzoor K, Deepthy M, Shantikumar VN. Osteointegration of titanium implant is sensitive to specific nanostructure morphology. Acta Biomater. 2012;8:1976-89.

[76] Variola F, Vetrone F, Richert L, Jedrzejowski P, Yi J-H, Zalzal S, et al. Improving biocompatibility of implantable metals by nanoscale modification of surfaces: an overview of strategies, fabrication methods, and challenges. Small. 2009;5:996-1006.

[77] Latella BA, Gan BK, Li H. Fracture toughness and adhesion of thermally grown titanium oxide on medical grade pure titanium. Surf Coat Tech. 2007;201:6325-31.

[78] Liu Z, Welsch G. Effects of oxygen and heat treatment on the mechanical properties of alpha and beta titanium alloys. MTA. 1988;19:527-42.

[79] Braem A, Van Mellaert L, Mattheys T, Hofmans D, De Waelheyns E, Geris L, et al. Staphylococcal biofilm growth on smooth and porous titanium coatings for biomedical applications. Journal of biomedical materials research Part A. 2014;102:215-24.

[80] Puckett SD, Taylor E, Raimondo T, Webster TJ. The relationship between the nanostructure of titanium surfaces and bacterial attachment. Biomaterials. 2010;31:706-13.

[81] Gedye R, Smith F, Westaway K, Ali H, Baldisera L, Laberge L, et al. The use of microwave ovens for rapid organic synthesis. Tetrahedron Lett 1986;27:279-82.

[82] Komarneni S, Roy R, Li Q. Microwave-hydrothermal synthesis of ceramic powders. Mater Res Bull. 1992;27:1393-405.

[83] de la Hoz A, Diaz-Ortiz A, Moreno A. Microwaves in organic synthesis. Thermal and non-thermal microwave effects. Chem Soc Rev. 2005;34:164-78.

[84] Wiesbrock F, Hoogenboom R, Schubert US. Microwave-assisted polymer synthesis: state-of-the-art and future perspectives. Macromol Rapid Comm. 2004;25:1739-64.

[85] Ibacache RAG, Vernon J, Sandhage KH, Boyan BD. Surface modification of implant devices. U.S. Patent Application 20140329052. November 6, 2014.

[86] Kitashima T, Liu LJ, Murakami H. Numerical analysis of oxygen transport in alpha titanium during isothermal oxidation. J Electrochem Soc. 2013;160:C441-C4.

[87] Ouchi C, Iizumi H, Mitao S. Effects of ultra-high purification and addition of interstitial elements on properties of pure titanium and titanium alloy. Mater Sci Eng A-Struct. 1998;243:186-95.

[88] Kofstad P, Hauffe K, Kjollesdal H. Investigation on the oxidation mechanism of titanium. Acta Chem Scand. 1958;12:239-66.

[89] Wu J-M. Low-temperature preparation of titania nanorods through direct oxidation of titanium with hydrogen peroxide. J Cryst Growth. 2004;269:347-55.

[90] Sun J, Gao L. pH effect on titania-phase transformation of precipitates from titanium tetrachloride solutions. J Am Chem Soc. 2002;85:2382-4.

[91] Zhang L, Tian L, Liu Y, Tan T, Liu D, Wang C. Synthesis of tapered tetragonal nanorods of anatase TiO2 with enhanced photocatalytic activity via a sol-hydrothermal process mediated by H2O2 and NH3. J Mater Chem A. 2015;3:15265-73.

[92] Li T, Tian B, Zhang J, Dong R, Wang T, Yang F. Facile Tailoring of Anatase TiO2 Morphology by Use of H2O2: From Microflowers with Dominant {101} Facets to Microspheres with Exposed {001} Facets. Ind Eng Chem Res. 2013;52:6704-12.

[93] Kobayashi M, Petrykin V, Tomita K, Kakihana M. Hydrothermal synthesis of brookite-type titanium dioxide with snowflake-like nanostructures using a water-soluble citratoperoxotitanate complex. J Cryst Growth. 2011;337:30-7.

[94] Morishima Y, Kobayashi M, Petrykin V, Kakihana M, Tomita K. Microwave-assisted hydrothermal synthesis of brookite nanoparticles from a water-soluble titanium complex and their photocatalytic activity. J Ceram Soc Jpn. 2007;115:826-30.

[95] Ryu YB, Lee MS, Jeong ED, Kim HG, Jung WY, Baek SH, et al. Hydrothermal synthesis of titanium dioxides from peroxotitanate solution using different amine group-containing organics and their photocatalytic activity. Catal Today. 2007;124:88-93.

[96] Qian Y, Chen Q, Chen Z, Fan C, Zhou G. Preparation of ultrafine powders of TiO2 by hydrothermal H2O2 oxidation starting from metallic Ti. J Mater Chem. 1993;3:203-5.

[97] Matthews A. The crystallization of anatase and rutile from amorphous titanium dioxide under hydrothermal conditions. Am Mineral. 1976;61:419-24.

[98] Cheng H, Ma J, Zhao Z, Qi L. Hydrothermal preparation of uniform nanosize rutile and anatase particles. Chem Mater. 1995;7:663-71.

[99] Aruna ST, Tirosh S, Zaban A. Nanosize rutile titania particle synthesis a hydrothermal method without mineralizers. J Mater Chem. 2000;10:2388-91.

[100] Finnegan MP, Zhang H, Banfield JF. Phase stability and transformation in titania nanoparticles in aqueous solutions dominated by surface energy. J Phys Chem C. 2007;111:1962-8.

[101] Hiroki A, LaVerne JA. Decomposition of hydrogen peroxide at water−ceramic oxide interfaces. J Phys Chem B. 2005;109:3364-70.

[102] Scharnweber D, Schlottig F, Oswald S, Becker K, Worch H. How is wettability of titanium surfaces influenced by their preparation and storage conditions. J Mater Sci-Mater M. 2010;21:525-32.

[103] Zuldesmi M, Waki A, Kuroda K, Okido M. Hydrothermal treatment of titanium alloys for the enhancement of osteoconductivity. Materials science & engineering C, Materials for biological applications. 2015;49:430-5.

[104] Zhao G, Schwartz Z, Wieland M, Rupp F, Geis-Gerstorfer J, Cochran DL, et al. High surface energy enhances cell response to titanium substrate microstructure. Journal of biomedical materials research Part A. 2005;74:49-58.

[105] Hori N, Att W, Ueno T, Sato N, Yamada M, Saruwatari L, et al. Age-dependent degradation of the protein adsorption capacity of titanium. J Dent Res. 2009;88:663-7.

[106] Wei J, Igarashi T, Okumori N, Igarashi T, Maetani T, Liu B, et al. Influence of surface wettability on competitive protein adsorption and initial attachment of osteoblasts. Biomedical materials (Bristol, England). 2009;4:045002.

[107] Van Noort R. Titanium: The implant material of today. J Mater Sci. 1987;22:3801-11.

[108] McCracken M. Dental implant materials: Commercially pure titanium and titanium alloys. J Prosthodont. 1999;8:40-3.

[109] Elias CN, Lima JHC, Valiev R, Meyers MA. Biomedical applications of titanium and its alloys. JOM. 2008;60:46-9.

[110] Pjetursson BE, Asgeirsson AG, Zwahlen M, Sailer I. Improvements in implant dentistry over the last decade: comparison of survival and complication rates in older and newer publications. The International journal of oral & maxillofacial implants. 2014;29 Suppl:308-24.

[111] Corbett KL, Losina E, Nti AA, Prokopetz JJZ, Katz JN. Population-based rates of revision of primary total hip arthroplasty: A systematic review. PLoS ONE. 2010;5:e13520.

[112] Mellado-Valero A, Ferrer Garcia JC, Herrera Ballester A, Labaig Rueda C. Effects of diabetes on the osseointegration of dental implants. Medicina oral, patologia oral y cirugia bucal. 2007;12:E38-43.

[113] Aro HT, Alm JJ, Moritz N, Makinen TJ, Lankinen P. Low BMD affects initial stability and delays stem osseointegration in cementless total hip arthroplasty in women: a 2-year RSA study of 39 patients. Acta orthopaedica. 2012;83:107-14.

[114] Kasat V, Ladda R. Smoking and dental implants. Journal of International Society of Preventive & Community Dentistry. 2012;2:38-41.

[115] McGuire MK, Wilson TG, Jr. Commentary: from normal scientific progress to game changers: the impact on periodontal clinical practice. Journal of periodontology. 2014;85:1001-5.

[116] Traini T, Mangano C, Sammons RL, Mangano F, Macchi A, Piattelli A. Direct laser metal sintering as a new approach to fabrication of an isoelastic functionally graded material for manufacture of porous titanium dental implants. Dental materials : official publication of the Academy of Dental Materials. 2008;24:1525-33.

[117] Murr LE, Quinones SA, Gaytan SM, Lopez MI, Rodela A, Martinez EY, et al. Microstructure and mechanical behavior of Ti–6Al–4V produced by rapid-layer manufacturing, for biomedical applications. J Mech Behav Biomed Mater. 2009;2:20-32.

[118] Amin Yavari S, van der Stok J, Chai YC, Wauthle R, Tahmasebi Birgani Z, Habibovic P, et al. Bone regeneration performance of surface-treated porous titanium. Biomaterials. 2014;35:6172-81.

[119] Cohen DJ, Cheng A, Kahn A, Aviram M, Whitehead AJ, Hyzy SL, et al. Novel osteogenic Ti-6Al-4V device for restoration of dental function in patients with large bone deficiencies: design, development and implementation. Sci Rep. 2016;6:20493.

[120] Schwarz F, Ferrari D, Herten M, Mihatovic I, Wieland M, Sager M, et al. Effects of surface hydrophilicity and microtopography on early stages of soft and hard tissue integration at non-submerged titanium implants: an immunohistochemical study in dogs. Journal of periodontology. 2007;78:2171-84.

[121] de Wild M, Schumacher R, Mayer K, Schkommodau E, Thoma D, Bredell M, et al. Bone regeneration by the osteoconductivity of porous titanium implants manufactured by selective laser melting: a histological and micro computed tomography study in the rabbit. Tissue engineering Part A. 2013;19:2645-54.

[122] Veltri M, Ferrari M, Balleri P. Correlation of radiographic fractal analysis with implant insertion torque in a rabbit trabecular bone model. The International journal of oral & maxillofacial implants. 2011;26:108-14.

[123] He FM, Yang GL, Zhao SF, Cheng ZP. Mechanical and histomorphometric evaluations of rough titanium implants treated with hydrofluoric acid/nitric acid solution in rabbit tibia. The International journal of oral & maxillofacial implants. 2011;26:115-22.

[124] Thorey F, Menzel H, Lorenz C, Gross G, Hoffmann A, Windhagen H. Osseointegration by bone morphogenetic protein-2 and transforming growth factor beta2 coated titanium implants in femora of New Zealand white rabbits. Indian journal of orthopaedics. 2011;45:57-62.

[125] Neyt JG, Buckwalter JA, Carroll NC. Use of animal models in musculoskeletal research. Iowa Orthop J. 1998;18:118-23.

[126] Olivares-Navarrete R, Gittens RA, Schneider JM, Hyzy SL, Haithcock DA, Ullrich PF, et al. Osteoblasts exhibit a more differentiated phenotype and increased bone morphogenetic protein production on titanium alloy substrates than on poly-ether-ether-ketone. Spine J. 2012;12:265-72.

[127] Maniatopoulos C, Rodriguez A, Deporter DA, Melcher AH. An improved method for preparing histological sections of metallic implants. The International journal of oral & maxillofacial implants. 1986;1:31-7.

[128] Lillie RD, Conn HJ, Biological Stain C. H.J. Conn's biological stains : a handbook on the nature and uses of the dyes employed in the biological laboratory. 9Th ed. / rev. With the Assistance of E.H. Stotz and V.M. Emmel. ed. Baltimore: Williams and Wilkins; 1977.

[129] del Cerro M, Cogen J, del Cerro C. Stevenel's Blue, an excellent stain for optical microscopical study of plastic embedded tissues. Microscopica acta. 1980;83:117-21.

[130] Salou L, Hoornaert A, Louarn G, Layrolle P. Enhanced osseointegration of titanium implants with nanostructured surfaces: An experimental study in rabbits. Acta Biomater. 2015;11:494-502.

[131] Brånemark R, Öhrnell L-O, Nilsson P, Thomsen P. Biomechanical characterization of osseointegration during healing: an experimental in vivo study in the rat. Biomaterials. 1997;18:969-78.

[132] Hotchkiss KM, Reddy GB, Hyzy SL, Schwartz Z, Boyan BD, Olivares-Navarrete R. Titanium surface characteristics, including topography and wettability, alter macrophage activation. Acta Biomater. 2016;31:425-34.

[133] Gittens RA, Olivares-Navarrete R, McLachlan T, Cai Y, Hyzy SL, Schneider JM, et al. Differential responses of osteoblast lineage cells to nanotopographically-modified,

microroughened titanium–aluminum–vanadium alloy surfaces. Biomaterials. 2012;33:8986-94.

[134] Wennerberg A, Jimbo R, Stübinger S, Obrecht M, Dard M, Berner S. Nanostructures and hydrophilicity influence osseointegration: a biomechanical study in the rabbit tibia. Clinical oral implants research. 2014;25:1041-50.

[135] Olivares-Navarrete R, Hyzy SL, Gittens RAs, Schneider JM, Haithcock DA, Ullrich PF, et al. Rough titanium alloys regulate osteoblast production of angiogenic factors. Spine J. 2013;13:1563-70.

[136] Santos EC, Osakada K, Shiomi M, Kitamura Y, Abe F. Microstructure and mechanical properties of pure titanium models fabricated by selective laser melting. Proc Inst Mech Eng C J Mech Eng Sci. 2004;218:711-9.

[137] Li D, Ferguson SJ, Beutler T, Cochran DL, Sittig C, Hirt HP, et al. Biomechanical comparison of the sandblasted and acid-etched and the machined and acid-etched titanium surface for dental implants. Journal of biomedical materials research. 2002;60:325-32.

[138] Fanchi M, Breschi L. Effects of acid-etching solutions on human enamel and dentin. Quintessence international (Berlin, Germany : 1985). 1995;26:431-5.

[139] Oh JM, Lee BG, Cho SW, Lee SW, Choi GS, Lim JW. Oxygen effects on the mechanical properties and lattice strain of Ti and Ti-6Al-4V. Met Mater Int. 2011;17:733-6.

[140] Martin JY, Schwartz Z, Hummert TW, Schraub DM, Simpson J, Lankford J, et al. Effect of titanium surface roughness on proliferation, differentiation, and protein synthesis of human osteoblast-like cells (MG63). Journal of biomedical materials research. 1995;29:389-401.

[141] Lincks J, Boyan BD, Blanchard CR, Lohmann CH, Liu Y, Cochran DL, et al. Response of MG63 osteoblast-like cells to titanium and titanium alloy is dependent on surface roughness and composition. Biomaterials. 1998;19:2219-32.

[142] Zinger O, Zhao G, Schwartz Z, Simpson J, Wieland M, Landolt D, et al. Differential regulation of osteoblasts by substrate microstructural features. Biomaterials. 2005;26:1837-47.

[143] Pattanayak DK, Fukuda A, Matsushita T, Takemoto M, Fujibayashi S, Sasaki K, et al. Bioactive Ti metal analogous to human cancellous bone: Fabrication by selective laser melting and chemical treatments. Acta Biomater. 2011;7:1398-406.

[144] Mangano F, Chambrone L, van Noort R, Miller C, Hatton P, Mangano C. Direct metal laser sintering titanium dental implants: a review of the current literature. International journal of biomaterials. 2014;2014:461534.

[145] Mapara M, Thomas BS, Bhat KM. Rabbit as an animal model for experimental research. Dent Res J. 2012;9:111-8.

[146] Yang GL, He FM, Yang XF, Wang XX, Zhao SF. Bone responses to titanium implants surface-roughened by sandblasted and double etched treatments in a rabbit model. Oral surgery, oral medicine, oral pathology, oral radiology, and endodontics. 2008;106:516-24.

[147] Le Guehennec L, Goyenvalle E, Lopez-Heredia M-A, Weiss P, Amouriq Y, Layrolle P. Histomorphometric analysis of the osseointegration of four different implant surfaces in the femoral epiphyses of rabbits. Clinical oral implants research. 2008;19:1103-10.

[148] Götz HE, Müller M, Emmel A, Holzwarth U, Erben RG, Stangl R. Effect of surface finish on the osseointegration of laser-treated titanium alloy implants. Biomaterials. 2004;25:4057-64.

[149] Sollazzo V, Pezzetti F, Scarano A, Piattelli A, Bignozzi CA, Massari L, et al. Zirconium oxide coating improves implant osseointegration in vivo. Dental materials : official publication of the Academy of Dental Materials. 2008;24:357-61.

[150] Pearce AI, Richards RG, Milz S, Schneider E, Pearce SG. Animal models for implant biomaterial research in bone: a review. European cells & materials. 2007;13:1-10.

[151] Suzuki K, Aoki K, Ohya K. Effects of surface roughness of titanium implants on bone remodeling activity of femur in rabbits. Bone. 1997;21:507-14.

[152] Sennerby L, Thomsen P, Ericson LE. Early tissue response to titanium implants inserted in rabbit cortical bone. J Mater Sci: Mater Med. 1993;4:240-50.

[153] Liu S, Broucek J, Virdi AS, Sumner DR. Limitations of Using Micro Computed Tomography to Predict Bone-Implant Contact and Mechanical Fixation. J Microsc. 2012;245:34-42.

[154] Butz F, Ogawa T, Chang T-L, Nishimura I. Three-dimensional bone-implant integration profiling using micro-computed tomography. The International journal of oral & maxillofacial implants. 2006;21:687-95.

[155] Vandeweghe S, Coelho PG, Vanhove C, Wennerberg A, Jimbo R. Utilizing micro-computed tomography to evaluate bone structure surrounding dental implants: A comparison with histomorphometry. J Biomed Mater Res B Appl Biomater. 2013;101:1259-66.

[156] Pak H-S, Yeo I-S, Yang J-H. A histomorphometric study of dental implants with different surface characteristics. J Adv Prosthodont. 2010;2:142-7.

[157] Kurtz S, Ong K, Lau E, Mowat F, Halpern M. Projections of primary and revision hip and knee arthroplasty in the United States from 2005 to 2030. J Bone Joint Surg Am. 2007;89:780-5.

[158] Hutmacher DW. Scaffolds in tissue engineering bone and cartilage. Biomaterials. 2000;21:2529-43.

[159] Bourke VA, Watchman CJ, Reith JD, Jorgensen ML, Dieudonnè A, Bolch WE. Spatial gradients of blood vessels and hematopoietic stem and progenitor cells within the marrow cavities of the human skeleton. Blood. 2009;114:4077-80.

[160] Zhang L, Hu J, Athanasiou KA. The role of tissue engineering in articular cartilage repair and regeneration. Crit Rev Biomed Eng. 2009;37:1-57.

[161] Hattori T, Müller C, Gebhard S, Bauer E, Pausch F, Schlund B, et al. SOX9 is a major negative regulator of cartilage vascularization, bone marrow formation and endochondral ossification. Development. 2010;137:901-11.

[162] Gentile P, Chiono V, Carmagnola I, Hatton PV. An Overview of Poly(lactic-co-glycolic) Acid (PLGA)-Based Biomaterials for Bone Tissue Engineering. Int J Mol Sci. 2014;15:3640-59.

[163] Middleton JC, Tipton AJ. Synthetic biodegradable polymers as orthopedic devices. Biomaterials. 2000;21:2335-46.

[164] Ulery BD, Nair LS, Laurencin CT. Biomedical applications of biodegradable polymers. J Polym Sci B Polym Phys. 2011;49:832-64.

[165] Neuss S, Blomenkamp I, Stainforth R, Boltersdorf D, Jansen M, Butz N, et al. The use of a shape-memory poly(ε-caprolactone)dimethacrylate network as a tissue engineering scaffold. Biomaterials. 2009;30:1697-705.

[166] Cheng CW, Solorio LD, Alsberg E. Decellularized tissue and cell-derived extracellular matrices as scaffolds for orthopaedic tissue engineering. Biotechnol Adv. 2014;32:462-84.

[167] Wang Y, Bella E, Lee CSD, Migliaresi C, Pelcastre L, Schwartz Z, et al. The synergistic effects of 3-D porous silk fibroin matrix scaffold properties and hydrodynamic environment in cartilage tissue regeneration. Biomaterials. 2010;31:4672-81.

[168] Wang Y, Kim HJ, Vunjak-Novakovic G, Kaplan DL. Stem cell-based tissue engineering with silk biomaterials. Biomaterials. 2006;27:6064-82.

[169] Kim UJ, Park J, Li C, Jin HJ, Valluzzi R, Kaplan DL. Structure and properties of silk hydrogels. Biomacromolecules. 2004;5:786-92.

[170] Nazarov R, Jin HJ, Kaplan DL. Porous 3-D scaffolds from regenerated silk fibroin. Biomacromolecules. 2004;5:718-26.

[171] Eggli PS, Muller W, Schenk RK. Porous hydroxyapatite and tricalcium phosphate cylinders with two different pore size ranges implanted in the cancellous bone of rabbits. A comparative histomorphometric and histologic study of bony ingrowth and implant substitution. Clin Orthop Relat Res. 1988:127-38.

[172] Rahaman MN, Day DE, Bal BS, Fu Q, Jung SB, Bonewald LF, et al. Bioactive glass in tissue engineering. Acta Biomater. 2011;7:2355-73.

[173] Hollister SJ. Porous scaffold design for tissue engineering. Nat Mater. 2005;4:518-24.

[174] Murphy CM, O'Brien FJ. Understanding the effect of mean pore size on cell activity in collagen-glycosaminoglycan scaffolds. Cell Adh Migr. 2010;4:377-81.

[175] Karageorgiou V, Kaplan D. Porosity of 3D biomaterial scaffolds and osteogenesis. Biomaterials. 2005;26:5474-91.

[176] Kim J, Ma T. Bioreactor strategy in bone tissue engineering: pre-culture and osteogenic differentiation under two flow configurations. Tissue engineering Part A. 2012;18:2354-64.

[177] Shimko DA, Shimko VF, Sander EA, Dickson KF, Nauman EA. Effect of porosity on the fluid flow characteristics and mechanical properties of tantalum scaffolds. J Biomed Mater Res B Appl Biomater. 2005;73:315-24.

[178] Perez RA, Mestres G. Role of pore size and morphology in musculo-skeletal tissue regeneration. Materials science & engineering C, Materials for biological applications.

[179] Byrne DP, Lacroix D, Planell JA, Kelly DJ, Prendergast PJ. Simulation of tissue differentiation in a scaffold as a function of porosity, Young's modulus and dissolution rate: Application of mechanobiological models in tissue engineering. Biomaterials. 2007;28:5544-54.

[180] Polo-Corrales L, Latorre-Esteves M, Ramirez-Vick JE. Scaffold Design for Bone Regeneration. J Nanosci Nanotechnol. 2014;14:15-56.

[181] Gariboldi MI, Best SM. Effect of ceramic scaffold architectural parameters on biological response. Front Bioeng Biotechnol. 2015;3:151.

[182] Chew SA, Arriaga M, Hinojosa V. Effects of surface area to volume ratio of plga scaffolds with different architectures on scaffold degradation characteristics and drug release kinetics. Journal of biomedical materials research Part A. 2016.

[183] Itälä AI, Ylänen HO, Ekholm C, Karlsson KH, Aro HT. Pore diameter of more than 100 μm is not requisite for bone ingrowth in rabbits. Journal of biomedical materials research. 2001;58:679-83.

[184] Prananingrum W, Naito Y, Galli S, Bae J, Sekine K, Hamada K, et al. Bone ingrowth of various porous titanium scaffolds produced by a moldless and space holder technique: an in vivo study in rabbits. Biomedical materials (Bristol, England). 2016;11:015012.

[185] Khoda AKM, Ozbolat IT, Koc B. Designing heterogeneous porous tissue scaffolds for additive manufacturing processes. Comput Aided Design. 2013;45:1507-23.

[186] Shih YR, Tseng KF, Lai HY, Lin CH, Lee OK. Matrix stiffness regulation of integrin-mediated mechanotransduction during osteogenic differentiation of human mesenchymal stem cells. J Bone Miner Res. 2011;26:730-8.

[187] Guvendiren M, Burdick JA. Stiffening hydrogels to probe short- and long-term cellular responses to dynamic mechanics. Nature communications. 2012;3:792.

[188] Brandl F, Sommer F, Goepferich A. Rational design of hydrogels for tissue engineering: Impact of physical factors on cell behavior. Biomaterials. 2007;28:134-46.

[189] Park H, Guo X, Temenoff JS, Tabata Y, Caplan AI, Kasper FK, et al. Effect of swelling ratio of injectable hydrogel composites on chondrogenic differentiation of encapsulated rabbit marrow mesenchymal stem cells in vitro. Biomacromolecules. 2009;10:541-6.

[190] Deville S. Freeze-casting of porous biomaterials: structure, properties and opportunities. Materials. 2010;3.

[191] Lv Q, Feng Q. Preparation of 3-D regenerated fibroin scaffolds with freeze drying method and freeze drying/foaming technique. J Mater Sci: Mater Med. 2006;17:1349-56.

[192] Haugh MG, Murphy CM, O'Brien FJ. Novel freeze-drying methods to produce a range of collagen-glycosaminoglycan scaffolds with tailored mean pore sizes. Tissue engineering Part C, Methods. 2010;16:887-94.

[193] Mikos AG, Temenoff JS. Formation of highly porous biodegradable scaffolds for tissue engineering2000.

[194] Chatterjee K, Kraigsley AM, Bolikal D, Kohn J, Simon CG. Gas-foamed scaffold gradients for combinatorial screening in 3D. Journal of functional biomaterials. 2012;3:173-82.

[195] Nam YS, Park TG. Porous biodegradable polymeric scaffolds prepared by thermally induced phase separation. Journal of biomedical materials research. 1999;47:8-17.

[196] Wang X, Zhu J, Yin L, Liu S, Zhang X, Ao Y, et al. Fabrication of electrospun silica-titania nanofibers with different silica content and evaluation of the morphology and osteoinductive properties. Journal of biomedical materials research Part A. 2012;100:3511-7.

[197] Huang H, Zhang X, Hu X, Shao Z, Zhu J, Dai L, et al. A functional biphasic biomaterial homing mesenchymal stem cells for in vivo cartilage regeneration. Biomaterials. 2014;35:9608-19.

[198] Li C, Wang L, Yang Z, Kim G, Chen H, Ge Z. A viscoelastic chitosan-modified three-dimensional porous poly(L-lactide-co-epsilon-caprolactone) scaffold for cartilage tissue engineering. Journal of biomaterials science Polymer edition. 2012;23:405-24.

[199] Huang H, Zhang X, Hu X, Dai L, Zhu J, Man Z, et al. Directing chondrogenic differentiation of mesenchymal stem cells with a solid-supported chitosan thermogel for cartilage tissue engineering. Biomedical materials (Bristol, England). 2014;9:035008.

[200] Cong Y, Liu S, Chen H. Fabrication of conductive polypyrrole nanofibers by electrospinning. J Nanomater. 2013;2013:6.

[201] Cheng A, Humayun A, Boyan BD, Schwartz Z. Enhanced osteoblast response to porosity and resolution of additively manufactured Ti-6Al-4V constructs with trabeculae-inspired porosity. 3D Print Addit Manuf. 2016;3:10-21.

[202] Wang X, Hao T, Qu J, Wang C, Chen H. Synthesis of Thermal Polymerizable Alginate-GMA Hydrogel for Cell Encapsulation. J Nanomater. 2015;2015:8.

[203] Xie J, Li X, Xia Y. Putting electrospun nanofibers to work for biomedical research. Macromol Rapid Comm. 2008;29:1775-92.

[204] Liu W, Thomopoulos S, Xia Y. Electrospun nanofibers for regenerative medicine. Adv Healthc Mater. 2012;1:10-25.

[205] Liu W, Yeh YC, Lipner J, Xie J, Sung HW, Thomopoulos S, et al. Enhancing the stiffness of electrospun nanofiber scaffolds with a controlled surface coating and mineralization. Langmuir. 2011;27:9088-93.

[206] Shao Z, Zhang X, Pi Y, Wang X, Jia Z, Zhu J, et al. Polycaprolactone electrospun mesh conjugated with an MSC affinity peptide for MSC homing in vivo. Biomaterials. 2012;33:3375-87.

[207] Agarwal S, Wendorff JH, Greiner A. Progress in the field of electrospinning for tissue engineering applications. Adv Mater. 2009;21:3343-51.

[208] Luo CJ, Nangrejo M, Edirisinghe M. A novel method of selecting solvents for polymer electrospinning. Polymer. 2010;51:1654-62.

[209] Matthews JA, Wnek GE, Simpson DG, Bowlin GL. Electrospinning of Collagen Nanofibers. Biomacromolecules. 2002;3:232-8.

[210] Jin H-J, Chen J, Karageorgiou V, Altman GH, Kaplan DL. Human bone marrow stromal cell responses on electrospun silk fibroin mats. Biomaterials. 2004;25:1039-47.

[211] Matthews JA, Boland ED, Wnek GE, Simpson DG, Bowlin GL. Electrospinning of Collagen Type II: A Feasibility Study. J Bioact Compat Pol. 2003;18:125-34.

[212] Li X, Xie J, Lipner J, Yuan X, Thomopoulos S, Xia Y. Nanofiber scaffolds with gradations in mineral content for mimicking the tendon-to-bone insertion site. Nano Lett. 2009;9:2763-8.

[213] Liu W, Lipner J, Moran CH, Feng L, Li X, Thomopoulos S, et al. Nanofibers: generation of electrospun nanofibers with controllable degrees of crimping through a simple, plasticizer-based treatment (adv. Mater. 16/2015). Adv Mater. 2015;27:2549.

[214] Liu W, Lipner J, Xie J, Manning CN, Thomopoulos S, Xia Y. Nanofiber scaffolds with gradients in mineral content for spatial control of osteogenesis. ACS Appl Mater Interfaces. 2014;6:2842-9.

[215] Xu S, Deng L, Zhang J, Yin L, Dong A. Composites of electrospun-fibers and hydrogels: A potential solution to current challenges in biological and biomedical field. J Biomed Mater Res B Appl Biomater. 2015:n/a-n/a.

[216] Li W-J, Laurencin CT, Caterson EJ, Tuan RS, Ko FK. Electrospun nanofibrous structure: A novel scaffold for tissue engineering. Journal of biomedical materials research. 2002;60:613-21.

[217] Allison CB, Rocky ST. Fiber diameter and seeding density influence chondrogenic differentiation of mesenchymal stem cells seeded on electrospun poly(ε -caprolactone) scaffolds. Biomedical materials (Bristol, England). 2015;10:015018.

[218] Eyre DR, Weis MA, Wu JJ. Articular cartilage collagen: an irreplaceable framework? European cells & materials. 2006;12:57-63.

[219] Zhang Y, Venugopal JR, El-Turki A, Ramakrishna S, Su B, Lim CT. Electrospun biomimetic nanocomposite nanofibers of hydroxyapatite/chitosan for bone tissue engineering. Biomaterials. 2008;29:4314-22.

[220] Sing SL, An J, Yeong WY, Wiria FE. Laser and electron-beam powder-bed additive manufacturing of metallic implants: A review on processes, materials and designs. J Orthop Res. 2015:n/a-n/a.

[221] Farre-Guasch E, Wolff J, Helder MN, Schulten EA, Forouzanfar T, Klein-Nulend J. Application of additive manufacturing in oral and maxillofacial surgery. Journal of oral and maxillofacial surgery : official journal of the American Association of Oral and Maxillofacial Surgeons. 2015;73:2408-18.

[222] Henkel J, Woodruff MA, Epari DR, Steck R, Glatt V, Dickinson IC, et al. Bone regeneration based on tissue engineering conceptions — A 21st century perspective. Bone Res. 2013;1:216-48.

[223] Tang D, Tare RS, Yang LY, Williams DF, Ou KL, Oreffo RO. Biofabrication of bone tissue: approaches, challenges and translation for bone regeneration. Biomaterials. 2016;83:363-82.

[224] Amini AR, Laurencin CT, Nukavarapu SP. Bone tissue engineering: Recent advances and challenges. Crit Rev Biomed Eng. 2012;40:363-408.

[225] Hutmacher DW, Cool S. Concepts of scaffold-based tissue engineering--the rationale to use solid free-form fabrication techniques. Journal of cellular and molecular medicine. 2007;11:654-69.

[226] Sturm S, Zhou S, Mai YW, Li Q. On stiffness of scaffolds for bone tissue engineering-a numerical study. Journal of biomechanics. 2010;43:1738-44.

[227] Wang X, Xu S, Zhou S, Xu W, Leary M, Choong P, et al. Topological design and additive manufacturing of porous metals for bone scaffolds and orthopaedic implants: A review. Biomaterials. 2016;83:127-41.

[228] Kasten P, Beyen I, Niemeyer P, Luginbühl R, Bohner M, Richter W. Porosity and pore size of β-tricalcium phosphate scaffold can influence protein production and osteogenic differentiation of human mesenchymal stem cells: An in vitro and in vivo study. Acta Biomater. 2008;4:1904-15.

[229] Li J, He L, Zhou C, Zhou Y, Bai Y, Lee FY, et al. 3D printing for regenerative medicine: From bench to bedside. MRS Bull. 2015;40:145-54.

[230] Tasoglu S, Demirci U. Bioprinting for stem cell research. Trends in biotechnology. 2013;31:10-9.

[231] Bose S, Vahabzadeh S, Bandyopadhyay A. Bone tissue engineering using 3D printing. Mater Today. 2013;16:496-504.

[232] Derby B. Printing and prototyping of tissues and scaffolds. Science. 2012;338:921-6.

[233] Di Bella C, Donati D, Fosang A, Wallace GG, Choong P. 3D bioprinting of cartilage for orthopedic surgeons: reading between the lines. Front Surg. 2015;2.

[234] Vrancken B, Thijs L, Kruth J-P, Van Humbeeck J. Heat treatment of Ti6Al4V produced by Selective Laser Melting: Microstructure and mechanical properties. J Alloy Compd. 2012;541:177-85.

[235] Xu W, Brandt M, Sun S, Elambasseril J, Liu Q, Latham K, et al. Additive manufacturing of strong and ductile Ti–6Al–4V by selective laser melting via in situ martensite decomposition. Acta Materialia. 2015;85:74-84.

[236] Weißmann V, Bader R, Hansmann H, Laufer N. Influence of the structural orientation on the mechanical properties of selective laser melted Ti6Al4V open-porous scaffolds. Mater Design.

[237] Dimitriou R, Tsiridis E, Giannoudis PV. Current concepts of molecular aspects of bone healing. Injury. 2005;36:1392-404.

[238] Amin Yavari S, Ahmadi SM, van der Stok J, Wauthle R, Riemslag AC, Janssen M, et al. Effects of bio-functionalizing surface treatments on the mechanical behavior of open porous titanium biomaterials. J Mech Behav Biomed Mater. 2014;36:109-19.

[239] Boyan BD, Cheng A, Olivares-Navarrete R, Schwartz Z. Implant surface design regulates mesenchymal stem cell differentiation and maturation. Adv Dent Res. 2016.

[240] Habibovic P, de Groot K. Osteoinductive biomaterials--properties and relevance in bone repair. Journal of tissue engineering and regenerative medicine. 2007;1:25-32.

[241] Zou XH, Zhi YL, Chen X, Jin HM, Wang LL, Jiang YZ, et al. Mesenchymal stem cell seeded knitted silk sling for the treatment of stress urinary incontinence. Biomaterials. 2010;31:4872-9.

[242] Dalby MJ, Gadegaard N, Tare R, Andar A, Riehle MO, Herzyk P, et al. The control of human mesenchymal cell differentiation using nanoscale symmetry and disorder. Nat Mater. 2007;6:997-1003.

[243] Han T, Chang B, Ding X, Yue G, Song W, Tang H, et al. Improved bone formation and ingrowth for the additively manufactured porous Ti6Al4V bone implants with strontium laden nanotube array coating. RSC Adv. 2016.

[244] Rho JY, Kuhn-Spearing L, Zioupos P. Mechanical properties and the hierarchical structure of bone. Medical engineering & physics. 1998;20:92-102.

[245] Cavalcanti-Adam EA, Aydin D, Hirschfeld-Warneken VC, Spatz JP. Cell adhesion and response to synthetic nanopatterned environments by steering receptor clustering and spatial location. HFSP journal. 2008;2:276-85.

[246] Zhu J, Cai Q, Zhang X, Hu X, Li L, Wang W, et al. Biological characteristics of mesenchymal stem cells grown on different topographical nanofibrous poly-L-lactide meshes. Journal of biomedical nanotechnology. 2013;9:1757-67.

[247] Yang Y, Kim K-H, Ong JL. A review on calcium phosphate coatings produced using a sputtering process—an alternative to plasma spraying. Biomaterials. 2005;26:327-37.

[248] Lai KA, Shen WJ, Chen CH, Yang CY, Hu WP, Chang GL. Failure of hydroxyapatite-coated acetabular cups. Ten-year follow-up of 85 Landos Atoll arthroplasties. The Journal of bone and joint surgery British volume. 2002;84:641-6.

[249] Bauer TW, Muschler GF. Bone graft materials: An overview of the basic science. Clin Orthop Relat Res. 2000;371:10-27.

[250] García-Gareta E, Coathup MJ, Blunn GW. Osteoinduction of bone grafting materials for bone repair and regeneration. Bone. 2015;81:112-21.

[251] Laurencin C, Khan Y, El-Amin SF. Bone graft substitutes. Expert Review of Medical Devices. 2006;3:49-57.

[252] Shah NJ, Macdonald ML, Beben YM, Padera RF, Samuel RE, Hammond PT. Tunable dual growth factor delivery from polyelectrolyte multilayer films. Biomaterials. 2011;32:6183-93.

[253] Sundelacruz S, Kaplan DL. Stem cell- and scaffold-based tissue engineering approaches to osteochondral regenerative medicine. Seminars in cell & developmental biology. 2009;20:646-55.

[254] Puppi D, Chiellini F, Piras AM, Chiellini E. Polymeric materials for bone and cartilage repair. Prog Polym Sci. 2010;35:403-40.

[255] Lee CH, Cook JL, Mendelson A, Moioli EK, Yao H, Mao JJ. Regeneration of the articular surface of the rabbit synovial joint by cell homing: a proof of concept study. Lancet. 2010;376:440-8.

[256] Karp JM, Leng Teo GS. Mesenchymal stem cell homing: The devil Is in the details. Cell Stem Cell. 2009;4:206-16.

[257] Discher DE, Mooney DJ, Zandstra PW. Growth factors, matrices, and forces combine and control stem cells. Science. 2009;324:1673-7.

[258] Dunehoo AL, Anderson M, Majumdar S, Kobayashi N, Berkland C, Siahaan TJ. Cell adhesion molecules for targeted drug delivery. J Pharm Sci. 2006;95:1856-72.

[259] Ruoslahti MDPaE. Variants of the cell recognition site of fibronectin that retain attachment-promoting activity. Proc Natl Acad Sci U S A. 1984;81:5985-8.

[260] Ruoslahti E, Pierschbacher MD. Arg-Gly-Asp: a versatile cell recognition signal. Cell. 1986;44:517-8.

[261] Hersel U, Dahmen C, Kessler H. RGD modified polymers: biomaterials for stimulated cell adhesion and beyond. Biomaterials. 2003;24:4385-415.

[262] Kim JY, Xin X, Moioli EK, Chung J, Lee CH, Chen M, et al. Regeneration of dental-pulp-like tissue by chemotaxis-induced cell homing. Tissue engineering Part A. 2010;16:3023-31.

[263] Si Y, Tsou CL, Croft K, Charo IF. CCR2 mediates hematopoietic stem and progenitor cell trafficking to sites of inflammation in mice. The Journal of clinical investigation. 2010;120:1192-203.

[264] Sarkar D, Spencer JA, Phillips JA, Zhao W, Schafer S, Spelke DP, et al. Engineered cell homing. Blood. 2011;118:e184-91.

[265] Man Z, Yin L, Shao Z, Zhang X, Hu X, Zhu J, et al. The effects of co-delivery of BMSC-affinity peptide and rhTGF-beta1 from coaxial electrospun scaffolds on chondrogenic differentiation. Biomaterials. 2014;35:5250-60.

[266] Zhu H, Yu D, Zhou Y, Wang C, Gao M, Jiang H, et al. Biological activity of a nanofibrous barrier membrane containing bone morphogenetic protein formed by core-shell electrospinning as a sustained delivery vehicle. J Biomed Mater Res B Appl Biomater. 2013;101:541-52.

[267] Dinopoulos H, Giannoudis PV. (iv) The use of bone morphogenetic proteins (BMPs) in long-bone non-unions. Current Orthopaedics. 2007;21:268-79.

[268] McKay WF, Peckham SM, Badura JM. A comprehensive clinical review of recombinant human bone morphogenetic protein-2 (INFUSE(®) Bone Graft). Int Orthop. 2007;31:729-34.

[269] Nune KC, Kumar A, Murr LE, Misra RDK. Interplay between self-assembled structure of bone morphogenetic protein-2 (BMP-2) and osteoblast functions in three-dimensional titanium alloy scaffolds: Stimulation of osteogenic activity. Journal of biomedical materials research Part A. 2016;104:517-32.

[270] Karageorgiou V, Meinel L, Hofmann S, Malhotra A, Volloch V, Kaplan D. Bone morphogenetic protein-2 decorated silk fibroin films induce osteogenic differentiation of human bone marrow stromal cells. Journal of biomedical materials research Part A. 2004;71:528-37.

[271] Reichert JC, Cipitria A, Epari DR, Saifzadeh S, Krishnakanth P, Berner A, et al. A tissue engineering solution for segmental defect regeneration in load-bearing long bones. Science translational medicine. 2012;4:141ra93.

[272] Ong KL, Villarraga ML, Lau E, Carreon LY, Kurtz SM, Glassman SD. Off-label use of bone morphogenetic proteins in the United States using administrative data. Spine (Phila Pa 1976). 2010;35:1794-800.

[273] Epstein NE. Complications due to the use of BMP/INFUSE in spine surgery: The evidence continues to mount. Surg Neurol Int. 2013;4:S343-S52.

[274] Hyzy SL, Olivares-Navarrete R, Schwartz Z, Boyan BD. BMP2 induces osteoblast apoptosis in a maturation state and noggin-dependent manner. J Cell Biochem. 2012;113:3236-45.

[275] Santo VE, Gomes ME, Mano JF, Reis RL. Controlled release strategies for bone, cartilage, and osteochondral engineering--Part II: challenges on the evolution from single to multiple bioactive factor delivery. Tissue engineering Part B, Reviews. 2013;19:327-52.

[276] Gothard D, Smith EL, Kanczler JM, Rashidi H, Qutachi O, Henstock J, et al. Tissue engineered bone using select growth factors: A comprehensive review of animal studies and clinical translation studies in man. European cells & materials. 2014;28:166-207; discussion -8.

[277] Salgado AJ, Coutinho OP, Reis RL. Bone tissue engineering: state of the art and future trends. Macromolecular bioscience. 2004;4:743-65.

[278] Falah M, Nierenberg G, Soudry M, Hayden M, Volpin G. Treatment of articular cartilage lesions of the knee. Int Orthop. 2010;34:621-30.

[279] Sridhar BV, Brock JL, Silver JS, Leight JL, Randolph MA, Anseth KS. Development of a cellularly degradable PEG hydrogel to promote articular cartilage extracellular matrix deposition. Adv Healthc Mater. 2015;4:702-13.

[280] Jayaraman P, Gandhimathi C, Venugopal JR, Becker DL, Ramakrishna S, Srinivasan DK. Controlled release of drugs in electrosprayed nanoparticles for bone tissue engineering. Adv Drug Deliv Rev. 2015;94:77-95.

[281] Gupta D, Venugopal J, Mitra S, Giri Dev VR, Ramakrishna S. Nanostructured biocomposite substrates by electrospinning and electrospraying for the mineralization of osteoblasts. Biomaterials. 2009;30:2085-94.

[282] Li X, Chen H. Lanthanide Yb3+/Ho3+ co-doped apatite with upconversion luminescence for discriminable tracking of in vivo samples. Under review. 2016.

[283] Zeng H, Li X, Xie F, Teng L, Chen H. Dextran-coated fluorapatite nanorods doped with lanthanides in labelling and directing osteogenic differentiation of bone marrow mesenchymal stem cells. J Mater Chem B. 2014;2:3609-17.

[284] Schnabel M, Marlovits S, Eckhoff G, Fichtel I, Gotzen L, Vecsei V, et al. Dedifferentiation-associated changes in morphology and gene expression in primary human articular chondrocytes in cell culture. Osteoarthritis and cartilage / OARS, Osteoarthritis Research Society. 2002;10:62-70.

[285] Leslie SK, Cohen DJ, Sedlaczek J, Pinsker EJ, Boyan BD, Schwartz Z. Controlled release of rat adipose-derived stem cells from alginate microbeads. Biomaterials. 2013;34:8172-84.

[286] Fedorovich NE, De Wijn JR, Verbout AJ, Alblas J, Dhert WJ. Three-dimensional fiber deposition of cell-laden, viable, patterned constructs for bone tissue printing. Tissue engineering Part A. 2008;14:127-33.

[287] Fedorovich NE, Schuurman W, Wijnberg HM, Prins HJ, van Weeren PR, Malda J, et al. Biofabrication of osteochondral tissue equivalents by printing topologically defined, cell-laden hydrogel scaffolds. Tissue engineering Part C, Methods. 2012;18:33-44.

[288] Rezwan K, Chen QZ, Blaker JJ, Boccaccini AR. Biodegradable and bioactive porous polymer/inorganic composite scaffolds for bone tissue engineering. Biomaterials. 2006;27:3413-31.

[289] Logeart-Avramoglou D, Anagnostou F, Bizios R, Petite H. Engineering bone: challenges and obstacles. Journal of cellular and molecular medicine. 2005;9:72-84.

[290] Ferraris S, Spriano S. Antibacterial titanium surfaces for medical implants. Materials science & engineering C, Materials for biological applications.

[291] Kumar S, Raj S, Kolanthai E, Sood AK, Sampath S, Chatterjee K. Chemical functionalization of graphene to augment stem cell osteogenesis and inhibit biofilm formation on polymer composites for orthopedic applications. ACS Appl Mater Interfaces. 2015;7:3237-52.

[292] Chavassieux PM, Chenu C, Valentin-Opran A, Merle B, Delmas PD, Meunier PJ, et al. Influence of experimental conditions on osteoblast activity in human primary bone cell cultures. J Bone Miner Res. 1990;5:337-43.

[293] Kohli N, Wright KT, Sammons RL, Jeys L, Snow M, Johnson WEB. An In vitro comparison of the incorporation, growth, and chondrogenic potential of human bone marrow versus adipose tissue mesenchymal stem cells in clinically relevant cell scaffolds used for cartilage repair. Cartilage. 2015.

[294] Banfi A, Muraglia A, Dozin B, Mastrogiacomo M, Cancedda R, Quarto R. Proliferation kinetics and differentiation potential of ex vivo expanded human bone marrow stromal cells: Implications for their use in cell therapy. Experimental hematology. 2000;28:707-15.

[295] Nunamaker DM. Experimental models of fracture repair. Clin Orthop Relat Res. 1998:S56-65.

[296] Lang TF. The bone-muscle relationship in men and women. Journal of osteoporosis. 2011;2011:702735.

[297] Lorenz J, Grassel S. Experimental osteoarthritis models in mice. Methods in molecular biology (Clifton, NJ). 2014;1194:401-19.

[298] Little CB, Smith MM. Animal models of osteoarthritis. Curr Rheumatol Rev. 2008;4:175-82.

[299] McIlwraith CW, Frisbie DD, Kawcak CE. The horse as a model of naturally occurring osteoarthritis. Bone Joint Res. 2012;1:297-309.

[300] Beutel BG, Danna NR, Granato R, Bonfante EA, Marin C, Tovar N, et al. Implant design and its effects on osseointegration over time within cortical and trabecular bone. J Biomed Mater Res B Appl Biomater. 2015:n/a-n/a.

[301] Hutmacher DW, Schantz JT, Lam CXF, Tan KC, Lim TC. State of the art and future directions of scaffold-based bone engineering from a biomaterials perspective. Journal of tissue engineering and regenerative medicine. 2007;1:245-60.

[302] Einhorn TA. Clinically applied models of bone regeneration in tissue engineering research. Clin Orthop Relat Res. 1999:S59-67.

[303] Guillotin B, Guillemot F. Cell patterning technologies for organotypic tissue fabrication. Trends in biotechnology. 2011;29:183-90.

[304] Barron JA, Krizman DB, Ringeisen BR. Laser printing of single cells: statistical analysis, cell viability, and stress. Annals of biomedical engineering. 2005;33:121-30.

[305] Simon CG, Jr., Yaszemski MJ, Ratcliffe A, Tomlins P, Luginbuehl R, Tesk JA. ASTM international workshop on standards and measurements for tissue engineering scaffolds. J Biomed Mater Res B Appl Biomater. 2015;103:949-59.

[306] Ikada Y. Challenges in tissue engineering. J R Soc Interface 2006 Oct 22;3(10):589-601
Challenges. 2006;3:589-601.

[307] Motamedian SR, Hosseinpour S, Ahsaie MG, Khojasteh A. Smart scaffolds in bone tissue engineering: A systematic review of literature. World J Stem Cells. 2015;7:657-68.

[308] Crowley C, Wong JM, Fisher DM, Khan WS. A systematic review on preclinical and clinical studies on the use of scaffolds for bone repair in skeletal defects. Current stem cell research & therapy. 2013;8:243-52.

[309] Orthopedic implants - A global market overview. Industry Experts; 2011.

[310] Rack HJ, Qazi JI. Titanium alloys for biomedical applications. Materials science & engineering C, Materials for biological applications. 2006;26:1269-77.

[311] Long M, Rack HJ. Titanium alloys in total joint replacement—a materials science perspective. Biomaterials. 1998;19:1621-39.

[312] Textor M, Sittig C, Frauchiger V, Tosatti S, Brunette DM. Properties and biological significance of natural oxide films on titanium and its alloys. Titanium in medicine: Springer; 2001. p. 171-230.

[313] Zhao G, Zinger O, Schwartz Z, Wieland M, Landolt D, Boyan BD. Osteoblast-like cells are sensitive to submicron-scale surface structure. Clinical oral implants research. 2006;17:258-64.

[314] Keselowsky BG, Wang L, Schwartz Z, Garcia AJ, Boyan BD. Integrin α5 controls osteoblastic proliferation and differentiation responses to titanium substrates presenting different roughness characteristics in a roughness independent manner. Journal of biomedical materials research Part A. 2007;80A:700-10.

[315] Bain CA, Moy PK. The association between the failure of dental implants and cigarette smoking. The International journal of oral & maxillofacial implants. 1993;8:1-13.

[316] Moy PK, Medina D, Shetty V, Aghaloo TL. Dental implant failure rates and associated risk factors. The International journal of oral & maxillofacial implants. 2005;20:569-77.

[317] Mahomed NN, Barrett JA, Katz JN, Phillips CB, Losina E, Lew RA, et al. Rates and outcomes of primary and revision total hip replacement in the United States Medicare population. J Bone Joint Surg Am. 2003;85:27-32.

[318] Lautenschlager EP, Monaghan P. Titanium and titanium alloys as dental materials. Int Dent J. 1993;43:245-53.

[319] Sumner DR, Turner TM, Igloria R, Urban RM, Galante JO. Functional adaptation and ingrowth of bone vary as a function of hip implant stiffness. Journal of biomechanics. 1998;31:909-17.

[320] Parthasarathy J, Starly B, Raman S, Christensen A. Mechanical evaluation of porous titanium (Ti6Al4V) structures with electron beam melting (EBM). J Mech Behav Biomed Mater. 2010;3:249-59.

[321] Sumner DR, Galante JO. Determinants of stress shielding: design versus materials versus interface. Clin Orthop Relat Res. 1992:202-12.

[322] van Noort R. The future of dental devices is digital. Dental Mater. 2012;28:3-12.

[323] Warnke PH, Douglas T, Wollny P, Sherry E, Steiner M, Galonska S, et al. Rapid prototyping: porous titanium alloy scaffolds produced by selective laser melting for bone tissue engineering. Tissue engineering Part C, Methods. 2009;15:115-24.

[324] Bertol LS, Júnior WK, Silva FPd, Aumund-Kopp C. Medical design: Direct metal laser sintering of Ti–6Al–4V. Mater Design. 2010;31:3982-8.

[325] Heinl P, Müller L, Körner C, Singer RF, Müller FA. Cellular Ti–6Al–4V structures with interconnected macro porosity for bone implants fabricated by selective electron beam melting. Acta Biomater. 2008;4:1536-44.

[326] Ryan G, Pandit A, Apatsidis DP. Fabrication methods of porous metals for use in orthopaedic applications. Biomaterials. 2006;27:2651-70.

[327] Xue W, Krishna BV, Bandyopadhyay A, Bose S. Processing and biocompatibility evaluation of laser processed porous titanium. Acta Biomater. 2007;3:1007-18.

[328] Jones AC, Arns CH, Sheppard AP, Hutmacher DW, Milthorpe BK, Knackstedt MA. Assessment of bone ingrowth into porous biomaterials using MICRO-CT. Biomaterials. 2007;28:2491-504.

[329] Boyan BD, Hummert TW, Dean DD, Schwartz Z. Role of material surfaces in regulating bone and cartilage cell response. Biomaterials. 1996;17:137-46.

[330] Gauthier O, Bouler J-M, Aguado E, Pilet P, Daculsi G. Macroporous biphasic calcium phosphate ceramics: influence of macropore diameter and macroporosity percentage on bone ingrowth. Biomaterials. 1998;19:133-9.

[331] Misch CE, Qu Z, Bidez MW. Mechanical properties of trabecular bone in the human mandible: implications for dental implant treatment planning and surgical placement. Journal of oral and maxillofacial surgery : official journal of the American Association of Oral and Maxillofacial Surgeons. 1999;57:700-6; discussion 6-8.

[332] McCalden RW, McGeough JA, Barker MB, Court-Brown CM. Age-related changes in the tensile properties of cortical bone. The relative importance of changes in porosity, mineralization, and microstructure. J Bone Joint Surg Am. 1993;75:1193-205.

[333] Seeman E. Pathogenesis of bone fragility in women and men. Lancet. 2002;359:1841-50.

[334] Sevilla P, Aparicio C, Planell JA, Gil FJ. Comparison of the mechanical properties between tantalum and nickel–titanium foams implant materials for bone ingrowth applications. J Alloy Compd. 2007;439:67-73.

[335] Ding M, Odgaard A, Danielsen CC, Hvid I. Mutual associations among microstructural, physical and mechanical properties of human cancellous bone. The Journal of bone and joint surgery British volume. 2002;84:900-7.

[336] Hollander DA, von Walter M, Wirtz T, Sellei R, Schmidt-Rohlfing B, Paar O, et al. Structural, mechanical and in vitro characterization of individually structured Ti–6Al–4V produced by direct laser forming. Biomaterials. 2006;27:955-63.

[337] Kieswetter K, Schwartz Z, Dean DD, Boyan BD. The role of implant surface characteristics in the healing of bone. Critical reviews in oral biology and medicine : an official publication of the American Association of Oral Biologists. 1996;7:329-45.

[338] Boyce BF, Xing L. Biology of RANK, RANKL, and osteoprotegerin. Arthritis research & therapy. 2007;9 Suppl 1:S1.

[339] Tsuruga E, Takita H, Itoh H, Wakisaka Y, Kuboki Y. Pore Size of Porous Hydroxyapatite as the Cell-Substratum Controls BMP-Induced Osteogenesis. J Biochem. 1997;121:317-24.

[340] Kilian KA, Bugarija B, Lahn BT, Mrksich M. Geometric cues for directing the differentiation of mesenchymal stem cells. Proc Natl Acad Sci U S A. 2010;107:4872-7.

[341] Stübinger S, Mosch I, Robotti P, Sidler M, Klein K, Ferguson SJ, et al. Histological and biomechanical analysis of porous additive manufactured implants made by direct metal laser sintering: A pilot study in sheep. J Biomed Mater Res B Appl Biomater. 2013;101:1154-63.

[342] Chia HN, Wu BM. Recent advances in 3D printing of biomaterials. J Biol Eng. 2015;9:4.

[343] Lang NP, Salvi GE, Huynh-Ba G, Ivanovski S, Donos N, Bosshardt DD. Early osseointegration to hydrophilic and hydrophobic implant surfaces in humans. Clinical oral implants research. 2011;22:349-56.

[344] Meldrum RD, Wurtz LD, Feinberg JR, Capello WN. Does smoking affect implant survivorship in total hip arthroplasty?: A preliminary retrospective case series. Iowa Orthop J. 2005;25:17-24.

[345] Jämsen E, Peltola M, Eskelinen A, Lehto MUK. Comorbid diseases as predictors of survival of primary total hip and knee replacements: a nationwide register-based study of 96 754 operations on patients with primary osteoarthritis. Ann Rheum Dis. 2013;72:1975-82.

[346] Oh I, Harris WH. Proximal strain distribution in the loaded femur. An in vitro comparison of the distributions in the intact femur and after insertion of different hip-replacement femoral components. J Bone Joint Surg Am. 1978;60:75-85.

[347] Jariwala SH, Lewis GS, Bushman ZJ, Adair JH, Donahue HJ. 3D printing of personalized artificial bone scaffolds. 3D Print Addit Manuf. 2015;2:56-64.

[348] Mangano F, Bazzoli M, Tettamanti L, Farronato D, Maineri M, Macchi A, et al. Custom-made, selective laser sintering (SLS) blade implants as a non-conventional solution for the prosthetic rehabilitation of extremely atrophied posterior mandible. Lasers in medical science. 2013;28:1241-7.

[349] Mangano C, Piattelli A, d'Avila S, Iezzi G, Mangano F, Onuma T, et al. Early human bone response to laser metal sintering surface topography: A histologic report. J Oral Implantol. 2010;36:91-6.

[350] Palmquist A, Snis A, Emanuelsson L, Browne M, Thomsen P. Long-term biocompatibility and osseointegration of electron beam melted, free-form–fabricated solid and porous titanium alloy: Experimental studies in sheep. J Biomater Appl. 2013.

[351] Geetha M, Singh AK, Asokamani R, Gogia AK. Ti based biomaterials, the ultimate choice for orthopaedic implants – A review. Prog Mater Sci. 2009;54:397-425.

[352] Krishna BV, Bose S, Bandyopadhyay A. Low stiffness porous Ti structures for load-bearing implants. Acta Biomater. 2007;3:997-1006.

[353] Parthasarathy J, Starly B, Raman S. A design for the additive manufacture of functionally graded porous structures with tailored mechanical properties for biomedical applications. J Manuf Process. 2011;13:160-70.

[354] Sallica-Leva E, Jardini AL, Fogagnolo JB. Microstructure and mechanical behavior of porous Ti–6Al–4V parts obtained by selective laser melting. J Mech Behav Biomed Mater. 2013;26:98-108.

[355] Roque WL, Alberich-Bayarri A. Tortuosity influence on the trabecular bone elasticity and mechanical competence. In: Tavares JMRS, Natal Jorge R, editors. Med Developments in Medical Image Processing and Computational Vision Springer International Publishing; 2015. p. 173-91.

[356] Reilly DT, Burstein AH, Frankel VH. The elastic modulus for bone. Journal of biomechanics. 1974;7:271-5.

[357] Ponader S, von Wilmowsky C, Widenmayer M, Lutz R, Heinl P, Körner C, et al. In vivo performance of selective electron beam-melted Ti-6Al-4V structures. Journal of biomedical materials research Part A. 2010;92A:56-62.

[358] Maniatopoulos C, Pilliar RM, Smith DC. Threaded versus porous-surfaced designs for implant stabilization in bone-endodontic implant model. Journal of biomedical materials research. 1986;20:1309-33.

[359] Czekanska EM, Stoddart MJ, Ralphs JR, Richards RG, Hayes JS. A phenotypic comparison of osteoblast cell lines versus human primary osteoblasts for biomaterials testing. Journal of biomedical materials research Part A. 2014;102:2636-43.

[360] Lohmann CH, Bonewald LF, Sisk MA, Sylvia VL, Cochran DL, Dean DD, et al. Maturation state determines the response of osteogenic cells to surface roughness and 1,25-dihydroxyvitamin D3. J Bone Miner Res. 2000;15:1169-80.

[361] Frosch KH, Barvencik F, Lohmann CH, Viereck V, Siggelkow H, Breme J, et al. Migration, matrix production and lamellar bone formation of human osteoblast-like cells in porous titanium implants. Cells, tissues, organs. 2002;170:214-27.

[362] Hsin IC, Yiwei W. Cell responses to surface and architecture of tissue engineering scaffolds. In: Eberli D, editor. Regenerative Medicine and Tissue Engineering: InTech; 2011.

[363] Kapur S, Baylink DJ, William Lau KH. Fluid flow shear stress stimulates human osteoblast proliferation and differentiation through multiple interacting and competing signal transduction pathways. Bone. 2003;32:241-51.

[364] Owan I, Burr DB, Turner CH, Qiu J, Tu Y, Onyia JE, et al. Mechanotransduction in bone: osteoblasts are more responsive to fluid forces than mechanical strain. The American journal of physiology. 1997;273:C810-5.

[365] Ruffo M, Tuck C, Hague R. Cost estimation for rapid manufacturing - laser sintering production for low to medium volumes. Proc Inst Mech Eng, B J Eng Manuf. 2006;220:1417-27.

[366] Frazier WE. Metal additive manufacturing: a review. J Mater Eng Perform. 2014;23:1917-28.

[367] Yang J, Cai H, Lv J, Zhang K, Leng H, Sun C, et al. In vivo study of a self-stabilizing artificial vertebral body fabricated by electron beam melting. Spine (Phila Pa 1976). 2014;39:E486-92.

[368] Mangano F, Luongo F, Shibli JA, Anil S, Mangano C. Maxillary overdentures supported by four splinted direct metal laser sintering implants: a 3-year prospective clinical study. Int J Dent. 2014:Article ID 252343.

[369] Asaoka K, Kuwayama N, Okuno O, Miura I. Mechanical properties and biomechanical compatibility of porous titanium for dental implants. Journal of biomedical materials research. 1985;19:699-713.

[370] Van der Stok J, Van der Jagt OP, Amin Yavari S, De Haas MFP, Waarsing JH, Jahr H, et al. Selective laser melting-produced porous titanium scaffolds regenerate bone in critical size cortical bone defects. J Orthop Res. 2013;31:792-9.

[371] Li JP, Habibovic P, van den Doel M, Wilson CE, de Wijn JR, van Blitterswijk CA, et al. Bone ingrowth in porous titanium implants produced by 3D fiber deposition. Biomaterials. 2007;28:2810-20.

[372] Steigenga JT, Al-Shammari KF, Nociti FH, Misch CE, Wang H-L. Dental implant design and its relationship to long-term implant success. Implant Dent. 2003;12:306-17.

[373] Pittenger MF, Mackay AM, Beck SC, Jaiswal RK, Douglas R, Mosca JD, et al. Multilineage potential of adult human mesenchymal stem cells. Science. 1999;284:143-7.

[374] Fischer S, Schulte M, Hirsch T, Lehnhardt M, Behr B. Mesenchymal stem cells in bone regeneration. In: Hayat MA, editor. Stem Cells and Cancer Stem Cells, Volume 10: Springer Netherlands; 2013. p. 3-11.

[375] Marsell R, Einhorn TA. The biology of fracture healing. Injury. 2011;42:551-5.

[376] Yang J, Wang J, Yuan T, Zhu XD, Xiang Z, Fan YJ, et al. The enhanced effect of surface microstructured porous titanium on adhesion and osteoblastic differentiation of mesenchymal stem cells. J Mater Sci - Mater Med. 2013;24:2235-46.

[377] Lv J, Jia Z, Li J, Wang Y, Yang J, Xiu P, et al. Electron beam melting fabrication of porous Ti6Al4V scaffolds: cytocompatibility and osteogenesis. Adv Eng Mater. 2015;17:1391-8.

[378] Hyzy SL, Cheng A, Cohen DJ, Yatzkaier G, Whitehead AJ, Clohessy RM, et al. Novel hydrophilic nanostructured microtexture on direct metal laser sintered Ti–6Al–4V surfaces enhances osteoblast response in vitro and osseointegration in a rabbit model. Journal of biomedical materials research Part A. 2016;104:2086-98.

[379] Chen J, Dosier CR, Park JH, De S, Guldberg RE, Boyan BD, et al. Mineralization of three-dimensional osteoblast cultures is enhanced by the interaction of 1α,25-dihydroxyvitamin D3 and BMP2 via two specific vitamin D receptors. Journal of tissue engineering and regenerative medicine. 2016;10:40-51.

[380] Dosier CR, Erdman CP, Park JH, Schwartz Z, Boyan BD, Guldberg RE. Resveratrol effect on osteogenic differentiation of rat and human adipose derived stem cells in a 3-D culture environment. J Mech Behav Biomed Mater. 2012;11:112-22.

[381] Raines AL, Sunwoo M, Gertzman AA, Thacker K, Guldberg RE, Schwartz Z, et al. Hyaluronic acid stimulates neovascularization during the regeneration of bone marrow after ablation. Journal of biomedical materials research Part A. 2011;96:575-83.

[382] Barbara D Boyan, Christoph H Lohmann, David D Dean, Victor L Sylvia, David L Cochran, Schwartz Z. Mechanisms involved in osteoblast response to implant surface morphology. Annu Rev Mater Res. 2001;31:357-71.

[383] Lian JB, Stein GS. Concepts of osteoblast growth and differentiation: basis for modulation of bone cell development and tissue formation. Critical reviews in oral biology and medicine : an official publication of the American Association of Oral Biologists. 1992;3:269-305.

[384] Beresford JN, Gallagher JA, Russell RG. 1,25-Dihydroxyvitamin D3 and human bone-derived cells in vitro: effects on alkaline phosphatase, type I collagen and proliferation. Endocrinology. 1986;119:1776-85.

[385] Yang HJ, Kim KJ, Kim MK, Lee SJ, Ryu YH, Seo BF, et al. The Stem Cell Potential and Multipotency of Human Adipose Tissue-Derived Stem Cells Vary by Cell Donor and Are Different from Those of Other Types of Stem Cells. Cells, tissues, organs. 2014;199:373-83.

[386] Bonewald LF, Harris SE, Rosser J, Dallas MR, Dallas SL, Camacho NP, et al. Von Kossa staining alone is not sufficient to confirm that mineralization in vitro represents bone formation. Calcif Tissue Int. 2003;72:537-47.

[387] Boyan BD, Bonewald LF, Paschalis EP, Lohmann CH, Rosser J, Cochran DL, et al. Osteoblast-mediated mineral deposition in culture is dependent on surface microtopography. Calcif Tissue Int. 2002;71:519-29.

[388] Wuthier RE, Gore ST. Partition of inorganic ions and phospholipids in isolated cell, membrane and matrix vesicle fractions: Evidence for Ca-Pi-acidic phospholipid complexes. Calc Tis Res. 1977;24:163-71.

[389] McLean FM, Keller PJ, Genge BR, Walters SA, Wuthier RE. Disposition of preformed mineral in matrix vesicles. Internal localization and association with alkaline phosphatase. J Biol Chem. 1987;262:10481-8.

[390] Boskey AL, Bullough PG, Vigorita V, Di Carlo E. Calcium-acidic phospholipid-phosphate complexes in human hydroxyapatite-containing pathologic deposits. Am J Pathol. 1988;133:22-9.

[391] Shah FA, Snis A, Matic A, Thomsen P, Palmquist A. 3D printed Ti6Al4V implant surface promotes bone maturation and retains a higher density of less aged osteocytes at the bone-implant interface. Acta Biomater. 2015.

[392] Wang XJ, Li YC, Lin JG, Hodgson PD, Wen CE. Apatite-inducing ability of titanium oxide layer on titanium surface: the effect of surface energy. J Mater Res. 2008;23:1682-8.

[393] Kokubo T, Miyaji F, Kim H-M, Nakamura T. Spontaneous formation of bonelike apatite layer on chemically treated titanium metals. J Am Ceram Soc. 1996;79:1127-9.

[394] Jonášová L, Müller FA, Helebrant A, Strnad J, Greil P. Biomimetic apatite formation on chemically treated titanium. Biomaterials. 2004;25:1187-94.

[395] Berglundh T, Abrahamsson I, Lang NP, Lindhe J. De novo alveolar bone formation adjacent to endosseous implants. Clinical oral implants research. 2003;14:251-62.

[396] Brauner E, Guarino G, Jamshir S, Papi P, Valentini V, Pompa V, et al. Evaluation of highly porous dental implants in postablative oral and maxillofacial cancer patients: a prospective pilot clinical case series report. Implant Dent 2015;24:631-7.

[397] Scarano A, Perrotti V, Artese L, Degidi M, Degidi D, Piattelli A, et al. Blood vessels are concentrated within the implant surface concavities: a histologic study in rabbit tibia. Odontology. 2013;102:259-66.

[398] Elias CN, Fernandes DJ, Resende CRS, Roestel J. Mechanical properties, surface morphology and stability of a modified commercially pure high strength titanium alloy for dental implants. Dental materials : official publication of the Academy of Dental Materials. 2015;31:e1-e13.

[399] Kim DG, Huja SS, Tee BC, Larsen PE, Kennedy KS, Chien HH, et al. Bone ingrowth and initial stability of titanium and porous tantalum dental implants: a pilot canine study. Implant Dent. 2013;22:399-405.

[400] Simion M, Trisi P, Piattelli A. Vertical ridge augmentation using a membrane technique associated with osseointegrated implants. The International journal of periodontics & restorative dentistry. 1994;14:496-511.

[401] Trisi P, Lazzara R, Rao W, Rebaudi A. Bone-implant contact and bone quality: evaluation of expected and actual bone contact on machined and osseotite implant surfaces. The International journal of periodontics & restorative dentistry. 2002;22:535-45.

[402] Jonitz-Heincke A, Wieding J, Schulze C, Hansmann D, Bader R. Comparative analysis of the oxygen supply and viability of human osteoblasts in three-dimensional titanium scaffolds produced by laser-beam or electron-beam melting. Materials. 2013;6:5398-409.

[403] Aghaloo TL, Moy PK. Which hard tissue augmentation techniques are the most successful in furnishing bony support for implant placement? The International journal of oral & maxillofacial implants. 2007;22 Suppl:49-70.

[404] Peterson B, Whang PG, Iglesias R, Wang JC, Lieberman JR. Osteoinductivity of commercially available demineralized bone matrix. Preparations in a spine fusion model. J Bone Joint Surg Am. 2004;86-A:2243-50.

[405] Esposito M, Grusovin MG, Felice P, Karatzopoulos G, Worthington HV, Coulthard P. The efficacy of horizontal and vertical bone augmentation procedures for dental implants - a Cochrane systematic review. Eur J Oral Implantol. 2009;2:167-84.

[406] Cheng A, Cohen DJ, Boyan BD, Schwartz Z. Laser sintered constructs with bio-inspired porosity and surface micro/nano roughness enhance mesenchymal stem cell differentiation and matrix mineralization in vitro. Calcif Tissue Int (In press). 2016.

[407] Iorio R, Robb WJ, Healy WL, Berry DJ, Hozack WJ, Kyle RF, et al. Orthopaedic surgeon workforce and volume assessment for total hip and knee replacement in the United States: Preparing for an epidemic. J Bone Joint Surg Am. 2008;90:1598-605.

[408] Kilkenny C, Browne W, Cuthill IC, Emerson M, Altman DG. Animal research: Reporting in vivo experiments: The ARRIVE guidelines. Br J Pharmacol. 2010;160:1577-9.

[409] Taniguchi N, Fujibayashi S, Takemoto M, Sasaki K, Otsuki B, Nakamura T, et al. Effect of pore size on bone ingrowth into porous titanium implants fabricated by additive manufacturing: An in vivo experiment. Materials science & engineering C, Materials for biological applications. 2016;59:690-701.

[410] Sakka S, Coulthard P. Bone quality: A reality for the process of osseointegration. Implant Dent. 2009;18:480-5.

[411] Miyamoto I, Tsuboi Y, Wada E, Suwa H, Iizuka T. Influence of cortical bone thickness and implant length on implant stability at the time of surgery—clinical, prospective, biomechanical, and imaging study. Bone. 2005;37:776-80.

[412] Matsuura T, Tokutomi K, Sasaki M, Katafuchi M, Mizumachi E, Sato H. Distinct characteristics of mandibular bone collagen relative to long bone collagen: relevance to clinical dentistry. Biomed Res Int. 2014;2014:9.

[413] Karl M, Freilich M, Wen B, Wei M, Shafer D, Kuhn L. Guided vertical bone regeneration by means of roughened and alkaline treated titanium implant surfaces. J Dent Implantol. 2011;27:145-57.

[414] Schiegnitz E, Palarie V, Nacu V, Al-Nawas B, Kammerer PW. Vertical osteoconductive characteristics of titanium implants with calcium-phosphate-coated surfaces - a pilot study in rabbits. Clin Implant Dent Relat Res. 2014;16:194-201.

[415] Bax EB, Wozney MJ, Ashhurst ED. Bone morphogenetic protein-2 increases the rate of callus formation after fracture of the rabbit tibia. Calcif Tissue Int. 2014;65:83-9.

[416] Bobyn JD, Pilliar RM, Cameron HU, Weatherly GC. Osteogenic phenomena across endosteal bone-implant spaces with porous surfaced intramedullary implants. Acta Orthop Scand. 1981;52:145-53.

[417] Davies JE. Understanding peri-implant endosseous healing. J Dent Educ. 2003;67:932-49.